

Die approbierte Originalversion dieser Dissertation ist an der Hauptbibliothek der Technischen Universität Wien aufgestellt (<http://www.ub.tuwien.ac.at>).

The approved original version of this thesis is available at the main library of the Vienna University of Technology (<http://www.ub.tuwien.ac.at/englweb/>).



DISSERTATION

Suspension-Tire-Behavior Models

ausgeführt zum Zwecke der Erlangung des akademischen Grades eines
Doktors der technischen Wissenschaften unter der Leitung von

Em.O.Univ.-Prof. Projektass. Dipl.-Ing. Dr.techn. Peter LUGNER
E325

Institut für Mechanik und Mechatronik

eingereicht an der Technischen Universität Wien
Fakultät für Maschinenwesen und Betriebswissenschaften

von

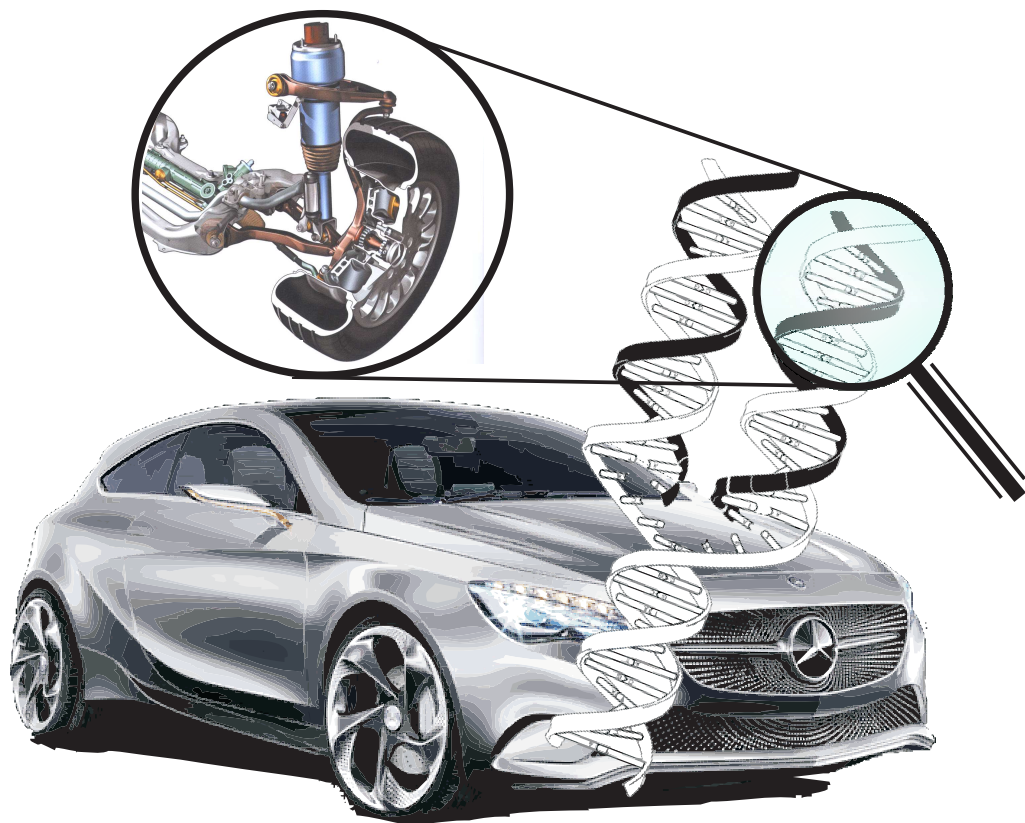
Magnus Lahti M.Sc.

Matrikelnummer: 0728667

Wacholderweg 10/2, 711 39 Ehningen, Deutschland

Wien, im April 2012

Suspension-Tire-Behavior Models



Magnus Lahti
Daimler AG

Ehningen
April 2012

Kurzfassung

Für die erfolgreiche Auslegung eines technischen Systems ist es wichtig, sein dynamisches Verhalten zu kennen. Die Verwendung von Simulationsmodellen stellt dazu einen der besten Zugänge dar. Hierzu ist es wünschenswert, eine Reihe von Simulationsmodellen mit unterschiedlichem Detaillierungsgrad sowie zuverlässige Übergänge zwischen den verschiedenen Modellebenen zur Verfügung zu haben [43].

Das Konzept des Einspurmodells wurde zuerst von Riekert und Schunck beschrieben [46] und ferner in Untersuchungen durch Ammon [1], Kobetz [20] und Meljnikov [34] weiterentwickelt (siehe auch Kapitel 4). Dieses Modellkonzept spielt bereits eine wichtige Rolle bei der Simulation des Fahrverhaltens und der allgemeinen Beschreibung der Fahrdynamik. Ein großer Vorteil dieses Modellansatzes besteht darin, dass seine Modellparameter mit Hilfe von fahrdynamischen Messungen bestimmt werden können. Das Modell beschreibt darüber hinaus das Fahrverhalten in einer Vielzahl von Fahrmanövern und ist ein ausgezeichnetes Werkzeug für den Aufbau eines Verständnisses der Fahrdynamik (siehe auch z.B. die Untersuchungen von Mitschke [36]). Allerdings werden die Modellparameter sehr stark durch die Fahrzeugkonfiguration (Beladungszustand, Bereifung, usw.) und Fahrzeugabstimmung (z.B. Kinematik oder Stabilisatorsteifigkeit) während der Messungen beeinflusst. Sobald eine andere Fahrzeugkonfiguration oder -abstimmung von Interesse ist, sind auch neue Messungen notwendig, um neue Modellparameter bestimmen zu können.

Das Hauptziel dieser Arbeit ist die Weiterentwicklung des Einspurmodells, so dass das Modell auch bei einer Extrapolation auf unterschiedliche Fahrzeugkonfigurationen und -abstimmungen verwendet werden kann, wodurch die oben genannten Nachteile überwunden sind. Die entwickelten Modellerweiterungen sollen eine Extrapolation auf unterschiedliche Reifen- und Fahrwerkseigenschaften (wie z.B. unterschiedliche Stabilisatorsteifigkeit oder ein anderes Wanksteuern) durch Anpassung von Parameterwerten im Modell erlauben. Das Modell soll auch eine Extrapolation auf verschiedene Beladungsvarianten (Masse und Massenverteilung) mit einfachen Ansätzen zulassen. Um dies zu realisieren, sind die vorderen und hinteren Seitenkraftkennlinien durch ein *Fahrwerk-Reifen-Wirkungsmodell* ersetzt worden, in welchem die Eigenschaften des Reifens und die Eigenschaften der Radaufhängung in eigenständigen Teilmodellen behandelt werden. Als Eingang für die Teilmodelle der Radaufhängung dienen Fahrzeugbewegungsgrößen. Diese Teilmodelle berechnen die vertikalen Radlasten, den Reifensturzwinkel und den Schräglaufwinkel, welche ferner als Eingaben für das Reifenmodell *Magic Formula MF-Tyre model Version 5.2* [51] verwendet werden. Schließlich werden die Seitenkräfte $F_{y,i}$ und die Rückstellmomente $M_{z,i}$ des Reifens ermittelt und in einem Synthese-Element in eine vordere und hintere Achsseitenkraft übertragen, um in den Bewegungsgleichungen des

Einspurmodells verwendet werden zu können.

In den weiteren Abschnitten wird ein Verfahren zur Bestimmung der Parameter des erweiterten Einspurmodells vorgestellt und eine Modellvalidierung durchgeführt, um die erreichte Genauigkeit festzustellen. Anstelle reale fahrdynamische Messungen zu verwenden, werden virtuelle Messungen an dem detaillierten MKS-Modell CASCADE-DA durchgeführt. Die Verwendung von Simulationen statt Messungen erlaubt die unmittelbare und gründliche Untersuchung, wie verschiedene Fahrzeugkonfigurationen oder -abstimmungen das Fahrverhalten beeinflussen. Darüber hinaus sind die erstellten Ergebnisse reproduzierbar, und Verfälschungen der Messdaten werden vermieden oder bei Bedarf synthetisch hinzugefügt.

Schließlich wird die Extrapolationsfähigkeit des entwickelten Modells untersucht. Zuerst wird gezeigt, dass sehr große Variationen der Stabilisatorsteifigkeit mit diesem Modell extrapoliert werden können. In einem zweiten Schritt wird dessen Extrapolationsfähigkeit auf andere Reifeneigenschaften nachgewiesen. In einem letzten Schritt werden Extrapolationen auf verschiedene Beladungszustände getestet. Für Fahrzeuge mit einer automatischen Niveauregulierung sind die vorgeschlagenen Extrapolationsansätze für verschiedene Beladungen genauso erfolgreich wie in den sonstigen Extrapolationsuntersuchungen. Bei Fahrzeugen ohne eine automatische Niveauregulierung, wie z.B. bei Radaufhängungen mit normalen Stahlfedern und herkömmlichen Dämpfern, sind die Extrapolationsansätze für verschiedene Beladungen nur erfolgreich bis zu einer stationären Querbeschleunigung von etwa 5.5 m/s^2 . Der Hauptgrund für das Nichterreichen der gleichen Genauigkeit in diesem Fall ist die Veränderung des statischen Einfederweges aufgrund der unterschiedlichen Beladungszustände, wodurch nicht nur unterschiedliche Rollzentrumshöhen, sondern auch eine Veränderung der Elastokinematik aufgrund der unterschiedlichen Kraftangriffspunkte in der Radaufhängung entstehen. Daher müssen die Parameter für die Elastokinematik (Spur- und Sturzwinkel) sowie die Rollzentrumshöhen für die verschiedenen Einfederwege angepasst werden. Die kinematischen Veränderungen aufgrund der unterschiedlichen Einfederzustände bei verschiedenen Beladungen sind bereits durch die Verwendung der Ergebnisse des Kinematikprüfstands berücksichtigt. Allerdings konnte ein Ansatz zur Untersuchung der veränderten Elastokinematik bei unterschiedlichen Einfederwegen nicht in diese Untersuchungen einbezogen werden und bleibt daher Gegenstand künftiger Arbeiten.

Abstract

For a successful design of an engineering system, it is essential to pay attention to its dynamic behavior. One of the best ways of doing this is by using simulations and for this, a range of simulation models with different levels of detail as well as reliable transitions between the different model levels is often desired [43].

The 2-wheel model concept as first described by Riekert and Schunck [46] and further developed in for instance Ammon [1], Kobetz [20] and Meljnikov [34] (see also Chapter 4) already plays an important role in simulating vehicle handling and describing vehicle dynamics. A major advantage of this model concept is that its model parameters can be identified using driving measurements of the vehicle of interest. The model furthermore describes vehicle handling in a wide range of driving maneuvers and is an excellent tool for understanding vehicle dynamics (see for instance the investigations by Mitschke [36]). The model parameters are, however, very specific for the particular vehicle set-up during the parameterization process, e.g. load condition, type of tires, etc. Any variation in vehicle set-up would consequently require a new set of driving measurements in order to identify new model parameters.

The main objective of this work is the further development of an extended 2-wheel model in order to overcome the model's drawbacks regarding extrapolation to different vehicle setups. Consequently, the developed model extensions enable an extrapolation to different tire properties and to different suspension setups (like for instance different anti-roll bar stiffness or different amount of roll steer) by changing parameter values in the model. The model also allows the vehicle behavior to be extrapolated for different loading conditions (mass and mass distribution) with simple approaches to change the model parameters. To realize this, the front and rear lateral axle force characteristics have been replaced by a *suspension-tire-behavior model* where the tire properties and the suspension properties have been separated in submodels. The suspension submodels use vehicle motion states as inputs when calculating the vertical tire load, tire camber angle and lateral side slip angle, which furthermore are used as inputs in the tire model, *Magic Formula MF-Tyre model version 5.2* [51]. Finally, the lateral tire forces, $F_{y,i}$, and tire aligning moments, $M_{z,i}$, calculated by the tire model are included in a synthesis element to a front and rear axle lateral force to be used in the 2-wheel model's equations of motion.

A method to identify the parameters in the extended 2-wheel model is furthermore presented followed by a validation of the model accuracy. Instead of using real driving measurements as a target in this process, virtual measurements were created with the detailed MBS model CASCaDE-DA. The use of simulations instead of measurements allow instant and thorough investigations of how a specific change in the vehicle setup influences the handling behavior. In addition, the received results are reproducible and unwanted influences from the environment

as well as problems connected with measurement data may be avoided or, if wanted, they can be added synthetically.

Last but not least, the extrapolation ability of the developed model is investigated. First, it is shown that even very severe anti-roll bar setups can be extrapolated with this model. In a second step, the extrapolation to different tire properties are done successfully. In a final step, extrapolation to different load variations have been tested. For vehicles equipped with an automatic ride height control system, the suggested approaches for extrapolation to different load conditions are as successful as for the previous extrapolation investigations. In case of vehicles without an automatic ride height control system, e.g. suspensions with normal coil springs and conventional dampers, the load extrapolation is only successful to a steady-state lateral acceleration of approximately 5.5 m/s^2 . The main reason for not reaching the same accuracy in this case is the change in initial suspension deflection due to the different loading condition, causing not only different roll center heights but also a change in the suspension compliance due to the different point of action for the forces acting in the suspension. Hence, the parameters regarding the suspension compliance (steer and camber angles) as well as the roll center heights would have to be adjusted for the different suspension deflections. The kinematic changes due to the different initial suspension deflection at different vehicle load conditions already have been taken into account by using the results from the kinematic test bench. However, to find an approach to calculate the new compliance behavior at different suspension deflections could not be included in these investigations and has therefore been left for future work.

Acknowledgements

This research project was carried out at the department *Vehicle Dynamics* in the area Group Research and Advanced Engineering at Daimler AG in collaboration with the Institute of Mechanics and Mechatronics at Vienna University of Technology, TU-Wien.

First of all I would like to thank Prof. Peter Lugner at TU-Wien for his valuable guidance and for providing me with feed-back throughout this work. I would also like to thank my senior manager Prof. Dieter Ammon for initiating this reseach project in the first place and for being a very important discussion partner regarding technical details of the work and for keeping me on track in this project. Furthermore my supervisor at Daimler AG, Dr. Jochen Rauh also deserves a special thanks and a lot of credit for his invaluable technical support and source of inspiration as well as giving me many important advices along the road. A thanks also goes to Prof. Bernhard Geringer at TU-Wien for his helpful support.

To all my colleagues at Daimler AG; thanks to you it has been a pleasure (and still is) to come to work every day. Many of you have also more or less contributed (direct and/or indirect) to my work with everything ranging from simple encouragements up to discussions and tips regarding technical issues. This is something I value very much and I'd like to mention a special thanks to Christoph Däsch who together with me worked in the project *Model Based Testing* where we even drove our 2-wheel models on the driving simulator. It is beyond doubt that all our work together has been a source to this work. I would also like to mention a few colleagues by name; Dr. Jürgen Haug, Thomas Schirle, Dr. Stephanie Knorr, Wolfgang Hurich, Steven Lange and Dr. Karl-Joseph Rieger, you have all in one way or another supported me throughout this work, thank you.

A special thanks also goes out to both my parents, without you I would never have been able to achieve this. Last but not least I would like to thank my wife, Shauna Dinelle, not only for her patience and understanding but also for her support in reading and correcting my english writing.

Magnus Lahti

Ehningen, April 2012

Contents

1	Introduction	1
1.1	Problem statement and purpose of this investigation	4
1.2	Literature overview	7
1.3	Conclusion of literature overview	10
2	Reference models	11
2.1	A CASCaDE overview	12
2.2	The CASCaDE-DA model	14
2.3	The CASCaDE-Classic model	15
2.3.1	Kinematics in the Classic model	15
2.3.2	Non-linear compliance approach	15
2.4	The used tire model – Magic Formula Version 5.2	16
2.5	The used reference vehicles	17
3	Direct and indirect factors influencing vehicle steering behavior	21
3.1	Static toe angles	22
3.2	Front steer angles	24
3.3	Rear steer angles	25
3.4	Camber angles	26
3.5	Track width change	27
3.6	Vertical tire load	27
3.6.1	Static weight distribution	27
3.6.2	Vertical load transfer during cornering	27
3.7	Driving/Braking forces	29
3.8	Aligning moment	30
4	2-wheel vehicle model	31
4.1	Equations of motion	32
4.2	Steering system	33
4.3	Kinematics	33
4.4	Lateral force characteristics	34
4.5	Lateral force dynamics	34
4.6	Roll degree of freedom	36
4.7	Simulation results with the 2-wheel model	37
5	A common base of comparing the 2-wheel with 3D-vehicle models	39
5.1	A first example of comparison	39

5.2	Method to consider important effects	43
6	Sensitivity analysis of suspension properties	49
6.1	Sensitivity of side slip angle	51
6.2	Sensitivity of vertical load transfer	56
6.3	Sensitivity of camber angle	59
6.4	Summary	62
7	The extended 2-wheel model	63
7.1	Structure of the model for lateral dynamics	65
7.2	Structure of the roll dynamics model	66
7.3	Axle force and moment element	70
7.4	Approach for tire normal force	72
7.5	Approach for suspension kinematics and compliance.	74
	7.5.1 Steer angles and tire side slip angles	75
	7.5.2 Tire camber angle	78
7.6	Summary of Chapter 7	79
8	The extended 2-wheel model – parameter identification process	81
8.1	The identification maneuver	81
8.2	The selected tire characteristics	82
8.3	Parameterization process	84
	8.3.1 Geometric and mass properties	84
	8.3.2 Parameters for the elastic roll moment characteristics	85
	8.3.3 Parameters for the roll damping characteristics	90
	8.3.4 Parameters for the steer angle approach	92
	8.3.5 Parameters for the tire camber angle approach	94
	8.3.6 Identification process	97
8.4	Resulting accuracy	98
9	The extended 2-wheel model – model verification	103
9.1	The verification maneuver	103
9.2	Simulation results	104
9.3	Test-to-test variation in real vehicle testing	108
10	Extrapolation using the extended 2-wheel model	111
10.1	Extrapolation to different anti-roll bar setups	111
	10.1.1 Investigated anti-roll bar setups	111
	10.1.2 Extrapolation approach for different anti-roll bar setups	115
	10.1.3 Extrapolation results for anti-roll bar setup 4 – ARB 4	115
10.2	Extrapolation to different tire characteristics	117
	10.2.1 Investigated tire characteristics	117
	10.2.2 Extrapolation approach for different tire characteristics	120
	10.2.3 Extrapolation results for different tire characteristics	120
10.3	Extrapolation to different loading conditions	122
	10.3.1 Investigated loading conditions	122
	10.3.2 Extrapolation approach for different loading conditions	124

10.3.3 Extrapolation results for load variation L2 and L3	126
10.3.4 Extrapolation results for load variation L4 and L5	129
11 Conclusions	133
References	136
Appendices	140
A Nomenclature	141
A.1 Common definitions and terminology	141
A.2 Abbreviations	141
A.3 Notation	142
A.4 Subscripts	142
A.5 Superscripts	143
B Additional extrapolation results	145
B.1 Anti-roll bar extrapolation results	146
B.1.1 Extrapolation results for ARB 2	146
B.1.2 Extrapolation results for ARB 3	147
B.1.3 Extrapolation results for ARB 5	148

Figures

1.1	Model classes with different level of model complexity.	2
1.2	Block representation of the conventional 2-wheel model.	5
1.3	Block representation of the suspension-tire model.	6
2.1	A CASCaDE overview presenting possible applicable tools.	12
2.2	Suspension components displayed for the CASCaDE-DA vehicle model.	14
2.3	Kinematics and compliance displacements shown for a wheel in the CASCaDE-Classic vehicle model.	16
2.4	Input and output vector of the Magic Formula Tire Model.	17
2.5	Illustration of a double wishbone suspension.	18
2.6	Illustration of a multi link suspension.	19
3.1	Explanation of steering behavior during a constant radius steady-state cornering.	21
3.2	Static steer angles indicating toe-in and toe-out.	22
3.3	Description of the influence of static steer angles at corner entry.	23
3.4	Ideal steer angles during cornering for side slip free rolling.	24
3.5	Simplified illustration of compliance steer.	24
3.6	Illustration of rear axle roll steer.	25
3.7	Definition of the tire camber angle and relation of camber angle vehicle roll angle.	26
3.8	Non-linear relation between lateral tire force and vertical tire load.	28
3.9	Description of the influence of static toe angles on the total lateral axle force when assuming linear vertical load dependence in the tire characteristics.	28
3.10	Example of how the longitudinal force influences the lateral force during combined slip conditions.	29
4.1	Vehicle seen from above describing the 2-wheel model concept.	31
4.2	Definitions and geometry of the simplified 2-wheel vehicle model	32
4.3	Steering ratio as a function of the steering wheel angle.	33
4.4	2-wheel model's lateral axle force characteristics.	35
4.5	Illustration of the roll model including cutting forces.	36
4.6	Measurement data in comparison with simulation results with the 2-wheel model in a double lane change maneuver.	38
4.7	Measurement data in comparison with simulation results with the 2-wheel model in a double lane change maneuver.	38
5.1	Comparison of the lateral forces in a 2-wheel model and a full vehicle model.	39
5.2	Block representation of the procedure for deriving the common base for comparing a 2-wheel model with a 3D-vehicle model.	40
5.3	Reference figures for the maneuver used in the sensitivity analysis.	41

5.4	Front (a) and rear (b) lateral axle force characteristics in the 2-wheel model. . .	42
5.5	Lateral force characteristics of the 2-wheel model in comparison to the summarized lateral tire forces in the 4-wheel model.	43
5.6	Illustration of the relation between the lateral tire force F_y and the self aligning moment M_z	44
5.7	Lateral force characteristics of the 2-wheel model in comparison to the summarized lateral tire forces in the 4-wheel model including the effect of the aligning moment.	45
5.8	$F_{y,j}^A$ in comparison to $F_{y,j}^{2T}$ when including the effect of the yaw moment caused by the longitudinal forces, Equation (5.9) and (5.10).	45
5.9	$F_{y,j}^A$ in comparison to $F_{y,j}^{2T}$ when including the steer angle contribution when calculating $F_{y,j}^{2T}$	46
5.10	$F_{y,j}^A$ in comparison to $F_{y,j}^{2T}$ when including the contribution to yaw moment from $J_\psi \dot{\Psi}$, Equation (5.13) and (5.14).	47
5.11	Illustration of the fore and aft movement of the wheels during cornering, causing a change of effective lever arm for the lateral force in the 2-wheel model. . . .	48
6.1	Investigation procedure for the sensitivity analysis of the suspension properties.	50
6.2	Illustration of vehicle kinematics used in a simplified expression for the side slip angle.	52
6.3	Resulting equivalent lateral axle force $F_y^{2T}(\alpha^A)$ due to a 10 % increase in side slip angle, in comparison to the originally identified lateral axle force $F_y^A(\alpha^A)$ of the 2-wheel model.	54
6.4	Resulting equivalent lateral axle force $F_y^{2T}(\alpha^A)$ when ignoring the change of steer angles at each tire due to kinematics and compliance, i.e. using the corresponding axle side slip angle α^A (as defined for the 2-wheel model) as side slip angle input to each tire.	54
6.5	Steer angles during the steady-state maneuver.	55
6.6	Resulting equivalent lateral axle force $F_y^{2T}(\alpha^A)$ when subtracting the static steer angle from the side slip angle at each tire.	55
6.7	Resulting equivalent lateral axle force $F_y^{2T}(\alpha^A)$ due to a 10 % increased vertical load transfer, in comparison to the originally identified lateral axle force $F_y^A(\alpha^A)$	57
6.8	Resulting equivalent lateral axle force $F_y^{2T}(\alpha^A)$ when the load transfer is excluded. This in comparison to the originally identified lateral axle force $F_y^A(\alpha^A)$	57
6.9	Lateral tire force plotted as a function of vertical load for two side slip angles.	58
6.10	As in Figure 6.9 but with lateral tire characteristics operating in the non-linear range of vertical load dependency.	58
6.11	Tire camber angles during the steady-state maneuver.	59
6.12	Resulting equivalent lateral axle force $F_y^{2T}(\alpha^A)$ due to a 10 % increase in tire camber angles in comparison to the identified original axle force $F_y^A(\alpha^A)$	60
6.13	Resulting equivalent lateral axle force $F_y^{2T}(\alpha^A)$ when the tire camber angles are set to zero.	61
6.14	Resulting equivalent lateral axle force $F_y^{2T}(\alpha^A)$ when the tire camber angle of each tire is set to be equal to the vehicle roll angle.	61

6.15	Resulting equivalent lateral axle force $F_y^{2T}(\alpha^A)$ when subtracting the static camber angle $\gamma_{0,i}$ from the total tire camber angle, caused by vehicle roll.	62
7.1	Outline of the tire suspension model.	63
7.2	Definitions and geometry of the extended 2-wheel vehicle model.	65
7.3	Illustration of the roll model including cutting forces.	67
7.4	Mass geometry of the vehicle roll model with an inclined roll axis.	68
7.5	Full view of the vehicle roll model.	69
7.6	Axle force and moment element in the extended 2-wheel model.	70
7.7	Yaw torque contributions from the components in Equation (7.17) and (7.18) over lateral acceleration during a steady-state maneuver.	71
7.8	Vertical load transfer during steady-state cornering on a vehicle (rear side).	72
7.9	Summarized vertical tire load of the inner and outer wheel pair during steady-state cornering.	73
7.10	Change of center of gravity height h_{CG} depending on lateral acceleration a_y during steady-state cornering (not with the reference vehicle).	74
7.11	In (a) the front steer angles δ_1 and δ_2 in relation to the rack displacement y_r (reference vehicle A).	75
7.12	Basic illustration of the compliance steer approach.	76
7.13	In (a) the steer angle at the front right wheel δ_2 as a function of roll angle in the test bench maneuver AJR and in (b) the same for the rear right wheel δ_4	77
7.14	Tire side slip angle.	77
7.15	Illustration of the tire camber angles, γ_i , and the camber angles in relation to the vehicle body, ϵ_i (rear axle).	78
7.16	In (a) the tire camber angles at the front axle, γ_1 and γ_2 , in relation to the rack displacement y_r (reference vehicle A).	79
8.1	Rack displacement and vehicle velocity during the identification maneuver.	82
8.2	Lateral tire force and aligning moment characteristics at pure side slip condition.	83
8.3	Tire cornering stiffness as a function of vertical tire load and tire dynamics.	83
8.4	Vertical force at the wheel hub over suspension deflection, $F_{z,hub,i}(\Delta z_i)$	86
8.5	Suspension roll moment over suspension roll angle, $M_{\phi,j}(\phi_{su,j})$, from the maneuvers SJR and AJR ; front axle in (a) and rear axle in (b).	87
8.6	In (a) the different starting points when derivating the roll moment characteristics for the two load cases (<i>base</i> and $+500N$) and in (b) the resulting roll moments from the SJR maneuver, $M_{\phi,SJR,r}(\phi_{su,r})$; here exemplified for the rear axle.	88
8.7	Total vehicle roll angle ϕ composed by suspension roll angle ϕ_{su} and roll angle due to vertical tire deflection ϕ_{ti}	89
8.8	Anti roll bar lever arm.	89
8.9	Approximated geometry for calculating damping ratio and damper velocities.	90
8.10	In (a) the damping characteristics in the front axle shock absorber and in (b) the resulting roll damping characteristics for the front axle, $M_{\phi,f}$ (reference vehicle A).	91
8.11	In (a) the damping characteristics in the rear axle shock absorber and in (b) the resulting roll damping characteristics for the rear axle, $M_{\phi,r}$ (reference vehicle A)	91

8.12	In (a) the front steer angles δ_1 and δ_2 in relation to the rack displacement y_r (reference vehicle A).	92
8.13	Front axle steering characteristics.	93
8.14	Rear axle steering characteristics.	93
8.15	In (a) the tire camber angles at the front axle, γ_1 and γ_2 , in relation to the rack displacement y_r (reference vehicle A).	95
8.16	In (a) the front right suspension camber angle as a function of wheel travel, $\epsilon_2(\Delta z_2)$, during the maneuvers SJR and AJR . In (b) the resulting tire camber angle as a function of suspension roll angle, $\gamma_2(\phi_{su,f})$, derived from the AJR maneuver.	95
8.17	In (a) the rear right suspension camber angle as a function of wheel travel, $\epsilon_4(\Delta z_4)$, during the maneuvers SJR and AJR . In (b) the resulting tire camber angle as a function of suspension roll angle, $\gamma_4(\phi_{su,r})$, derived from the AJR maneuver.	96
8.18	Lateral acceleration a_y in comparison between the CASCaDE model (solid line) and the extended 2-wheel model (dashed line).	99
8.19	Yaw rate $\dot{\Psi}$ in comparison between the CASCaDE model (solid line) and the extended 2-wheel model (dashed line).	100
8.20	Vehicle side slip angle β in comparison between the CASCaDE model (solid line) and the extended 2-wheel model (dashed line).	100
8.21	Roll angle ϕ in comparison between the CASCaDE model (solid line) and the extended 2-wheel model (dashed line).	101
9.1	Rack displacement during the verification maneuver.	104
9.2	Comparison between the CASCaDE model (solid line) and the extended 2-wheel model (dashed line). In (a) lateral acceleration a_y and in (b) yaw rate $\dot{\Psi}$	104
9.3	Comparison between the CASCaDE model (solid line) and the extended 2-wheel model (dashed line). In (a) vehicle side slip angle β and in (b) vehicle roll angle ϕ	105
9.4	Comparison between the CASCaDE model (solid line) and the extended 2-wheel model (dashed line). In (a) lateral acceleration a_y and in (b) a zoomed view of the figure in (a).	105
9.5	Comparison between the CASCaDE model (solid line) and the extended 2-wheel model (dashed line). In (a) yaw rate $\dot{\Psi}$ and in (b) a zoomed view of the figure in (a).	106
9.6	Comparison between the CASCaDE model (solid line) and the extended 2-wheel model (dashed line). In (a) vehicle side slip angle β and in (b) a zoomed view of the figure in (a).	106
9.7	Comparison between the CASCaDE model (solid line) and the extended 2-wheel model (dashed line). In (a) vehicle roll angle ϕ and in (b) a zoomed view of the figure in (a).	107
9.8	Driving robot implemented in test vehicle, from [49].	108
9.9	Resulting lateral acceleration a_y and yaw rate $\dot{\Psi}$ during 8 step-steer maneuvers.	109
9.10	Resulting vehicle side slip angle β and vehicle roll angle ϕ during 8 step-steer maneuvers.	110

9.11	Vehicle longitudinal velocity v_x during the 8 step-steer maneuvers.	110
10.1	Comparison of the lateral acceleration achieved with the different ARB configurations ARB 1 to ARB 5	113
10.2	Comparison of the yaw rate achieved with the different ARB configurations ARB 1 to ARB 5	113
10.3	Comparison of the vehicle side slip angle achieved with the different ARB configurations ARB 1 to ARB 5	114
10.4	Comparison of the roll angle achieved with the different ARB configurations ARB 1 to ARB 5	114
10.5	Extrapolation results for ARB 4 , lateral acceleration and yaw rate.	115
10.6	Extrapolation results for ARB 4 , vehicle side slip angle and roll angle.	116
10.7	Lateral force and aligning moment characteristics of tire 1 and 2 at pure side slip condition.	118
10.8	Tire cornering stiffness as a function of vertical tire load and tire dynamics for tire 1 and 2.	118
10.9	Comparison in vehicle response with tire 1 and tire 2, lateral acceleration and yaw rate.	119
10.10	Comparison in vehicle response with tire 1 and tire 2, vehicle side slip angle and roll angle.	119
10.11	Extrapolation results for tire 2, lateral acceleration and yaw rate.	120
10.12	Extrapolation results for tire 2, vehicle side slip angle and roll angle.	121
10.13	Loads for the mass variations.	122
10.14	Comparison of simulation outputs for the different load variations L1-L5 , lateral acceleration and yaw rate.	123
10.15	Comparison of simulation outputs for the different load variations L1-L5 , vehicle side slip angle and roll angle.	124
10.16	New sprung mass height due to suspension deflection.	125
10.17	Extrapolation results for load variation L2 , lateral acceleration and yaw rate.	126
10.18	Extrapolation results for load variation L2 , vehicle side slip angle and roll angle.	127
10.19	Extrapolation results for load variation L3 , lateral acceleration and yaw rate.	128
10.20	Extrapolation results for load variation L3 , vehicle side slip angle and roll angle.	128
10.21	Extrapolation results for load variation L4 , lateral acceleration and yaw rate.	130
10.22	Extrapolation results for load variation L4 , vehicle side slip angle and roll angle.	130
10.23	Extrapolation results for load variation L5 , lateral acceleration and yaw rate.	131
10.24	Extrapolation results for load variation L5 , vehicle side slip angle and roll angle.	132
11.1	Outline of the tire suspension model.	133
B.1	Extrapolation results for ARB 2 , lateral acceleration and yaw rate.	146
B.2	Extrapolation results for ARB 2 , vehicle side slip angle and roll angle.	146
B.3	Extrapolation results for ARB 3 , lateral acceleration and yaw rate.	147
B.4	Extrapolation results for ARB 3 , vehicle side slip angle and roll angle.	147
B.5	Extrapolation results for ARB 5 , lateral acceleration and yaw rate.	148
B.6	Extrapolation results for ARB 5 , vehicle side slip angle and roll angle.	148

Tables

2.1	Reference vehicle overview.	18
6.1	Results for disturbing the side slip angles during steady-state cornering.	53
6.2	Results for disturbing the vertical load transfer during steady-state cornering.	56
6.3	Results for disturbing the camber angles during steady-state cornering.	60
8.1	Mass and geometry parameters.	85
8.2	Parameters for elastic roll moment characteristics.	88
8.3	Parameters for roll damping characteristics	91
8.4	Parameters for the steer angle approach.	94
8.5	Parameters for the tire camber angle approach.	96
8.6	Start and end values in the optimization process.	98
8.7	Root mean square (RMS) error and maximum error listed for the model outputs during the verification maneuver.	99
9.1	Root mean square (RMS) error and absolute value of the maximum error listed for the model outputs during the verification maneuver.	107
9.2	Resulting envelope maximum deviation and RMS deviation during 8 step-steer maneuvers.	109
10.1	Investigated anti-roll bar set-ups.	112
10.2	Root mean square (RMS) error and maximum error for the extrapolation results with ARB 4	116
10.3	Root mean square (RMS) error and maximum error for the extrapolation results with tire 2.	121
10.4	Mass geometry and principal moments of inertia of the loads used to create the load variations L1 (base vehicle), L2 and L3 , see also Table 10.5.	122
10.5	Most relevant extrapolated mass parameters in the extended 2-wheel model for the different load variations.	126
10.6	Root mean square (RMS) error and maximum error for the extrapolation results with load variation L2	127
10.7	Root mean square (RMS) error and maximum error for the extrapolation results with load variation L3	128
10.8	Root mean square (RMS) error and maximum error for the extrapolation results with load variation L4	130
10.9	Root mean square (RMS) error and maximum error for the extrapolation results with load variation L5	131

Chapter 1

Introduction

In order to improve traffic safety, great efforts are made to enhance vehicle dynamics regarding handling. This requires a good understanding of the system interaction between vehicle, driver and environment, i.e. the resulting vehicle reactions to driver inputs as well as the response due to environmental interferences. In this aspect, the handling properties of the vehicle have to be adjusted to fit the skills of the driver. The vehicle has to have a steady straight line stability, high cornering speed limit, the best possible manageable behavior in non stationary states and give clear and correct state feedback to the driver [53].

The design of the wheel suspension in a car regarding its handling properties is, and always has been, done through testing and experience. Throughout the years, systematic testing procedures have been developed in the form of driving maneuvers with corresponding evaluation criteria and serve today as an important tool in the development process. With shorter product life cycles and with a steady increase in complexity due to new technologies, the relative time for testing with prototypes is also becoming shorter. With this, the quality requirements can only be fulfilled by a more efficient development process and in this sense, the application of CAE (Computer Aided Engineering) is of indisputable importance. The traditional recursive development method with the use of a prototype still remains the main method. However, by the use of simulation analysis, it is possible to build these prototypes more target oriented from the beginning and thus save valuable time. Additionally, after the prototype has been built, simulation keeps serving as an analysis tool revealing the progressive changes for further improvements.

The characteristics of the wheel suspensions have an essential impact on the ride and handling properties of a vehicle. Furthermore, the interaction between different effects and their consequences on the vehicle dynamics are difficult to overview due to the multiplicity of operating conditions of the suspensions. Indeed the tires have the largest impact on vehicle handling, however, the extent in which the potential of the tires are exploited, highly depends on the properties of the suspensions. The wheel suspensions of today are designed in order to position the wheels as accurately as possible, dependent of vertical wheel travel and steering inputs. In addition, compliance¹ effects are built in by design so that the wheel position is also changing with external load [22]. Without the possibility of computer simulations, the solution of this

¹Definition: The characteristic of deforming under external load

complex non-linear optimization problem is, as earlier mentioned, left out to the intuition and experience of the development engineers. As a matter of fact, simulation is an ideal tool in order to examine the impacts of structural changes under arbitrary conditions, i.e. making the effect of certain changes transparent to the developer. Through simulation, the influences on other criteria due to a specific change can rapidly be analyzed. In addition, the received results are reproducible and unwanted influences from the environment as well as problems connected with measurement data may be avoided or, if wanted, they can be added synthetically.

It is important though that simulation models are not deployed as a sort of *black box*. If using the model without considering its limits and drawbacks, essential features of the system may be obscured, leading to a false evaluation of the system and in the end leaves the user with useless results. In order to use simulation efficiently, it is very important to be aware of the characteristics, limitations and possibilities of an applied model [32]. The choice of model complexity is furthermore a key tradeoff in the art of CAE. This choice should be made so that the model is reproducing all considered effects in the analyzed system. Since this demand in many cases is more or less fulfilled by a larger range of models, a rule of thumb is to choose the model with the least level of complexity. Ideally, engineers would use a very detailed *Multi Body System* (MBS) vehicle model in combination with an optimization strategy to find the best design. However, solving the optimization problem with many competing targets for the complete system is generally considered too complex. Instead, the problem may be broken down at several levels where in one step, the overall targets of the suspension are specified by the use of a behavior model of less complexity, and in the next step, a more detailed model is used to refine the design parameters of the vehicle [6]. It must therefore be a major goal to have a complete model family, which guarantees reliable transitions between the different model levels [43].

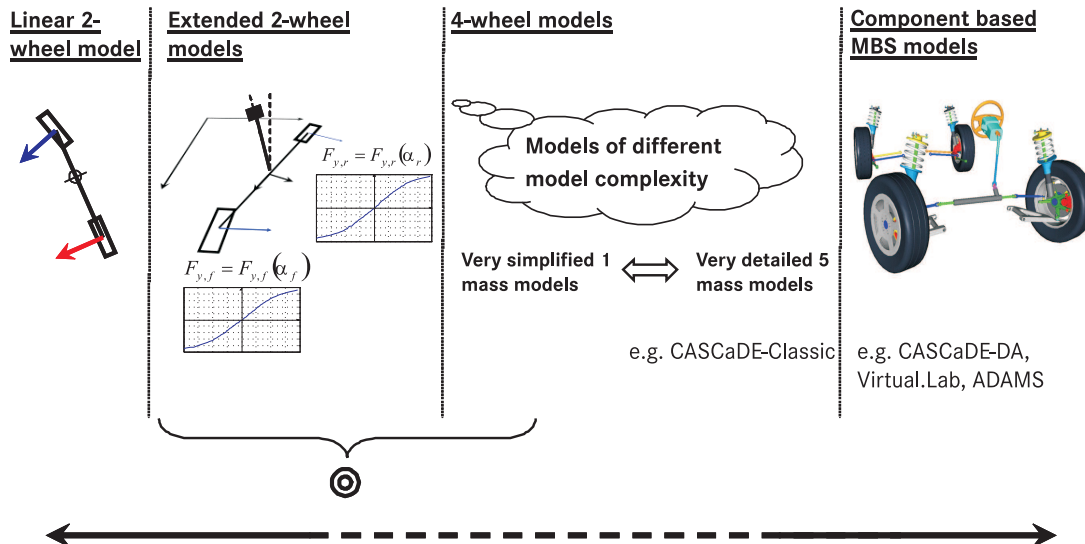


Figure 1.1: Model classes with different level of model complexity.

When discussing vehicle handling models, it is important to first define different complexity levels and their corresponding boundary conditions. Starting with the so called behavior models, see left side of Figure 1.1, simple physical relations are used to explain and analyze vehicle

dynamics. Models of this type are derived by analyzing the complete real system and summarizing different features into common properties. Among these models, the conventional *linear 2-wheel model* from Riekert and Schunck [46] is here defined to be the basic level. The next class is the *extended 2-wheel model*, where non-linearities are introduced in order to extend the model's validity range. The level of extension might vary within this model class depending what the model is intended for, but the modeling concept with the 2-wheel model as the base is still obvious. On the third modeling level, *the 4-wheel models*, the model complexity level within the model concept is not clearly defined since some 4-wheel models are modeled as five mass models, i.e. one body mass and four wheel masses, whereas other 4-wheel models only take the body mass into consideration neglecting the wheel masses. In addition, the level of complexity in how the kinematics and compliance of the suspension are modeled as well as simplifications in the equations of motion varies. A model within this class is one of the reference models for this investigation, the so called CASCaDE²-Classic model, which is described in Section 2.3. The top level considered here embraces the *component based MBS models* where every link and bushing in the suspension is considered as components in the models. An example in this model class is the second reference model in this investigation, the CASCaDE-DA model, described in Section 2.2. Other examples can be found in commercial tools like ADAMS [37] and Virtual.Lab [26]. Vehicle models in this class are certainly 4-wheel models as well but are depicting the suspension dynamics less abstract than the functional suspension models. Consequently these models are more complex due to the additional components that have to be modeled and parameterized, but at the same time are easier to relate to since they are assembled from components related to real parts, e.g. the models have moveable linkage hard points and bushing stiffness which is the case with a real vehicle as well.

Further aspects of the model classes presented in Figure 1.1 are:

- performance range
- transparency of model parameters and characteristics
- exchangeability – analysis potential

The first point, performance range, defines to what extent the model is valid. On the side of the behavior models, the quality of the models strongly depends on the implemented extensions and the range in which the model parameters have been identified. The output quality of these models can therefore be very good in a specific situation and worthless in another. On the other side of the complexity range in Figure 1.1, the component based MBS models, the system behavior is closer to a real vehicle for all driving situations and the performance range can therefore be considered larger in general. This, however, does not say anything about the accuracy of the results which in certain maneuvers can be as good in a behavior model as in a complex MBS model.

The transparency of model parameters is the second aspect distinguishing the different model classes, i.e. how easy it is to understand how, and in what extent, each parameter influences the total vehicle behavior. The model parameters in a behavior model are relatively few and

²CASCaDE stands for *Computer Aided Simulation of Car, Driver and Environment* and is the name of an in-house developed CAE-tool at Daimler AG

therefore easy to overview. The influence of each parameter is also more or less easy to understand. It can therefore be said that the transparency of a behavior model is evident. This is normally not the case for the component based MBS models as the amount of required model parameters tends to grow immensely when using models more to the right in Figure 1.1, with sinking model transparency as a result.

The third property, exchangeability, regards the extent in which the model can be used in system analysis. In a behavior model, each parameter or function is a conclusion of different effects in the vehicle and suspension. This makes it feasible, at least in theory, to exchange or modify a behavior parameter without thinking of how to realize this change in a real vehicle. In a behavior model the overall rear axle stiffness can, for instance, be changed by varying only one parameter. In the model class to the very right in Figure 1.1, the component based MBS models, this is a more challenging task since the axle stiffness can be tuned by changing a lot of different parameters which have cross influences on other effects as well. Conversely, the more complex models allow single components to be exchanged in order to perform a component based analysis such as investigating different damper settings.

1.1 Problem statement and purpose of this investigation

The main objective of this investigation is the model class defined as the *extended 2-wheel model*, second from the left in Figure 1.1. Such a model, a non-linear 2-wheel model including a roll model like the one presented in Chapter 4 (see also Ammon [1], Kobetz [20] and Meljnikov [34]), represents the vehicle handling behavior in a wide range of driving maneuvers. Its model parameters can be identified from driving measurements with the vehicle of interest. These model parameters are physical valued but yet abstract in a way since one parameter can cover a wide range of vehicle properties. An example of this is the axle force characteristics of the 2-wheel model, which describes the force generation at that axle; hence it contains the properties of the two tires and their interaction with the suspension while generating vehicle lateral forces. This type of model also makes the model parameters very specific for the vehicle setup used during the measurements, e.g. loading condition, type of tires, etc, and each variation in vehicle setup requires a new set of driving maneuvers to be measured in order to identify the new model parameters.

In order to explain the contribution of this investigation, a basic overview of the conventional 2-wheel model as it looks today (for more details see Chapter 4 or Ammon [1], Kobetz [20] and Meljnikov [34]) is presented in Figure 1.2. The inputs to this model are the steering wheel angle from the driver δ_D and the vehicle longitudinal velocity v_x which are used to simulate the outputs, e.g. yaw rate $\dot{\psi}$, lateral acceleration a_y , vehicle side slip angle β , roll angle φ and roll velocity $\dot{\varphi}$ to mention the most essential outputs. The simulation model of the steering system generates a steer angle δ as input to the *axle lateral force element* at the front axle. Together with the lateral velocity of the axle $v_{y,j}$ and the vehicle longitudinal velocity (in the vehicle center plane), the steer angle generates a side slip angle of the axle which results in a static lateral axle force. In order to capture the dynamic force build-up, the dynamic lateral force is modeled by a first order differential equation from Böhm [5]. The same block is applied for the rear axle but without the steer angle as input. Finally, the applied lateral forces of the axles

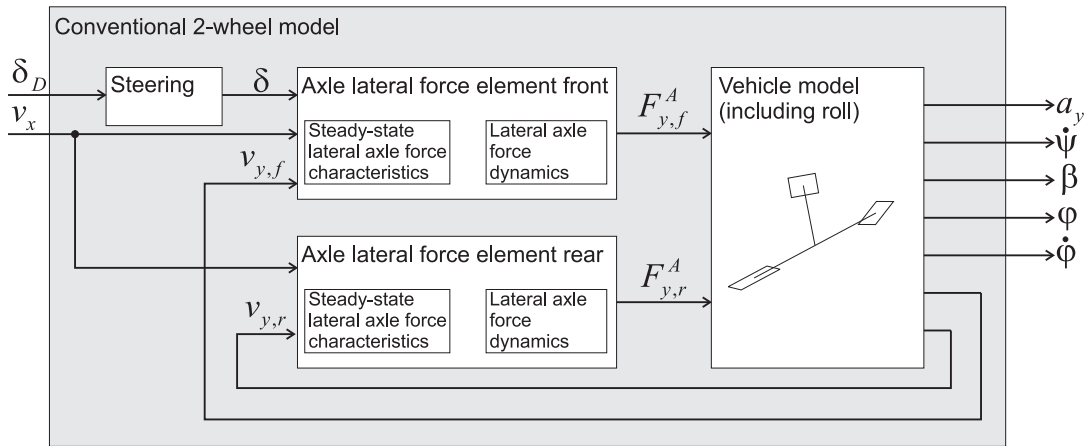


Figure 1.2: Block representation of the conventional 2-wheel model.

result in a motion of the vehicle body.

Mitschke [36] makes use of a linear 2-wheel model in a theoretical investigation of how different changes in vehicle setup, e.g. vehicle loading condition, will influence the vehicle behavior in different maneuvers. The results of Mitschke's investigations are excellent examples of how a simplified vehicle model can be used in order to increase the overall understanding for vehicle dynamics. Nevertheless, in order to give an accurate answer regarding how much the vehicle response will change for a different vehicle setup, a more sophisticated model approach is required. This is especially the case when predicting the change in behavior with different sets of tires due to the strong tire-suspension interactions. The extended 2-wheel model automatically considers this tire-suspension interaction (it is simply included in the parameters) but it is not explicitly modeled.

When using driving measurements to identify the parameters of the extended 2-wheel model, a validation of those measurements is automatically achieved since a sensor error, or for instance an error in the documented sensor position, result in obviously wrong parameters and will ruin the identification process. The model parameters can furthermore be used as an additional analysis tool when comparing different vehicles.

The extended 2-wheel model can also be used at the driving simulator when comparing benchmark vehicles [24]. For this, an extended steering model is required which is capable of giving a correct steering wheel moment as feed-back to the driver including the effects of the hydraulic-assisted power steering. Such a steering model, which is possible to be identified by use of only a few additional test-bench measurements together with the normal driving experiments, can be found in [7]. The only requirement for performing benchmark vehicle comparisons on a driving simulator is that the vehicles of interest have been measured in a set of necessary on-road driving maneuvers in order to identify the model parameters, whereas more complicated models require for instance kinematic and compliance tests, tire parameters, component parameters, etc.

A very important shortcoming of the extended non-linear 2-wheel model is its inability to predict the vehicle behavior for different vehicle setups other than the setup used when identifying its model parameters. Hence, the extended 2-wheel model as it is today lacks the ability to

accurately predict the vehicle behavior for different loading conditions and component changes such as for instance different tires, suspension geometry or anti-roll bar stiffness. The scope of this investigation is therefore to develop a suspension model for the 2-wheel model concept that will enable:

- changing the tires,
- changing significant properties in the wheel suspension such as different spring stiffness, amount of roll steer or damping characteristics,
- change of loading conditions (mass and mass geometry including moments of inertia).

The benefit of such a model is evident in the vehicle development process where all vehicles have to be tested in several driving maneuvers in order to confirm a particular desired driving behavior. This test procedure has to be performed for all approved tires, loading conditions and at different tire pressures. Any discrepancies in vehicle behavior have to be improved by changes in the vehicle model setup which again has to be validated with more testing.

The model being developed in this investigation can be parameterized from driving measurements with one known tire and at one loading condition. All other tire combinations and loading conditions can be simulated and analyzed in the computer and any inconsistency in vehicle behavior can be taken care of in simulations before changing the hardware in the prototype vehicle. This does not replace performing the driving tests completely but enables a faster development process and consequently saves time and money.

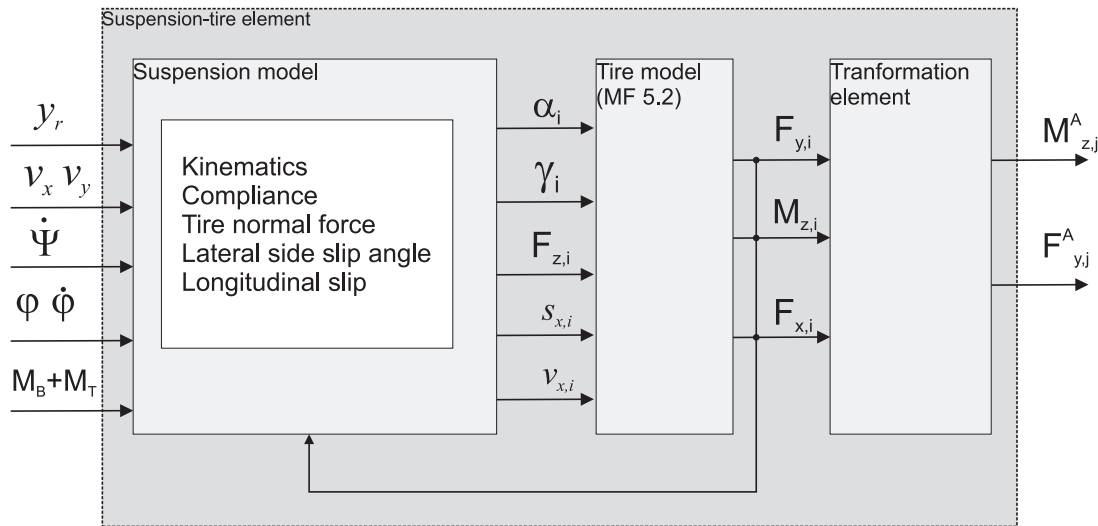


Figure 1.3: Block representation of the suspension-tire element.

Figure 1.3 presents the *Suspension-Tire element* which in the extended 2-wheel model replaces the *axle lateral force element* found in the conventional 2-wheel model. Note that the steering model has to provide the steering rack position y_r as input instead of the steer angle δ as in the conventional 2-wheel model. The vehicle motion states together with the brake and drive torques (M_B and M_T) are furthermore used as inputs when the suspension model calculates the

side slip angles α_i , the camber angles γ_i , the tire vertical loads $F_{z,i}$ and the longitudinal tire slips $s_{x,i}$. The outputs of the suspension model are then used as inputs to the tire model MF 5.2 when calculating tire forces and moments. In addition to the mentioned inputs, MF 5.2 uses the longitudinal velocity of each wheel $v_{x,i}$ as inputs in order to calculate the dynamic lateral tire forces $F_{y,i}$, the dynamic longitudinal tire forces $F_{x,i}$ and the dynamic aligning moments $M_{z,i}$. Note also that these forces are fed back to be inputs to the suspension model in order to be used in the compliance calculations. In a final step, the tire forces and moments of each axle are transformed to a lateral axle force $F_{y,j}^A$ and an axle aligning moment $M_{z,j}^A$ which can be used in the extended 2-wheel model's equations of motion.

1.2 Literature overview

To support the motivation and scope of this investigation, the existing state of knowledge on the area of vehicle behavior models will be discussed. The range of relevant literature is in fact already illustrated in Figure 1.1, i.e. no more than the model classes addressed in that figure will be treated here. In addition to this, the art of modeling can be divided into two aspects: In some cases, for instance when models are used in control algorithms, the model has to reproduce the real system as well as possible regardless if the model is physically motivated or not. The other modeling aspect is when the model is used to serve as a base when studying the influence of structural changes or to increase the understanding of the system. Then, a physically interpretable model is required which is transparent regarding its parameters. The latter aspect of modeling is considered here.

Ever since Rieker and Schunck [46] in 1940 presented a simple physical model approach to take the first steps towards theoretical analysis of vehicle dynamics, numerous amounts of models have been developed for this purpose. With the so called bicycle model, better named 2-wheel model, they analyzed vehicle stability and side wind stability. Even today, the 2-wheel model concept is being used for analysis and the well known works of A. Zomotor [54] and Mitschke [36] should be mentioned. In many cases, the 2-wheel model has been coupled with a roll model. A good example of this is Minakawa and Higuchi [35], who couple the linear 2-wheel model with a linear roll model considering an inclined roll axis and principle moments of inertia. With this model, the influence of rolling caused by a yaw movement due to the inclined roll axle is examined featuring vehicle stability.

One of the latest works done in the direction of the 2-wheel model is the work of Meljnikov [34] where, besides the roll model, non-linear side force characteristics are introduced and effects like roll steer and load transfer are discussed. The dynamical properties of the lateral axle force are captured with a linear first order dynamical system from [5] and the principle of hierarchical identification of subsystems is applied. Kobetz [20] uses a similar approach of a 2-wheel model as Meljnikov, but focuses on the challenge of identification using driving measurements, whereas Meljnikov focuses on the constitution of the theoretical model. The work of Z. Zomotor [55] is also based on the same model approach but with some modifications in order to enable on-line identification.

The above mentioned 2-wheel models of Meljnikov [34] and Kobetz [20] are closely related to this investigation and are therefore reviewed separately in Chapter 4. The models in Meljnikov

and Kobetz all make use of non-linear side force characteristics for the front and rear axle respectively. These summarize the tire and axle properties with the consequence that so called compliance steer and roll steer effects are all included in the lateral axle force characteristics. This is also the case for the effect of vertical load transfer due to lateral acceleration, which due to the non-linear tire properties reduces the total lateral axle force. Meljnikov [34] discusses the introduction of, for instance, roll steer factors to separate this effect from the side force characteristic curves but in order to better understand the effects in the wheel suspension, a more detailed model of the axle is required.

Regarding vehicle handling, all models beyond the complexity level of the extended 2-wheel models presented in Meljnikov [34] and Kobetz [20] are some type of 4-wheel model. These are furthermore ranging up to the most complex component based MBS models, where the analyst builds up the model by providing the details about the rigid bodies, their kinematic constraints and the system topology. For the purpose of vehicle simulation numerous commercial MBS software's have been developed, e.g. ADAMS [37] and Virtual.Lab [26]. These allow the user to build up vehicle models by use of component libraries for links, springs, dampers, etc, without knowledge of deriving the equations of motion or how to solve these. Component models such as the bushing model found in [23] and flexible frames can be included as well. These types of models are not the target in this investigation and are therefore not further discussed here.

Regarding vehicle handling analysis, models of less complexity may be used. Therefore many works utilize simplifications in complex models in order to, for instance, gain less calculation time without losing too much accuracy, e.g. Keßler [19] and Frik [10]. Keßler [19] examines how simplifications in the equations of motion influence the handling of the vehicle by comparisons of simulations with a reference model. Frik [10] builds up a reference model as well and examines the required model complexity for handling simulations. By use of the reference model, the possibilities of simplifications in the model and in the equations of motion are revealed. Both Keßler and Frik make use of characteristic maps of the wheel suspension kinematics. One distinct difference between the works is the maneuvers in which the simplifications are validated: Frik focuses on the horizontal motion of the vehicle, whereas Keßler includes the presence of vertical inputs.

Many papers are deriving a model to perform theoretical studies of how different parameters are influencing the behavior of a vehicle, e.g. [22, 13]. Gnadler [13] examines the influence of the height and inclination of the roll axis and the inertia tensor using a four wheel model. An arbitrary linkage of wheel masses to the body is achieved through a fictive diagonal suspension link. The model considers non-linear springs and dampers, different anti-roll bar variants, tire characteristics as function of load, slip angle and camber angle as well as traction effects that may be distributed between left and right dependent on the type of drive train and wind forces. In Kuralay [22], a theoretical survey is given of the changes in driving behavior due to variations in the elasticity of the wheel suspension joints, steering and tire parameters. The simulation model used, a simplified 4-wheel model with a fictive suspension link, has 19 degrees of freedom and the calculations were carried out for two vehicles with different types of independent suspension. The survey was performed on 4 maneuvers: steady state cornering, impulse-type steering wheel input, braking from steady state cornering and finally braking from straight ahead driving with uneven brake pull.

The main scope in the work of Sorgatz [50] is the modeling of a 23 Degrees of Freedom (DOF)

model to describe the limit behavior of the vehicle. The model comprises a general five masses approach, which in comparison to Gnadler [13] does not contain restrictions to a certain mass symmetry and is not simplified with small angle approximations. For the suspension kinematics, a model has been developed that takes into account the non fixed steering point of rotation and the non vehicle fixed roll axis. For the spring and damper characteristics, approaches with arbitrary non-linearity are being considered. The same have been implemented for the steering and camber changes due to wheel bounce, which are being considered either independently for each wheel or coupled with the other wheel side, e.g. for a rigid axle. The anti roll bars and steering damper characteristics are linear. The aerodynamics has been considered with a non linear approach regarding the 6 DOF of the vehicle body. The model is restricted to an even road. Besides the modeling part, the work also presents a comparison between simulations and experiments.

Some theoretical studies of vehicle behavior by use of 4 wheel models have also been performed by Desoyer and Slibar [8], Lugner [27, 28] and Lugner et al [29]. Desoyer and Slibar examine the utilized friction and slip angle of the tires during steady-state cornering by use of a simplified 4-wheel model. Lugner [27], continues this investigation with the addition of a banked road. The work in [27] is followed up by Lugner et al [29], where the influence of braking in the curve is investigated as well. For this, a special maneuver is used where the model first does straight line driving followed by a curve with transient curvature and finally, proceeds with a constant radius. In the middle of the transient part, the model starts braking. Through the complete trajectory, a bank angle of the road is considered. The models used in [8, 27, 29] are more or less similar. The influence of steering angles of the wheels, as well as of traction and lateral forces are considered. The tire characteristics are approximated out of measured values. In Lugner et al [29], the camber influence has also been regarded.

In [28], Lugner uses almost the same maneuver as in [29]. The difference is that the braking takes place in the cornering part with constant radius. In this paper, the influence of the mechanical description of the car and the mathematical approximation of the tire behavior on the theoretical simulated vehicle behavior is investigated. Two model approaches and two different tire approximations are stated.

4-wheel models have also been identified by use of experimental data. Russo et al. [48], make use of extended Kalman filter to find the parameters of such a model. The maneuver for the identification is a step steering wheel input and the results are validated with the maneuvers steady state cornering and double lane change. For the tire model, a Pacejka formula has been applied but its parameters are not identified except for the relaxation length, i.e. the tire parameter for the dynamic force build-up. A fixed roll axis is furthermore assumed and camber influences neglected.

Lugner et al [30] also compare experimental results to a complex four wheel model. This model is made for simulation of arbitrary inputs influencing both lateral and longitudinal vehicle dynamics. Every wheel is treated separately and changes in attitude due to both spring deflection and lateral and longitudinal forces are taken into account. The tire characteristics are taking arbitrary slip conditions into account. Evaluation and results from the maneuvers steady state cornering, frequency response, steering wheel angle step input and emergency braking out of steady state cornering, are discussed.

Some other works do comparison with measurements as well, e.g. [41, 38]. Otto [41] examines the power-off effects at steady state cornering and the corresponding objective evaluation criteria. By use of the 2-wheel model from Mitschke [36], he first discusses the effects of vertical load changes and traction forces during this maneuver. In order to further check these results, and to be able to examine effects like compliance steer due to traction forces, he makes use of a 4-wheel model with a fixed roll axle. Steering effects due to body roll, lateral force and traction force are taken in consideration with linear functions. Vertical loads are calculated by use of the pitch model presented in Mitschke [36]. Finally some possible structural changes of the suspension design are discussed in order to counteract unwanted effects during power-off cornering.

Paknia [42] uses an already identified non-linear 4-wheel model similar to the CASCaDE-Classic to show that it is possible to identify tire parameters using normal handling maneuvers. The kinematics and compliance of the model had been identified through test bench measurements and the start parameters for the tire parameter optimization had been determined from tire test bench measurements. Two different test vehicles were used in the investigations and the tire parameters were tuned through an optimization process with the result of a better fit between simulation and measurements. It is important to remember in this case that errors or drawbacks in the used vehicle model will inevitably be covered up by adjusting the tire parameters.

1.3 Conclusion of literature overview

Vehicle models chosen for handling simulations either remain within the conventional 2-wheel model concept or, if using an additional (non-linear) tire model, take a leap to at least a four wheel model, in many cases including a functional description of the suspension kinematics and compliance and a complete set of equations of motion. In many investigations where a four wheel model was simplified, the objective was to reduce simulation time. A model approach separating the tires from the rest of the suspension while remaining within the 2-wheel model concept could not be found in literature and seems to be an advanced practically oriented approach. Assuming known tire properties for identifying the vehicle and suspension parameters from driving measurements could not be found in this literature.

Proposing a suspension-tire model to form an extended 2-wheel model, including only the most important vehicle and suspension characteristics as well as assuming known tire parameters adds a new model class, closing the gap between the non-linear 2-wheel models and the functional four wheel models like for instance the CASCaDE-Classic model.

Chapter 2

Reference models

In the beginning of all modeling processes, a model concept is derived from a problem specification. This model concept is then applied in a mathematical model which is furthermore implemented in software to be simulated and validated. For this process, some kind of information about the system to be modeled has to exist. In many cases this link is a set of measurements revealing the system response due to different inputs. One example of a vehicle dynamics model developed from driving measurements is the non-linear 2-wheel model presented in [34]. This behavior model is based on the traditional 2-wheel model coupled with an additional roll model and non-linear side force characteristics and steering ratio. In order to capture the dynamic properties of the lateral force, the axle force build-up is modeled with a first order differential equation. This model class is also used as a base for this investigation and is described separately in Chapter 4.

Part of the scope of this investigation is to extend the above mentioned 2-wheel model. With this, a new modeling task has begun and so is the need for information about the system to be modeled. Measurements could be used for this task. However, measurements inevitably hold some level of inaccuracy and noise. In addition, the possibility of making adjustments in the wheel suspension in order to isolate and investigate certain effects would be strongly limited by the extra work load and expenses involved. An alternative, especially when creating simplified vehicle models, is to use a complex component based vehicle model as a reference. Even if a model of this type is nothing more than a representation of the reality, the overall system behavior is equivalent to the real vehicle and discrepancies in model outputs can often directly be explained by insufficient accuracy of model parameters. In addition to avoiding measurement related problems, the use of a reference model opens up an increased possibility of analysis as known properties can simply be influenced or even eliminated in order to increase the understanding of that or other effects. This is the most important advantage of using models instead of measurements of a real vehicle. Another benefit is that virtual sensors can be placed out as preferred. For these reasons, this investigation uses mainly simulations of reference models when investigating the effects of different suspension properties. The measurements are, however, always present in parallel in order not to lose contact with the real system and always has to be employed in the end for evaluation and validation.

2.1 A CASCaDE overview

The reference models described in this chapter are all implemented in CASCaDE (Computer Aided Simulation of Car Driver and Environment), which is an in-house developed simulation software at the research unit of Daimler AG, see overview in Figure 2.1. CASCaDE can be seen as a roof under which an abundance of programs and data files concerning vehicle dynamics are gathered. CASCaDE comprises for example different levels of car models, a kinematics and compliance test bench, aerodynamics, driver models, road models, visualization and animation tools, optimization and identification tools, different component models for tire, shock absorber, power steering, brake hydraulics, ABS controller and rubber bushings to mention a few. The software is mainly written in C and FORTRAN and coupling with models from other software, so called co-simulation, is also possible.

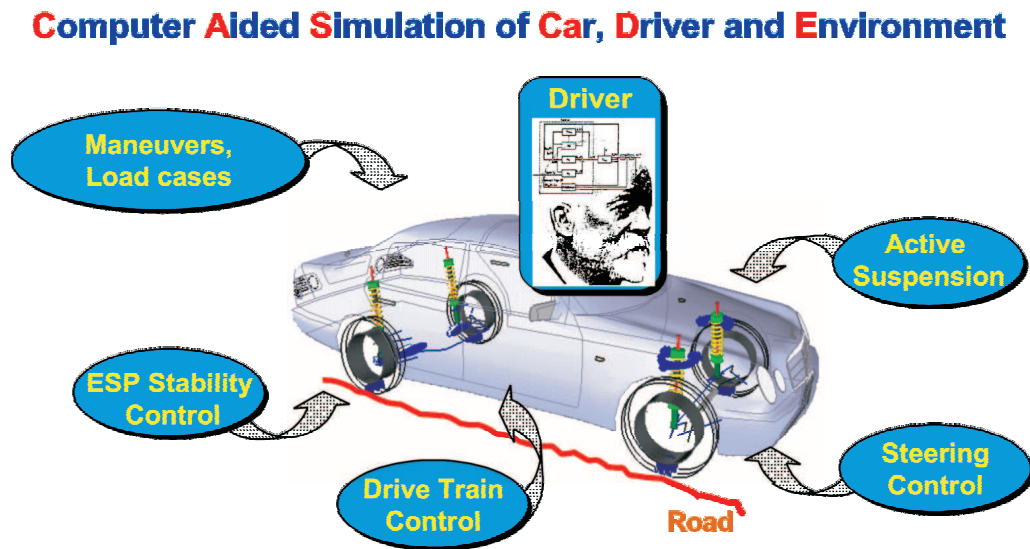


Figure 2.1: A CASCaDE overview presenting possible applicable tools within the simulation environment.

The dynamic properties of modern vehicles are strongly determined by the kinematics and compliance properties of the vehicle's wheel suspension. As this enables a better adaptation of the vehicle steering properties to different driving conditions, it also has the consequence of a stronger non-linear kinematics and compliance interaction in the wheel suspension. In order to completely understand and furthermore simulate, analyze and optimize the properties of a suspension, a suitable mechanical modeling is required. For this task three different suspension model categories exist:

- Kinematic models,
- combined kinematic and compliance models,
- combined kinematic and compliance models that consider inertia properties of the system components.

Since elasticity is purposely built into the suspension of modern cars, a pure kinematics model is not sufficient for the included investigations. Hence, only the second and third model category will be described here.

The choice of model category depends mainly on the required accuracy and simulation time. A basic matter for both of these requirements is if the suspension properties can be determined in a preprocessing step or if they have to be calculated during the simulation. The second model category presented above corresponds to the model class with preprocessed suspension properties and will be referred to as the *CASCaDE-Classic model*, briefly the *Classic model*, and is described in Section 2.3. The third category above is represented in CASCaDE by the Dynamic Suspension Model (German: **D**ynamischen **A**chsmodelle). A brief description of this so called *DA model*, is found in Section 2.2.

The tire simulation models main tasks are; to represent the steady state force and moment characteristics, reproduce the vertical stiffness and damping properties, perform the 3D kinematics calculation of the wheel, consider the road surface contact evaluation, model the kinematics and kinetics of the tire contact patch, and finally, to model the tire dynamics and vibrations. To fulfill these tasks many different tire models exist which are more or less specialized to fulfill some of these demands. State of the art tire models regarding vehicle dynamics can be divided into three different categories by means of different complexity level and application spectra [2]:

- Characteristic models, e.g. the Pacejka tire model [4, 51] or TMeasy [47, 15],
- Semi-physical models, e.g. BRIT [12], SWIFT Tyre [18, 31],
- Physical, detailed tire-structural models, e.g. RMOD-K [39], F-Tire [11]

The above mentioned tire models are all coupled in CASCaDE with a common tire interface, i.e. both the Classic and the DA model can be simulated with any of these tire models. Again, this allows for instance the model being developed to be simulated with the same tire model as the reference model and in this way isolate the influence of the tires.

The model parameters in the characteristic models are adjusted to fit to measurement data corresponding to normal driving conditions and have the advantage of low simulation time in handling simulations. For high dynamics simulations, such as braking with Antilock Braking System (ABS), at least a semi-physical model like the BRIT model is required. The physical, detailed tire-structural models are here excluded since their complexity level is not required in the range of handling simulations.

2.2 The CASCaDE-DA model

The component oriented and dynamical suspension model (German: **D**ynamisches **A**chsmodell) CASCaDE-DA was developed in order to perform detailed analysis concerning the dynamical behavior of the wheel suspensions. CASCaDE-DA is a pure component based MBS tool specialized for vehicle simulations where the kinematics and compliance properties of the suspension are described by equations of motion which are solved during the simulation. The DA model considers the spatial non-linear elasticity and damping effects of the bushings, forces and moments of inertia of the links, and related friction and play effects. In combination with the sophisticated physical tire simulation model BRIT and comparable models for the power steering hydraulics, an efficient simulation tool for the analysis of the entire suspension system dynamics as well as for the entire vehicle system dynamics is obtained [3]. In comparison to the quasi static tabular models like the Classic model (described later in this chapter), the DA model represents the suspension's dynamical behavior in detail. This is made possible since the DA model, besides the non-linear kinematics and compliance properties, also considers the system components 3D-inertia properties, i.e. the inertia properties of the suspension links. With this approach, steady-state vibration phenomena as well as transient response problems of the suspension system like shimmy, steering roughness, or excitations due to misbalanced wheels can be investigated efficiently [3].

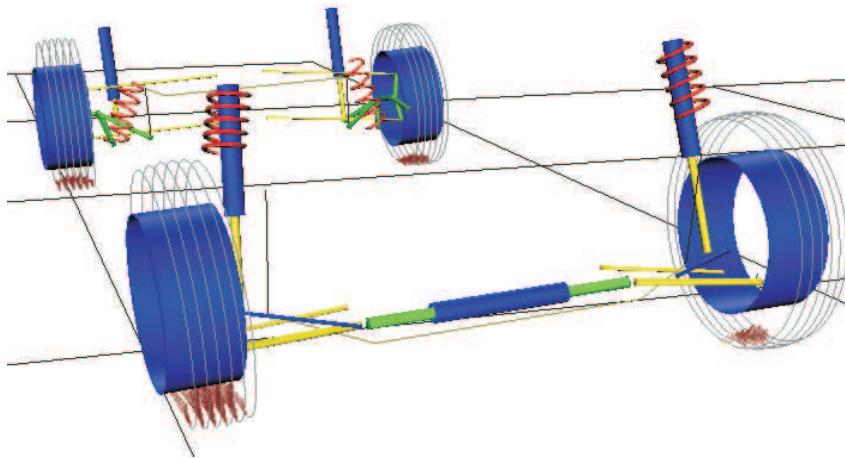


Figure 2.2: Suspension components displayed for the CASCaDE-DA vehicle model.

DA is strictly object oriented with a decentralized integration. With this integration approach, the numerical precision does not reach the accuracy of the sophisticated multi purpose integrators. However, the accuracy is still considerably better than the inaccuracy due to model simplifications [3]. The advantage of the decentralized integration is the flexibility by the special treatment of, for instance, stiff system components such as dry friction.

The DA core consists of the so called component catalogue where all the single suspension components are to be found as modules. All these components have different levels of complexity. For instance the simplest brake model is made up of only a functional relation between brake pressure and maximum brake torque, whereas some of the tire models are very extensive.

A strong benefit of this object oriented modeling catalogue is the high flexibility when adding new components. Another benefit is the possibility to reuse existing components when implementing new suspension concepts. Different suspensions such as double wishbone suspension, McPherson suspension, multi link suspension and four link suspension are implemented as pre-made templates.

2.3 The CASCaDE-Classic model

2.3.1 Kinematics in the Classic model

If the complete dynamic performance of the suspension is not required, the kinematics and compliance properties of the suspension can be identified in a preprocessing step. For the kinematics of an independent wheel suspension, a system with either one or two degrees of freedom (DOF) will appear, depending on if it is a steered axle or not. A non-steered axle can be described with the wheel bounce as the only DOF. The second DOF for a steered axle is either the rack displacement if it is a rack-and-pinion steering, or the pitman arm rotation on a recirculating-ball steering.

In the Classic model approach, the kinematical position of the wheel carrier in relation to the vehicle body is completely calculated in a pre-processing for all operating states. Subsequently the resulting look-up fields and look-up tables are approximated with polynomials giving the wheel carrier's longitudinal and lateral displacement $\mathbf{r}_i = (r_{x,i}, r_{y,i})^T$ together with its three rotational coordinates $\boldsymbol{\sigma}_i = (\sigma_{x,i}, \sigma_{y,i}, \sigma_{z,i})^T$ as functions of vertical wheel travel z_i and steer input δ_i of wheel i ;

$$\begin{bmatrix} \mathbf{r}_i \\ \boldsymbol{\sigma}_i \end{bmatrix} = \begin{bmatrix} \mathbf{r}^{kin}(z_i, \delta_i) \\ \boldsymbol{\sigma}^{kin}(z_i, \delta_i) \end{bmatrix} \quad (2.1)$$

In the case of a non steered axle, this is reduced to a dependency of wheel bounce only. For the calculation of these kinematic polynomials, suspension hard points are fed into ECCO (Elastokinematics Computation and Optimization) which is a separate program in CASCaDE.

2.3.2 Non-linear compliance approach

Along with the spring and damper, a wheel suspension consists of several flexible parts connecting components. The flexibility of the suspension leads to additional displacements and rotations of the wheel carrier under influence of tire forces and moments. These compliance displacements are here modeled with polynomials which are parameterized using compliance test bench measurements. For this, at least a vehicle prototype is required. An alternative to test bench measurements of a prototype is to approximate the compliance properties by use of a more detailed MBS model including links and non-linear spatial bushings, e.g. the earlier described CASCaDE-DA model.

Considered in these non-linear compliance polynomials are the induced steer and camber angle $\Delta\sigma_z$ and $\Delta\sigma_x$, as well as longitudinal wheel deflection Δr_x , due to lateral and longitudinal forces

F_y and F_x , together with the aligning moment M_z , driving or braking moment M_y , and the overturning moment M_x , all defined in the wheel center. The extra hat ($\hat{\cdot}$) defines the load on the opposite wheel, so the coupling between left and right side of the axle is also considered.

$$\Delta\sigma_z = \xi_1 F_y + \xi_2 \hat{F}_y + (\xi_3 M_z + \xi_4 \hat{M}_x) + \xi_5 F_x + \xi_6 M_y + \xi_7 M_y^2 \quad (2.2)$$

$$\Delta\sigma_x = \xi_8 M_x + \xi_9 \hat{M}_x + \xi_{10} F_x + \xi_{11} M_y + \xi_{12} M_y^2 \quad (2.3)$$

$$\Delta r_x = \xi_{13} F_x + \xi_{14} M_y + \xi_{15} M_y^2 \quad (2.4)$$

The calculated deflections in Equation (2.2) to (2.4), are subsequently superimposed on the kinematical displacements with a time delay for numerical stability. The approach representing the suspension properties through kinematic polynomials and superimposed deflections due to compliance has proven to be an efficient tool for many vehicle dynamics tasks. Due to the absence of a prototype in the early development stadium, the required suspension tables and parameters must however be created in the computer.

Besides the case when the kinematics is prepared in a pre-processing step, the Classic model can also be used in an online mode where the kinematics is calculated during the simulation. This is necessary in order to simulate rigid axles where the numbers of DOF's in general are greater than the two DOF practical for look-up tables or polynomials.

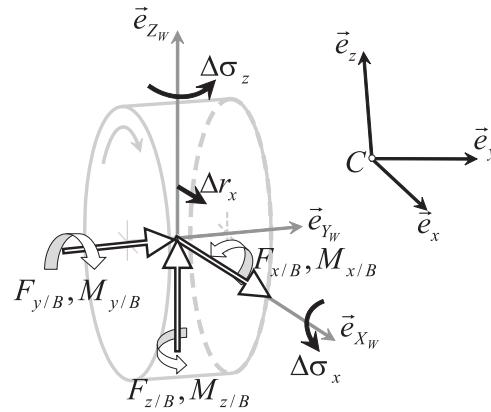


Figure 2.3: Wheel carrier displacements ($\Delta\sigma_x$, $\Delta\sigma_z$, Δr_x) in relation to the vehicle body due to compliance in CASCaDE-Classic.

2.4 The used tire model – Magic Formula Version 5.2

The reference models described above are in all investigations equipped with the tire model MF 5.2 (Magic Formula version 5.2) described in [51]. Since the mid-eighties, the Magic Formula has been developed as a joint effort by Volvo AB and Delft University of Technology with the objective of describing the tire characteristics with a limited set of parameters. Magic Formula provides a set of mathematical equations describing the force characteristics of a tire. The parameters in these equations can be derived from a large set of measured tire data, where the tire has been rolled over a given surface at various loads and orientations.

Figure 2.4 presents the inputs and outputs in MF 5.2. The longitudinal slip, s_x , side slip angle α , wheel camber γ and the vertical tire load F_z make up the input vector (see definitions in [51]), resulting from the wheel moving relative to the road. The forces, F_y and F_x , and the moments, M_x , M_y and M_z , are tire model outputs assumed to act on a rigid disc with inertial properties equal to the undeflected tire.

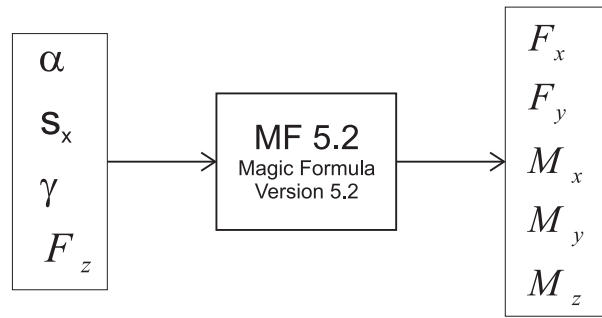


Figure 2.4: Input and output vector of the Magic Formula Tire Model.

The Magic Formula is built around the general sine-type function

$$Y(x) = D \sin(C \arctan(Bx - E(Bx - \arctan(Bx)))) \quad (2.5)$$

Where $Y(x)$ is either lateral tire force F_y as a function of side slip angle α or longitudinal tire force F_x as a function of longitudinal slip s_x . Each of the parameters B , C , D and E are furthermore functions of specific tire parameters which together with the model inputs, α , s_x , γ and F_z , completes the formula. The self aligning moment M_z is calculated by using the lateral force F_y and the pneumatic trail n_P , which is calculated with the second general formula, the cosine-type:

$$Y(x) = D \cos(C \arctan(Bx - E(Bx - \arctan(Bx)))) \quad (2.6)$$

Both pure and combined slip conditions are treated in the MF 5.2. The transient tire behavior with respect to handling is moreover represented by a set of differential equations [51]. Approaches to handle ply steer and conicity have also been implemented. The reader is referred to the manual [51] for further descriptions of how the MF 5.2 Tire Model works and how each parameter effects the shape of the curve.

The MF 5.2 comply with two main standards developed by car manufacturers, tire suppliers and research laboratories since 1991 [51]. The first standard is described in the TYDEX-Format [52] and defines an interface between tire measurements and tire models. This standard also specifies tire measurement procedures in a way that it contains all necessary items to fit tire models to the data. The second standard developed specifies an interface between tire models and simulation tools and is called the Standard Tire Interface (STI) [45]. This standard allows a wide range of tire models to be used in many different simulation tools.

Furthermore, MF 5.2 is created using coordinate systems according to the ISO orientation and all parameters, inputs and outputs are defined in SI units. All this builds a solid foundation for sharing tire model parameters and future model updates, which is one of the main reasons for using this tire model in this investigation.

2.5 The used reference vehicles

Two types of vehicles have been chosen as reference vehicles. *Vehicle A* is a midsize sedan with an average tire and a common tire size. As a contrast, *Vehicle B* is a sporty roadster

with low profile tires and different tire size front and rear. Table 2.1 gives an overview of the reference vehicles.

Both reference vehicles are simulated with the CASCaDE-DA model but also CASCaDE-Classic models are available for cross reference simulations. Figure 2.5(a) depicts a double wishbone suspension and Figure 2.5(b) shows its animated version from the CASCaDE-DA simulation model. A similar presentation for the multi link suspension can be found in Figure 2.6(a) and 2.6(b). The model of the McPherson front suspension of vehicle A is built up by the same procedure.

	Vehicle A	Vehicle B
Vehicle type	Midsized sedan	Roadster
Front Suspension	McPherson	Double wishbone.
Rear Suspension	Multi link	Double wishbone.
Tires	205/55 R16	Front: 265/35 R19 Rear: 295/30 R20
Steering	hydraulically power assisted rack-and-pinion steering	hydraulically power assisted rack-and-pinion steering
Drive train	Rear wheel drive	Rear wheel drive
Anti-roll bar	front and rear	front and rear
Vehicle mass	1840 kg	1796 kg

Table 2.1: Reference vehicle overview.

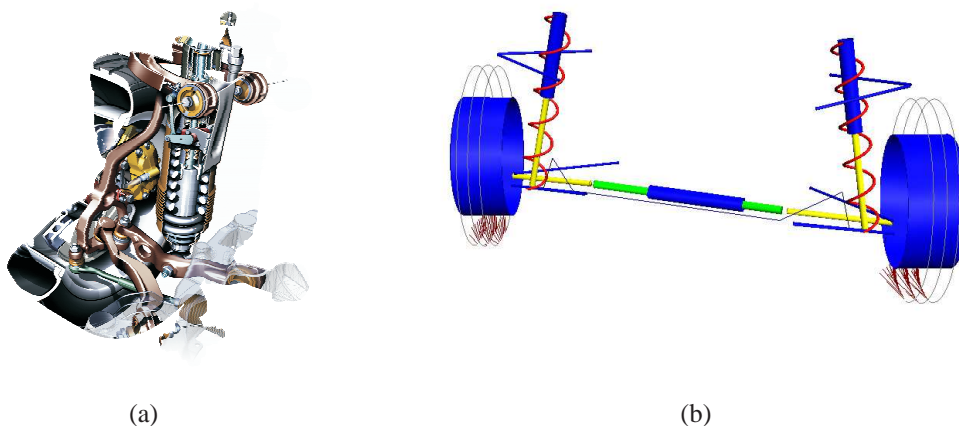


Figure 2.5: Illustration of a double wishbone suspension and an animation of its simulation model equivalence.

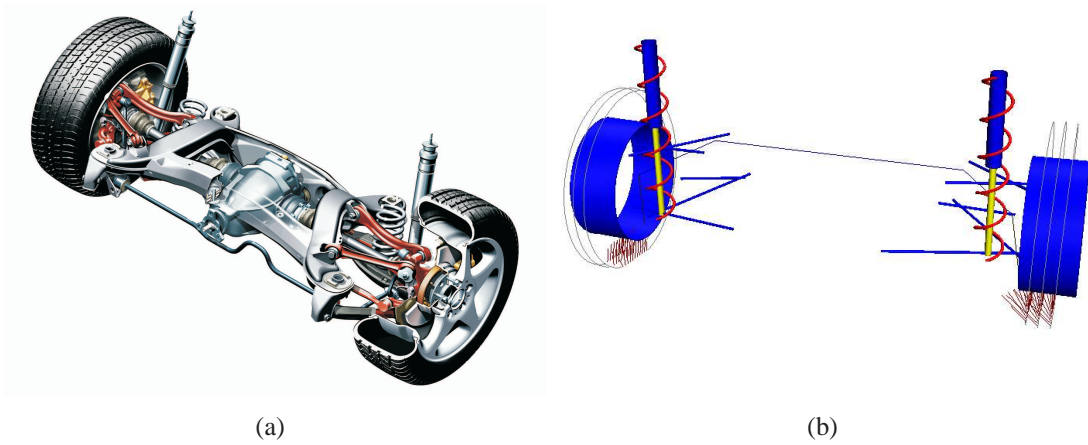


Figure 2.6: Illustration of a multi link suspension and an animation of its simulation model equivalence.

Chapter 3

Direct and indirect factors influencing vehicle steering behavior

Vehicle steering behavior depends on several factors in the suspension design as well as the tire properties and can be measured in for instance the constant-radius test method. This test method requires driving the test vehicle at several speeds over a circular path of known radius. The steering behavior is determined from data obtained while driving the vehicle at successively higher speeds on the constant-radius path. Figure 3.1 shows an example of three different possible steering behaviors during the constant-radius test. The most common case is the under steering vehicle, where more steer angle is required in order to stay on the constant radius path at higher lateral accelerations. A neutral steering vehicle would require the same steer angle during the whole range of lateral acceleration and the over steering vehicle would even require smaller steer angles with increased lateral acceleration. Since an unwanted rear axle drift (due to an over steering vehicle set-up) can lead to critical situations, most modern vehicles are designed to be more or less under steering during steady-state cornering [14]. However, at very high lateral accelerations, the steering behavior could turn into neutral and even over steer, especially for a rear wheel driven vehicle driven on ice, see Mitschke [36].

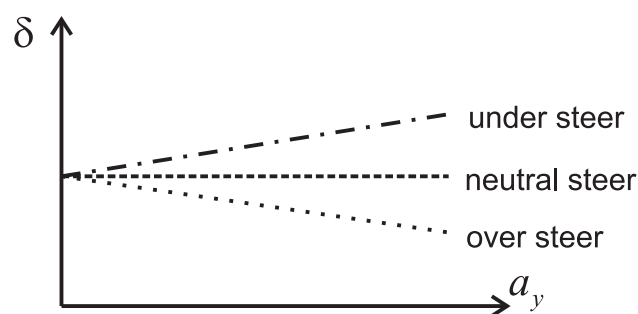


Figure 3.1: Explanation of over, under and neutral steering behavior during constant radius steady-state cornering.

If a modification of a factor leads to an increased necessary steering wheel angle to reach a

certain driving state during cornering, this modification is said to have caused more under steer. Conversely, a modification leading to a decreased necessary steering wheel angle causes less under steer, i.e. works in an over steering direction (even though the vehicle still is defined to be under steering).

Different design factors influence the vehicle steering behavior directly and indirectly. Hence, one single factor not only produces a direct under or over steering effect, but it also has an influence on other factors. As a result, these other factors produce under or over steering effects as well, which either assist or oppose the direct effects and therefore either increase or decrease the resulting change in steering behavior. This will be exemplified with the front axle anti-roll bar: A stiffer anti-roll bar will increase the front roll stiffness, with a resulting increased weight transfer on the front axle during cornering, and consequently producing an under steering effect due to the non linearities in the tire characteristics (see Section 3.6.2). The change of vertical load transfer is the direct effect. Simultaneously, the increased roll stiffness results in reduced vehicle roll. If the vehicle has a built-in roll under steer (see Section 3.2), the reduced vehicle roll will inevitably result in less roll under steer, counteracting the direct effect of more under steer due to a stiffer anti-roll bar. As a matter of fact, a vehicle equipped with tires insensitive to vertical load change, i.e. making the vehicle less sensitive to vertical load transfer during cornering, in combination with a considerable amount of roll under steer, the final combined effect produced by an increased anti-roll bar stiffness is a less under steering vehicle.

Since all design factors give rise to both direct and indirect under or over steering effects, that complement or oppose each other, the resulting effect can be under steering, over steering or even neutral. The direct and indirect influence on under-over steer due to different design factors will be discussed in the following sections.

3.1 Static toe angles

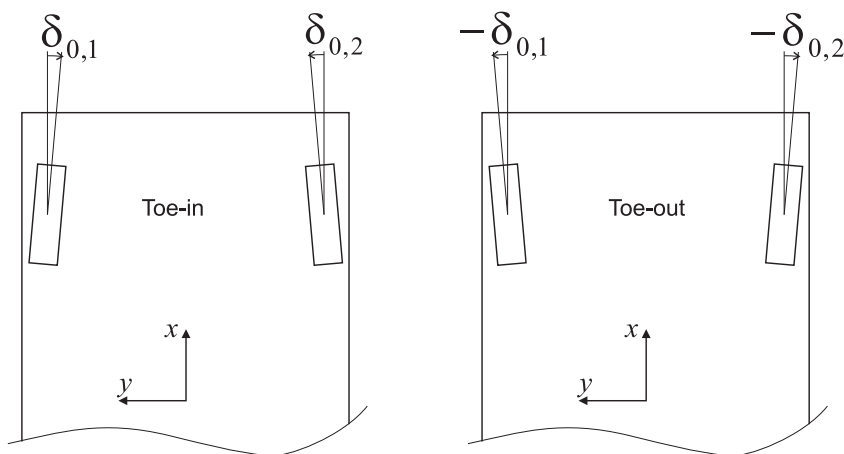


Figure 3.2: Static steer angles on the front axle with no steering wheel input, also called toe angles. The static steer angle is called toe-in when the wheels converge towards the front, i.e. the steer angle of the right wheel is positive in a right orthogonal reference frame.

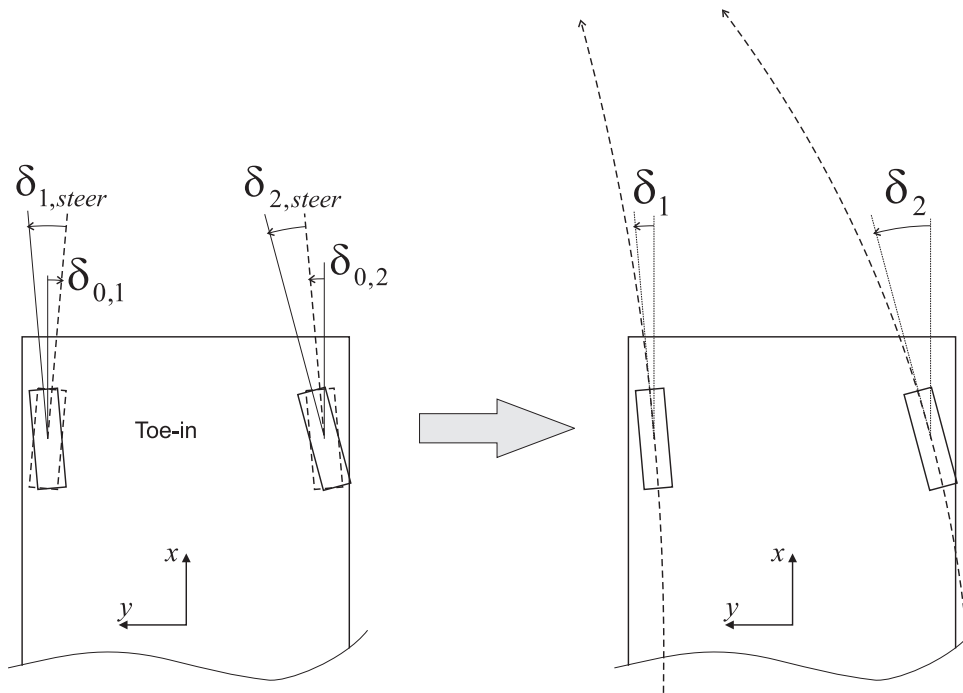


Figure 3.3: For static toe-in: At corner entry, the change of the steer angles left and right due to the steering action of the driver are approximately equal, $\delta_{1,steer} \approx \delta_{2,steer}$. These steer angles together with the static toe-in angles $\delta_{0,1}$ and $\delta_{0,2}$, makes the inner tire trace an arc with larger radius than the outer tire.

The static toe angle is an alignment parameter that describes how the wheel is oriented with respect to the longitudinal x-axis in straight ahead driving. If the wheels are pointing toward each other observed from a top view, they are said to have *toe-in*. If they are pointing away from each other, they are *toe-out*, see Figure 3.2. The same definitions of toe angles apply for both the front and the rear wheels.

Static toe influences how a car behaves upon corner entry. With more toe-in on the front axle, it will be harder to make the wheels turn into a corner. The reason for this is exemplified by observing a vehicle with toe-in on the front axle. As the driver begins to turn the vehicle to the left, the left and right tires will be turned initially with the same steer angle $\delta_{i,steer}$ with the consequence of the left front tire pointing only slightly to the left while the right-front tire is pointing much more to the left, see Figure 3.3. However, according to geometry of a free rolling vehicle, the left front tire needs to be turned with a greater angle than the right-front tire since the left front tire is on the inside of the corner and hence, must trace an arc with a smaller radius than the outside tire, see Figure 3.4. On the other hand, with toe-in, the left front tire is in fact trying to trace an arc with a larger radius than the right front tire, see right side of Figure 3.3. This means that the left front tire will be fighting the right front tire and make it difficult to make the car turn into the corner. The opposite yields for a vehicle with toe-out as this will be more similar to the ideal steering condition illustrated in Figure 3.4. As the vehicle is already in the turn, the vertical load transfer from the inside to the outside tire will diminish the effect of static toe, i.e. the effect is only observable upon corner entry.

In addition to corner-entry handling, static toe influences straight line driving. The same rea-

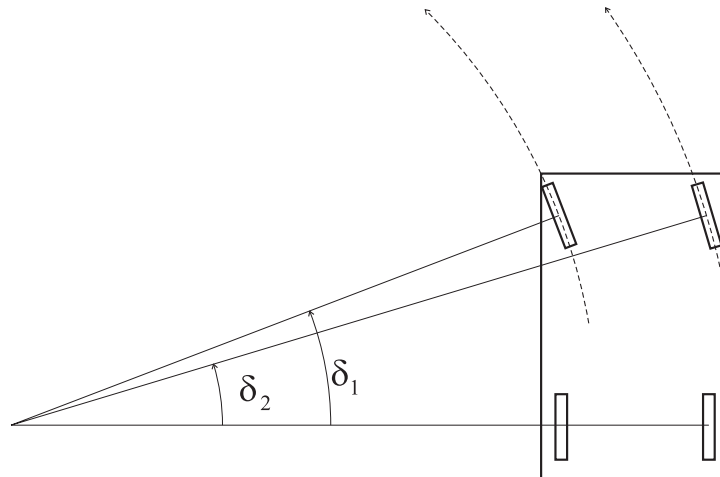


Figure 3.4: Ideally, the inner wheel has to steer more than the outer tire during cornering.

soning as for corner entry can be applied to explain this and hence, toe-in will improve (while toe-out worsens) straight line driving.

3.2 Front steer angles

Due to steering gear compliance and front end structure flexibility, the front steer angles will be influenced by the tire lateral forces during cornering. A simplified model of this is shown in Figure 3.5. The result of this is that the outer wheel in general will flex towards toe-out and the inner towards toe-in resulting in reduced side slip angles on the front tires and consequently less lateral tire force. Hence, more compliance on the front axle will cause a more under steering vehicle.

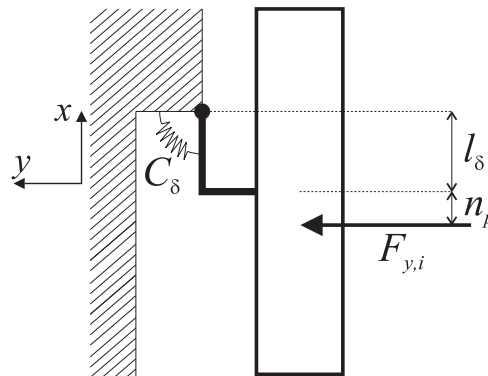


Figure 3.5: Simplified illustration of compliance steer.

Due to suspension kinematics, the steer angles change over wheel travel, i.e. in jounce and rebound (front roll steer). These kinematic steer angles add to the steer angles due to compliance and can either be an additive or reductive factor. If the geometrical toe-change (on the front axle) gives toe-out in jounce and toe-in in rebound, the side slip angles will be further reduced (due to the different wheel travel during cornering) and it will add to the direct under steering effect from compliance. The kinematics may, however, be designed to oppose the compliance toe-change (toe-in in jounce and toe-out in rebound) and consequently cause less under steer.

Indirect effect: If the summarized toe-change on the front axle is toe-out in jounce and toe-in

in rebound, this will cause less side slip angle front and consequently less aligning moment. Hence, the direct under steering effect of compliance steer front will be followed by an indirect effect causing less under steer, the reduction of aligning moment (explained in Section 3.8). This makes the total effect of steer angle changes on the front axle less effective than on the rear.

3.3 Rear steer angles

In the case where the rear wheels due to kinematics turn to toe-in in jounce and toe-out in rebound (rear roll steer), the rear wheels will turn in the same direction as the front wheels during cornering, see Figure 3.6. The direct effect of this is an increase in side slip angles at the rear tires and consequently increased lateral tire forces which tend to reduce the vehicle yaw moment, i.e. causing an under steering effect.

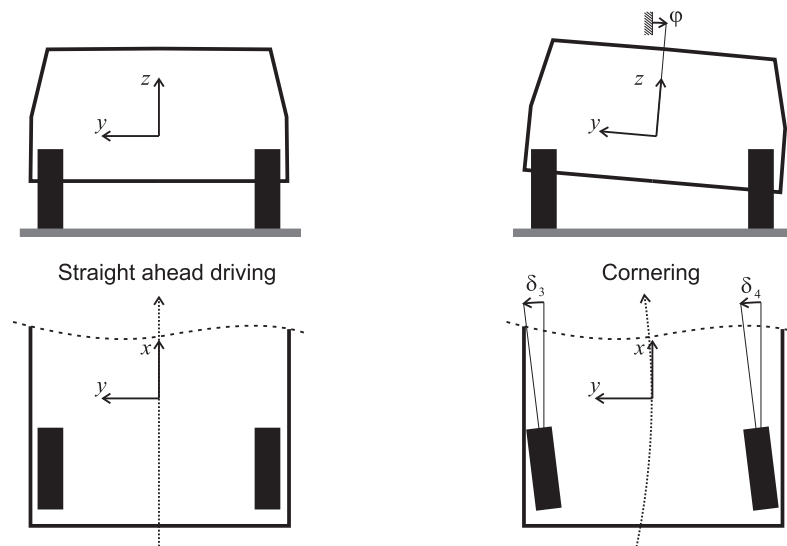


Figure 3.6: Steer angle change on the rear wheels due to kinematics during cornering, i.e. rear axle roll steer.

An indirect effect of the increased side slip angle is an increase in aligning moment which also works against the vehicle yaw moment and hence, provides additional under steer.

Simultaneously, more lateral force means an increased shift of tire normal force towards the outer tire which on the rear axle is causing less under steer. Also, in addition to the geometrical toe-change, the increased lateral tire forces and aligning moments will cause additional toe-changes due to compliance. Depending on the rear axle design, this indirect effect may work in either an under steering or over steering direction.

The relative effect of a change in rear axle steer angles is, in general, more significant than at the front axle. This can be explained by observing the lateral axle force characteristics in the 2-wheel model, see Section 4.4. The lateral axle force characteristic of the rear axle is normally stiffer than the front and a change in steer angle will therefore cause more change in lateral force on the rear axle than on the front.

3.4 Camber angles

The camber angles of the wheels in relation to the road surface γ_i are generating lateral forces according to the left side in Figure 3.7 which either will reduce or add lateral force to the lateral tire force created by the pure side slip angle.

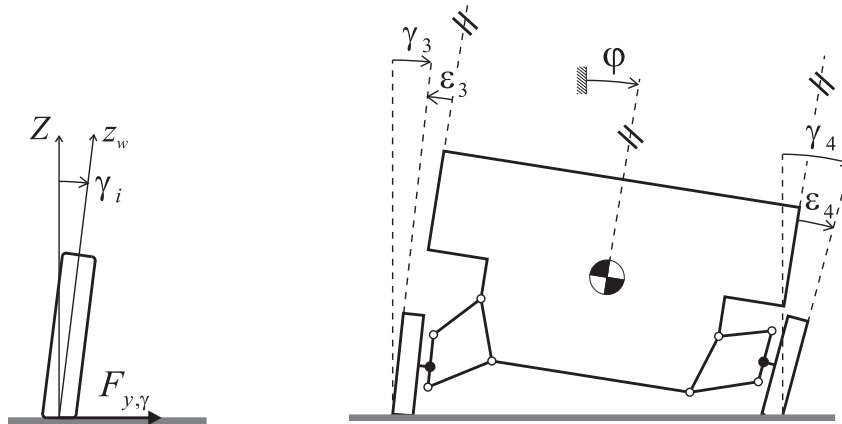


Figure 3.7: To the left: Definition of the camber induced lateral force $F_{y,\gamma}$. To the right: Example of camber angles during cornering and how the camber angle in relation to the road γ_i relates to the vehicle roll angle ϕ together with the camber angle in relation to the vehicle body ϵ_i .

On individual suspensions, these camber angles can be broken down to a geometrical camber angle in relation to the vehicle body ϵ_i and a camber angle influenced by the vehicle body roll, see Figure 3.7. Observe that the camber angle in relation to the body ϵ_i is defined positive as the top of the wheel leans towards the outside of the vehicle. The camber angle in relation to the body changes due to kinematics and compliance as the vehicle is cornering and how this camber angle changes can be influenced by suspension design. As the vehicle leans towards the outside of the turn during cornering, the resulting camber angle in relation to the road surface is (here exemplified for the rear axle):

$$\gamma_3 = \phi - \epsilon_3 \quad (3.1)$$

$$\gamma_4 = \phi + \epsilon_4 \quad (3.2)$$

Assuming that the camber angle in relation to the road leans towards the outside of the turn as they do in Figure 3.7, the camber force will counteract the lateral tire force created by the side slip angle. On the front axle, this corresponds to an under steering effect and on the rear axle the opposite.

To analyze the influence on steering behavior when changing the camber angle in relation to the body (ϵ_i), the outer tire during cornering will be observed since this tire will have more vertical load and hence, have the largest lateral force contribution in the axle. Reducing the geometrical camber contribution on the front axle will reduce the lateral camber force (which counteract the lateral tire force generated by the side slip angle, see Figure 3.7) and as a result, the front axle will produce more total lateral force, i.e. an over steering effect. The opposite discussion applies for the rear axle.

3.5 Track width change

The roll center height is also related to how the track changes with wheel travel, i.e. jounce and rebound. For instance, changing the suspension design to cause more tread change at the front axle, the roll centre will be located higher. This will increase the amount of vertical tire load shifted towards the outer wheel during cornering and result in more under steer, as explained in Section 3.6.2.

Simultaneously, raising the roll center height will also decrease the roll lever arm. Hence, an increase of tread change causes a reduction of the moment causing roll and thus a decrease of vehicle roll angle.

3.6 Vertical tire load

3.6.1 Static weight distribution

As the axle load increases, the cornering stiffness of that axle raises as well. Due to the non-linearity of the tire characteristics, the cornering stiffness will increase less than proportional to the increase in vertical load. By shifting the weight distribution towards more front axle weight, the cornering stiffness front is also increased but with less percentage as the static front axle weight changes. The opposite will happen on the rear axle, i.e. the cornering stiffness decreases due to the decreased static vertical load. This decrease of cornering stiffness on the rear axle is however closer to proportional compared to the increase on the front axle (in relation to the axle load change), and hence, the total result of shifting more weight towards the front is therefore an under steering effect. This is the direct effect.

A very important issue in the above conclusion about weight distribution is that it is based on the assumption of negligible changes of, for instance, roll steer due to changed axle load. The discussion is thus only completely valid when discussing the design weight distribution, where the suspension kinematics (toe angles and camber angles) can be kept constant. If the weight distribution is changed by means of loading, an indirect effect appears due to a change of roll steer and changed camber angles with an under steering or over steering effect as a result. The indirect effect might in some cases be more important than the direct effect, with a resulting total effect opposite than the above mentioned direct effect.

3.6.2 Vertical load transfer during cornering

During cornering, the tire normal force is shifted towards the outer wheels. How the shift in tire normal force is distributed between the front and rear axle is mainly dependent on the roll stiffness distribution and the roll center heights front and rear respectively. Due to the nonlinear dependency of lateral tire forces as a function of tire normal force, an increased shift in tire normal force during cornering will inevitably reduce the sum of lateral tire forces at the considered axle, see Figure 3.8. If the front-rear distribution of the tire normal force shift is

changed to increase at the front axle, the sum of the lateral tire forces at the front axle will experience more decrease than at the rear which corresponds to a direct under steering effect. Conversely, an over steering effect would be produced if the vertical load transfer distribution would be changed to be increased at the rear axle.

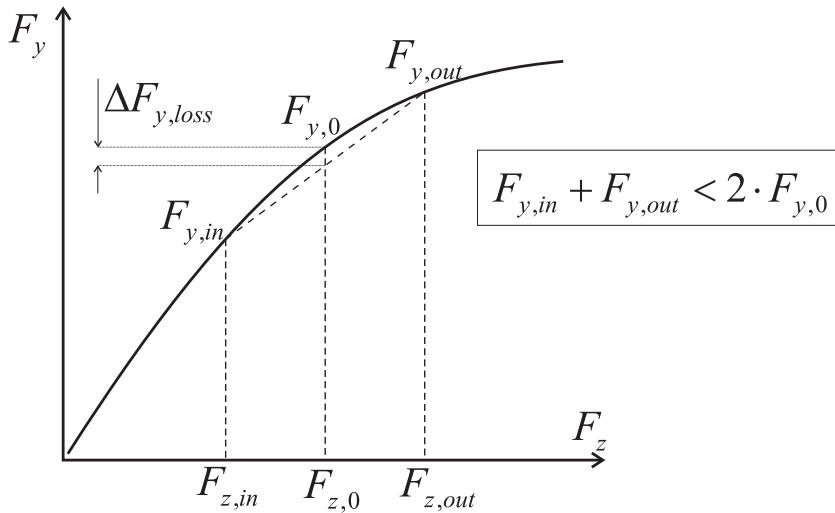


Figure 3.8: Non-linear relation between lateral force and vertical tire load for constant side slip angle α . This non-linearity in combination with the vertical load transfer during cornering, cause the total lateral force of the axle to be smaller than if no load transfer would occur.

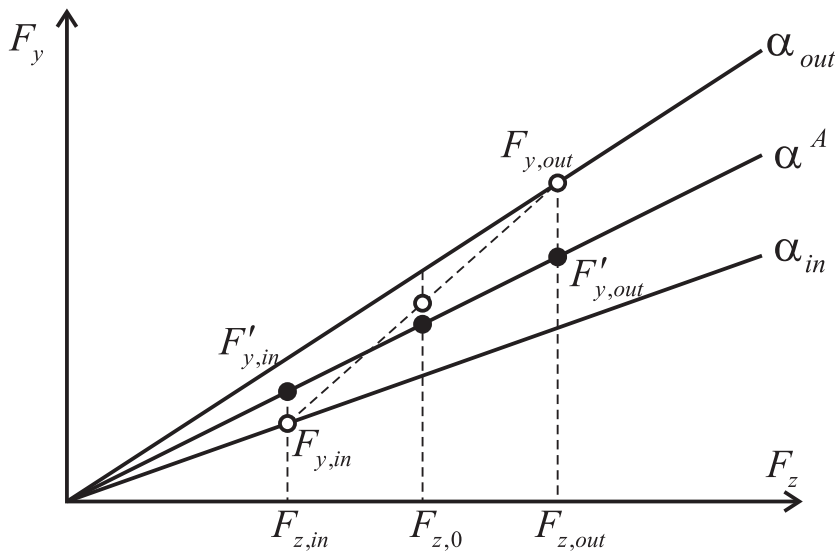


Figure 3.9: Lateral tire force plotted as a function of vertical load in the linear range plotted for the axle side slip angle and for the side slip angle of the inner and outer tire (mainly differentiated due to static toe-in). The filled black dots display the resulting lateral forces if no static toe-in is present and the circles if including static toe-in. The result is an increase in the average lateral force due to static toe-in.

If the tires are operated in the range where the vertical load dependency is still fairly linear, an indirect effect to load transfer can be observed due to static toe-in. This effect will be more evident on the rear axle due to the fact that the rear tires experience smaller side slip angle than

the front, making the change of side slip angle due to static toe more significant. Figure 3.9 displays the lateral force as a function of the vertical tire load for the rear axle side slip angle α^A and the side slip angle of the outer and inner tire, α_{out} and α_{in} , which are different mainly due to the static toe angle. The mean value of the tire forces if no static toe angle is present is shown with the filled black dots and including the influence of static toe is shown with circles. Hence, if the axle has significant static toe-in and the tires are in a linear region in relation to vertical load, the result of tire normal force shift will counteract the direct effect by creating more lateral axle force.

3.7 Driving/Braking forces

The direct effect of longitudinal tire forces is a reduction of the lateral tire forces according to the friction ellipse at combined slip conditions, see Figure 3.10. Hence, increasing the amount of the longitudinal force at a certain side slip angle will reduce the lateral force. Power application on a front wheel driven vehicle consequently reduces the lateral tire forces front, i.e. an under steering effect. The reverse yields by power application on a rear wheel driven vehicle. The changed steering behavior due to power application is particularly present at limit slip conditions.

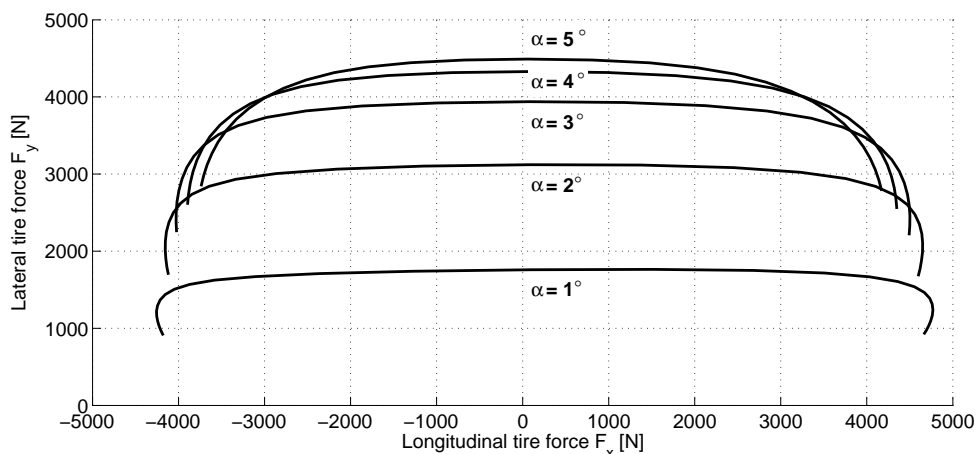


Figure 3.10: Example of how the longitudinal force influences the lateral force during combined slip conditions. The figure shows simulated tire characteristics of a performance tire (255/40 R18) using MF 5.2 at steady-state conditions with constant vertical tire load $F_z = 4500 \text{ N}$.

There are some indirect effects of power application. The longitudinal acceleration due to the longitudinal tire forces will cause vertical load transfer between the front and rear axle. The change in vertical load will influence the lateral tire forces and result in under steering and over steering effects. In addition, pitching of the vehicle will change the kinematic steering effects and, again, produce a certain amount of under or over steer. The longitudinal tire forces will also change the steer angles of the wheels due to compliance and hence, change the side slip angles and consequently the steering properties of the vehicle.

Different longitudinal forces on the inside and outside wheel during cornering are for instance created as a differential fails in completely compensating the rotational velocity difference be-

tween the inner and outer wheel. Hence, the outer wheel need to roll faster but is decelerated due to friction effects in the differential (the friction is in some cases intended by design or caused by an active differential). The inner wheel, on the contrary, needs to go slower but becomes accelerated. The consequence is that the differential will transfer more moment to the slower (inner) wheel. A non-ideal differential is a differential with locking effects due to friction or with built-in differential lock. It will provide the inner wheel with more driving torque (longitudinal force) and due to that, will create an under steering yaw moment. Simultaneously, the different longitudinal forces left and right will cause additional steer angles due to suspension compliance, either supporting or depressing the direct under steering effect.

Brake forces influence the lateral forces in the same way as the drive forces. However, the brake forces are normally determined by a fix brake force distribution between the front and rear axle, whereas a front or rear wheel driven vehicle only apply drive forces to one of the axles. This fix brake distribution normally cause more brake forces on the front than on the rear axle (due to stability reasons). Consequently, the direct effect of braking during steady-state cornering is under steer since the lateral forces on the front axle are more reduced than on the rear. An indirect effect of brake forces is the shift of vertical load towards the front axle, causing more lateral force at the same side slip angle. Hence, an effect causing less under steer. Furthermore, the suspension compliance due to longitudinal forces could be designed to either increase or decrease the under steer during braking in the corner.

3.8 Aligning moment

Since the lateral force is applied at a distance behind the centerline of the wheel, an aligning moment is produced which adds an anti-yawing moment on the vehicle during cornering. Hence, the aligning moment is trying to turn the vehicle in an under steering direction. A further effect on the aligning moment is the changed steer angles due to compliance. The steer angles are reduced due to the aligning moment, which on the front axle gives an under steering effect and on the rear axle the opposite.

Chapter 4

2-wheel vehicle model

The most important task of vehicle behavior models is the ability of reproducing the vehicle body movements due to typical driving inputs. For this purpose, the vehicle body can be considered to be a rigid body responding to forces and moments of different sources. An aim will be to describe these acting forces as far as possible without a modeling of the force transfer properties in the tire road interface or a thorough description of the suspension kinematics and compliance properties. They have to be modeled with as simple formulations as possible like those partially already known in behavior models (e.g. [46, 34, 20, 1]). Consequently, the behavior models do not need to be extended with additional rigid bodies which are transferring forces to the vehicle body over additional mechanical bindings. During strict translational movements, the whole vehicle mass can be used whereas during heave motions only the sprung mass is moved, which normally is about just less than 90 % of the total vehicle mass. In the frame of this modeling, it is sufficient to use the total mass also for heave motions of the model and to adjust the total heave behavior by use of other model parameters.

The linear 2-wheel model from Riekert and Schunck [46] is the first model presented in an attempt of describing the vehicle movements due to the inputs steering wheel angle and longitudinal speed. The theory behind this model builds on the assumption that the lateral forces of each axle are summed together in one linear axle force element located in the middle of the track, see Figure 4.1. The subscript f and r will define the front and rear axle respectively. Subscript j is used when both front and rear are intended. The equations of motion in the model of Riekert and Schunck are linearized and the vehicle center of gravity height is neglected, i.e. the center of gravity is set at ground level. Due to these assumptions, this model's validity range is limited to a maximum of about 4 m/s^2 lateral acceleration.

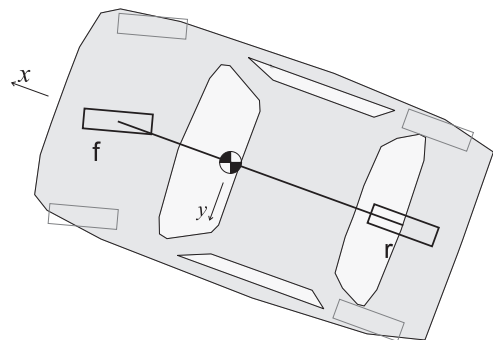


Figure 4.1: Vehicle seen from above describing the 2-wheel model concept.

This 2-wheel vehicle behavior model is based on the integration of the physical properties of the wheel suspension in the simplest form as possible. Consequently, the significant effects of many different vehicle components are summarized into certain overall relations. A consideration of single effects would increase the model complexity as well as the testing program needed to parameterize it.

Several vehicle models based on this principle can be found in literature, e.g. [20, 34, 55, 1] to mention a few, where important non-linearities have been added to extend the model's validity range. For clarity and since an extended version of this model class serves as a starting point for the investigations, the model equations will be derived in the following.

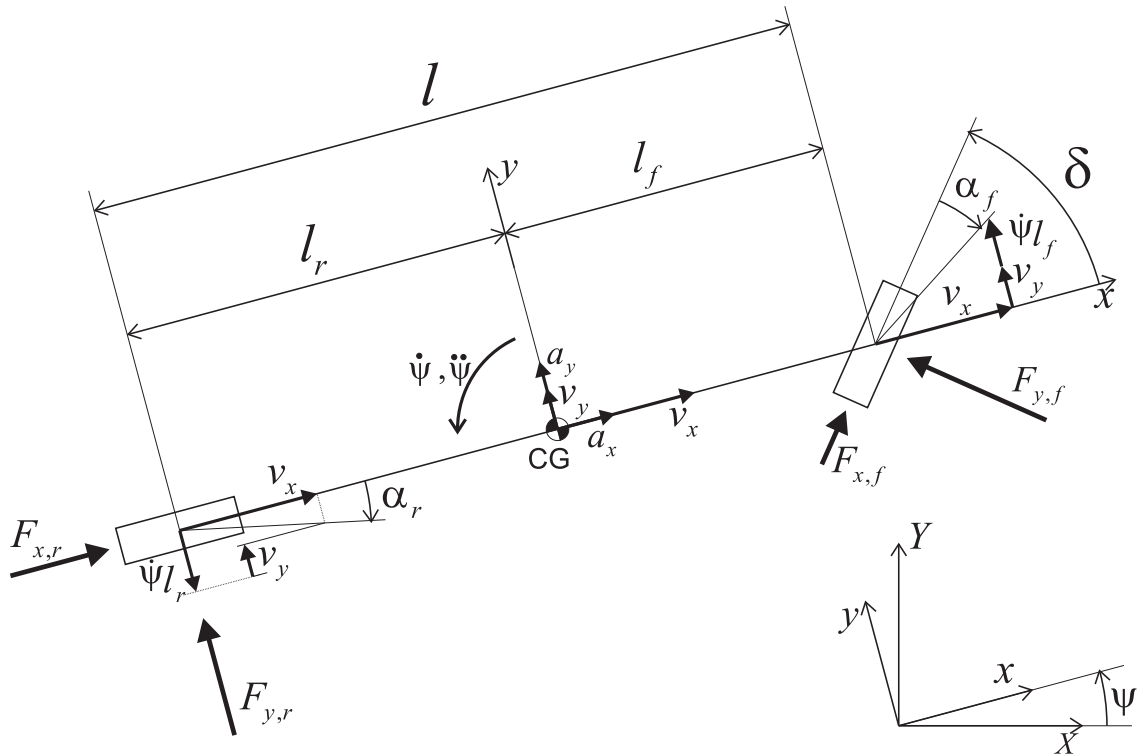


Figure 4.2: Definitions and geometry of the simplified 2-wheel vehicle model.

4.1 Equations of motion

Figure 4.2 displays the forces and distances used in the following equations of motion.

$$m \cdot a_x = F_{x,f} \cdot \cos \delta + F_{x,r} - F_{y,f} \cdot \sin \delta \quad (4.1)$$

$$m \cdot a_y = F_{y,f} \cdot \cos \delta + F_{y,r} + F_{x,f} \cdot \sin \delta \quad (4.2)$$

$$J_\psi \cdot \ddot{\psi} = l_f \cdot (F_{y,f} \cdot \cos \delta + F_{x,f} \cdot \sin \delta) - l_r \cdot F_{y,r} \quad (4.3)$$

Consequently in the linear 2-wheel model, the substitutions $\cos \delta \cong 1$ and $\sin \delta \cong \delta$ are introduced, assuming small angles in general (see also kinematics). In many applications, the equation for the longitudinal motion is neglected by setting the longitudinal velocity as an input

to the model and thus, leave out Equation (4.1). As a consequence, the influences of $F_{x,j}$ in Equation (4.2) and (4.3) are neglected.

4.2 Steering system

The lowest mechanical eigenfrequency of a steering system without power steering is significantly higher than those relevant for the vehicle handling [34] and is therefore neglected. An introduction of an additional steering elasticity is also avoided in this model. A power steering however, can influence the dynamical properties of the vehicle also at lower frequencies which can not be depicted with a rigid steering system.

The steer angle δ is often assumed to have a proportional relation to the steering wheel angle δ_H , i.e. $\delta = \delta_H/i_s$ where i_s is the steering ratio. Generally for the 2-wheel model i_s is assumed to be constant. In reality, this steering ratio is dependent of the steering wheel angle $i_s = i_s(\delta_H)$, see Figure 4.3, [20].

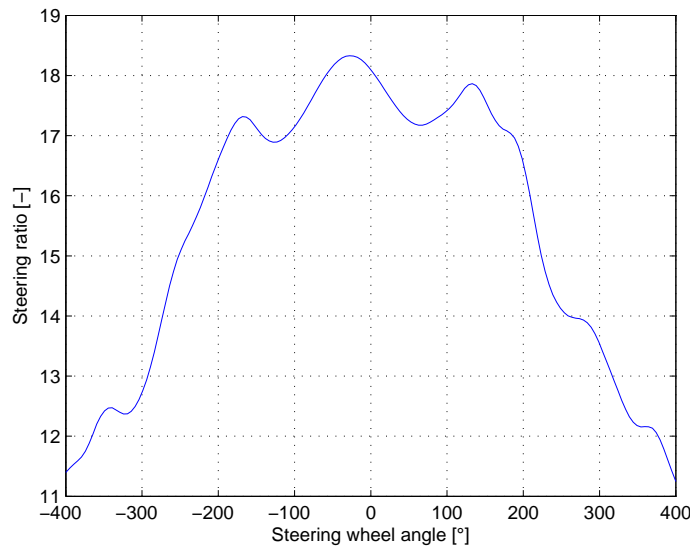


Figure 4.3: Steering ratio as a function of the steering wheel angle.

4.3 Kinematics

Kinematics gives the longitudinal and lateral accelerations:

$$a_x = \dot{v}_x - v_y \cdot \dot{\Psi} \quad (4.4)$$

$$a_y = \dot{v}_y + v_x \cdot \dot{\Psi} \quad (4.5)$$

The lateral force at each axle is given as a function (or as a look-up table) of the side slip angle α_j of the axle. From the kinematics and the geometry in the 2-wheel model, the side slip angles at the front and rear axle are given in linearized form by:

$$\alpha_f = \delta - \frac{l_f \dot{\psi} + v_y}{v_x} \quad (4.6)$$

$$\alpha_r = \frac{l_r \dot{\psi} - v_y}{v_x} \quad (4.7)$$

4.4 Lateral force characteristics

In the original 2-wheel model of Riekert and Schunck [46], the lateral force was modeled to have a linear relation to the side slip angle. This is one of the main reasons why the validity range of this model is limited. In the model extensions made by for instance Meljnikov [34], this relation was extended to be non-linear. One way of identifying this relation is to measure the vehicle in a steady-state maneuver where the yaw acceleration is $\ddot{\psi} \approx 0$. In doing this, the lateral acceleration a_y , the yaw rate $\dot{\psi}$, the steer angle δ and the vehicle longitudinal and lateral velocity, v_x and v_y , have to be measured. More about the measuring setup can be found in Kobetz [20].

If neglecting the influence of the longitudinal forces and with $\cos \delta \approx 1$, the Equations (4.2) and (4.3) can be combined to give:

$$F_{y,f} = ma_y \frac{l_r}{l} \quad (4.8)$$

$$F_{y,r} = ma_y \frac{l_f}{l} \quad (4.9)$$

For the measured lateral acceleration, corresponding side slip angles exist, see Equation (4.6) and (4.7), which finally builds the lateral force characteristics of each axle, $F_{y,j} = F_{y,j}(\alpha_j)$ – principally a nonlinear relationship. This axle force characteristics can be fitted with an empirical formula. However, in this investigation it is always stored as a look-up table as displayed in Figure 4.4.

4.5 Lateral force dynamics

The simple relation between lateral axle force and axle slip angle as presented in Figure 4.4 is only entirely valid during steady-state driving. During dynamics, the lateral force for each tire, and consequently the whole axle, will have a time delay due to the build up of the lateral force. This effect will be explained in the following.

In comparison to the longitudinal forces, the time delayed build-up of the lateral tire forces plays a more important role in vehicle handling. At a rolling tire, the cleats of the tire tread enter the tire patch un-deflected and have to be laterally deflected before transmitting lateral forces to

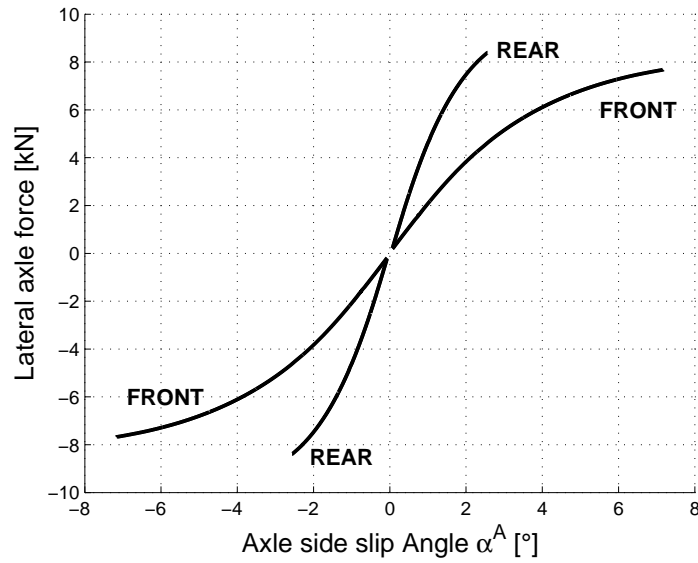


Figure 4.4: Lateral axle force characteristics of the 2-wheel model (look-up table).

the vehicle. Therefore, a change in lateral slip angle will produce the complete effect when the cleats have moved through the tire patch. Consequently, the tires will be reacting faster on slip angle changes at higher speeds. The distance required for the tire to build up lateral forces is defined as the relaxation length $l_{e,j}$. In addition, at larger slip angles, the tire is reacting faster than at smaller slip angles. At a vertical load increase, the lateral force build-up will also be delayed since the cleats have to be additionally deflected before transmitting an extra lateral force but this smaller effect will be neglected.

In order to capture this lateral force build-up, a simple approach from Böhm [5] is used described by a first order differential equation:

$$\frac{C_{\alpha,j}}{C_{y,j} \cdot v_x} \dot{F}_j^{dyn} + F_j^{dyn} = F_{y,j}^{stat} \quad (4.10)$$

where F_j^{stat} is the static force discussed earlier and F_j^{dyn} defines the actual force to be used in the equations of motion. The relation between the cornering stiffness $C_{\alpha,j}$ and the lateral stiffness $C_{y,j}$ provides the relaxation length $l_{e,j}$ which is a part of the first order system's time constant T_j :

$$\frac{C_{\alpha,j}}{C_{y,j} \cdot v_x} = \frac{l_{e,j}}{v_x} = T_j \quad (4.11)$$

The faster tire reaction at higher lateral forces, i.e. at higher slip angles, will not be depicted with this approach, Ammon [1].

The vertical load transfer during dynamic maneuvers will appear time delayed in comparison to the vertical load transfer at steady-state cornering. This is caused by the vehicle's roll dynamics, i.e. a combination of inertia properties of the vehicle body, shock absorbers, anti-roll bar stiffness, spring stiffness and suspension kinematics. The decrease in total lateral axle force due

to an increased vertical load difference between inside and outside tire, is already included in the 2-wheel model steady-state axle force characteristics in Figure 4.4. However, the influence of the dynamic vertical load transfer is not explicitly formulated since it can not be separated from other effects at steady-state cornering. The reduction of the total lateral axle force is more important at higher lateral accelerations since the vertical load transfer to the outside tire will be large enough for the tire properties to reach their non-linear range.

4.6 Roll degree of freedom

Up until now, the height of the vehicle's center of mass has been neglected. In order to capture the vehicle's roll movement, the vehicle center of mass is set at the height Δh above an assumed horizontal roll axis located in RC (roll center) see Figure 4.5.

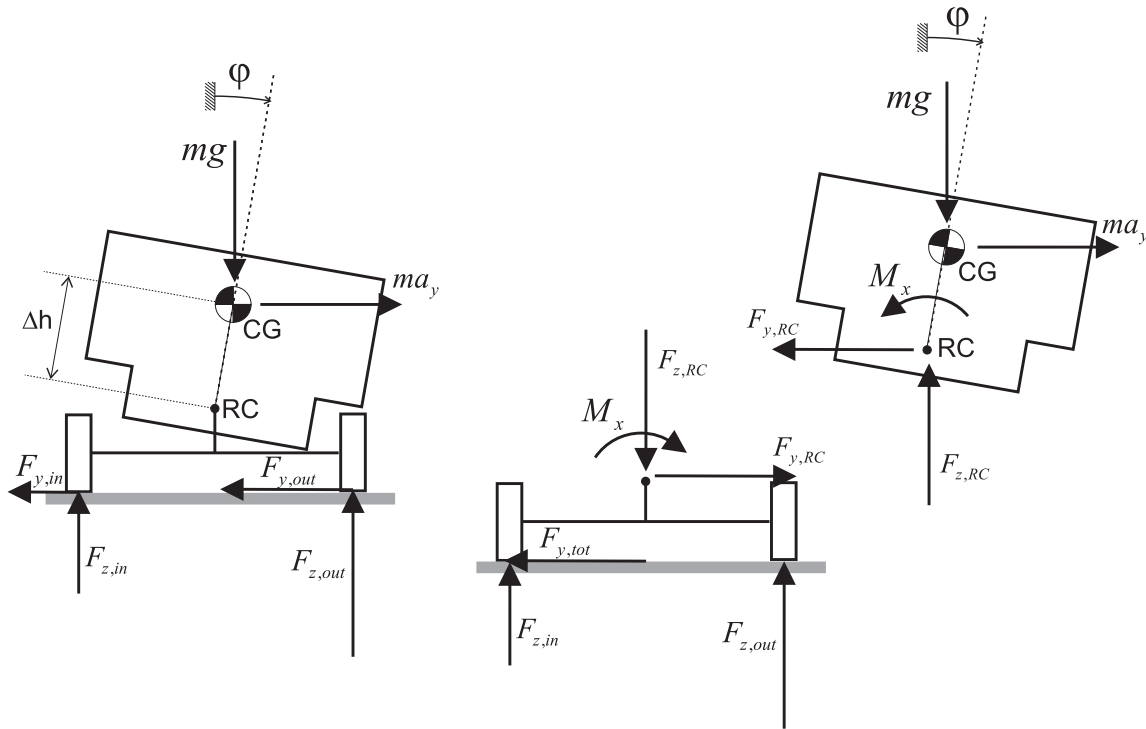


Figure 4.5: Roll model seen from behind.

The roll moment M_x is modeled by a roll stiffness and roll damping. The following equation of motion results for the roll movement defined around the centre of gravity (CG):

$$J_\phi \cdot \ddot{\phi} = F_{y,RC} \cdot \Delta h \cos \phi + F_{z,RC} \cdot \Delta h \sin \phi - (d_\phi \cdot \dot{\phi} + k_\phi \cdot \phi) \quad (4.12)$$

and with neglecting the un-sprung mass with $F_{y,in} + F_{y,out} = F_{y,tot} = F_{y,RC} = ma_y$; $F_{z,in} + F_{z,out} = F_{z,RC} = mg$, and small roll angles ϕ , it follows:

$$J_\phi \cdot \ddot{\phi} = ma_y \Delta h + mg \Delta h \phi - d_\phi \cdot \dot{\phi} - k_\phi \cdot \phi \quad (4.13)$$

The total roll stiffness k_ϕ is made up from the vertical spring stiffness of the suspension springs together with the anti-roll bars in combination with the geometrical influences of where these springs are acting. d_ϕ is the total roll damping made up of the damper characteristics and geometrical influence where they are acting. J_ϕ is the roll moment of inertia around the center of gravity. Moreover, the roll moment due to lateral mass displacement can be included in an effective roll stiffness $k_\phi^{eff} = k_\phi - mg\Delta h$ giving the following simplified roll equation.

$$J_\phi \cdot \ddot{\phi} = ma_y \Delta h - d_\phi \cdot \dot{\phi} - k_\phi^{eff} \cdot \phi \quad (4.14)$$

In order to describe the roll motion's influence upon the lateral dynamics, the kinematics have to be modified, i.e. the following side slip angle calculation is used [1]:

$$\alpha_f = \delta - \frac{l_f \cdot \dot{\psi} + v_y + \Delta h \cdot \dot{\phi}}{v_x} \quad (4.15)$$

$$\alpha_r = \frac{l_r \cdot \dot{\psi} - v_y - \Delta h \cdot \dot{\phi}}{v_x} \quad (4.16)$$

Hence, the roll rate has an influence on the contact calculation which is an important effect during strongly dynamical maneuvers.

Important assumptions in this roll model are:

- The roll center (roll axis) is fixed. This is not completely the case, especially not for independent suspensions.
- The roll axis is horizontal, i.e. the coupling between roll and yaw motion is neglected.
- The spring stiffness and damping rates of tires and suspension from front and rear axle respectively, are concluded in an applied overall vehicle roll moment.

4.7 Simulation results with the 2-wheel model

To conclude this chapter, a few simulation results with the 2-wheel model will be demonstrated. The 2-wheel model parameters have been identified from driving measurement data using an in-house developed tool at Daimler AG. This tool handles everything from pre-processing of measurement data to the automatic parameter identification. An early stage of this tool is described in [20] and further literature can be found in [24] and [21].

The resulting model quality is illustrated by comparing the simulation results with the measurements in a double lane change maneuver. The measured steering wheel angle δ_D and the longitudinal velocity v_x were used as inputs to the simulation model. Figure 4.6(a) displays the lateral acceleration and Figure 4.6(b) the yaw rate, both showing a very good correlation despite the severe lateral maneuver. The small deviation in vehicle side slip angle seen in Figure 4.7(a) is mainly due to the strong level of noise in the sensor measuring the lateral velocity. The accuracy of the roll angle is confirmed in Figure 4.7(b).

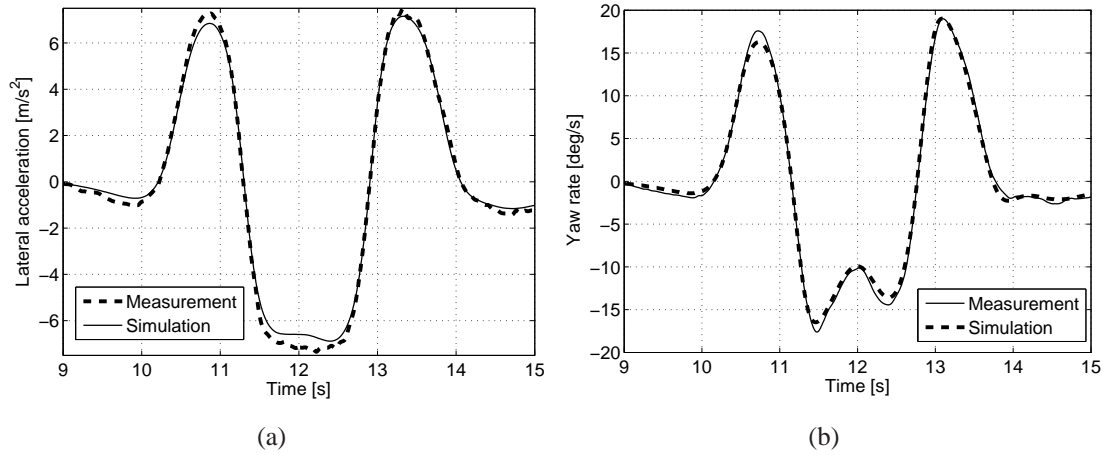


Figure 4.6: Measurement data in comparison with simulation results with the 2-wheel model in a double lane change maneuver, lateral acceleration in CG (a) and yaw rate (b).

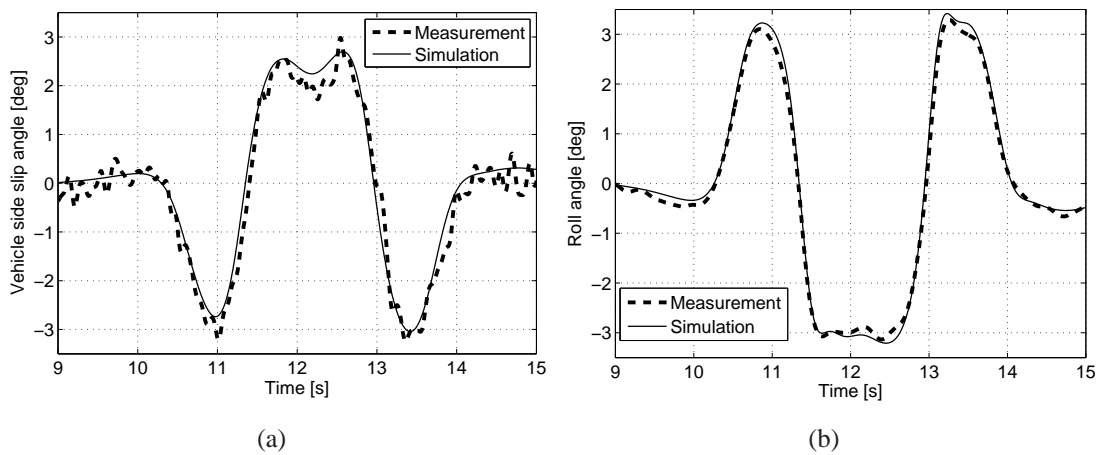


Figure 4.7: Measurement data in comparison with simulation results with the 2-wheel model in a double lane change maneuver, vehicle side slip angle in (a) and roll angle in (b).

Chapter 5

A common base of comparing the 2-wheel with 3D-vehicle models

A central topic of this chapter is to calculate the lateral axle force characteristics $F_{y,j}^A(\alpha^A)$ of the 2-wheel model assuming known tire forces and moments during a steady-state maneuver. Reference vehicle A described in Section 2.5 has been used throughout all investigations in this chapter.

5.1 A first example of comparison

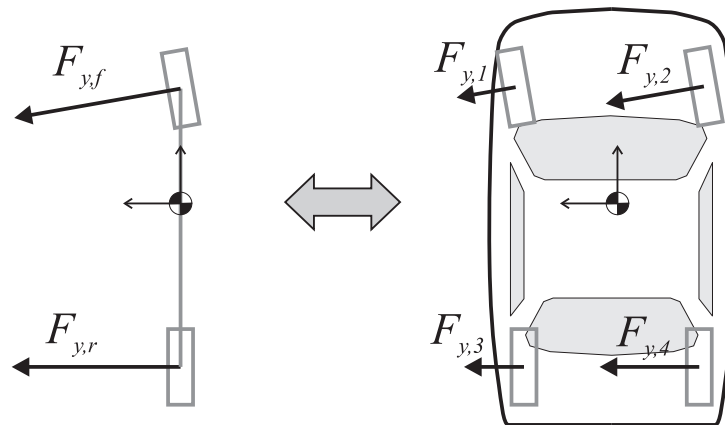


Figure 5.1: The lateral forces acting on the 2-wheel model in comparison to the lateral tire forces of a full vehicle model.

A simple vehicle model like the 2-wheel model can in many cases calculate the vehicle motion states nearly as accurate as a sophisticated MBS model approach. However, due to the limited amount of outputs in comparison to the detailed MBS model, the 2-wheel model will never provide the same analysis potential as the detailed MBS model. Nevertheless, when focusing mainly on the motion states of the vehicle body during handling, the 2-wheel model will still

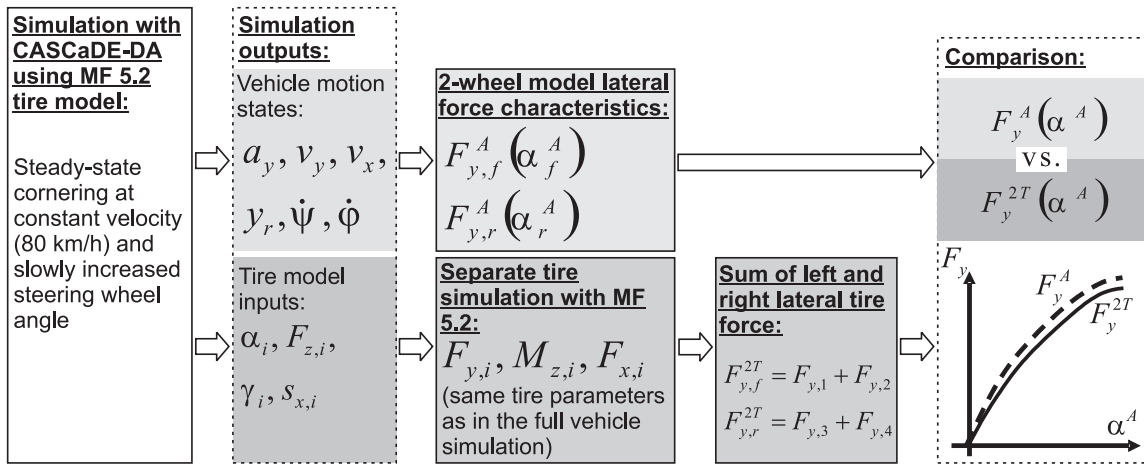


Figure 5.2: Block representation of the procedure for deriving the common base for comparing a 2-wheel model with a 3D-vehicle model.

provide the sufficient outputs during the maneuvers of interest. Despite the fact that the properties of the two tires and the suspension of an axle are lumped together into one single axle force element in the 2-wheel model, the two model classes; the 2-wheel model and the full vehicle model CASCaDE-DA, will be compared here by using the axle force element in the 2-wheel model as a base. In a very simplified manner this means that the sum of the left and right lateral tire forces of an axle in the MBS model will be compared to the corresponding lateral axle force characteristics in the 2-wheel model, see Figure 5.1.

The investigation described above is simple to carry out when using a complex MBS vehicle model as a reference. Figure 5.2 shows a block representation of this investigation. Starting to the left in the figure, a full vehicle simulation is performed using the reference model CASCaDE-DA equipped with the tire model MF 5.2, both described in Chapter 2. A number of states in this full vehicle simulation are recorded and used in this investigation: The lateral acceleration a_y , lateral velocity v_y , longitudinal velocity v_x , rack displacement in the steering system y_r and the yaw rate $\dot{\psi}$, are used to identify the lateral force characteristics of the 2-wheel model $F_y^A(\alpha^A)$ according the Equations (4.8), (4.9), (4.15) and (4.16), see upper path in Figure 5.2. Moreover, the inputs to the tire model during the full vehicle simulation: side slip angle α_i , tire camber angle γ_i , vertical tire load $F_{z,i}$ and longitudinal slip $s_{x,i}$ are also recorded in order to be used when simulating the tire model separately and in this manner calculate the tire forces and moments independently, see lower path in Figure 5.2. Finally, the lateral force characteristics from the 2-wheel model, $F_y^A(\alpha^A)$, and the lateral force characteristics calculated from the two tires, i.e. $F_y^{2T}(\alpha^A)$, are compared, see right block in Figure 5.2.

The maneuver used for this investigation is a steady-state cornering maneuver driven at constant velocity. In this maneuver, the vehicle is driven straight ahead at a constant velocity of 80 km/h. The lateral acceleration is increased by increasing the steering wheel angle slowly so that time dependent effects can be neglected, until the vehicle reaches the maximum possible lateral acceleration. The steering wheel angle and the axle side slip angle front and rear are displayed as a functions of lateral acceleration in the Figures 5.3(a) and 5.3(b).

When observing the equations of motion of the 2-wheel model during steady-state cornering,

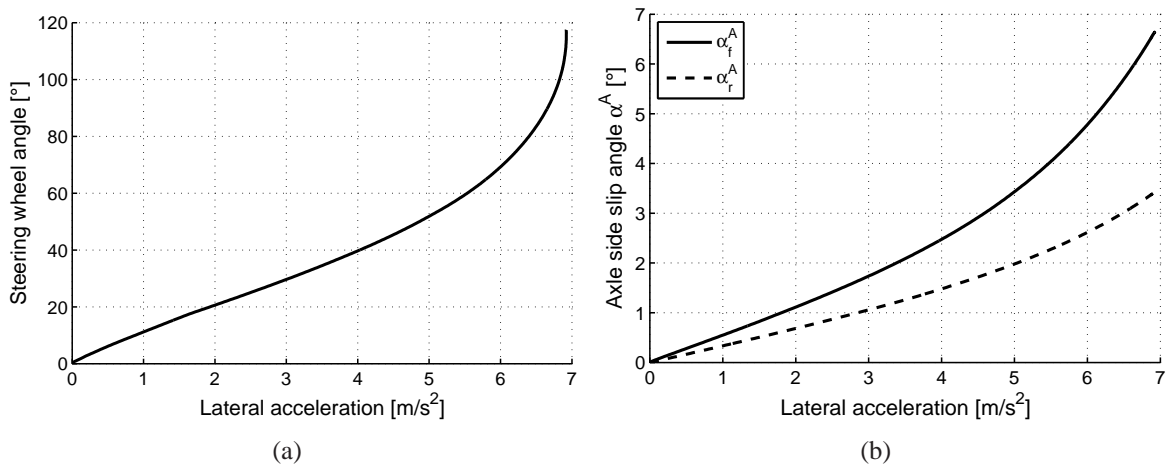


Figure 5.3: Reference figures for the maneuver used in the sensitivity analysis. Figure (a) shows the steering wheel angle as a function of the lateral acceleration. Figure (b) depicts the side slip angles for the front and rear axle in relation to the lateral acceleration.

and without aerodynamic forces, the sum of the lateral axle forces acting on a vehicle is directly related to the lateral acceleration of the vehicle. The yaw acceleration is subsequently associated to the relation between the lateral axle forces acting at the front and rear axle together with the distances these forces are acting from the center of gravity, see Equations (4.8) and (4.9). With this in mind, it is easy to believe that the lateral axle force characteristics in the 2-wheel model will correspond to the sum of the lateral tire forces of the vehicle in question during the same steady-state cornering maneuver.

By using the simulation inputs and outputs of the reference model CASCaDE-DA during a steady state maneuver, the lateral axle force characteristics of the 2-wheel model, $F_y^A(\alpha^A)$, can be identified as described in Chapter 4. Equations (5.1) to (5.4) lists these relations again where the simulation outputs v_x , v_y , a_y and $\dot{\psi}$ from the simulations with CASCaDE-DA are used to compose the lateral axle force characteristics $F_y^A(\alpha^A)$, which are also shown in Figure 5.4. Note that the rack displacement is used when calculating the steer angle δ used in Equation (5.1).

$$\alpha_f^A = \delta(y_r) - \frac{l_f \dot{\psi} + v_y}{v_x} \quad (5.1)$$

$$\alpha_r^A = \frac{l_r \dot{\psi} - v_y}{v_x} \quad (5.2)$$

$$F_{y,f}^A = ma_y \frac{l_r}{l} \quad (5.3)$$

$$F_{y,r}^A = ma_y \frac{l_f}{l} \quad (5.4)$$

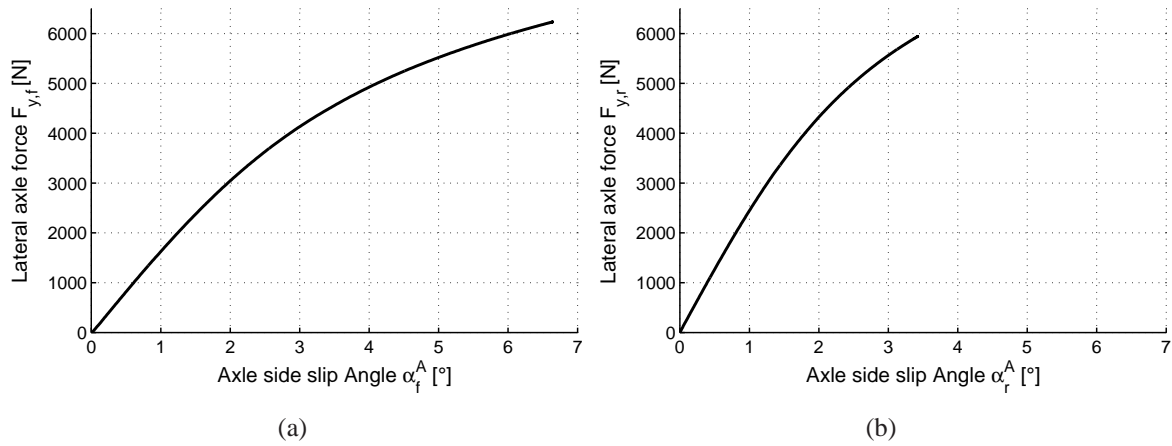


Figure 5.4: Front (a) and rear (b) lateral axle force characteristics in the 2-wheel model (from a different vehicle than in Figure 4.4). Since these force characteristics have been generated from simulation results with an absolutely symmetric simulation model on a flat road surface, the positive and negative branch are mirror symmetric and therefore only the positive branch is displayed here. With driving measurements, the positive and negative branches are not necessarily symmetric since simple factors like for instance loading condition, ply-steer effects in the tires and asymmetric suspension (due to e.g. tolerances in suspension components) could cause a non-symmetric vehicle behavior.

The lateral tire forces calculated in the reference model CASCaDE-DA during the same steady state maneuver are furthermore summarized to get the total lateral force acting at the front $F_{y,f}^{2T}(\alpha_f^A)$ and rear $F_{y,r}^{2T}(\alpha_r^A)$ axle. This is made assuming small steer angles and neglecting the influence of longitudinal forces:

$$F_{y,f}^{2T} = F_{y,1} + F_{y,2} \quad (5.5)$$

$$F_{y,r}^{2T} = F_{y,3} + F_{y,4} \quad (5.6)$$

The forces $F_{y,f}^{2T}(\alpha_f^A)$ and $F_{y,r}^{2T}(\alpha_r^A)$ will be referred to as the *equivalent lateral force characteristics* and are always calculated using the tire forces in the CASCaDE-DA simulations. Hence, F_y^A corresponds to the lateral axle force in the 2-wheel model and F_y^{2T} is an equivalent lateral axle force calculated from tire outputs. As will be seen later, the lateral axle force in the 2-wheel model is not simply equal to the sum of the lateral tire forces and an approach to calculate a correct equivalent lateral axle force characteristics from tire forces will therefore be derived.

Aerodynamics also influences the lateral axle force characteristics in the 2-wheel model. However, in order to simplify the comparison in this investigation, the aerodynamic forces are neglected by simply turning off the aerodynamics in both simulation models. This is also done under the assumption that the aerodynamics has a small influence at the velocities driven in this maneuver and eliminating it makes the evaluation of other effects more evident.

Another important effect to exclude at this point is the influence of elasticity in the steering system. This is done by using the rack displacement as input to the 2-wheel model instead of the more commonly used steering wheel angle when calculating the lateral force characteristics of the 2-wheel model. This means that a ratio between the rack displacement and the mean front steer angle of the front wheels is used, instead of the conventional ratio between the steering wheel angle and mean steer angle of the front wheels.

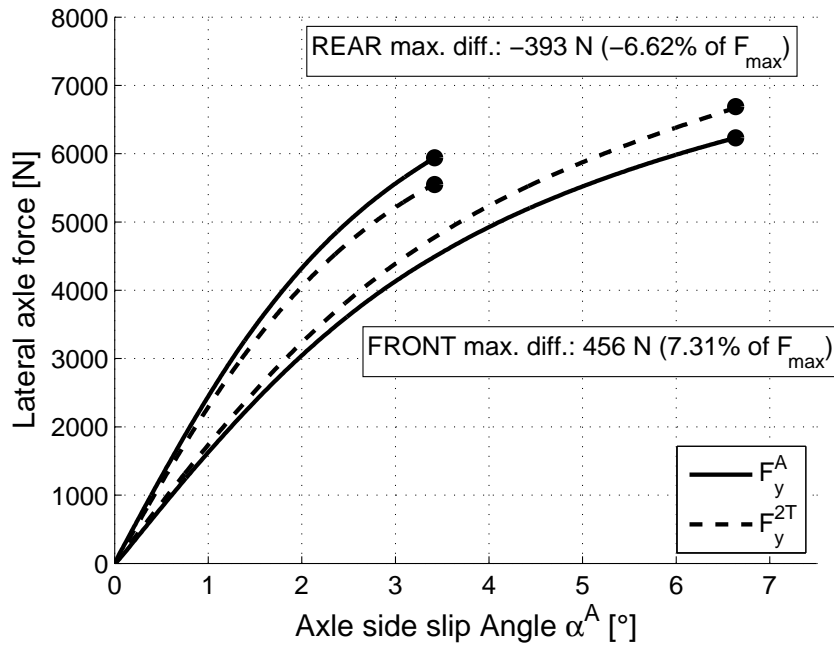


Figure 5.5: Lateral force characteristics of the 2-wheel model according to the Equations (4.6) to (4.9), in comparison to the summarized lateral tire forces in the Equations (5.5) and (5.6). Note that the side slip angle of each axle (Equations (4.6) and (4.7)) is used on the x-axis also for the 4-wheel model.

Figure 5.5 shows the difference (for both the front and rear axle) between the sum of the lateral tire forces according to the Equations (5.5) and (5.6) and the identified lateral axle force characteristics in the 2-wheel model according to the Equations (5.1) to (5.4). The difference is always calculated in relation to the solid line representing $F_y^A(\alpha^A)$ and is 456 N (7.31 % of $F_{y,max}^A$) on the front axle and -393 N (-6.62% of $F_{y,max}^A$) on the rear. The relative values in percent are always set in relation to the maximum value of the corresponding lateral axle force characteristics, i.e. $F_{y,max}^A = \max(F_y^A)$.

5.2 Method to consider important effects

As already discussed in Chapter 3, there are numerous effects influencing the steering behavior of the vehicle. One significant effect that has been overseen when simply adding the lateral tire forces together, and assuming they act at the center of the axle, is the aligning moment at the tire contact point. The aligning moment will try to turn the vehicle out of the turn and it is caused by the fact that the lateral tire force actually acts behind the tire contact point. Instead of having the lateral force act at a point behind the contact point as it does in reality, the force is reduced to the contact point. This conversion involves the addition of the aligning moment, see Figure 5.6(a) and 5.6(b).

In order to take this aligning moment into consideration, the aligning moments from the four tires are summarized to a free moment acting on the vehicle body. This free moment is furthermore converted into a force couple acting at the front and rear axle using the wheel base, since this is the location of comparison with the lateral axle force characteristics of the 2-wheel

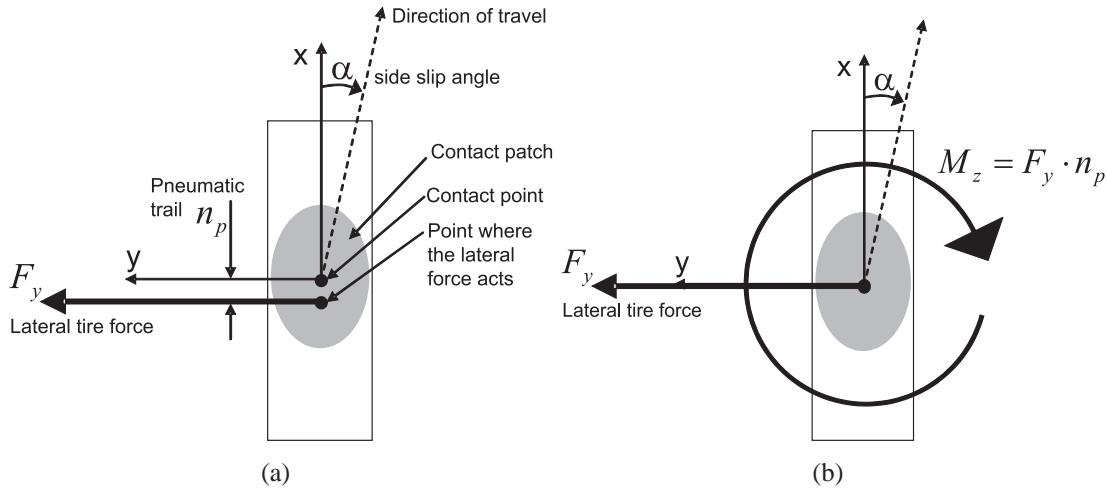


Figure 5.6: The lateral tire force F_y as it acts on the tire in reality (a). In (b) the lateral tire force is reduced to the tire contact point producing the self aligning torque M_z .

model. This results in the following equation to be used when considering the effect of the aligning moment:

$$F_{y,f}^{2T} = F_{y,1} + F_{y,2} + \frac{1}{l} \sum_{i=1}^4 M_{z,i} \quad (5.7)$$

$$F_{y,r}^{2T} = F_{y,3} + F_{y,4} - \frac{1}{l} \sum_{i=1}^4 M_{z,i} \quad (5.8)$$

The aligning moment is negative when the lateral force is positive, which explains the positive sign before the aligning moment in Equation (5.7).

Figure 5.7 shows the result when considering also the aligning moment. This correction brings the result closer to the target with the difference front being 260 N (4.17 % of $F_{y,max}^A$) and rear being -198 N (-3.33 % of $F_{y,max}^A$)

As discussed in Section 3.7, locking effects due to inner friction in a differential will cause slightly different fore and aft forces on the inside and outside wheel while propelling during cornering. Equation (5.9) and (5.10) takes this into consideration when calculating $F_{y,j}^{2T}$ and Figure 5.8 displays the results in comparison to $F_{y,j}^A$. The difference is now down to 166 N (2.66 % of $F_{y,max}^A$) on the front axle and -104 N (-1.74 % of $F_{y,max}^A$) on the rear.

$$F_{y,f}^{2T} = F_{y,1} + F_{y,2} + \frac{1}{l} \sum_{i=1}^4 M_{z,i} + \frac{1}{l} \left((F_{x,2} - F_{x,1}) \frac{b_f}{2} + (F_{x,4} - F_{x,3}) \frac{b_r}{2} \right) \quad (5.9)$$

$$F_{y,r}^{2T} = F_{y,3} + F_{y,4} - \frac{1}{l} \sum_{i=1}^4 M_{z,i} - \frac{1}{l} \left((F_{x,2} - F_{x,1}) \frac{b_f}{2} + (F_{x,4} - F_{x,3}) \frac{b_r}{2} \right) \quad (5.10)$$

So far, the steer angles have been neglected. Hence, the lateral tire forces were assumed to act perpendicular to the vehicle body. When considering the steer angles, the lateral forces

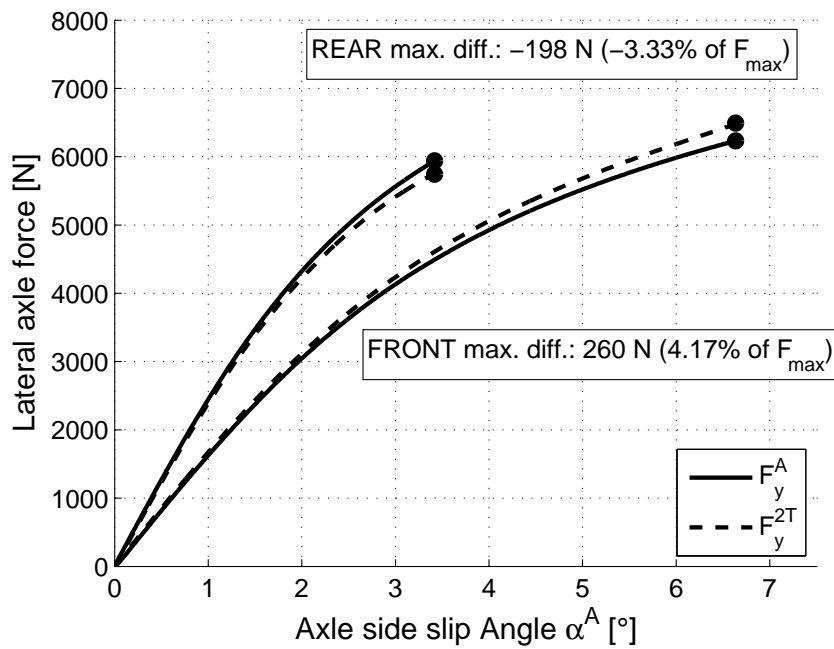


Figure 5.7: Lateral force characteristics of the 2-wheel model in comparison to the summarized lateral tire forces when considering the effect of aligning moments.

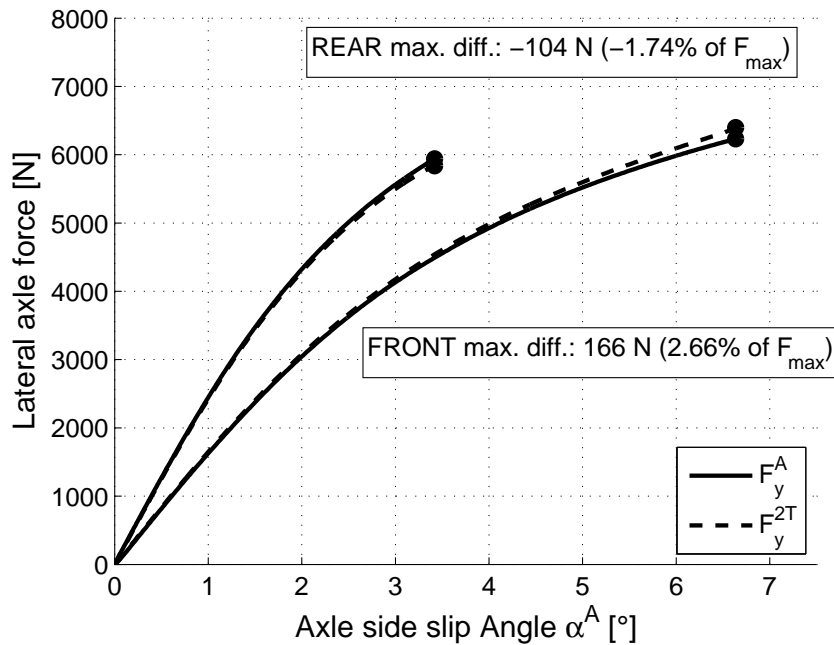


Figure 5.8: $F_{y,j}^A$ in comparison to $F_{y,j}^{2T}$ when including the effect of the yaw moment caused by the longitudinal forces, Equation (5.9) and (5.10).

mainly on the front axle will also have a longitudinal component causing a yaw moment. The significantly larger lateral force on the outside front wheel will thus cause a counteracting yaw moment. A small angle approximation is possible, i.e. $\cos \delta_i \approx 1$ and $\sin \delta_i \approx \delta_i$. Equation (5.11) and (5.12) define the approach considering the steer angles when calculating $F_{y,j}^{2T}$ and

Figure 5.9 shows the resulting comparison with 43 N (0.69 % of $F_{y,max}^A$) difference on the front axle and -23 N (-0.38 % of $F_{y,max}^A$) difference on the rear axle.

$$F_{y,f}^{2T} = F_{y,1} + F_{y,2} + \frac{1}{l} \sum_{i=1}^4 M_{z,i} + \frac{1}{l} \left((F_{x,2} - F_{x,1}) \frac{b_f}{2} + (F_{x,4} - F_{x,3}) \frac{b_r}{2} \right) + \frac{1}{l} \left((F_{y,1} \delta_1 - F_{y,2} \delta_2) \frac{b_f}{2} + (F_{y,3} \delta_3 - F_{y,4} \delta_4) \frac{b_r}{2} \right) \quad (5.11)$$

$$F_{y,r}^{2T} = F_{y,3} + F_{y,4} - \frac{1}{l} \sum_{i=1}^4 M_{z,i} - \frac{1}{l} \left((F_{x,2} - F_{x,1}) \frac{b_f}{2} + (F_{x,4} - F_{x,3}) \frac{b_r}{2} \right) - \frac{1}{l} \left((F_{y,1} \delta_1 - F_{y,2} \delta_2) \frac{b_f}{2} + (F_{y,3} \delta_3 - F_{y,4} \delta_4) \frac{b_r}{2} \right) \quad (5.12)$$

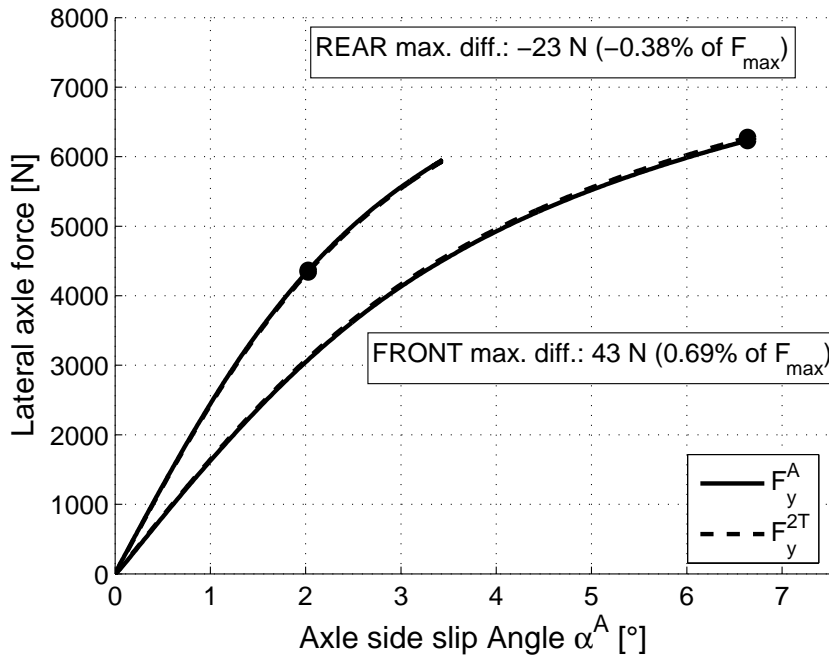


Figure 5.9: $F_{y,j}^A$ in comparison to $F_{y,j}^{2T}$ when including the steer angle contribution when calculating $F_{y,j}^{2T}$.

Despite a very small disagreement between $F_{y,j}^A$ and $F_{y,j}^{2T}$ in Figure 5.9, a final error contribution will be analyzed - the yaw inertia. When deriving the expression for the lateral axle forces $F_{y,j}^A$, a steady-state condition is assumed with the yaw acceleration being small, i.e. $\ddot{\psi} \approx 0$. This is not completely true, especially when observing real measurement data. If not assuming the yaw acceleration $\ddot{\psi}$ to be negligible, the equations of motion in Equation (4.2) and (4.3) will give the following expression for the lateral axle forces:

$$F_{y,f}^A = m a_y \frac{l_r}{l} + J_\psi \ddot{\psi} \frac{1}{l} \quad (5.13)$$

$$F_{y,r}^A = ma_y \frac{l_f}{l} - J_\psi \ddot{\psi} \frac{1}{l} \quad (5.14)$$

In this investigation, simulation results are used instead of measurements, allowing the maneuvers to be run with extreme accuracy. The steady state cornering maneuver can also be driven over a much longer time in simulations, assuring a well achieved steady-state condition to be reached. Figure 5.10 illustrates the comparison of $F_{y,j}^{2T}$ and $F_{y,j}^A$ when including the yaw inertia into the calculations. The difference falls to 35 N (0.56 % of $F_{y,max}^A$) on the front axle and -14 N (-0.24 % of $F_{y,max}^A$) on the rear axle.

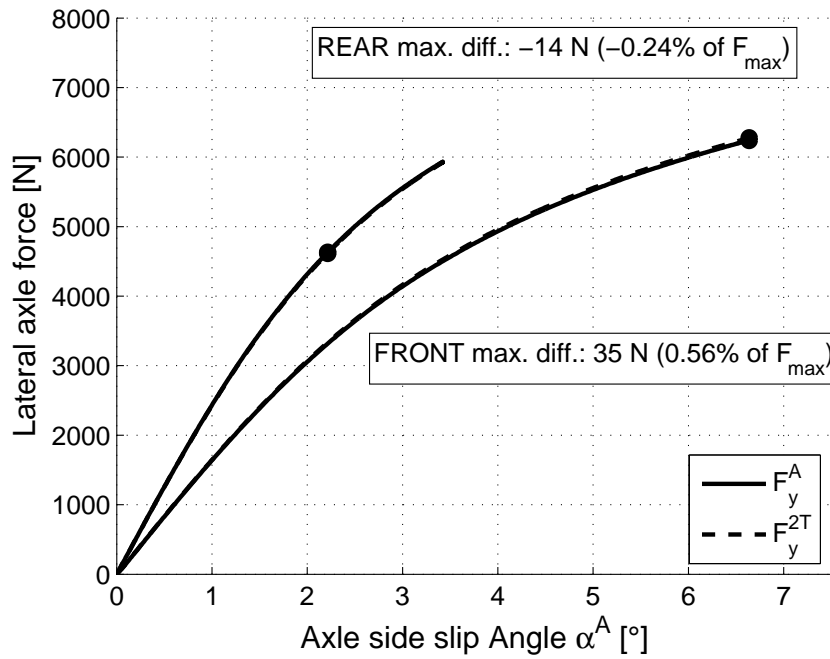


Figure 5.10: $F_{y,j}^A$ in comparison to $F_{y,j}^{2T}$ when including the contribution to yaw moment from $J_\psi \ddot{\psi}$, Equation (5.13) and (5.14).

The remaining difference could be related to several effects discussed in Chapter 3. On the other hand, most remaining effects presented in Chapter 3 are related to how the tire inputs are influenced, like for instance the vertical load or the change of camber angle, and how these changes influence the self steer of the vehicle due to the resulting different forces. However, these effects are not relevant in this investigation since the tire outputs from the simulation are used. One remaining effect however, is the movement of the tire contact point in relation to the vehicle body due to kinematics and compliance. This consequently moves the point at where the tire forces are acting. During the steady state cornering, the roll movement of the vehicle caused by the lateral acceleration will make the outer wheels go into jounce and the inner to rebound. Due to the fore and aft movement of the wheel over jounce and rebound, the lever arm over which the lateral tire force will create a yaw moment will change. Since the lateral forces of the outer tires become significantly more important than the inner lateral forces due to increased vertical load, this will have the net effect of moving the effective lateral force of the axle rearward with increasing lateral acceleration. Hence, this effect causes an under steering effect due to the fact that the lateral force on the front will get less lever arm to turn the vehicle

into the turn, and the lateral force on the rear will get a larger lever arm to counteract the yaw movement of the vehicle. This is illustrated in Figure 5.11.

The effect of the changed tire contact position due to kinematic and compliance is however too small to be taken into consideration. Accordingly, the approach to calculate the lateral axle forces $F_{y,j}^A$ in Equation (5.13) and (5.14), as well as the approach to calculate the equivalent lateral axle force $F_{y,j}^{2T}$ in Equation (5.11) and (5.12), will be used in the further investigations presented in Chapter 6.

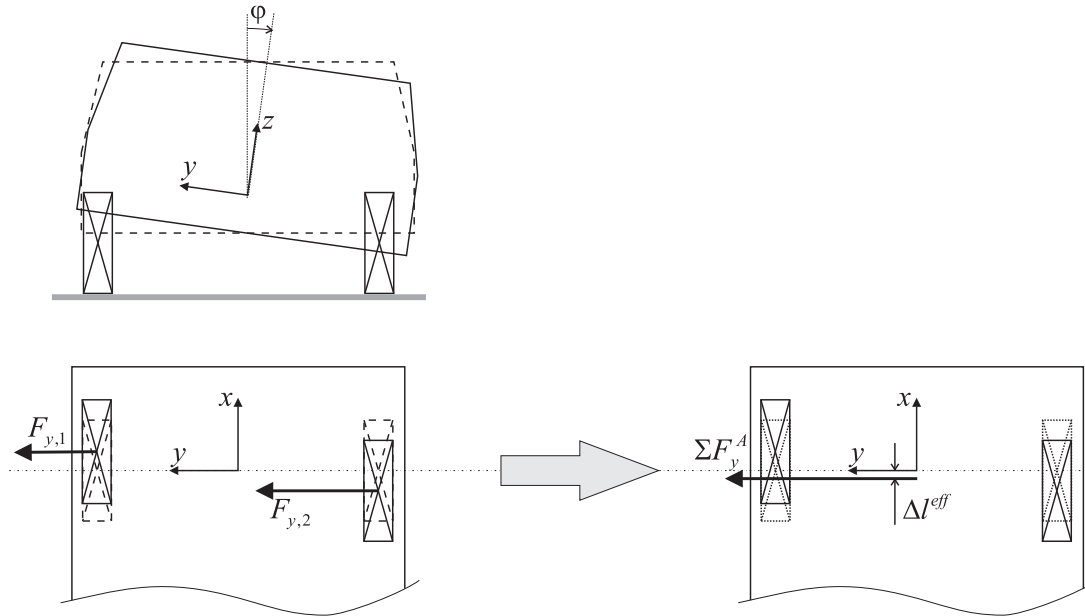


Figure 5.11: The fore and aft movement of the wheels due to kinematics and compliance moves the point at where the lateral tire force acts. Consequently the corresponding total lateral force in the axle ΣF_y^A will act at a distance Δl^{eff} behind the centre of the axle.

Chapter 6

Sensitivity analysis of suspension properties

This Chapter builds on the method developed in Chapter 5 and presents a sensitivity analysis of the suspension properties in relation to the lateral force characteristics of the 2-wheel model. The sensitivity investigation classifies the suspension properties and serves as a foundation for the required accuracy in the suspension model that is to be derived in Chapter 7. Reference vehicle A described in Section 2.5 has been used throughout all investigations in this chapter.

The objective of this investigation is to develop a suspension model which uses the vehicle motion states as inputs, in order to calculate the inputs for the tire model (in this case the tire model MF 5.2 presented in chapter 2). The tire model furthermore calculates the forces that are used in the equations of motion to calculate the movement of the vehicle. In order to know how accurate different parts in the suspension model have to be modeled, it is important to know how a model error in the suspension module influences the results. For that reason, this Chapter presents a sensitivity analysis of the suspension properties in regards to the lateral force characteristics of the 2-wheel model using the method of comparison derived in Chapter 5.

The procedure of this investigation is presented in Figure 6.1, starting to the left with a full vehicle simulation of a steady-state cornering maneuver using the reference model CASCaDE-DA with the tire model MF 5.2, both described in Chapter 2. Several states in this full vehicle simulation are recorded as simulation outputs in order to be used in this investigation: The lateral acceleration a_y , vehicle side slip angle β , rack displacement in the steering system y_r , yaw rate $\dot{\psi}$ and the yaw acceleration $\ddot{\psi}$, are used to identify the lateral force characteristics of the 2-wheel model $F_y^A(\alpha^A)$ according to Equations (5.13) and (5.14). Moreover, the inputs to the tire model during the full vehicle simulation; side slip angle α_i , tire camber angle γ_i , vertical tire load $F_{z,i}$ and longitudinal slip s_x are also recorded in order to be used when simulating the MF 5.2 tire model in a second simulation step. The received tire forces and moments from this second simulation step are furthermore manipulated by using the method derived in Chapter 5 to get the equivalent lateral force characteristics of the 2-wheel model, i.e. $F_y^{2T}(\alpha^A)$ as defined in Equation (5.11) and (5.12). Finally, the equivalent lateral force characteristics, $F_y^{2T}(\alpha^A)$, are compared to the identified lateral force characteristics of the 2-wheel model $F_y^A(\alpha^A)$. By disturbing the tire inputs when simulating the tires separately in the second simulation step, the

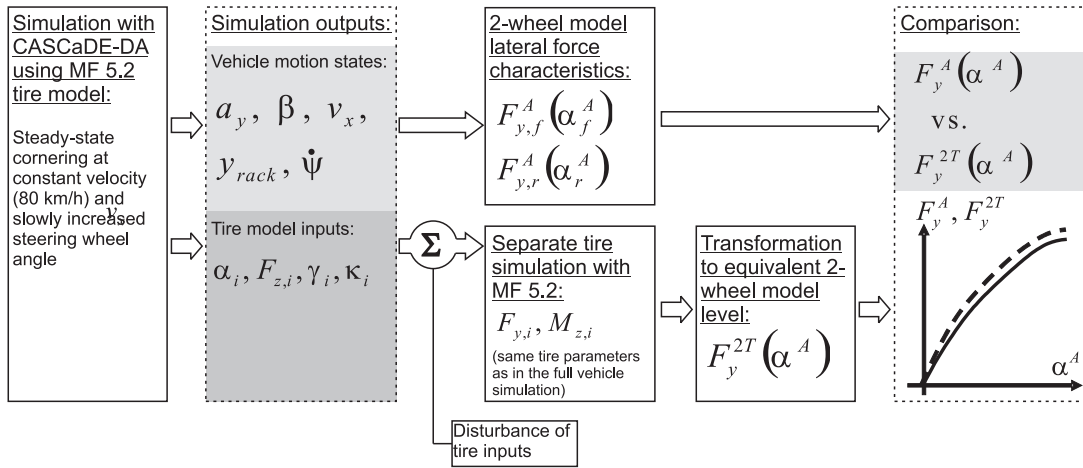


Figure 6.1: Investigation procedure for the sensitivity analysis of the suspension properties.

resulting change in the equivalent 2-wheel model lateral force characteristics $F_y^{2T}(\alpha^A)$ can be observed and evaluated in comparison to the originally identified lateral force characteristics of the 2-wheel model $F_y^A(\alpha^A)$.

The disturbances added to the tire inputs of the MF 5.2 tire model have to be related to what a model error in a suspension model would cause. By only altering one tire input and keeping the other tire inputs intact, the influence of this virtually created model error can be seen in the equivalent 2-wheel model force characteristics F_y^{2T} . If a disturbance is causing a large change, it will also have a large impact on the self steer behavior of the vehicle as well and hence, the corresponding part of the suspension model has to be modeled very accurately.

This way of investigating the influence of different tire inputs is very simple to perform. If the suspension in the reference model would have been altered in order to obtain the same change as the disturbances added to the tire inputs in this investigation, it would have been a very difficult task not to change other tire inputs unintentionally. However, this way of performing the investigation also does not completely correspond to how the axle force characteristics would change if the suspension in the reference model would be adjusted to create the same change in tire input. A steer angle change due to roll would, for instance, also change the vertical load at a certain tire side slip angle. Hence, the result would be a generally different set of tire inputs at a specific driving state with a slightly different resulting force vector. Nevertheless, the amount of difference between the equivalent lateral force characteristics and the identified lateral force characteristics of the 2-wheel model will reveal the sensitivity of that particular part of the suspension model.

Also, the inputs to the tire models are consequences of the generated tire forces and moments. A change in a tire input will therefore create different tire forces which furthermore will influence the tire inputs. Therefore, the disturbances added in this investigation have to be relatively small in comparison to the actual inputs if the output of the sensitivity analysis should be valid. Consequently, as with most sensitivity analysis, the result is only valid around the specific driving state and for small disturbances.

The calculation of the vertical load is a very good example of how the tire input disturbances

have to be related to a possible model error: The static wheel load of each tire is easy to measure using a scale, i.e. the model parameters regarding static wheel load can be considered confident, whereas the load transfer during cornering has to be calculated using a model approach. Therefore, it makes sense to add the vertical load disturbance to the load transfer only, without changing the static tire load. By doing this, the resulting equivalent lateral axle force characteristics F_y^{2T} will show the result of an error in the modeled load transfer rather than examining the load dependency of the tires.

An increase in vertical load transfer on both the front and rear axle would correspond to an error in for instance center of gravity height or track width. If the vertical load transfer is increased on the front axle when simultaneously decreased at the rear axle, this could for instance correspond to a model error in roll stiffness distribution between the front and rear axle.

This investigation includes number of different disturbances to:

- the side slip angles
- the vertical load transfer
- the camber angles

In all investigations, the maximum difference between the lateral force characteristics of the 2-wheel model F_y^A (Equation (5.13) and (5.14)) and the equivalent lateral force characteristics F_y^{2T} (Equation (5.11) and (5.12)) developed in Chapter 5 are evaluated. The axle side slip angle α_j^A (Equation (5.1) and (5.2)) is furthermore used as the reference channel in all investigations.

The spot where the maximum difference in lateral axle force occurs is marked in the figures with black dots. In addition, the resulting maximum force differences are also normalized with the maximum lateral axle force of the front and rear axle respectively to obtain a relative measure.

6.1 Sensitivity of side slip angle

The tire side slip angle α_i is a very important tire input regarding the lateral force generation and is defined in the magic formula tire model version 5.2 [51] to depend on the lateral and longitudinal velocity of the tire contact point, i.e. $v_{y,i}$ and $v_{x,i}$ (see also Figure 6.2(a)):

$$\alpha_i = \arctan \frac{v_{y,i}}{|v_{x,i}|} \quad (6.1)$$

During e.g. steady-state cornering, the vehicle longitudinal velocity v_x , the vehicle lateral velocity v_y and the yaw rate $\dot{\psi}$, can be used to create a simplified expression of the side slip angle

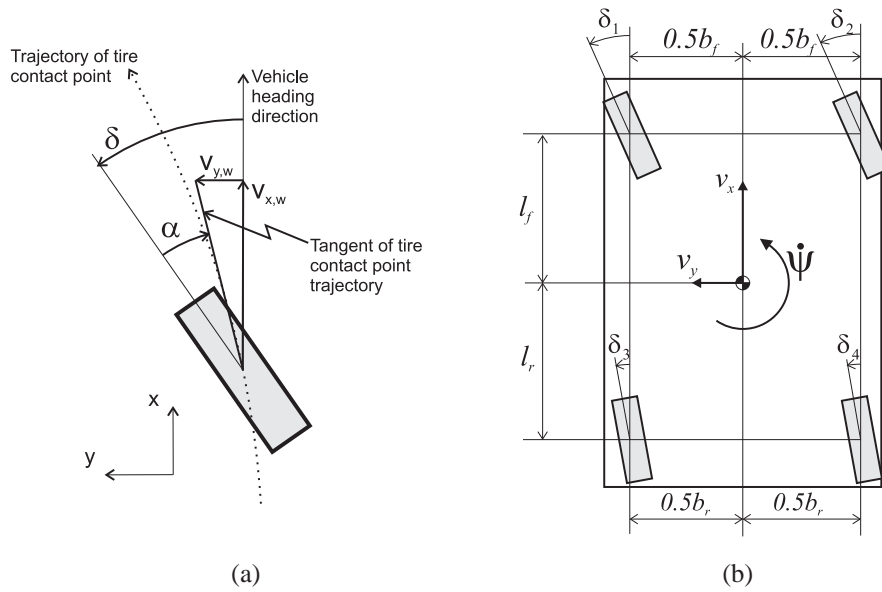


Figure 6.2: (a): Definition of side slip angle in MF 5.2 with $v_{y,i}$ being the lateral velocity of the tire contact point and $v_{x,i}$ longitudinal component of the tire contact point velocity. (b): Illustration of the distances and vehicle kinematics used to derive a simplified expression of the tire side slip angles. Due to the steady-state cornering condition, the influence of the roll velocity can be neglected in the calculations of the side slip angles in Equations (6.2) to (6.2). The lateral displacement of the CG due to the roll angle has also been neglected.

of each tire (see also Figure 6.2(b)):

$$\alpha_1 = - \left(\delta_1 - \arctan \frac{v_y + l_f \dot{\psi}}{v_x - 0.5b_f \dot{\psi}} \right) \quad (6.2)$$

$$\alpha_2 = - \left(\delta_2 - \arctan \frac{v_y + l_f \dot{\psi}}{v_x + 0.5b_f \dot{\psi}} \right) \quad (6.3)$$

$$\alpha_3 = - \left(\delta_3 - \arctan \frac{v_y - l_r \dot{\psi}}{v_x - 0.5b_r \dot{\psi}} \right) \quad (6.4)$$

$$\alpha_4 = - \left(\delta_4 - \arctan \frac{v_y - l_r \dot{\psi}}{v_x + 0.5b_r \dot{\psi}} \right) \quad (6.5)$$

Hence, the steer angle of each wheel δ_i has a direct influence on the side slip angle. The steer angles δ_i contain static toe-in $\delta_{0,i}$, steer angles due to suspension jounce and rebound $\delta_{k,i}$, compliance steer $\delta_{c,i}$ and steer angles due to driver steering inputs $\delta_{\delta,i}$. Due to the steady-state cornering condition, the influence of the roll velocity has been neglected in the side slip angle calculations. The lateral displacement of the CG due to the roll angle has also been neglected.

By disturbing the side slip angle with measures related to a model error in computing the steer angle of each wheel (and keeping the other tire inputs intact), the influence of a steer angle model error can be seen in the equivalent 2-wheel model lateral force characteristics. It is important to remember though, that changing the side slip angle, with the consequence of a change of tire lateral force, will change the vehicle movement and consequently the side slip angle, i.e. they are coupled. This investigation builds on decoupling the tire inputs and will therefore only give an indication of how significant the change is decoupled from other effects.

Table 6.1 presents the different disturbances applied to the side slip angle together with the resulting maximum difference between F_y^A (Equation (5.13) and (5.14)) and F_y^{2T} (Equation (5.11) and (5.12)), both with the axle side slip angle α^A as reference (Equation (5.1) and (5.2)).

The investigations in this Chapter will be labeled **S1**, **S2**, ..., **Sn** in ordered to ease the reading and viewing of figures and tables. The sensitivity analysis regarding the side slip angles are labeled **S1**, **S2** and **S3**:

- S1** The first investigation adds a 10 % increase of the lateral side slip angle to each tire α_i , resulting in the different equivalent lateral axle force $F_y^{2T}(\alpha^A)$ in comparison to the originally identified lateral axle force $F_y^A(\alpha^A)$ depicted in Figure 6.3. Relative to the maximum of the original lateral axle force, the 10 percent increase in tire side slip angle causes about 6 percent increase in the equivalent lateral axle forces.
- S2** The change in steer angles due to kinematics and compliance (and consequently the side slip angles) is the objective of the second investigation. If assuming the side slip angle at each tire to be equal to the side slip angle of the corresponding axle, the effects of static toe angles, roll steer and compliance steer are all eliminated in theory. The result of this is shown in Figure 6.4. In order to put the results of **S2** into perspective, Figure 6.5 displays the steer angles during this steady-state maneuver with the axle side slip angles α_f and α_r used as reference variables in order to ease the comparison with Figure 6.4.
- S3** In the third investigation the static toe angle is subtracted from the side slip angle at each tire in order to examine the effect of toe-in on the lateral axle force. As seen in Figure 6.6, this decreases F_y^{2T} both at the front and rear axle. The cornering stiffness on the rear axle is also decreased when removing toe-in.

Label	Description	Formulation	Delta (relative to F_{max})
S1 Fig. 6.3	10 % increase of the tire side slip angles α_i .	$\alpha_i = 1.1 \cdot \alpha_i$	Front: 391 N (6.27%) Rear: 353 N (5.96%)
S2 Fig. 6.4	Axle side slip angle α^A used as input to the respective tires.	$\alpha_i = \begin{cases} \alpha_f^A & i = 1, 2 \\ \alpha_r^A & i = 3, 4 \end{cases}$	Front: 836 N (13.39%) Rear: -251 N (-4.23%)
S3 Fig. 6.6	Static toe angle $\delta_{0,i}$ subtracted from the tire side slip angle.	$\alpha_i = \alpha_i \pm \delta_{0,i}$ $\delta_{0,2} = 0.14^\circ$ $\delta_{0,4} = 0.45^\circ$	Front: -55 N (-0.88%) Rear: -244 N (-4.11%)

Table 6.1: Results for disturbing the side slip angles during steady-state cornering showing the difference between the lateral axle force characteristics of the two wheel model $F_y^A(\alpha^A)$ and the equivalent lateral axle force $F_y^{2T}(\alpha^A)$.

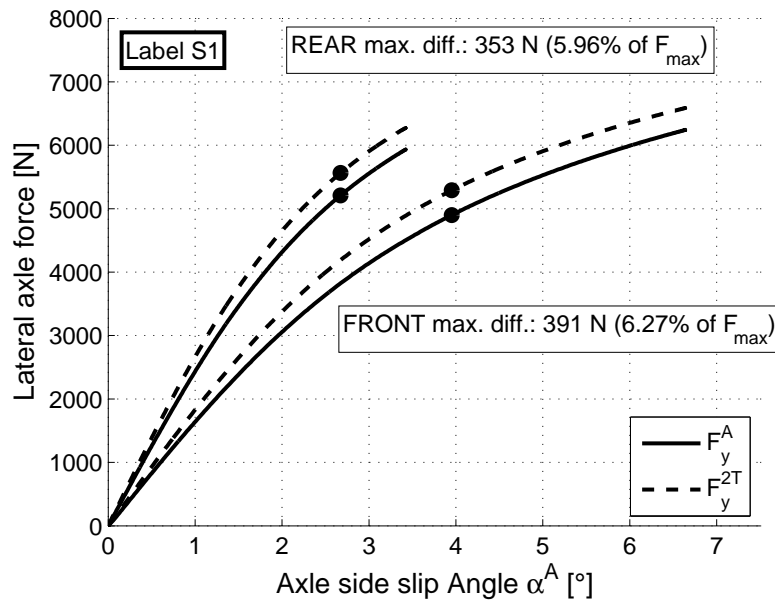


Figure 6.3: Resulting equivalent lateral axle force $F_y^{2T}(\alpha^A)$ due to a 10 % increase in side slip angle, in comparison to the originally identified lateral axle force $F_y^A(\alpha^A)$ of the 2-wheel model.

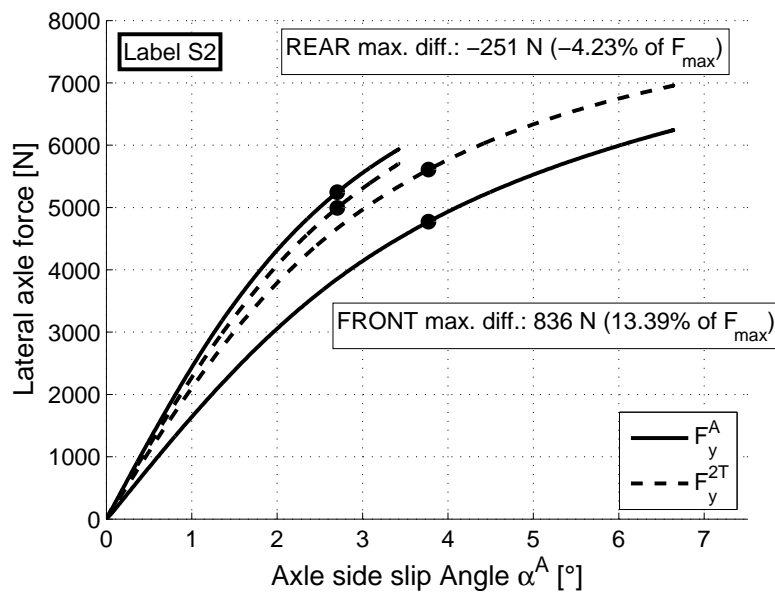


Figure 6.4: Resulting equivalent lateral axle force $F_y^{2T}(\alpha^A)$ when ignoring the change of steer angles at each tire due to kinematics and compliance, i.e. using the corresponding axle side slip angle α^A (as defined for the 2-wheel model) as side slip angle input to each tire.

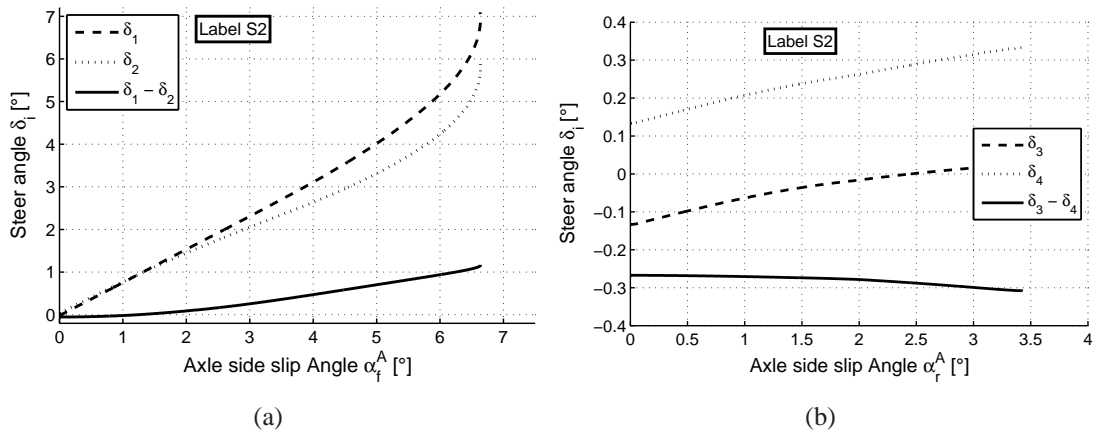


Figure 6.5: Steer angles δ_i as a function of axle side slip angle α_j during the steady-state maneuver, in (a) the front and in (b) the rear axle.

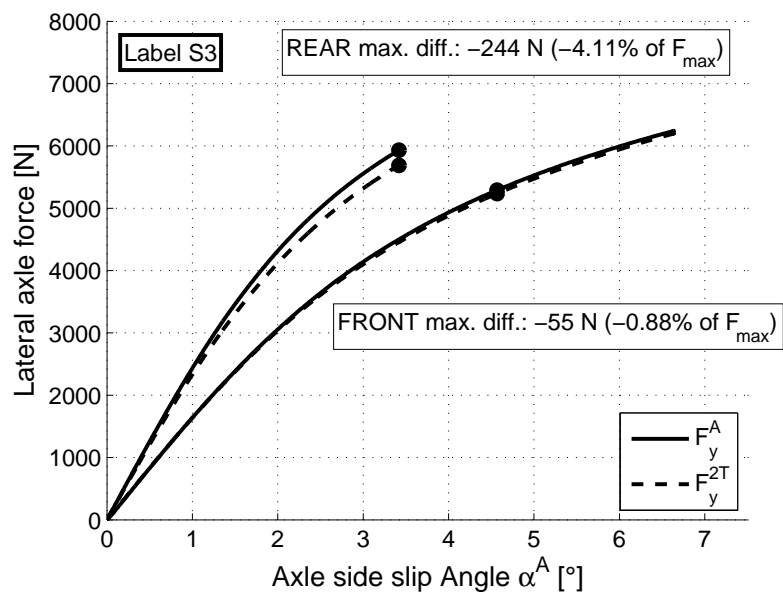


Figure 6.6: Resulting equivalent lateral axle force $F_y^{2T}(\alpha^A)$ when subtracting the static steer angle from the side slip angle at each tire.

6.2 Sensitivity of vertical load transfer

As already discussed in Section 3.6.2 and illustrated in Figure 3.8, the vertical load transfer during cornering will decrease the total lateral axle force of the axle due to the non-linear vertical load dependency of the tire. Sensitivity analysis **S4** and **S5** investigate how the vertical load transfer influence the lateral axle forces:

S4 In the investigation labeled S4 the vertical load transfer at each axle is increased by 10 %. This results in a clear decrease of the front lateral axle force which correlates to theory, see Figure 6.7. The rear axle does not change much which can be explained by the fact that the vertical load transfer on the front axle is more significant than on the rear; at maximum lateral acceleration $a_{y,max}$, the outer front tire will experience a 90 percent increase in vertical load in comparison to straight-line driving whereas the outer rear tire will only experience a 55 percent increase. However, this is not the only explanation as will be seen in the next investigation.

S5 Figure 6.8 shows the result of having no vertical load transfer during cornering. As can be seen for the front axle, this investigation again confirms the theory of a decreased total lateral axle force due to the vertical load transfer since the equivalent lateral axle force $F_{y,f}^{2T}$ (which was produced excluding the vertical load transfer) is larger than $F_{y,f}^A$ which includes the vertical load transfer. On the rear axle, however, the equivalent lateral axle force $F_{y,r}^{2T}$ has been decreased in the absence of vertical load transfer. This result makes the influence of the indirect self-steer effects evident: Figure 6.9 illustrates how the lateral forces, $F_{y,in}$ and $F_{y,out}$, depend on the vertical tire loads $F_{z,in}$ and $F_{z,out}$ (here linear). This has been plotted for two side slip angles; the outer and the inner, differentiated mainly by the static toe angle. In the case of no load transfer, the outer lateral tire force $F'_{y,out}$ and the inner lateral tire force $F'_{y,in}$, will have the mean value $\frac{1}{2}F'_{y,axle}$ (filled black dots in Figure 6.9). Taking the vertical load transfer into account, the lateral force of the outer and inner tires, i.e. $F_{y,in}$ and $F_{y,out}$, will have a mean value $\frac{1}{2}F'_{y,axle}$ (circles in Figure 6.9), where $\frac{1}{2}F_{y,axle} \geq \frac{1}{2}F'_{y,axle}$.

Table 6.2 concludes the investigations made on vertical load sensitivity.

Label	Description	Formulation	Delta (relative to F_{max})
S4 Fig. 6.7	Vertical load transfer during cornering increased by 10 %.	$F_{z,i} = F_{z0,i} \pm 1.1 \cdot \Delta F_{z,i}$	Front: -264 N (-4.23%) Rear: -96 N (-1.63%)
S5 Fig. 6.8	No vertical load transfer.	$F_{z,i} = \frac{1}{2}F_z^A$	Front: 1583 N (25.35%) Rear: 254 N (4.28%)

Table 6.2: Resulting difference between the lateral axle force characteristics of the two wheel model $F_y^A(\alpha^A)$ and the equivalent lateral axle force $F_y^{2T}(\alpha^A)$ when disturbing the vertical load transfer during steady-state cornering.

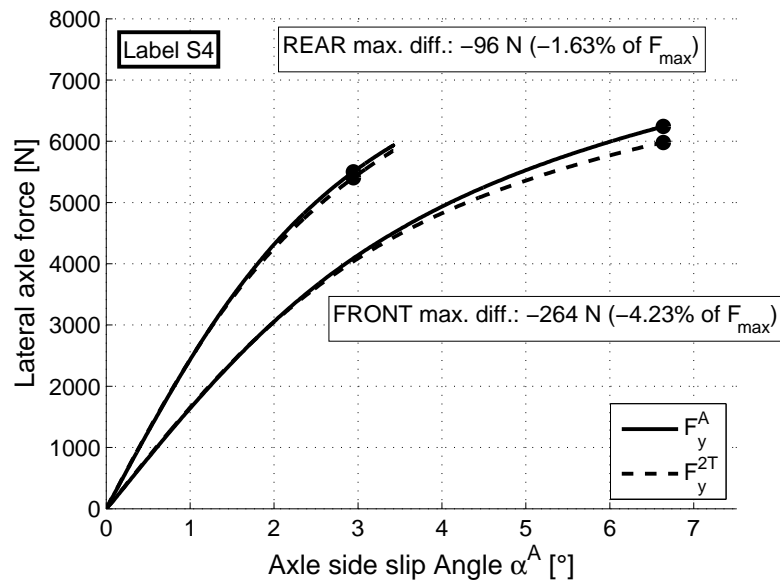


Figure 6.7: Resulting equivalent lateral axle force $F_y^{2T}(\alpha^A)$ due to a 10 % increased vertical load transfer, in comparison to the originally identified lateral axle force $F_y^A(\alpha^A)$.

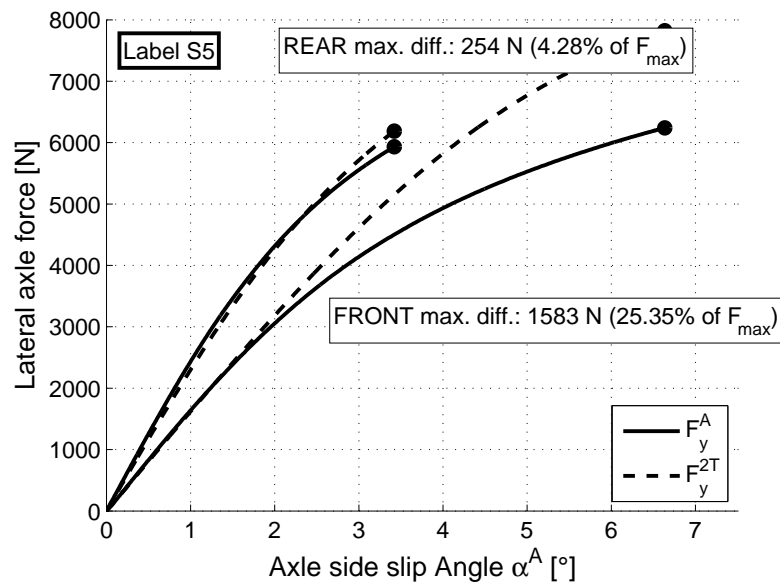


Figure 6.8: Resulting equivalent lateral axle force $F_y^{2T}(\alpha^A)$ when the load transfer is excluded. This in comparison to the originally identified lateral axle force $F_y^A(\alpha^A)$.

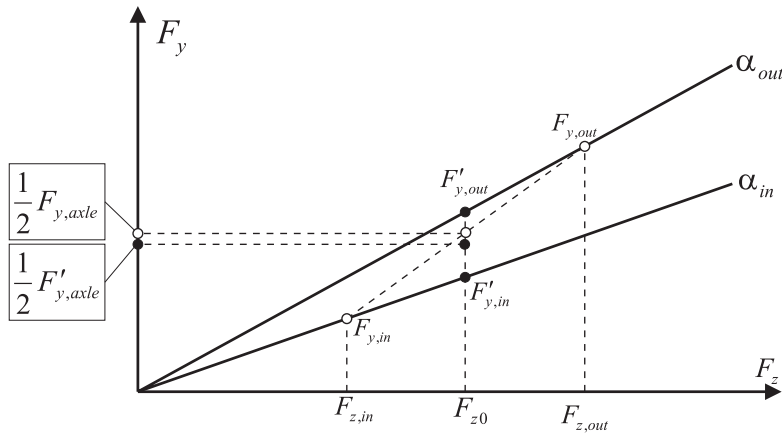


Figure 6.9: Lateral tire force plotted as a function of vertical load for two side slip angles; for the inner and outer tire, mainly differentiated due to the static toe-in. The filled black dots display the resulting lateral forces without considering the vertical load transfer and the circles display the case when including the vertical load transfer. The result is a decreased total lateral axle force due to the different inner and outer side slip angles despite the exclusion of vertical load transfer, see also Figure 3.9.

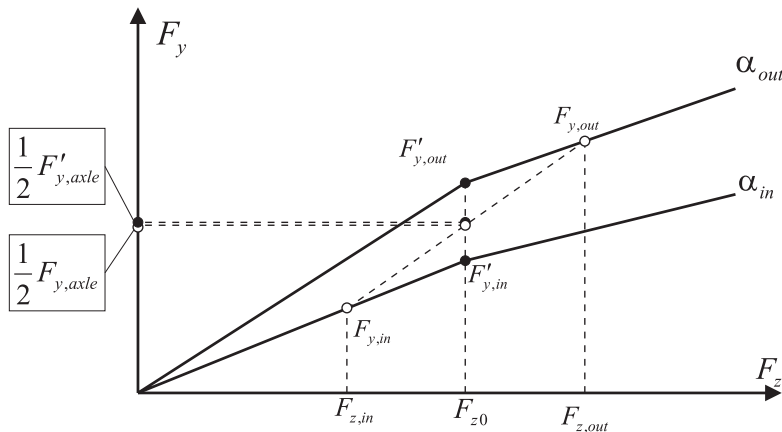


Figure 6.10: As in Figure 6.9 but with lateral tire characteristics operating in the non-linear range of vertical load dependency. This non-linearity results in decreasing the effect explained in Figure 6.9.

This effect, $\frac{1}{2}F_{y,axle} \geq \frac{1}{2}F'_{y,axle}$, is not as evident on the front axle due to several reasons: First, the static toe angle on the front axle is smaller than on the rear; $\delta_{0,f} = 0.026^\circ$ and $\delta_{0,r} = 0.14^\circ$, i.e. the static toe angle on the rear axle is about 4 % of the maximum axle side slip angle $\alpha_{max,rear} \approx 3.4^\circ$, whereas the front static toe angle corresponds to only about 0.4 % of the maximum axle side slip angle, $\alpha_{max,front} \approx 6.6^\circ$. Also, the non-linear vertical load dependency decreases the effect of different side slip angles due to static toe, see Figure 6.10 illustrating the same as Figure 6.9 but with the tire characteristics operating in the non-linear range of vertical load dependency.

The effect described in Figure 6.9 gives an additional explanation to why the rear axle doesn't show as much decrease as the front axle in lateral axle force as a consequence of more vertical load transfer (Label **S4**, Figure 6.7).

6.3 Sensitivity of camber angle

The tire camber angle is the angle between the road Z-axis and the wheel plane, see Figure 3.7, defined in a right orthogonal reference frame. How this influence the lateral axle forces will be investigated in sensitivity analysis **S6**, **S7**, **S8** and **S9**:

S6 In the investigation labeled **S6** the camber angles are increased by 10 %. Figure 6.12 displays the resulting lateral axle force characteristics and as expected this has only a very small influence on the total lateral axle force.

S7 Completely ignoring the camber angles is however not justified as can be seen in investigation **S7**, illustrated in Figure 6.13. The camber angles have the effect of decreasing the total lateral axle force on both axles.

S8 Investigation **S8** examines the possibility of using the vehicle roll angle as the tire camber angle, i.e. to neglect static camber and camber angle change due to kinematics and compliance. As Figure 6.14 illustrates, this causes a very small error on the front axle and a smaller error on the rear axle in comparison to ignoring the camber angle totally as in **S7**.

S9 Subtracting the static camber angle from the total camber angle as in investigation **S9** creates a small but, on the rear axle yet an important effect on the total lateral axle force, see Figure 6.15.

In order to better follow investigation **S6** to **S9**, Figure 6.11 displays the tire camber angles in the CASCaDE reference model during the steady-state maneuver using the axle side slip angles α_f and α_r as reference variables. The static camber angle $\gamma_{0,j}$ is on the front axle $\gamma_{0,f} = 0.28^\circ$ and on the rear axle $\gamma_{0,r} = -2.14^\circ$.

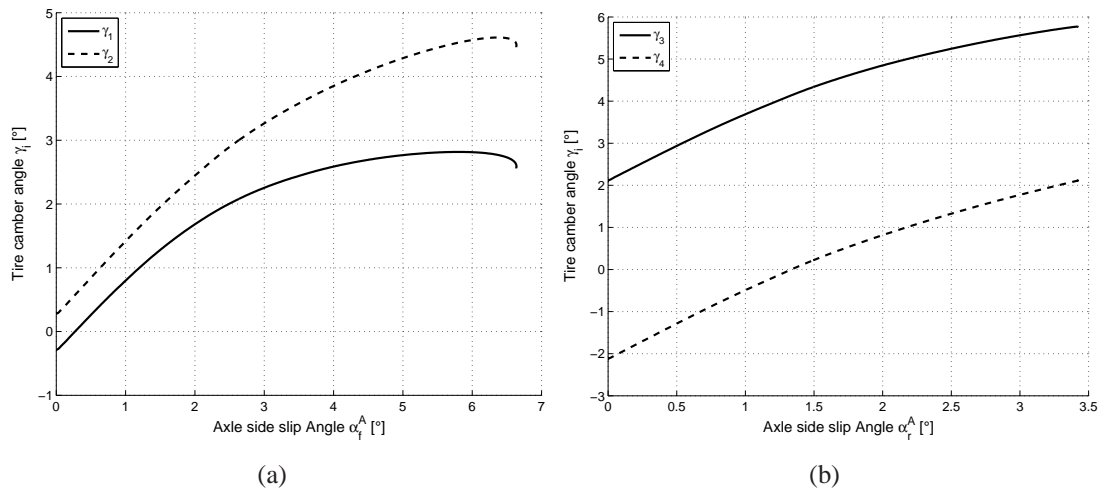


Figure 6.11: Tire camber angles γ_i as a function of axle side slip angle α_j during the steady-state maneuver, in (a) the front and in (b) the rear axle.

Table 6.3 presents a summary of the investigations made on tire camber angle sensitivity.

Label	Description	Formulation	Delta (relative to F_{max})
S6 Fig. 6.12	Tire camber angle γ_i increased by 10 %.	$\gamma_i = 1.1 \cdot \gamma_i$	Front: -33 N (-0.52%) Rear: -65 N (-1.1%)
S7 Fig. 6.13	Tire camber angle neglected.	$\gamma_i = 0$	Front: 639 N (10.23%) Rear: 387 N (6.52%)
S8 Fig. 6.14	Tire camber angle equals vehicle roll angle.	$\gamma_i = \varphi$	Front: 37 N (0.6%) Rear: -250 N (-4.22%)
S9 Fig. 6.15	Static camber angle $\gamma_{i,0}$ subtracted from the tire camber angle.	$\gamma_i = \pm \gamma_{i,0}$	Front: 61 N (0.98%) Rear: -195 N (-3.28%)

Table 6.3: Concluding table of the difference in lateral axle force characteristics of the two wheel model $F_y^A(\alpha^A)$ and the equivalent lateral axle force $F_y^{2T}(\alpha^A)$ when disturbing the camber angles during steady-state cornering.

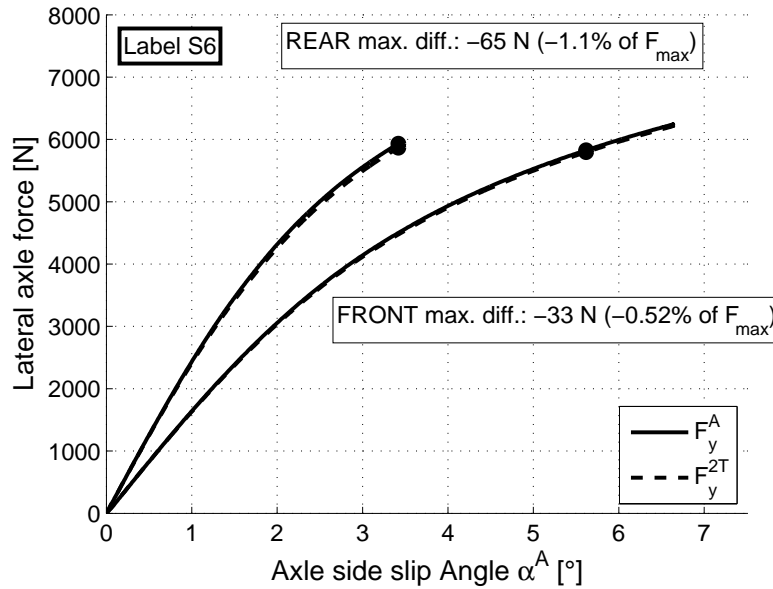


Figure 6.12: Resulting equivalent lateral axle force $F_y^{2T}(\alpha^A)$ due to a 10 % increase in tire camber angles in comparison to the identified original axle force $F_y^A(\alpha^A)$.

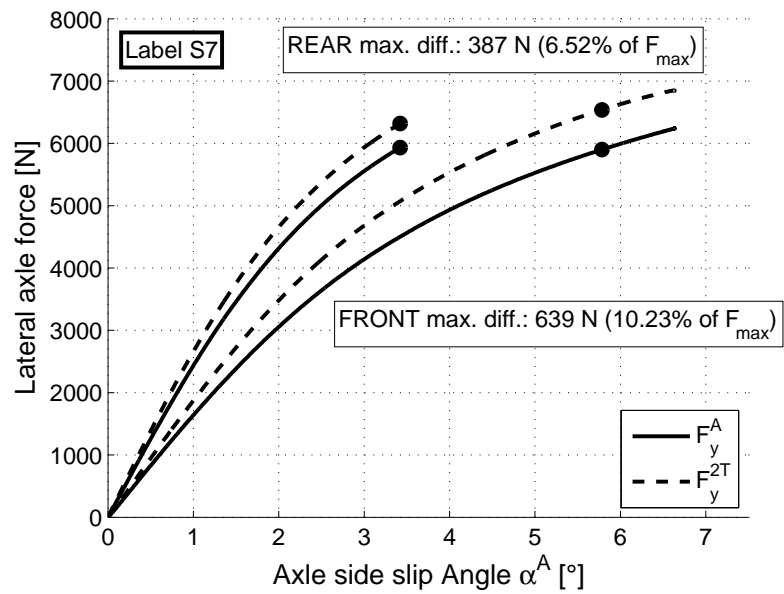


Figure 6.13: Resulting equivalent lateral axle force $F_y^{2T}(\alpha^A)$ when the tire camber angles are set to zero.

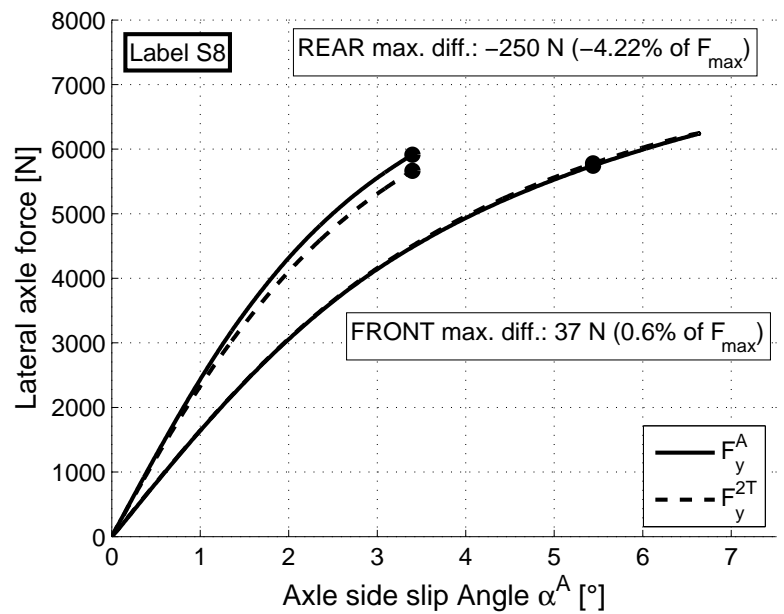


Figure 6.14: Resulting equivalent lateral axle force $F_y^{2T}(\alpha^A)$ when the tire camber angle of each tire is set to be equal to the vehicle roll angle.

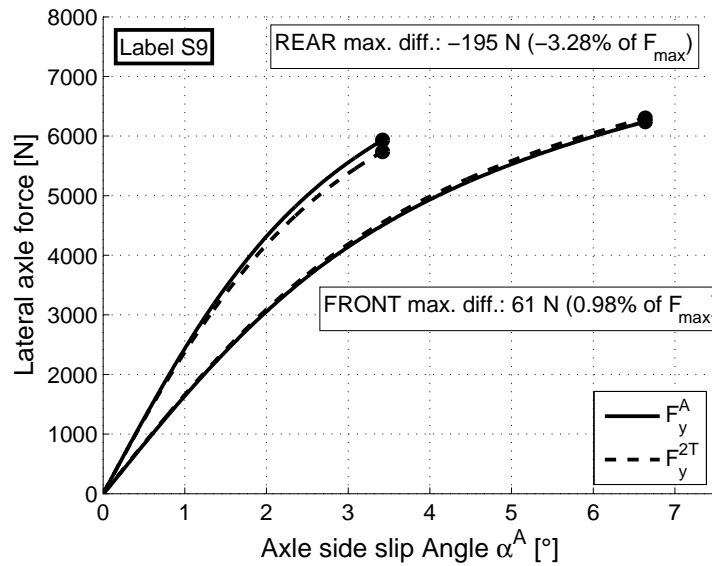


Figure 6.15: Resulting equivalent lateral axle force $F_y^{2T}(\alpha^A)$ when subtracting the static camber angle $\gamma_{0,i}$ from the total tire camber angle, caused by vehicle roll.

6.4 Summary

The results presented in this sensitivity analysis are certainly very depending on the vehicle design, the wheel suspension set-up and foremost the tire properties. If repeating this investigation with the same vehicle but with a different type of tire, some results would be similar and some would change drastically. A wider tire is for instance more sensitive to camber angles, i.e. generates more camber force, which would have a large influence in investigation **S6**, **S7**, **S8** and **S9**. Tires can also be more or less vertical load dependent which would cause different results in investigations **S4** and **S5**.

The vehicle loading condition as well as the kinematics and compliance setup of the suspension also influence how and in what extent the lateral axle force will be influenced in these investigations.

Also when repeating the investigations made in this chapter with other vehicles and with different tires, it is clear that the investigations regarding the side slip angle and the tire normal force always play a very important role. It will also be apparent that the camber angles will also gain in importance if a tire with more camber sensitivity is used. The camber angle impact will, however, never become as important as the side slip angle and the tire normal force. It can also be concluded though, that the camber angles can not be neglected in the suspension model. Even if setting the tire camber angles equal to the vehicle roll angle would not be sufficient when modeling the suspension.

This investigation also confirms the common knowledge that the steer angles have to be modeled very carefully due to their direct influence on the tire side slip angles. Secondly, the tire vertical loads are the second most important part of the suspension model followed by the tire camber angles.

Chapter 7

The extended 2-wheel model

The 2-wheel vehicle model described in Chapter 4 is a product of many years of research and development since Riekert and Schunck first presented the model concept in 1940 [46]. The investigations in this chapter introduces a further development of the model concept, where the axle force characteristics described in Section 4.4 are replaced by a suspension-tire element. Figure 7.1 shows the principle of this element where a suspension model uses the vehicle motion states in order to calculate inputs for a tire model. The tire model, *Magic Formula MF-Tyre model version 5.2* [51], furthermore calculates the horizontal tire forces and moments for the left and right side tire respectively, which are summarized to compose an overall axle force and moment. Consequently, the suspension and tire properties will be separated in the model presented here in contrast to the conventional 2-wheel model where the axle force characteristics is a combination of vehicle, tire and suspension properties.

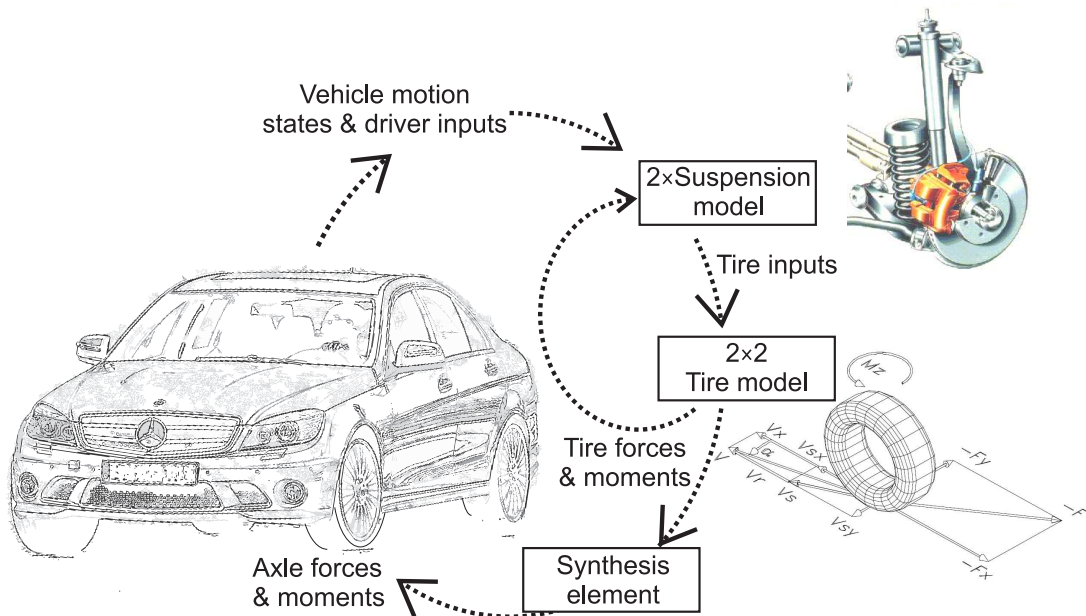


Figure 7.1: Outline of the tire suspension model.

This new model will be called the *extended 2-wheel model* and will be described including its

subcomponents in the simplified suspension model. These subcomponents must be complex enough to capture all important effects yet at the same time simple enough to allow the model parameters to be identified in a parameterization process using measurements from driving maneuvers and a suspension test bench. Within this process, the tire characteristics for a given road are assumed to be known at all times, i.e. the friction conditions are assumed constant and the tire model parameters are given.¹ The objective of this model is to enable a straight forward identification of the vehicle and the suspension in order to utilize simulation when predicting the vehicle's handling with different sets of tires.

The suspension model uses steering inputs as well as the motion states of the vehicle body when calculating the inputs for the tire model. This requires the suspension properties to be separated into sub models that for each tire i compute:

- Vertical tire load, $F_{z,i}$
- Steer angle, δ_i
- Tire camber angle, γ_i
- Wheel to road contact kinematics

Both suspension kinematics and compliance will be considered in these subcomponents.

It is very important to remember that the motion states of a vehicle are a result of mainly the tire forces, which are a reaction of the state in which the tires are operating. The operating states of the tires furthermore depend on the suspension properties together with the vehicle motion states. Hence, the properties of the vehicle, suspensions and tires are strongly interrelated and consequently, an error in one of the subcomponents in a simulation model (vehicle, suspension or tire model) will produce a chain of incorrect states in other subcomponents. Accordingly, the simulation models for vehicle, tire and suspension therefore have to be considered as one complete system.

The key to success is that the structure of the developed model strongly relates to the structure of a real vehicle. Hence, all important effects like for instance roll steer or changing vertical tire loads during cornering are included in the model. Consequently, the structure of the model depicts the vehicle behavior in all relevant motion states and only parameter variation is necessary in order to match the behavior of the extended 2-wheel model with the behavior of the reference vehicle. With an insufficient model structure, the strategy of matching the vehicle behavior by parameter variation would fail, i.e. only with a well balanced model structure the strategy will succeed.

The model parameters for the simulation model developed in this chapter will be identified in a process described in Chapter 8. This will be followed by a documentation of the model validity in Chapter 9 as well as examples in Chapter 10 on how to use the model for parameter variations, such as different loading conditions, different tires and other anti-roll bar setups.

¹The tire parameters are identified from test bench measurements by the tire supplier. Both the extended 2-wheel model and the reference simulation model CASCaDE-DA are simulated with the same set of tire model parameters.

The investigations in Chapter 8 to 10 will in this way justify the applied simplifications and assumptions presented here in Chapter 7.

7.1 Structure of the model for lateral dynamics

The model structure of the extended 2-wheel model is very similar to the model presented in Chapter 4. As described in Equation (7.1) and (7.2), only the yaw equation of motion has been modified by adding the axle aligning moments front and rear, $M_{z,f}^{2T}$ and $M_{z,r}^{2T}$. Figure 7.2 illustrates the model structure regarding the yaw, lateral and longitudinal dynamics including the model geometry (to simplify the expressions, small angle approximation has been applied, i.e. $\cos \delta \approx 1$ and $\sin \delta \approx \delta$).

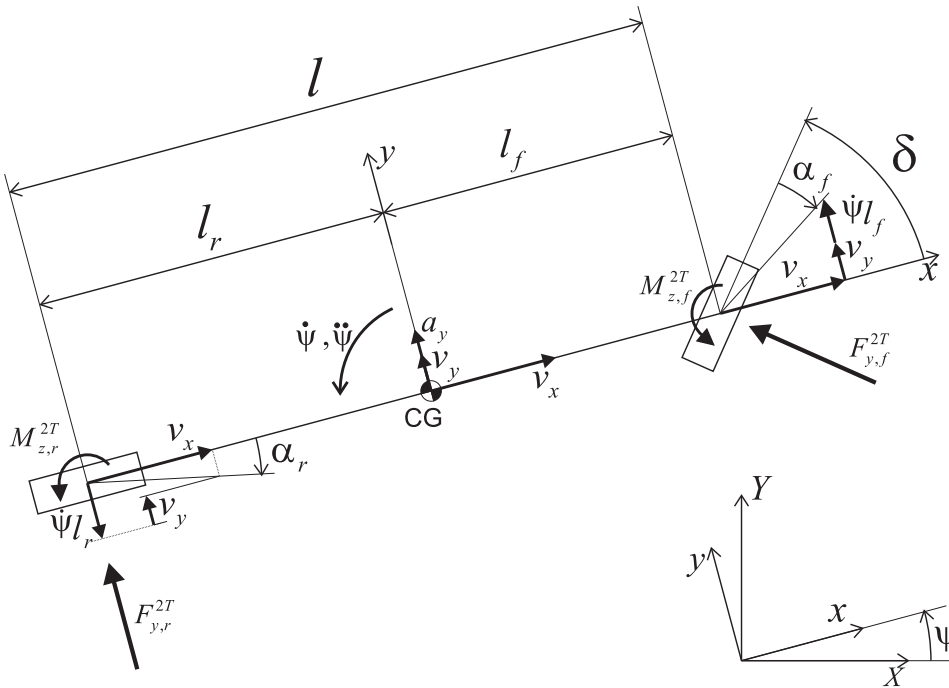


Figure 7.2: Definitions and geometry of the extended 2-wheel vehicle model.

$$m \cdot a_y = F_{y,f}^{2T} + F_{y,r}^{2T} \quad (7.1)$$

$$J_\psi \cdot \ddot{\psi} = l_f \cdot F_{y,f}^{2T} - l_r \cdot F_{y,r}^{2T} + M_{z,f}^{2T} + M_{z,r}^{2T} \quad (7.2)$$

In the same way as in the conventional 2-wheel model presented in Chapter 4, the vehicle longitudinal velocity will be an input to the model instead of being a motion state in the model. Hence, the longitudinal degree of freedom is neglected and, thereby, this model only considers pure lateral dynamics.

The steering wheel angle, δ_D , is the second model input in the conventional 2-wheel model presented in Chapter 4, which subsequently is translated into a front steer angle, δ , to be used in

the model equations. Instead of this, the model presented here will use the rack displacement, y_r , as an input in order to separate the suspension from the steering system. As a result, the dynamics of the steering system is completely separated from the suspension model. Section 7.5.1 describes how the steering rack position is used in the extended 2-wheel model. If the steering wheel angle would be needed as a model input, for instance if driving this model on a driving simulator, a separate steering model as described in [7] with the rack displacement and rack force as interface to the suspension model, could be applied (see also [24]).

7.2 Structure of the roll dynamics model

The structure of the roll model, however, has changed significantly in comparison to the model presented in Chapter 4. First of all, the sprung mass, m_s , has been separated from the unsprung mass² of each axle, $m_{us,j}$, hence $m = m_s + \sum m_{us}$. Secondly, the vehicle roll angle, φ , has been divided into a suspension roll angle, φ_{su} , and a roll angle caused by tire vertical deflection, φ_{ti} . The third and final modification in the roll model is that the reactional roll moments from the springs and dampers are calculated separately for the front and rear axle respectively. Accordingly, the roll moment of axle j is defined as:

$$M_{x,j} = M_{\varphi,j}(\varphi_{su,j}) + M_{\dot{\varphi},j}(\dot{\varphi}_{su,j}) \quad (7.3)$$

where the non-linear function for elastic roll moment, $M_{\varphi,j}(\varphi_{su,j})$, can be derived mainly from the suspension springs and the anti-roll bar but it inevitably also includes the elasticities in the rubber bushings and the bump stops in combination with the suspension kinematics. $M_{\dot{\varphi},j}(\dot{\varphi}_{su,j})$ is a non-linear function which summarizes the roll damping originating mainly from the shock absorbers (as well as suspension friction effects).

Figure 7.3 illustrates the structure of the roll model with one simplification: The front and rear axles are concluded to one axle (this simplification is only temporary when deriving the roll model). Small angle approximation is applied for the roll angle, i.e. $\cos \varphi \approx 1$ and $\sin \varphi \approx \varphi$, so the height of the sprung mass h_s remains the same during vehicle roll as in a non-roll condition. Heave motion of the vehicle body is also neglected and the distance between the (sprung mass) center of gravity and the roll centers front and rear are assumed to be constant, i.e. the roll lever arm $\Delta h = h_s - h_{RC}$ is a constant parameter. This is a noticeable simplification, especially for conventional independent wheel suspensions. The remark in Section 7.4 puts the simplification of neglecting vehicle heave/dive during roll into perspective.

The equation of motion for the roll degree of freedom can be derived using the free body diagram in the upper right corner of Figure 7.3.

$$J_{\varphi,s} \cdot \ddot{\varphi} = m_s \cdot \Delta h (a_{y,s} + g\varphi) - (M_{x,f} + M_{x,r}) \quad (7.4)$$

Note that the equation of motion for roll is derived around the mass center of the sprung mass, m_s , using the moment of inertia for the sprung mass, $J_{\varphi,s}$. In order to use the lateral acceleration

²The unsprung mass is the weight of the various parts of a vehicle that are not carried on the springs, e.g. wheels, axles and brakes

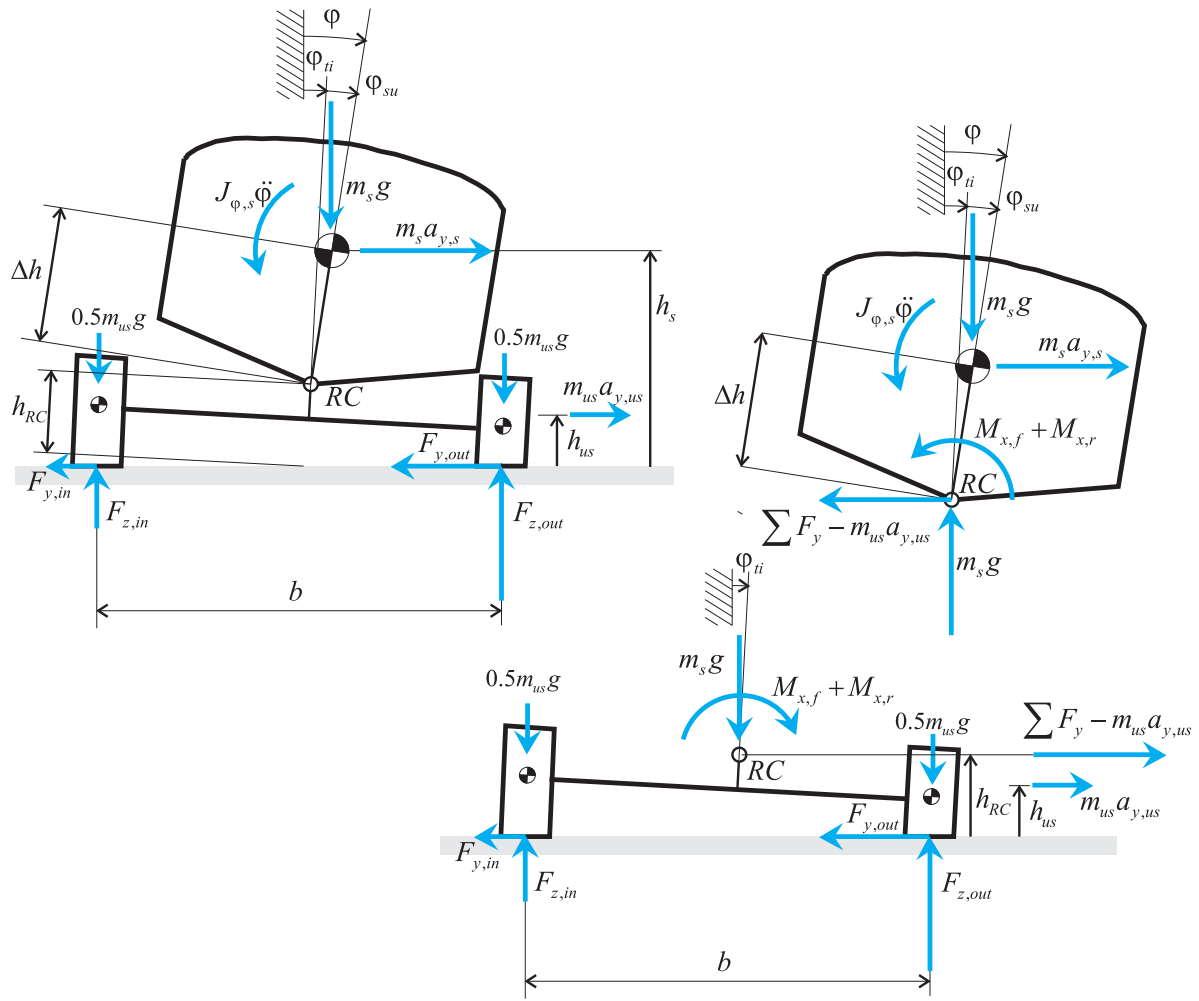


Figure 7.3: Roll model seen from behind and the cut system with cutting forces to the right. The vehicle roll angle ϕ is divided in suspension roll angle ϕ_{su} and roll angle caused by tire vertical deflection ϕ_{ti} .

of the sprung mass, $a_{y,s}$, as an input to the roll model, the following relation was used:

$$m_s a_{y,s} = \sum_{j=f,r} F_{y,j} - m_{us,j} a_{y,us,j} \quad (7.5)$$

Figure 7.4 show the mass geometry for the roll model with different axle geometry front and rear. Splitting the total vehicle mass into a sprung and an unsprung mass also require a slightly different mass geometry. The difference in mass geometry is not large and could in some cases even be neglected but since all necessary parameters are at hand, Equation (7.6) to (7.10) presents the necessary calculations. The center of gravity height, h_{CG} , will normally be smaller than the height of the sprung mass, h_s , and is given by the following relationship:

$$h_{CG} m = h_s m_s + \sum_{j=f,r} h_{us,j} m_{us,j} \quad (7.6)$$

$h_{us,j}$ is the height over ground for the unsprung masses. In the same way, the longitudinal center of gravity position for the sprung mass, $l_{f,s}$, can be calculated using the mass distribution for

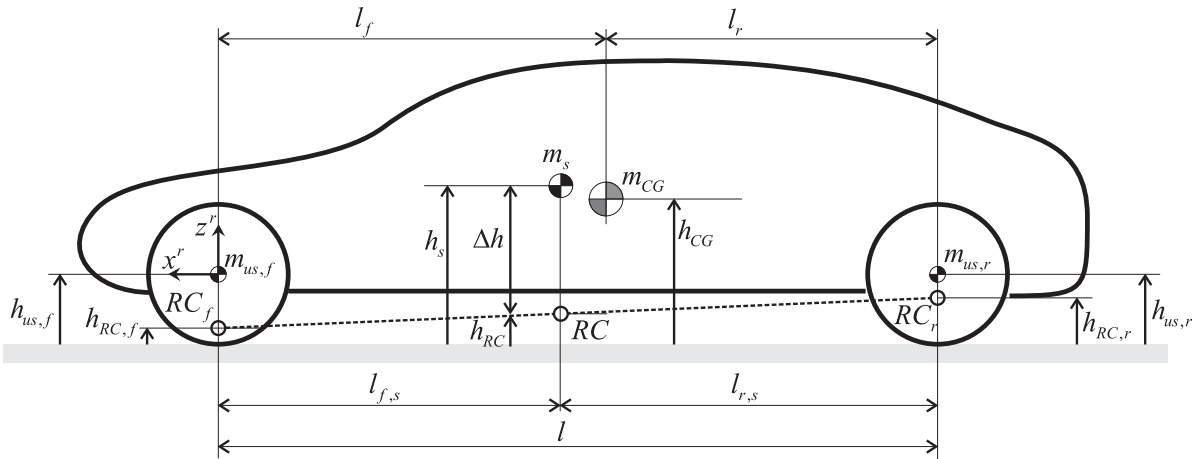


Figure 7.4: Mass geometry of the vehicle roll model with an inclined roll axis.

the total vehicle.

$$l_{f,s} = \frac{m_{CG}l_f - m_{us,r}l}{m_s} \quad (7.7)$$

With different roll center heights front and rear, the roll center height under the sprung mass, m_s , is calculated by the linear relationship:

$$h_{RC} = \frac{l_{r,s}h_{RC,f} + l_{f,s}h_{RC,r}}{l} \quad (7.8)$$

and accordingly, the roll lever arm in the roll model is $\Delta h = h_s - h_{RC}$.

The moment of inertia for the total vehicle (including the un-sprung masses) around the x-axis, J_x , can be calculated using the parallel-axis theorem (also known as Huygens-Steiner theorem) to be (see also Figure 7.5):

$$J_x = J_{\phi,s} + m_s(h_s - h_{CG})^2 + \sum_{j=f,r} m_{us,j} \left((h_{CG} - h_{us,j})^2 + \left(\frac{b_j}{2}\right)^2 \right) \quad (7.9)$$

The moments of inertia for the unsprung masses have been neglected.

All geometric parameters required in order to calculate accelerations and velocities in different positions in the roll model are hereby defined. The center of gravity lateral acceleration, a_y , will for instance be calculated by Equation (7.1) but the roll model needs the lateral acceleration of the sprung mass, $a_{y,s}$, which is given by:

$$a_{y,s} = a_y + \ddot{\Psi}(l_f - l_{f,s}) - \ddot{\Phi}(h_s - h_{CG}) \quad , \quad a_y = a_{y,CG} \quad (7.10)$$

The lateral acceleration of the unsprung masses are furthermore simplified to be equal to the lateral acceleration of the corresponding roll center, here exemplified for the front axle:

$$a_{y,us,f} = a_{y,s} + \ddot{\Psi}l_{f,s} + \ddot{\Phi}(h_s - h_{RC,f}) \quad , \quad (7.11)$$

Figure 7.5 presents the roll model as a whole, i.e. when including also the front and rear axle. A similar roll model can be found in Mitschke [36]. However, the model from Mitschke summarizes the roll stiffness of tires and suspension to an axle roll stiffness and it only considers the tire normal forces at steady-state cornering.

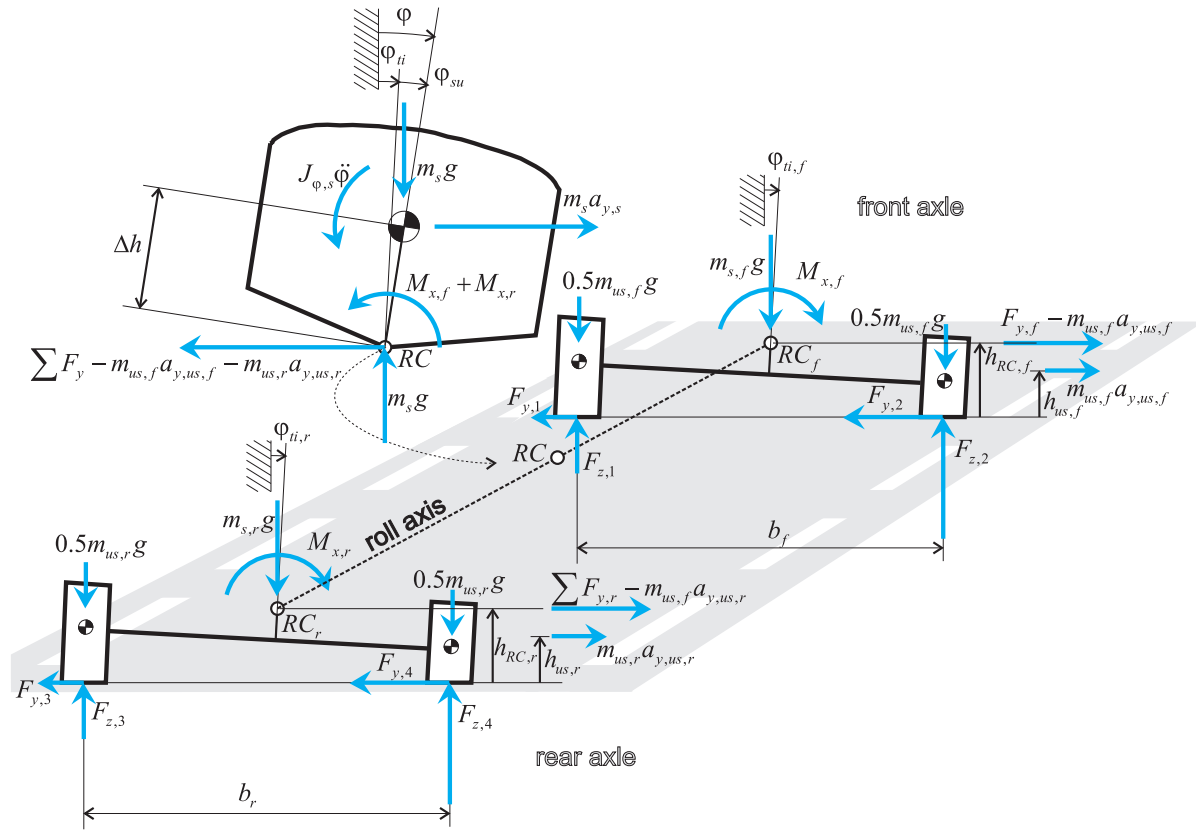


Figure 7.5: Full view of the vehicle roll model featuring an inclined roll axis, a sprung mass for the vehicle body, unsprung masses at each axle, separate roll angle for suspension roll, $\phi_{su,j}$, and tire roll, $\phi_{ti,j}$, at the front and rear axle respectively.

A vehicle only has the roll angle ϕ . However, the suspension and tire roll angles on the front and rear axle are separate states in this model approach. Since the roll moment of inertia of the unsprung masses are neglected in this model, the moment equilibrium around the roll center for the front and rear axle read:

$$M_{x,f} + (F_{y,f} + m_{s,f}g\phi_{ti,f})h_{RC,f} - m_{us,f}a_{y,us,f}(h_{RC,f} - h_{us,f}) = C_{\phi,ti,f}\phi_{ti,f} \quad (7.12)$$

$$M_{x,r} + (F_{y,r} + m_{s,r}g\phi_{ti,r})h_{RC,r} - m_{us,r}a_{y,us,r}(h_{RC,r} - h_{us,r}) = C_{\phi,ti,r}\phi_{ti,r} \quad (7.13)$$

The sprung mass resting on each of the axles is here denoted $m_{s,j}$ and is defined as:

$$m_{s,f} = m_s g \frac{l_{r,s}}{l} \quad m_{s,r} = m_s g \frac{l_{f,s}}{l} \quad (7.14)$$

$M_{x,j}$ denote the front and rear axle roll moments from springs and dampers as defined in Equation 7.3. The suspension roll angles, $\phi_{su,j}$, are furthermore derived from vehicle roll angle and tire roll angle, i.e. $\phi_{su,j} = \phi - \phi_{ti,j}$. Consequently, Equations (7.12) and (7.13) represent two first order differential equations which have to be solved.

7.3 Axle force and moment element

In Chapter 4 the lateral axle force element makes use of the axle side slip angle, α_j^A , as an input to calculate the static lateral force, $F_{y,j}^A$. The axle side slip angle, α_j^A , is calculated using the axle steer angle, δ_f (at the front axle); the vehicle longitudinal velocity, v_x ; the vehicle lateral velocity, v_y ; the yaw rate, $\dot{\psi}$; and the vehicle geometry parameters, l_f and l_r . In contrast to this, the axle force element in the extended 2-wheel model makes use of a larger set of vehicle motion states as inputs but the principle of an axle force element remain the same. Figure 7.6 displays the workflow in this element.

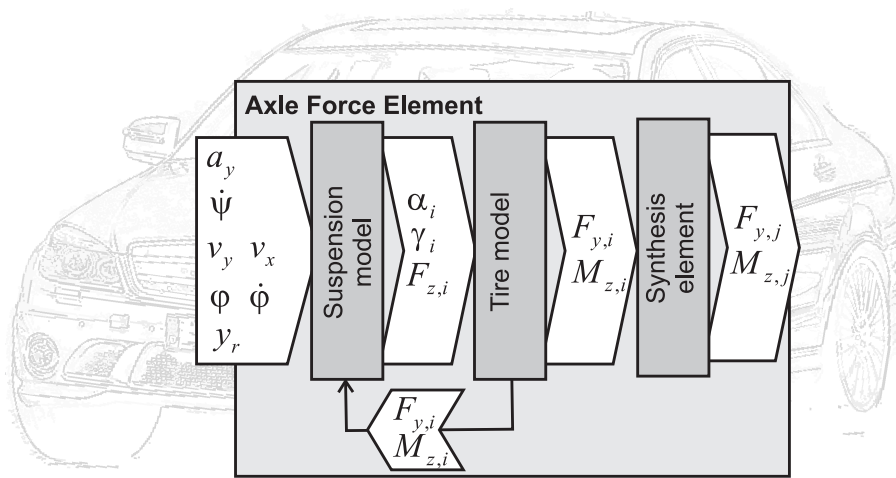


Figure 7.6: Axle force and moment element in the extended 2-wheel model.

The vehicle motion states are used as input for the suspension model which calculates the tire side slip angles, α_i ; tire camber angles, $\gamma_{i,r}$; and vertical loads, $F_{z,i}$ as inputs to the tire model, MF 5.2. Simultaneously, the tire lateral forces, $F_{y,i}$, and aligning moments, $M_{z,i}$, are used as inputs for the compliance elements in the suspension model, resulting in an algebraic loop which can be solved by a quasi-static approach. Finally, the tire forces and moments (left and right) are converted to an equivalent lateral axle force, $F_{y,j}^{2T}$, and aligning moment, $M_{z,j}^{2T}$, to be used in the equations of motion for the extended 2-wheel model.

It is important to mention that the axle aligning moment, $M_{z,j}^{2T}$, is not simply the sum of the aligning moments in the left and right tire. As shown in Chapter 5, unequal longitudinal forces left and right due to locking effects in the differential also creates a vehicle yaw moment which can be summarized in a differential yaw moment, $\Delta M_r = (F_{x,4} - F_{x,3})b_r/2$. However, the impact of the differential will here be neglected (virtually in the simulations by using an ideal differential) since this investigation focuses only on the pure lateral dynamics. The lateral tire forces also have a component in vehicle longitudinal direction due to the steer angles δ_i , causing a

vehicle yaw moment as well. Both these yaw moments will be added to the aligning moments.

$$F_{y,f}^{2T} = F_{y,1} + F_{y,2} \quad (7.15)$$

$$F_{y,r}^{2T} = F_{y,3} + F_{y,4} \quad (7.16)$$

$$M_{z,f}^{2T} = M_{z,1} + M_{z,2} + (F_{y,1}\delta_1 - F_{y,2}\delta_2) \frac{b_f}{2} \quad (7.17)$$

$$M_{z,r}^{2T} = M_{z,3} + M_{z,4} + (F_{y,3}\delta_3 - F_{y,4}\delta_4) \frac{b_r}{2} \quad (7.18)$$

Figure 7.7 shows the contributions from the different components in Equation (7.17) and (7.18) when the reference vehicle is driven in a steady-state maneuver. Only the rear axle is propelled and the contribution from longitudinal forces on the front axle can be explained by the rolling resistance, which on the outer tire (with more vertical tire load) will provide more negative longitudinal force and in this way cause a yaw torque, i.e. cause an under steering contribution. As can be seen in Figure 7.7, the term from lateral force in combination with the steer angles can be neglected on the rear axle. In case of a vehicle with an open but non-ideal differential, i.e. a differential with inner friction causing it to partially lock during cornering, this effect has to be considered in Equation (7.17) and (7.18) respectively, depending on which is the driven axle.

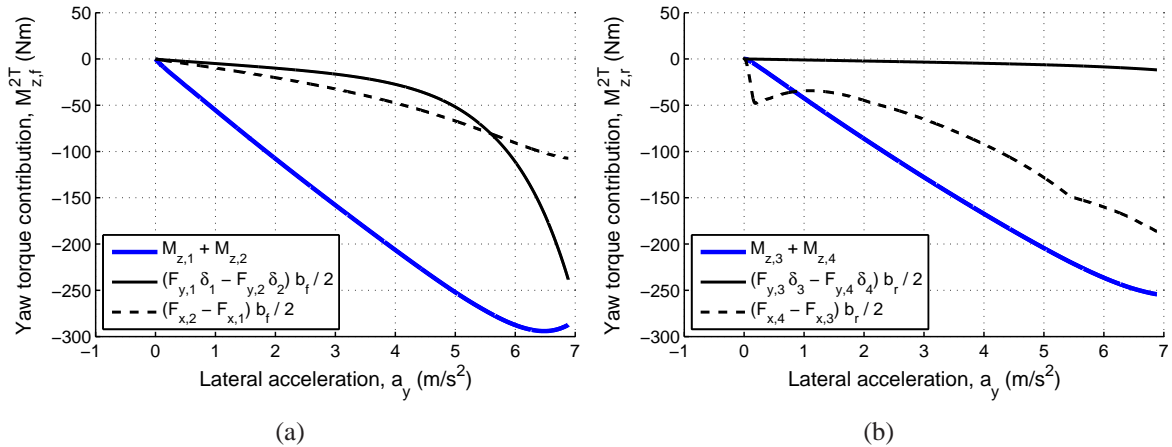


Figure 7.7: Yaw torque contributions from the components in Equation (7.17) and (7.18) over lateral acceleration during a steady-state maneuver. In (a) the front axle and in (b) the rear axle.

Note that Equations (7.15) through (7.18) directly present the dynamic lateral force and aligning moments. Hence, the dynamic tire force calculation is treated completely by the tire model MF 5.2 as described in [51]. This is a notable difference to the conventional 2-wheel model presented in Chapter 4 where a dynamic lateral axle force was calculated separately.

7.4 Approach for tire normal force

The roll model presented in Section 7.2 already provides the fundament for calculating the tire normal forces. With this roll model, both elastic and damping elements as well as suspension kinematics have been considered. Also a tire change is enabled with this roll model since the tire roll stiffness is separated from the roll stiffness in the suspension.

After using Equations (7.12) and (7.13), the tire roll angles at the front and rear axle are known. Equation (7.19) to (7.22) presents the approach used in this investigation to calculate the tire vertical load during lateral driving dynamics.

$$F_{z,1} = F_{z,0,1} - C_{\varphi,ti,f} \varphi_{ti,f} \frac{1}{b_f} \quad (7.19)$$

$$F_{z,2} = F_{z,0,2} + C_{\varphi,ti,f} \varphi_{ti,f} \frac{1}{b_f} \quad (7.20)$$

$$F_{z,3} = F_{z,0,3} - C_{\varphi,ti,r} \varphi_{ti,r} \frac{1}{b_r} \quad (7.21)$$

$$F_{z,4} = F_{z,0,4} + C_{\varphi,ti,r} \varphi_{ti,r} \frac{1}{b_r} \quad (7.22)$$

$F_{z,0,i}$ is a parameter in the extended 2-wheel model corresponding to the tire vertical load when the vehicle is standing still on a flat surface.

A remark regarding the simplification of the tire normal force calculation:

As the vehicle is driving a steady-state cornering maneuver, the tire normal forces will increase

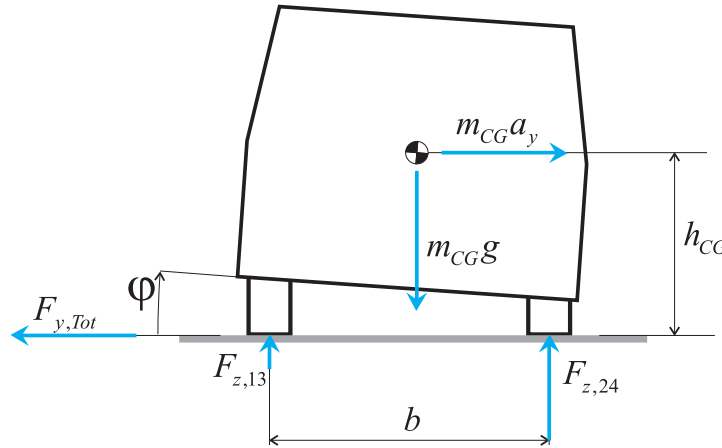


Figure 7.8: Vertical load transfer during steady-state cornering on a vehicle (rear side). The vertical load on the inner and outer wheel pair are concluded in the vertical loads $F_{z,13}$ and $F_{z,24}$ respectively.

on the outer wheel pair and decrease on the inner wheel pair. This will be referred to as a *vertical load shift*.

If denoting the sum of the inner and outer wheel pair as $F_{z,13}$ and $F_{z,24}$ respectively, see Figure 7.8, and with small angle approximation, it can be shown that the summarized tire load of the

inner and outer wheel pair are:

$$F_{z,13} = \frac{mg}{2} - \frac{ma_y h_{CG} + mgh_{CG}\phi}{b} \quad (7.23)$$

$$F_{z,24} = \frac{mg}{2} + \frac{ma_y h_{CG} + mgh_{CG}\phi}{b} \quad (7.24)$$

Figure 7.9 displays the sum of tire normal forces of the inner and outer wheel pair during a simulated steady-state cornering maneuver (constant radius test) with the reference model CASCaDE-DA in comparison to the results from the estimations in Equation (7.23) and (7.24). The quantities used in the estimations are the same as identified in Chapter 8.

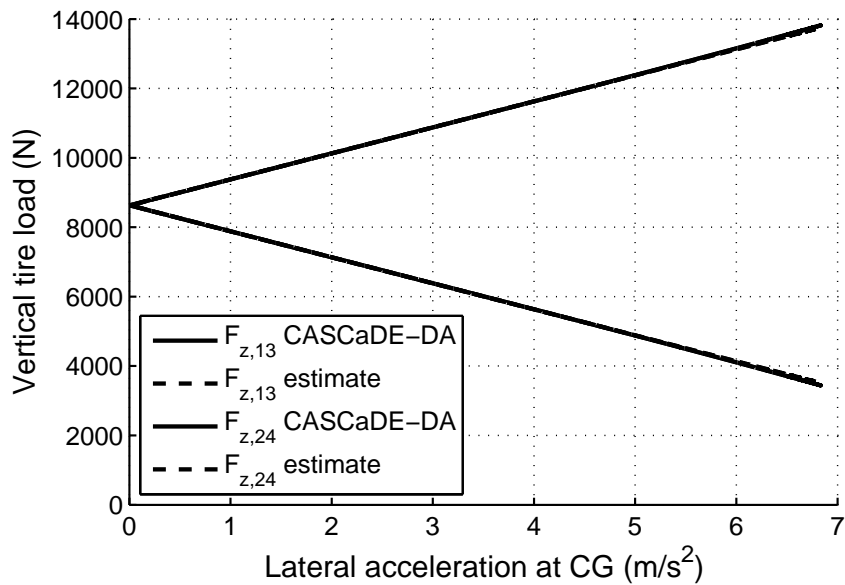


Figure 7.9: Summarized vertical tire load of the inner and outer wheel pair during steady-state cornering in comparison to the approach presented in Equation (7.23) and (7.24).

In this case the linear approach is sufficient. However, for some vehicles the vehicle body heaves (or dives) during roll due to jacking effects, i.e. changing the center of gravity height, h_{CG} , which cause a non-linear increase (or decrease) of vertical tire load at higher lateral accelerations. The track width will also change during roll and in this way influence the tire normal forces but this effect is secondary in comparison to body heave. A change in vertical load due to non-linear stiffness in the suspension springs will not be seen here as this would only change the ratio of roll moment supported by the front and rear axle.

Figure 7.10 displays how the center of gravity height, h_{CG} , changes as a function of lateral acceleration in an different vehicle, also during a steady-state cornering maneuver. In order to improve the estimation, the body heave (or dive) could be integrated in the tire vertical load estimation as a function over lateral acceleration, i.e. $h_{CG} = h_{CG}(a_y)$. However, the gain in accuracy does not motivate the increase in complexity with one more parameter to be identified. The center of gravity height is therefore considered to be a constant parameter and vertical body motion (heave/dive) is neglected. The same reasoning is applicable for the track width change as a function of vehicle roll angle.

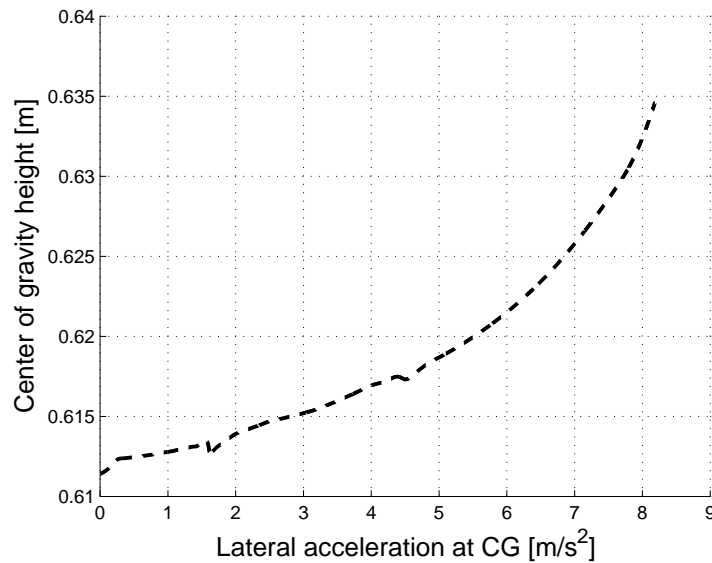


Figure 7.10: Change of center of gravity height h_{CG} depending on lateral acceleration a_y during steady-state cornering (not with the reference vehicle).

If the effect of heave (or dive) during cornering is to be considered, a more detailed suspension model is required, like for instance CASCaDE-DA. A good suspension set-up will, however, cause a minimal amount of heave/dive during cornering, i.e. a constant $h_{CG} = h_{CG}(a_y)$.

7.5 Approach for suspension kinematics and compliance.

As already mentioned, the positioning of the wheels in relation to the road influences the generated tire forces and consequently the handling of the vehicle. The linkage attachment points determine the pure kinematic behavior of the suspension, i.e. how the steer and camber angle changes with wheel travel (jounce and rebound). Moreover, elasticities in mainly rubber bushings, but also in the vehicle body and suspension parts, will allow the suspension to deflect under load resulting in additional changes in steer and camber angles. The amount of deflection (for a specific load case) due to compliance depends on a combination of the suspension kinematics and the elasticities of the suspension components: The suspension kinematics influences how the forces are distributed over the different elasticities and the total suspension deflection results from a combination of the deflections in the different components.

When deriving approaches to calculate steer and camber angles in the extended 2-wheel model, it is not necessary to perform a thorough analysis of the interaction between suspension kinematics and the compliance in different suspension components. If an extensive model for kinematics and compliance is needed, a model class similar to the CASCaDE-Classic model should be used instead, see Section 2.3. For the extended 2-wheel model, general functional approaches are required which are able to capture the most important suspension properties regarding vehicle handling.

7.5.1 Steer angles and tire side slip angles

The suspension steer angles are important due to their direct influence on the tire side slip angles. In order to separate the suspension from the steering system, the rack displacement y_r will be used here as an input to represent the driver's steering inputs, instead of the steering wheel angle δ_D as in Chapter 4. Hence, the dynamics of the steering system is excluded from the suspension model and could be treated in a separate steering model as described in for instance [7] with the steering rack displacement and force as interface to the suspension model. The steer angles are approximated with the following approach:

$$\delta_1 = -\delta_f(-y_r) - \delta_{0,f} + \delta_{c,1}(F_{y,1}, M_{z,1}) - \delta_{\varphi,f}(-\varphi_{su,f}) \quad (7.25)$$

$$\delta_2 = \delta_f(y_r) + \delta_{0,f} + \delta_{c,2}(F_{y,2}, M_{z,2}) + \delta_{\varphi,f}(\varphi_{su,f}) \quad (7.26)$$

$$\delta_3 = -\delta_{0,r} + \delta_{c,3}(F_{y,3}, M_{z,3}) - \delta_{\varphi,r}(-\varphi_{su,r}) \quad (7.27)$$

$$\delta_4 = \delta_{0,r} + \delta_{c,4}(F_{y,4}, M_{z,4}) + \delta_{\varphi,r}(\varphi_{su,r}) \quad (7.28)$$

The steer angles δ_i are defined positive according to a right hand orthogonal reference frame. As a consequence, the parameter for static toe in, $\delta_{0,j}$, which by definition is positive when the wheels converge towards the front, is here defined positive on the right hand side and negative on the left.

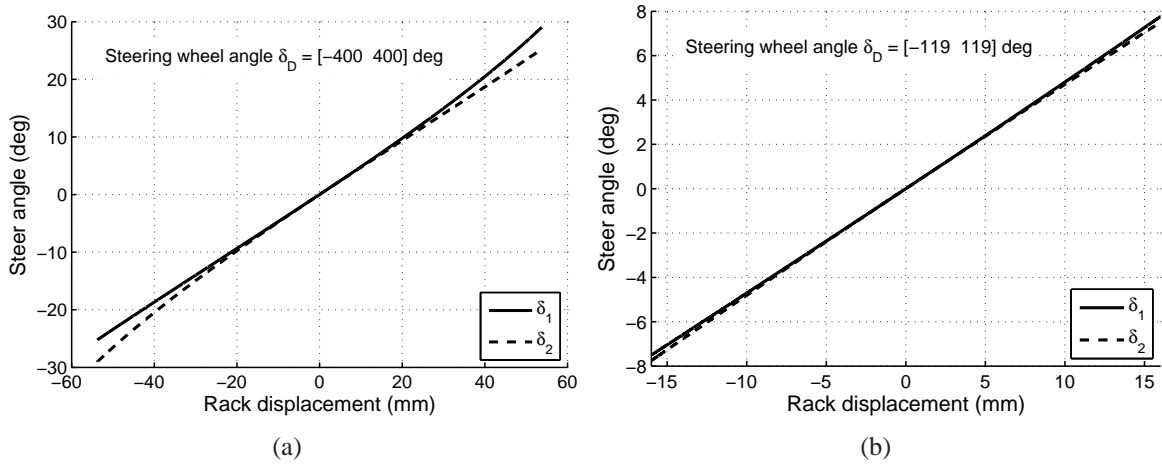


Figure 7.11: In (a) the front steer angles δ_1 and δ_2 in relation to the rack displacement y_r (reference vehicle A). Note that the characteristics for δ_1 is symmetric to origin with δ_2 . (b) shows a zoom of (a) with rack displacements corresponding to steering wheel inputs reached during normal handling maneuvers, i.e. $\delta_D = [-120 \ 120]$.

$\delta_f(y_r)$ is the steer angle caused by a steering wheel input and is defined as a function of rack displacement, y_r . Figure 7.11(a) shows the relation between the rack displacement and the front steer angles δ_1 and δ_2 in reference vehicle A. The left and right side wheel suspensions are in general designed to be symmetric, allowing both the left and right side to be described by a single function regarding the steer angle over rack displacement. This is also the case in reference vehicle A which explains the minus signs in Equation (7.25), i.e. $-\delta_f(-y_r)$. Furthermore, Figure 7.11(b) shows a closeup of Figure 7.11(a), with rack displacements corresponding to

steering inputs reached during normal handling maneuvers, i.e. $\delta_D = [-120 \ 120]$ degrees. It is evident that even within this range, a linear relationship would not be sufficient.

Suspension compliance gives rise to further changes in steer angles under load. The approach for calculating the compliance steer angles, $\delta_{c,i}$, is illustrated in Figure 7.12. During lateral

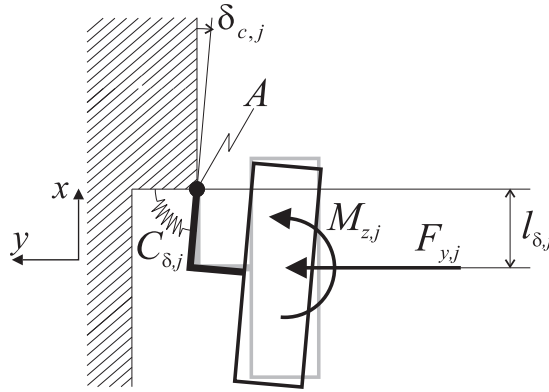


Figure 7.12: Basic illustration of the compliance steer approach.

forces, the wheel will pivot around point A with the torsion steering stiffness $C_{\delta,j}$. The collective steering arm length, $l_{\delta,j}$, make up the lever arm for the lateral forces. The pivoting point A can also be located behind the center of the wheel depending on the suspension kinematics and compliance properties, causing the length $l_{\delta,j}$ to be negative. Equation (7.29) concludes the approach for the compliance steer angles, $\delta_{c,i}$:

$$\delta_{c,i}(F_{y,i}, M_{z,i}) = (M_{z,i} - l_{\delta,j}F_{y,i}) \frac{1}{C_{\delta,j}} \quad (7.29)$$

The compliance steer angles $\delta_{c,i}$ are superposed on the steer angles δ_i with a quasi-static approach. This has been realized by using results from the previous time step.

Finally, $\delta_{\phi,j}(\phi_{su,j})$ describes the kinematic steer angle change during wheel travel, i.e. jounce and rebound, and is also called roll steer. Figure 7.13 show how the steer angle change as a function of vehicle roll angle calculated from the steer angles during alternating jounce and rebound at a test bench (more about how to calculate the roll steer function can be found in Section 8.3.4). Only the right wheels were plotted here (front right wheel in (a) and rear right wheel in (b)) since the left wheels will behave axis-symmetric to the plots for the right wheels (for a vehicle with symmetric suspension). Depending on the suspension design, a non-linear approach might be necessary. The front axle on the reference vehicle for instance require a non-linear approach whereas the rear could be approximated with a linear approach. Since the test bench measurements already contain all necessary information to parameterize a non-linear roll-steer approach, such an approach will be used here independent of the suspension design.

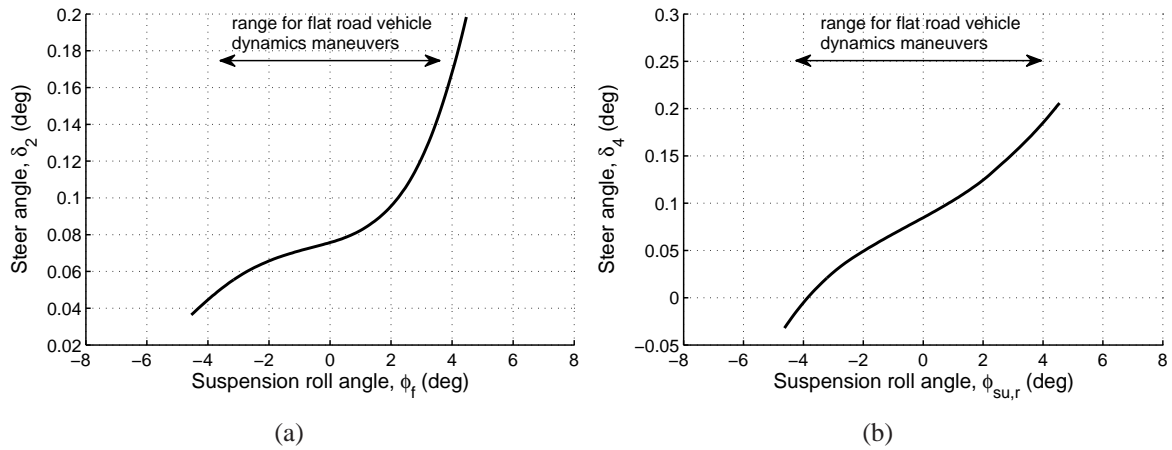


Figure 7.13: In (a) the steer angle at the front right wheel δ_2 as a function of roll angle in the test bench maneuver **AJR** and in (b) the same for the rear right wheel δ_4 .

The tire side slip angle, α , is simply defined as the angle between the wheel plane and the tangent to the trajectory of the center of tire contact point. Hence, the side slip angle is the difference between the steer angle of the wheel and the angle at which the tire contact point is moving in relation to the vehicle's direction of travel, see Figure 7.14. The velocity of the tire contact point defined in the vehicle reference frame, $v_{x,w}$ and $v_{y,w}$, is achieved by a transformation of the center of gravity velocity to the tire contact point. In this model, only the yaw and roll rate are taken into consideration in this transformation and the distance between the center of gravity position and the tire contact point is assumed to be fixed. Hence, effects in the suspension kinematics influencing the tire contact velocity, such as camber angle change or lateral movement of the wheel during jounce and rebound, are neglected. Equation (7.30) to (7.33) presents the approach to calculate the side slip angles α_i , see Figure 7.5.

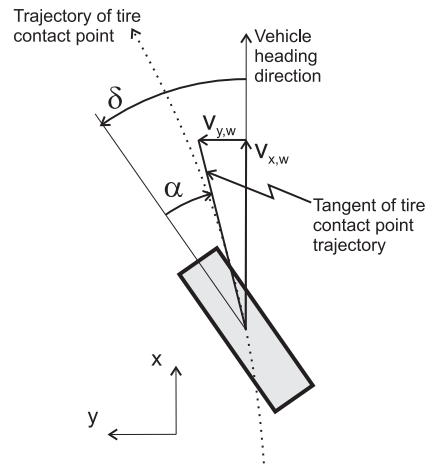


Figure 7.14: Tire side slip angle.

$$\alpha_1 = \delta_1 - \frac{v_y + l_f \dot{\psi} + (h_{CG} - h_{RC}) \dot{\phi}_{su} + h_{RC} \dot{\phi}_{ti}}{v_x} \quad (7.30)$$

$$\alpha_2 = \delta_2 - \frac{v_y + l_f \dot{\psi} + (h_{CG} - h_{RC}) \dot{\phi}_{su} + h_{RC} \dot{\phi}_{ti}}{v_x} \quad (7.31)$$

$$\alpha_3 = \delta_4 - \frac{v_y - l_r \dot{\psi} + (h_{CG} - h_{RC}) \dot{\phi}_{su} + h_{RC} \dot{\phi}_{ti}}{v_x} \quad (7.32)$$

$$\alpha_4 = \delta_4 - \frac{v_y - l_r \dot{\psi} + (h_{CG} - h_{RC}) \dot{\phi}_{su} + h_{RC} \dot{\phi}_{ti}}{v_x} \quad (7.33)$$

7.5.2 Tire camber angle

For normal passenger tires of today, lateral tire forces and moments produced by camber angles are small in comparison to the forces generated from side slip angles of the same magnitude. Nevertheless, tire forces due to tire camber angles still deliver an important contribution to the handling of the vehicle. To exemplify this, the front right wheel in the reference vehicle during a steady-state cornering maneuver at about 7 m/s^2 lateral acceleration generates approximately 5 kN lateral force (at $\alpha = 5.3 \text{ deg}$, $\gamma = 4.9 \text{ deg}$ and $F_z = 7.5 \text{ kN}$). In the same operating state but with neglected tire camber angle, i.e. $\gamma = 0 \text{ deg}$, the tire would generate 500 N more lateral force. This would then have to be compensated for in the suspension model by for instance incorrect steer angles or vertical tire loads.

Generally, the suspension camber angle, ε , is defined as the angle between the vehicle z-axis and the wheel plane and is positive when inclined outward relative to the vehicle body [17]. However, the approach here refers to the camber angle of the tire in relation to the road, γ , i.e. the angle between the wheel plane and the normal to the road, and is defined positive according to a right hand orthogonal reference frame. This definition is used since the tire camber angle, γ , will be used as a direct input to the tire model.

Figure 7.15 show how the tire camber angles, γ_i , are related to the vehicle roll angle, φ , and the body camber angles, ε_i , in an independent wheel suspension. The suspension camber angle,

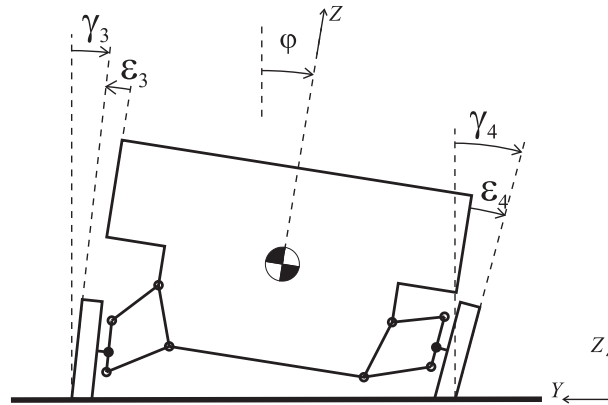


Figure 7.15: Illustration of the tire camber angles, γ_i , and the camber angles in relation to the vehicle body, ε_i (rear axle).

ε_i , can furthermore be described by a static camber angle, $\varepsilon_{0,j}$, and camber angle depending on vehicle roll, $\varepsilon_{\varphi,j}(\varphi_{su,j})$. The tire camber angles can now be described as:

$$\gamma_1 = \varphi - \varepsilon_1 = \varphi - (\varepsilon_{0,f} + \varepsilon_{\varphi,f}(-\varphi_{su,f})) \quad (7.34)$$

$$\gamma_2 = \varphi + \varepsilon_2 = \varphi + (\varepsilon_{0,f} + \varepsilon_{\varphi,f}(\varphi_{su,f})) \quad (7.35)$$

$$\gamma_3 = \varphi - \varepsilon_3 = \varphi - (\varepsilon_{0,r} + \varepsilon_{\varphi,r}(-\varphi_{su,r})) \quad (7.36)$$

$$\gamma_4 = \varphi + \varepsilon_4 = \varphi + (\varepsilon_{0,r} + \varepsilon_{\varphi,r}(\varphi_{su,r})) \quad (7.37)$$

In addition to the camber angle change due to vehicle roll angle, the camber angles on the front axle are influenced by steering inputs as well. $\gamma_{\delta,f}(y_r)$ describes the change in tire camber

angle caused by steering wheel inputs and is defined as a function of rack displacement, y_r . Figure 7.16(a) shows the relation between the rack displacement and the tire camber angles at the front axle, i.e. γ_1 and γ_2 in reference vehicle A. Figure 7.16(b) presents a closeup of

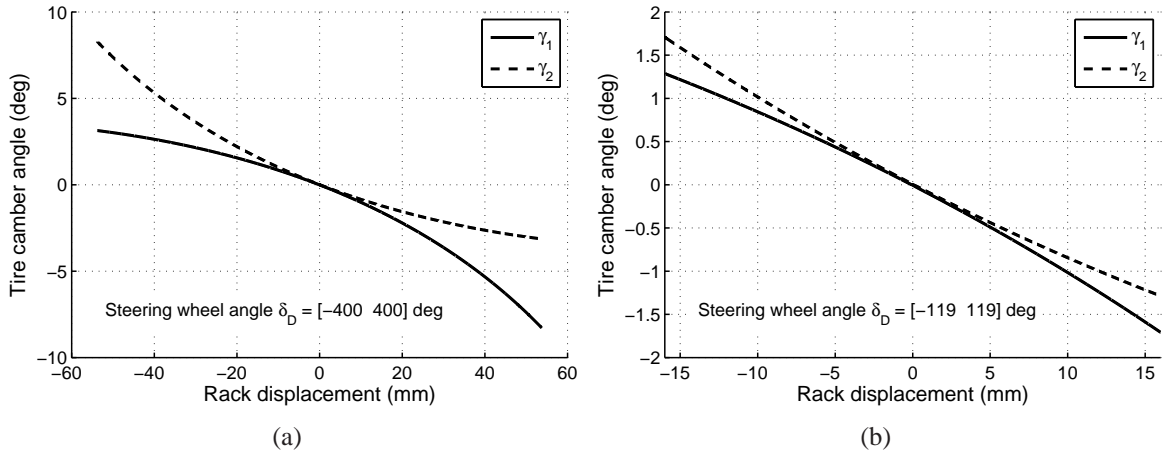


Figure 7.16: In (a) the tire camber angles at the front axle, γ_1 and γ_2 , in relation to the rack displacement y_r (reference vehicle A). (b) shows a zoom of (a) capturing rack displacements corresponding to steering wheel inputs reached during normal handling maneuvers, i.e. $\delta_D = [-120 \ 120]$.

Figure 7.16(a) with rack displacements corresponding to steering inputs reached during normal handling maneuvers, i.e. $\delta_D = [-120 \ 120]$ degrees. The tire camber angles achieved at large steering inputs are large enough to be considered in the suspension model.

If including also the tire camber angle change due to steering inputs, the final approach to calculate the tire camber angles reads:

$$\gamma_1 = \varphi - \varepsilon_1 = \varphi - (\varepsilon_{0,f} + \varepsilon_{\varphi,f}(-\varphi_{su,f})) - \gamma_{\delta,f}(-y_r) \quad (7.38)$$

$$\gamma_2 = \varphi + \varepsilon_2 = \varphi + (\varepsilon_{0,f} + \varepsilon_{\varphi,f}(\varphi_{su,f})) + \gamma_{\delta,f}(y_r) \quad (7.39)$$

$$\gamma_3 = \varphi - \varepsilon_3 = \varphi - (\varepsilon_{0,r} + \varepsilon_{\varphi,r}(-\varphi_{su,r})) \quad (7.40)$$

$$\gamma_4 = \varphi + \varepsilon_4 = \varphi + (\varepsilon_{0,r} + \varepsilon_{\varphi,r}(\varphi_{su,r})) \quad (7.41)$$

7.6 Summary of Chapter 7

The suspension model presented in this investigation together with the Magic Formula tire model MF 5.2, form the so called *suspension-tire element* which replaces the axle force characteristics used in the conventional non-linear 2-wheel model. The suspension tire element is a part of the extended 2-wheel model featuring the possibility to change tires within the 2-wheel model concept. Another benefit is the possibility of using a 2-wheel model when investigating how changes in the vehicle set-up (like different anti-roll bar stiffness or other loading conditions) will change the vehicle handling. Prior to the extended 2-wheel model, such investigations would have required more detailed vehicle models like for instance the CASCaDE-Classic or the CASCaDE-DA model (see Sections 2.2 and 2.3).

The extended 2-wheel model could also be used for simulating a vehicle with an active roll stabilization (ARS) system without changing the model structure. The only change required is to add an active roll moment front and rear, $\Delta M_{ARS,j}$, to the total roll moment $M_{x,j}$ in Equation 7.3.

The identification process for the extended 2-wheel model will be presented in Chapter 8 followed by a documentation of the model validity in Chapter 9. The possibility of using the extended 2-wheel model when extrapolating the vehicle behavior in different loading conditions, other anti-roll bar setups or with different tire properties will be investigated in Chapter 10.

Chapter 8

The extended 2-wheel model – parameter identification process

This chapter presents a method to identify the model parameters in the extended 2-wheel model. Simulations with the vehicle model CASCaDE-DA are used here as a reference instead of real life measurements with a test vehicle, i.e. the simulations with the CASCaDE-DA model can be seen as a sort of virtual measurements. In this investigation, both the CASCaDE-DA model and the extended 2-wheel model use the exact same MF 5.2 tire model with the same tire characteristics, i.e. the same tire model parameters. The objective of the identification process is to get the extended 2-wheel model to simulate the same vehicle behavior as the virtual measurements with CASCaDE-DA.

The core of the identification process is described in Section 8.3 but first the used identification maneuver and the tire characteristics will be described.

8.1 The identification maneuver

In the identification process for the extended 2-wheel model, a wide range of driving maneuvers are required where all possible lateral motion states are excited. This includes steering wheel inputs causing the vehicle motion to be:

- steady-state motion – covering the whole range of possible steady-state lateral accelerations,
- oscillating motion – covering the frequency range achievable by steering wheel inputs (approximately up to 2.5 Hz),
- transient motion – including the after oscillations.

In addition to this, these driving states have to be driven at different longitudinal velocities since this influences the vehicle response as well. Vehicle aerodynamics is one effect causing different vehicle response at different velocities and becomes especially important at higher velocities.

Another effect which is more important at lower velocities is the tire transient behavior (also included in the transient tire model approaches in [5] and [51]).

Instead of using a number of different standardized driving maneuvers, one identification maneuver incorporating all the above mentioned driving states is suggested.¹ Figure 8.1 displays the rack displacement, y_r , and the vehicle longitudinal velocity, v_x , (both inputs to the extended 2-wheel model) during the identification maneuver. The maximum amplitude of $y_r \approx 16$ mm corresponds to a steering wheel angle amplitude of $\delta_D = 120$ degrees. The first part of the maneuver, i.e. the steering sweep², the two step steer inputs and the steady state cornering maneuver, is driven at a constant speed of 60 km/h. The second part is a repetition of the first part regarding the steering inputs but the driving speed is increased to 120 km/h and the steering wheel angle amplitudes are decreased in order to reach similar lateral acceleration levels as in the first part.

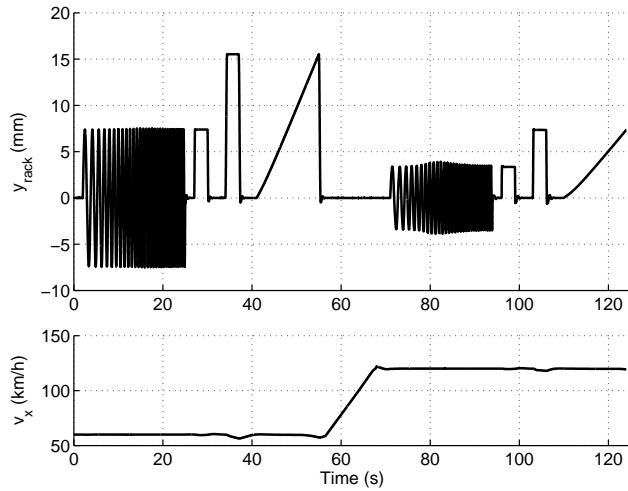


Figure 8.1: Rack displacement and vehicle velocity during the identification maneuver.

The steering wheel amplitudes during the steering sweeps have been selected to achieve a medium lateral steady-state acceleration of $a_y \approx 4$ m/s². The steering wheel angle amplitude at the two step steer inputs has been chosen in order to achieve a medium lateral steady-state acceleration of ≈ 4 m/s² followed by a higher lateral acceleration of $a_y \approx 7$ m/s². The lateral acceleration in the constant velocity steady-state cornering ranges within $\approx 0 - 7$ m/s². The resulting vehicle motion, including the lateral acceleration, will be shown in Section 8.4.

Note that no steering inputs are made during the acceleration part between the two velocity levels. This is made deliberately since the investigations presented here only consider the lateral dynamics of the vehicle.

8.2 The selected tire characteristics

It is very important to study the tire model behavior within the intended use case before performing vehicle dynamics simulations. For this purpose, the so called *tire fingerprint*, presented in for instance [44], has been applied. In this fingerprint, the tire is evaluated at different loads and the results are presented in a set of standardized plots.

¹This was done only to simplify the implementation, a number of different standardized driving maneuvers would have worked as well

²Steering sweep: Sinusoidal steering wheel input with increasing input frequency and constant steering wheel amplitude.

Figure 8.2 and 8.3 present the parts of the fingerprint which are important for vehicle handling simulations. Figure 8.2(a) shows according to MF 5.2 the lateral force characteristics, $F_y(\alpha)$, and Figure 8.2(b) shows the aligning moment, $M_z(\alpha)$, at pure side slip conditions. The cornering stiffness, $C_\alpha = \left. \frac{\partial F_y}{\partial \alpha} \right|_{\alpha=0}$, as a function of vertical tire load is shown in Figure 8.3(a). Conclusively the tire dynamics is exemplified with a step response in Figure 8.3(b). The tire vertical load is kept constant at 4000 N during a side slip angle step input of 3 degrees at 40 km/h longitudinal velocity. 90 % of the steady state lateral force is reached after 110 ms.

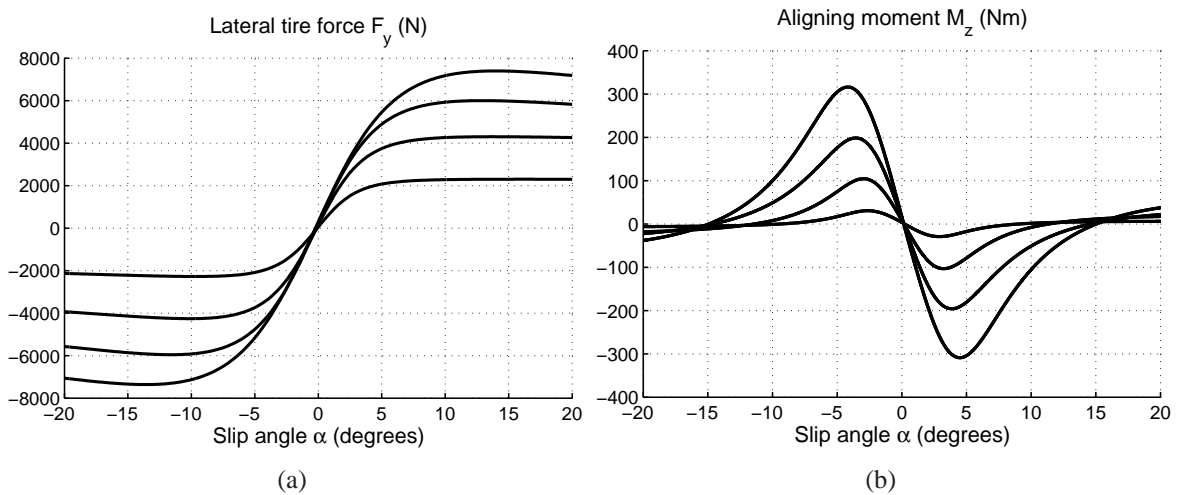


Figure 8.2: Lateral tire force and aligning moment characteristics at pure side slip condition. The characteristics are generated at the vertical tire loads $F_z = 2000, 4000, 6000$ and 8000 N

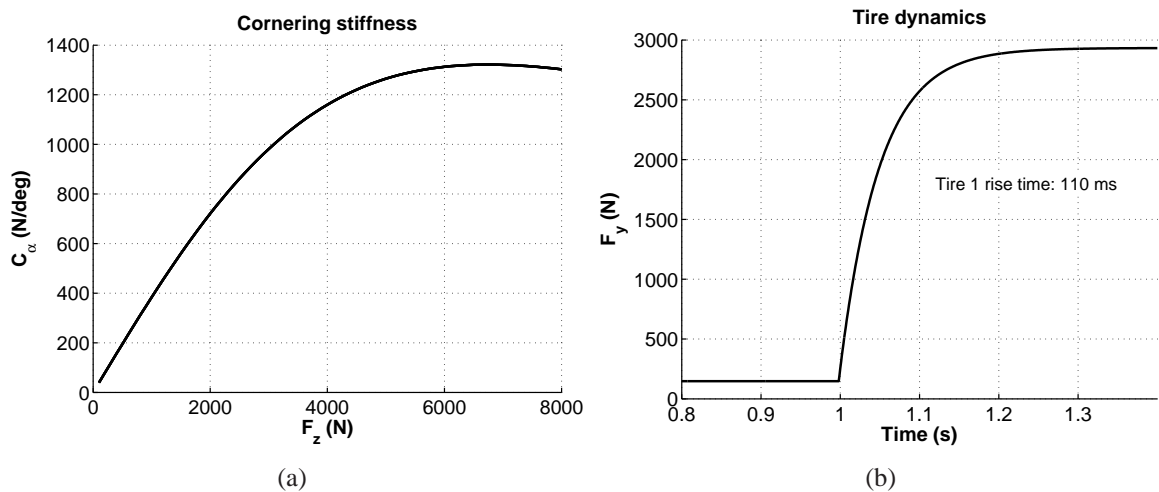


Figure 8.3: In (a) the tire cornering stiffness as a function of vertical tire load and in (b) a step response exemplifying the tire dynamics (tire vertical load 4000 N during a side slip angle step of 3 degrees and 40 km/h longitudinal velocity). 90 % of the steady state lateral force is reached after 110 ms.

8.3 Parameterization process

The process of parameterizing the extended 2-wheel model and the suspension-tire model is described in this section. Many parameters can be measured directly and a few are left to be identified in an identification process described in Subsection 8.3.6.

8.3.1 Geometric and mass properties

The first parameters to decide are the wheel base, l , the track width on each axle, b_f and b_r , and the static corner loads, $F_{z0,i}$, which should all be measured as the vehicle is standing still on a flat horizontal surface in the base loading condition. This represents the base condition when identifying the rest of the parameters in the suspension model. From the static loading condition of each corner and the wheel base, the longitudinal center of gravity position can be derived and described by the distance from the front and rear axle respectively.

$$l_f = \frac{F_{z0,3} + F_{z0,4}}{F_{z0,1} + F_{z0,2} + F_{z0,3} + F_{z0,4}} \cdot l \quad (8.1)$$

$$l_r = l - l_f \quad (8.2)$$

In these investigations, the center of gravity has been placed in the middle of the vehicle laterally in order to simplify the calculations but the model is not limited to this condition.

The total vehicle mass is derived from the static corner loads and is furthermore divided in a sprung and unsprung mass, i.e. $\sum F_{z0,i}/g = m_{CG} = m_s + m_{us}$. The unsprung mass is the weight of the various parts of a vehicle that are not carried on the springs, e.g. wheels, axles and brakes. Other parts of the suspension, like for instance suspension linkages, dampers and springs are all partially part of the sprung and the unsprung masses since they follow both the body motion as well as the motion of the wheels. Nevertheless, the weight of the latter parts will be neglected in the 2-wheel model and the unsprung mass is therefore defined as the total weight of the wheel (tire and rim), the wheel carrier, the brake disk and the brake calliper unit. Since these components are different on the front and rear axle, the unsprung mass is divided in two different parameters, i.e. $m_{CG} = m_s + m_{us,f} + m_{us,r}$. The weight of the unsprung masses are normally known in the development process but could also be measured or estimated. Since most of the unsprung mass is gathered around the wheel center, the height of the unsprung masses, $h_{us,f}$ and $h_{us,r}$, are here estimated to be equal to the radius of the wheels.

The roll lever arm, Δh ; the yaw inertia, J_ψ ; the roll inertia of the sprung mass, $J_{\phi,s}$; and the roll center heights of each axle, $h_{RC,f}$ and $h_{RC,r}$, are all possible to measure but will here be identified using driving measurements. The process for this is described in subsection 8.3.6.

Table 8.1 summarizes the identified length and mass parameters as well as the derived parameters (from Section 7.2) for *Vehicle A*, described in Section 2.5.

Parameter	Value	Unit	Source
l	2.720	m	Measured
b_f	1.484	m	Measured
b_r	1.480	m	Measured
$F_{z,0,1}$	4417	N	Measured
$F_{z,0,2}$	4417	N	Measured
$F_{z,0,3}$	4213	N	Measured
$F_{z,0,4}$	4213	N	Measured
$h_{us,f}$	0.293	m	Measured
$h_{us,r}$	0.294	m	Measured
$m_{us,f}$	62	kg	Measured
$m_{us,r}$	56	kg	Measured
Δh	0.54	m	Identified in Subsection 8.3.6
J_ψ	2708	kgm^2	Identified in Subsection 8.3.6
$J_{\phi,s}$	486	kgm^2	Identified in Subsection 8.3.6
$h_{RC,f}$	0.011	m	Identified in Subsection 8.3.6
$h_{RC,r}$	0.075	m	Identified in Subsection 8.3.6
m_{CG}	1759.5	kg	Derived from other parameters
l_f	1.328	m	Derived from other parameters
l_r	1.392	m	Derived from other parameters
m_s	1641.5	kg	Derived from other parameters
$l_{f,s}$	1.330	m	Derived from other parameters
$l_{r,s}$	1.390	m	Derived from other parameters
h_{RC}	0.042	m	Derived from other parameters
h_s	0.581	m	Derived from other parameters
h_{CG}	0.563	m	Derived from other parameters
J_x	584	kgm^2	Derived from other parameters

Table 8.1: Mass and geometry parameters for *Vehicle A*, described in Section 2.5.

8.3.2 Parameters for the elastic roll moment characteristics

The elastic roll moment, $M_{\phi,j}(\phi_{su,j})$, can be derived mainly from the suspension springs and the anti-roll bar but it inevitably also includes the elasticities in the rubber bushings and the bump stops in combination with the suspension kinematics. Measurements from a suspension

test bench (not including the tires) will be used to explain the composition of the roll stiffness. In these measurements, the vehicle body is held fixed while the wheels are moved in jounce and rebound, providing the required force at the wheel hub, $F_{z,hub,i}$, over suspension deflection, Δz_i , in two load cases:

- **SJR** Synchronized **J**ounce and **R**ebound of both left and right wheels simultaneously, i.e. $\Delta z_{left} = \Delta z_{right}$.
- **AJR** Alternating **J**ounce and **R**ebound of the left and right wheel, i.e. $\Delta z_{left} = -\Delta z_{right}$.

In the first load case, **SJR**, only the suspension springs are activated (plus the compliance of rubber bushings) and in the second load case, **AJR**, the anti-roll bar is also contributing to the required force.

Figure 8.4 show the resulting vertical force at the wheel hub, $F_{z,hub,i}$, over suspension deflection Δz_i , during the maneuvers **SJR** and **AJR**. The force at $\Delta z_i = 0 \text{ mm}$ corresponds to the vertical tire load when the vehicle is standing still on a flat surface in the base load condition. The coil springs are normally linear and the non-linearity seen in $F_{z,hub,i}(\Delta z_i)$ is created by the additional jounce and rebound stops.

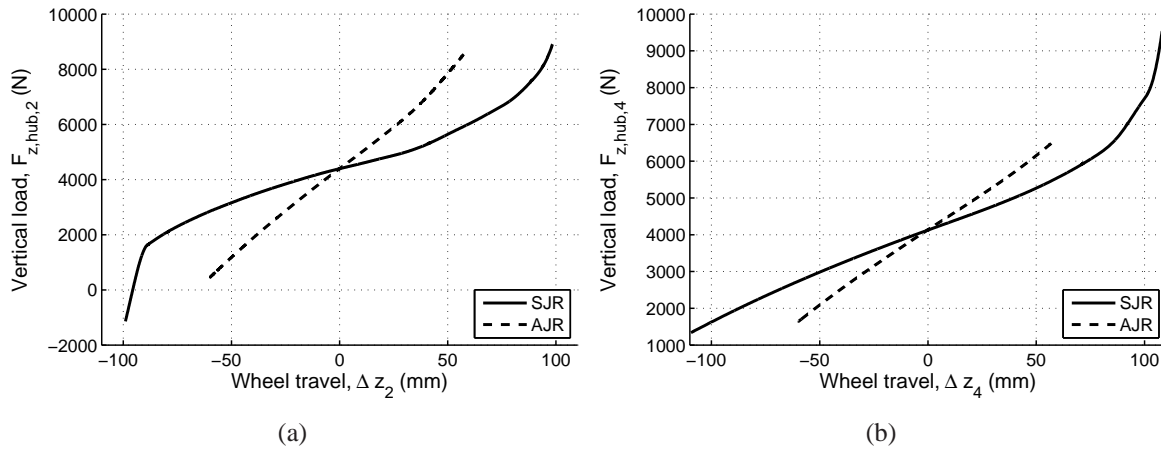


Figure 8.4: Vertical force at the wheel hub over suspension deflection, $F_{z,hub,i}(\Delta z_i)$, during the maneuvers **SJR** and **AJR**; front right corner in (a) and rear right corner in (b) for *Vehicle A*, described in Section 2.5.

The left and right characteristics for vertical force over suspension deflection, $F_{z,hub,i}(\Delta z_i)$, can be converted to a roll moment over suspension roll angle, $M_{\phi,j}(\phi_{su,j})$. This is here exemplified for the front axle by inserting a range of suspension deflections, Δz_f , to get the suspension roll moment:

$$M_{\phi,f} = F_{z,hub,2}(\Delta z_f) \cdot 0.5b_f - F_{z,hub,1}(-\Delta z_f) \cdot 0.5b_f \quad (8.3)$$

with the corresponding suspension roll angle:

$$\phi_{su,j} = \frac{\Delta z_f}{0.5b_f} \quad (8.4)$$

Figure 8.5 shows the resulting front and rear suspension roll moment over suspension roll angle, $M_{\phi,j}(\phi_{su,j})$, for the maneuvers **SJR** and **AJR**. The gray box defines the range of suspension roll angles achieved with reference vehicle A during the identification maneuver described in Section 8.1 driving on a flat road, i.e. the range relevant for the objective of this vehicle model.

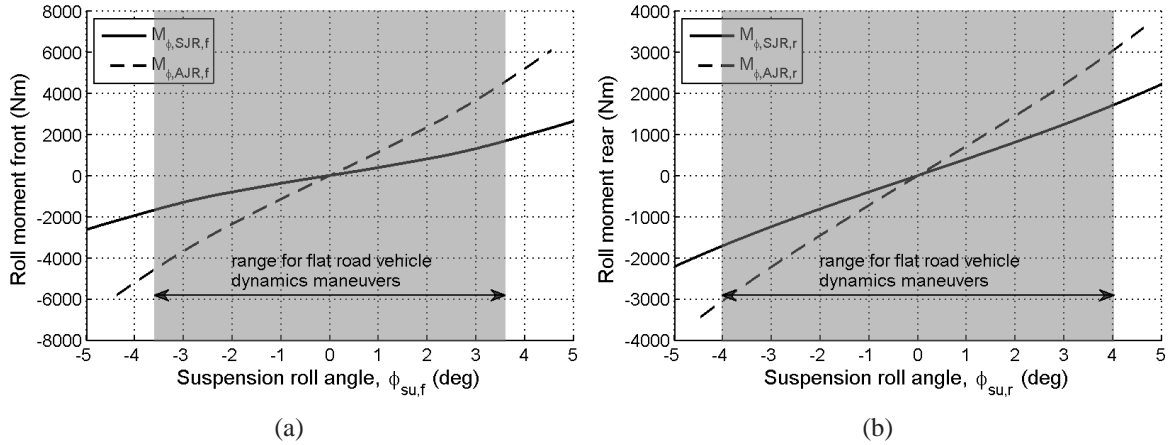


Figure 8.5: Suspension roll moment over suspension roll angle, $M_{\phi,j}(\phi_{su,j})$, from the maneuvers **SJR** and **AJR**; front axle in (a) and rear axle in (b).

Only the roll moment derived from the **AJR** maneuver is required for the roll model in the extended 2-wheel model, i.e.:

$$M_{\phi,j}(\phi_{su,j}) = M_{\phi,AJR,j}(\phi_{su,j}) \quad (8.5)$$

is sufficient for simple simulations. However, in a vehicle without ride height control system (as in most vehicles with coil springs), the suspension will be differently deflected at different loading conditions. Consequently, the initial position on the curve for force over wheel travel in the **SJR** maneuver will be different and therefore also cause a different roll moment characteristics, $M_{\phi,j}(\phi_{su,j})$. This is exemplified in Figure 8.6(a) and 8.6(b).

In addition to this, the anti-roll bar need to be a separate parameter in the extended 2-wheel model in order to enable an anti-roll bar change. Since the extended 2-wheel model should enable extrapolation to different load conditions and varying degrees of anti-roll bar stiffness, the elastic roll moment will be divided in a roll moment from the suspension springs only, here defined as $M_{\phi,SJR,j}(\phi_{su,j})$, since it originates from the **SJR** maneuver, and a roll moment from the anti-roll bar:

$$M_{\phi,j}(\phi_{su,j}) = M_{\phi,SJR,j}(\phi_{su,j}) + C_{\phi,ARB,j}\phi_{su,j} \quad (8.6)$$

The roll moment from the suspension springs is furthermore derived from the force over wheel travel characteristics, $F_{z,SJR,j}(\Delta z_j)$, and will therefore change depending on how the suspension is deflected at different loading conditions, i.e. $F_{z,SJR,f}(\Delta z_f)$ gives $M_{\phi,SJR,f}(\phi_{su,f})$ according to Equation 8.3 and 8.4. The anti-roll bar stiffness, $C_{\phi,ARB,j}$, will be derived from the difference in roll moment between the **AJR** and **SJR** maneuvers, i.e. between $M_{\phi,AJR,j}$ and $M_{\phi,SJR,j}$.

As described in the roll model and illustrated in Figure 7.3, the tire deflection during cornering also contributes to the overall roll angle. The tire radial stiffness, $C_{z,ti}$, can be converted to a tire

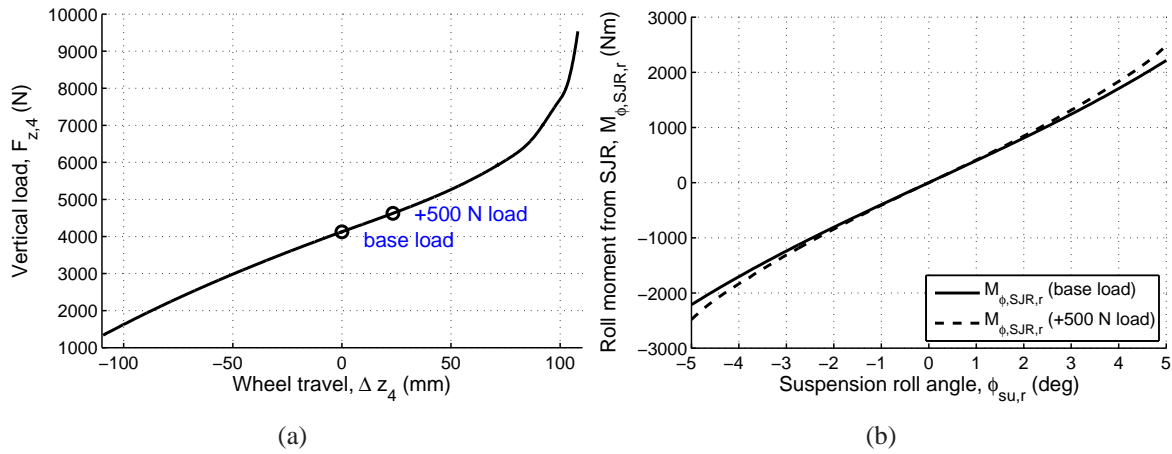


Figure 8.6: In (a) the different starting points when derivating the roll moment characteristics for the two load cases (*base* and *+500N*) and in (b) the resulting roll moments from the **SJR** maneuver, $M_{\phi,SJR,r}(\phi_{su,r})$; here exemplified for the rear axle.

roll stiffness $C_{\phi,ti}$ by:

$$C_{\phi,ti} = \frac{C_{z,ti} \cdot b_j^2}{2} \quad (8.7)$$

Table 8.2 conclude the parameters in the extended 2-wheel model related to the elastic roll moment characteristics.

Look-up table	Shown in Figure:	Unit	Source
$F_{z,SJR,f}(z_f)$	8.4(a)	$N(m)$	Measured on test bench
$F_{z,SJR,r}(z_r)$	8.4(b)	$N(m)$	Measured on test bench
$M_{\phi,SJR,f}(\phi_{su,f})$	8.5(a)	$Nm(deg)$	Derived from other characteristics
$M_{\phi,SJR,r}(\phi_{su,r})$	8.5(b)	$Nm(deg)$	Derived from other characteristics
Parameter	Value	Unit	Source
$C_{ARB,f}$	756.5	Nm/deg	Derived from other characteristics
$C_{ARB,r}$	315.3	Nm/deg	Derived from other characteristics
$C_{\phi,ti,f}$	36310	Nm/deg	Derived from tire parameters
$C_{\phi,ti,r}$	36139	Nm/deg	Derived from tire parameters

Table 8.2: Parameters for elastic roll moment characteristics for *Vehicle A*, described in Section 2.5.

A remark regarding separating the tire roll stiffness The overall axle roll stiffness is given by the suspension roll stiffness, $C_{\phi,su}$, in series with the roll stiffness from the tire radial stiffness, $C_{\phi,ti}$, see Figure 8.7:

$$\frac{1}{C_{\phi}} = \frac{1}{C_{\phi,su}} + \frac{1}{C_{\phi,ti}} \quad (8.8)$$

To exemplify the involvement of the tire deflection in regards to vehicle roll angle, the resulting total roll stiffness of an axle C_{ϕ} is calculated using typical parameters; $b = 1.46 \text{ m}$, $C_{z,ti} = 189 \text{ kN/m}$ and $C_{z,AJR} = 38 \text{ kN/m}$. Equation (8.7) and (8.8) gives a total roll stiffness of 588.2 Nm/deg when including the influence of the tires, and 706.8 Nm/deg when neglecting tire influence, in this case a 20 % difference.

A remark regarding the anti-roll bar stiffness:

Using a roll angle dependent roll stiffness for the anti-roll bar, $C_{\phi,ARB,j}$, is sufficient for the extended 2-wheel model. However, this approach does not exclude the possibility to estimate the torsional stiffness of the anti-roll bar itself. Via the suspension kinematics, the roll stiffness $C_{\phi,ARB}$, can be translated into a pure torsion stiffness of the anti roll bar.

By defining an anti roll bar lever arm l_{ARB} as the distance between the anti roll bar attachment point and the anti roll bar center line, see Figure 8.8, and in addition define $i_{z,ARB}$ as the translation ratio between vertical wheel travel z_{wheel} and vertical displacement of the anti roll bar attachment point z_{ARB} , i.e. $z_{ARB} = i_{z,ARB} \cdot z_{wheel}$, a translation ratio from roll angle to anti roll bar torsion angle can be estimated as:

$$i_{\phi \rightarrow ARB} = \frac{b_j}{i_{z,ARB} \cdot l_{ARB}} \quad (8.9)$$

With the ratio $i_{\phi \rightarrow ARB}$, the axle roll stiffness originating from the anti roll bar $C_{\phi,ARB}$ can be converted to a pure torsion stiffness of the anti roll bar C_{ARB} :

$$C_{ARB} = \frac{C_{\phi,ARB}}{i_{\phi \rightarrow ARB}} \quad (8.10)$$

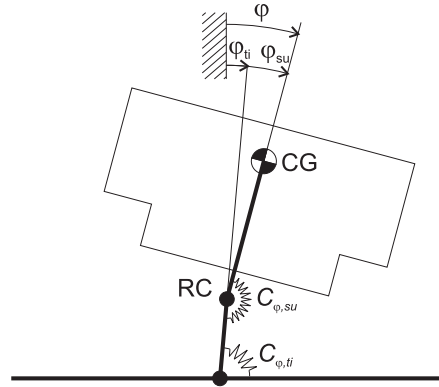


Figure 8.7: Total vehicle roll angle ϕ composed by suspension roll angle ϕ_{su} and roll angle due to vertical tire deflection ϕ_{ti} .

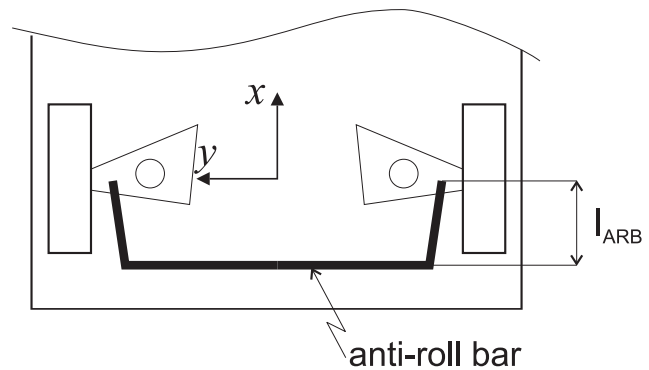


Figure 8.8: Anti roll bar lever arm.

8.3.3 Parameters for the roll damping characteristics

The suspension roll damping characteristics, $M_{\dot{\phi},j}(\dot{\phi}_{su,j})$, can be derived from the shock absorber characteristics, $F_{d,j}(\Delta\dot{z}_j)$ and the suspension kinematics:

$$M_{\dot{\phi},j} = (F_{d,j}(\dot{z}_{d,j}) - F_{d,j}(-\dot{z}_{d,j})) \frac{b_j}{2} i_{d,j} \quad (8.11)$$

$i_{d,j}$ is the damper ratio on the axle j and describes the ratio between wheel travel (when holding the vehicle body fixed) and damper deflection. This ratio can be expressed in a simplified manner as:

$$i_{d,j} = \frac{l_{d,j}}{l_{w,j}} \quad (8.12)$$

where $l_{d,j}$ is the distance between the inner attachment point of the lower control arm and the damper attachment point, see Figure 8.9. $l_{w,j}$ is the distance between the inner attachment point of the lower control arm and the contact point of the wheel. If neglecting body heave motion, the damper velocity (while driving on a flat road) can be approximated as:

$$|\dot{z}_{d,j}| = \underbrace{\dot{\phi} \frac{b_j}{2}}_{\dot{z}_{w,j}} i_{d,j} \quad (8.13)$$

Figure 8.10(a) shows the damping characteristics for the front axle shock absorber in the reference vehicle A and Figure 8.10(b) shows the resulting roll damping characteristics derived using Equation (8.11) to (8.13). The gray box in Figure 8.10(b) defines the suspension roll rate achieved with reference vehicle A during a range of flat road handling maneuvers, i.e. the range relevant for the objective of this vehicle model. Figure 8.11(a) and 8.11(b) show the same characteristics for the rear axle in reference vehicle A. This example shows the difficulty in finding a generalized approximation for the roll damping characteristics. At the rear axle, a linear roll damping approach would be sufficient for vehicle A, whereas the front axle requires a non linear roll damping approach. Since this depends on the shock absorber damping characteristics, the extended 2-wheel model will use a look-up table as in Figure 8.10(b) and 8.11(b).

Table 8.3 sum up the parameters for the roll damping characteristics.

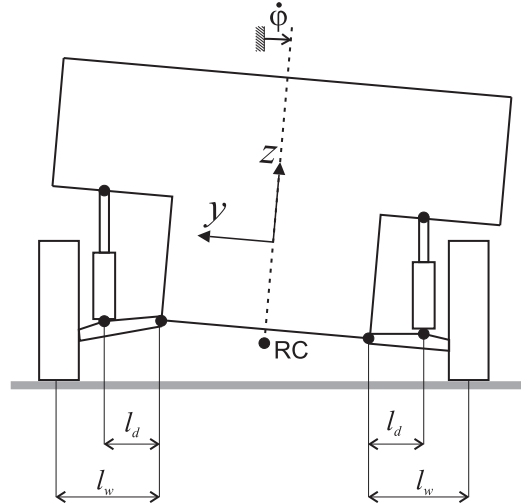


Figure 8.9: Approximated geometry for calculating damping ratio and damper velocities.

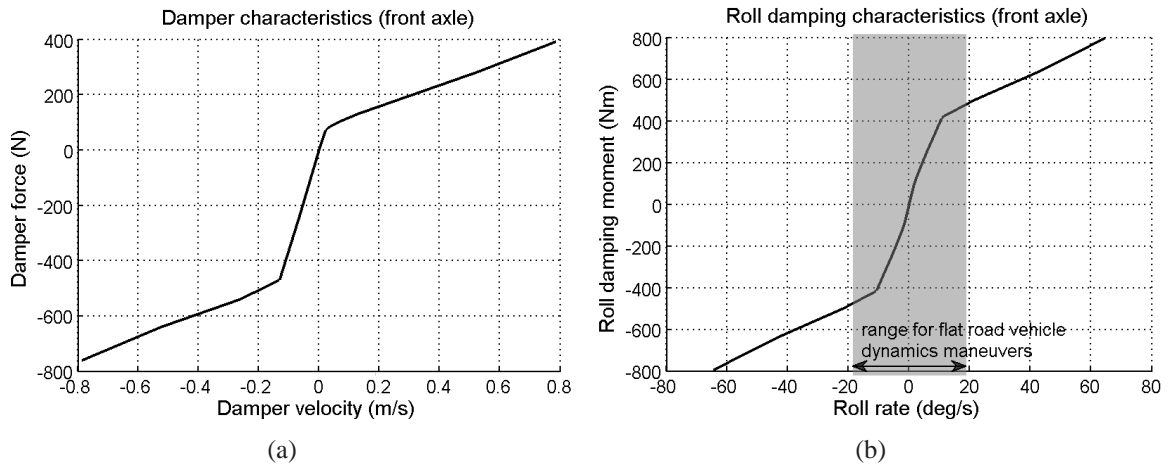


Figure 8.10: In (a) the damping characteristics in the front axle shock absorber and in (b) the resulting roll damping characteristics for the front axle, $M_{\dot{\phi},f}$ (reference vehicle A).

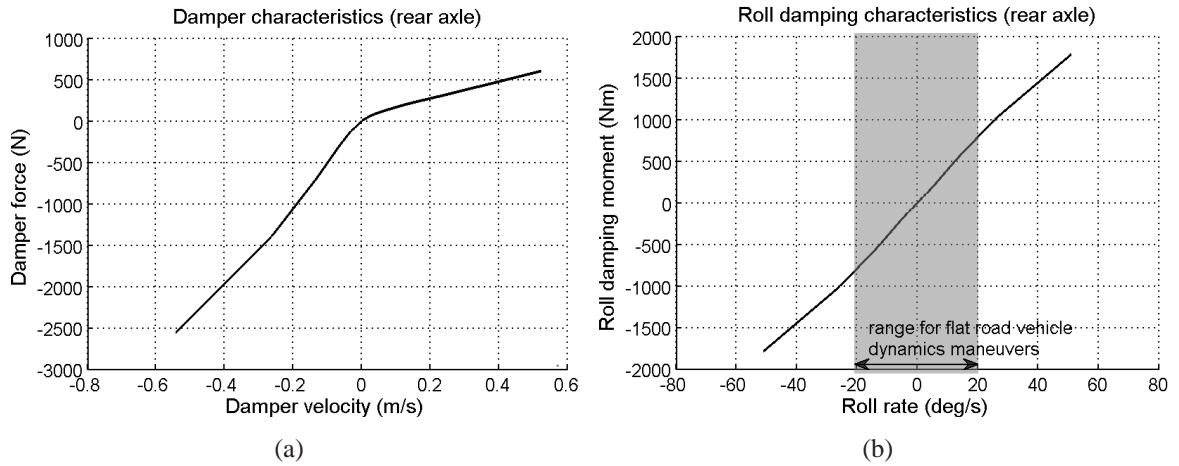


Figure 8.11: In (a) the damping characteristics in the rear axle shock absorber and in (b) the resulting roll damping characteristics for the rear axle, $M_{\dot{\phi},r}$ (reference vehicle A)

Look-up table	Shown in Figure:	Unit	Source
$F_{d,f}(\dot{z}_{d,f})$	8.10(a)	$N(m/s)$	Measured
$F_{d,r}(\dot{z}_{d,r})$	8.11(a)	$N(m/s)$	Measured
$M_{\dot{\phi},f}(\dot{\phi}_{su,f})$	8.10(b)	$Nm(deg/s)$	Derived from damper parameters
$M_{\dot{\phi},r}(\dot{\phi}_{su,r})$	8.11(b)	$Nm(deg/s)$	Derived from damper parameters
Parameter	Value	Unit	Source
$i_{d,f}$	0.95	—	Measured
$i_{d,r}$	0.8	—	Measured

Table 8.3: Parameters for roll damping characteristics for *Vehicle A*, described in Section 2.5.

8.3.4 Parameters for the steer angle approach

A steering test bench is required in order to measure the parameters related directly to steering inputs, e.g. front steer angle as a function of rack input, $\delta_f(y_r)$. In this steering test bench, the front wheels are standing on turntables supported by ball bearings which enables the wheels to turn and slide in the horizontal plane almost frictionless during steering maneuvers. This construction minimizes front axle deformations due to compliance and as a result, the kinematic behavior can be measured more accurately.

Only one measurement on the steering test bench is required here. In this maneuver, the steering wheel angle, δ_D , is turned slowly ($\dot{\delta}_D \approx 20 \text{ deg/s}$) all the way to the left limit stop, then back to the right limit stop and finally back to the straight ahead position. At the same time, the steering rack position, y_r ; the front steer angles, δ_i ; and the tire camber angles, γ_i , are measured.

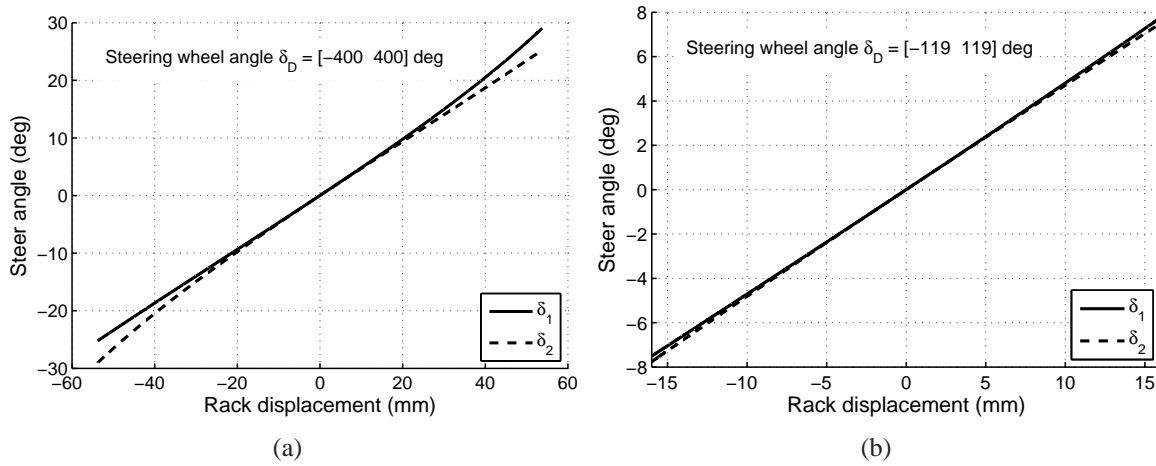


Figure 8.12: In (a) the front steer angles δ_1 and δ_2 in relation to the rack displacement y_r (reference vehicle A). Note that the characteristics for δ_1 is symmetric to origin with δ_2 . (b) shows a zoom of (a) with rack displacements corresponding to steering wheel inputs reached during normal handling maneuvers, i.e. $\delta_D = [-120 \ 120]$.

Figure 8.12 shows the resulting front steer angle characteristics as a function of steering rack position, $\delta_f(y_r)$, which here will be approximated with a sixth degree polynomial. The polynomial coefficient describing the offset at zero steering rack input, p_{7,δ_y} , will here always be zero since this steer angle is considered by the static steer angle, $\delta_{0,f}$. Table 8.4 lists the polynomial coefficients for the characteristics shown in Figure 8.12.

$$\delta_f(y_r) = \sum_{i=1}^7 p_{i,\delta_y} \cdot y_r^{7-i} \quad (8.14)$$

The static steer angles, $\delta_{0,j}$, and the roll steer characteristics, $\delta_{\varphi,j}(\varphi_{su,j})$, are extracted from the **AJR** maneuver. As can be seen in Figure 8.13(a), the steer angle change over suspension deflection is different in the **SJR** maneuver than in the **AJR** maneuver. Due to the vertical force required to compress the suspension springs, neither of the two maneuvers will provide the true kinematic suspension characteristics – it will always be a mix of kinematics and compliance. However, more or less the same vertical forces will act on the suspension during vehicle roll

as in the **AJR** maneuver. In addition to this, roll steer describes the steer angle change due to vehicle roll which is not necessarily defined to be a strictly kinematic occurrence. Consequently, the roll steering characteristics obtained with the **AJR** maneuver will here be used to define the sought after roll steer characteristics $\delta_{\phi,j}(\phi_{su,j})$, see Figure 8.13(b).

Analogously, Figure 8.14 show the rear axle steering characteristics. The difference between the **SJR** and the **AJR** maneuver is not as apparent on the rear axle as on the front axle due to the stiffer rear axle design. In this case, the rear axle has a more symmetric roll steering behavior than on the front axle, i.e. the steer angle change in jounce and rebound are quite similar. This highly depends on the suspension design and it can therefore not be concluded that the rear axle always has a linear roll steer characteristics.

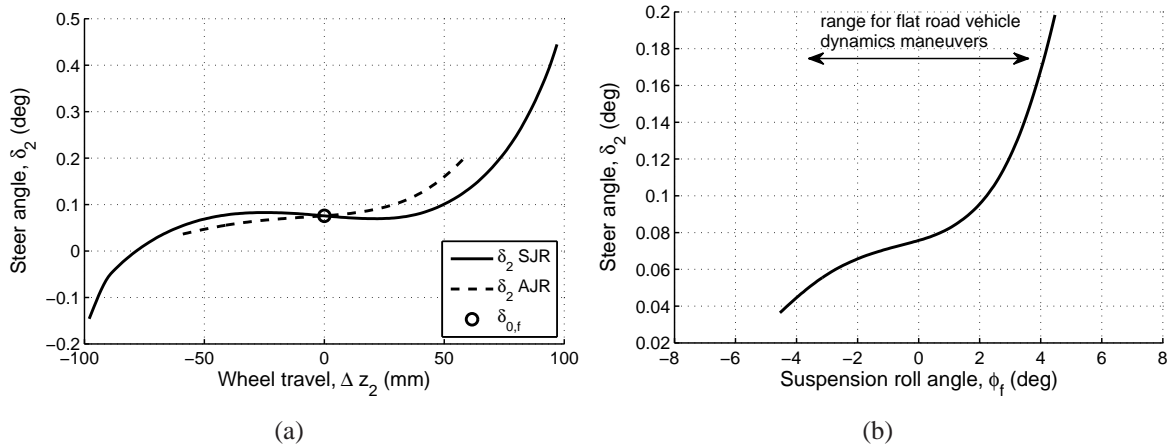


Figure 8.13: Front axle steering characteristics. In (a) the steer angle change over suspension deflection and in (b) the corresponding roll steer characteristics, $\delta_{\phi,f}(\phi_{su,f})$.

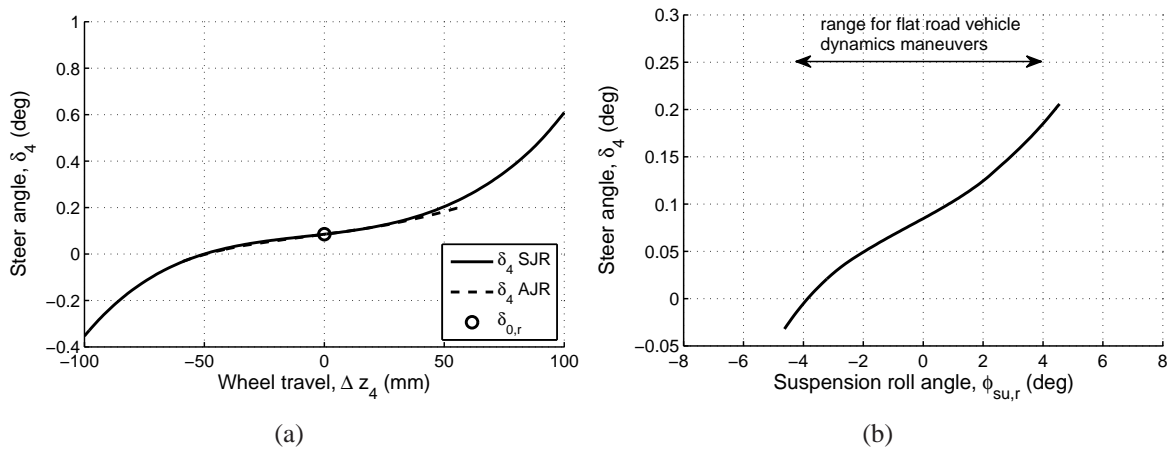


Figure 8.14: Rear axle steering characteristics. In (a) the steer angle change over suspension deflection and in (b) the corresponding roll steer characteristics, $\delta_{\phi,r}(\phi_{su,r})$.

Steer angle change due to lateral tire forces and moments is the final part to be identified in the steer angle approach. This could also be measured at a suspension test bench but would require a more complex test procedure than provided in the **SJR/AJR** maneuvers. Due to

this, the parameters for the compliance steer approach, $l_{\delta,j}$ and $C_{\delta,j}$, will be found through the identification process described in Subsection 8.3.6.

Parameter	Value	Unit	Source
$\delta_f(y_r)$	Polynomial	$deg(mm)$	Measured on test bench
p_{1,δ_y}	$-7.9559 \cdot 10^{-12}$		
p_{2,δ_y}	$8.4128 \cdot 10^{-10}$		
p_{3,δ_y}	$-3.7393 \cdot 10^{-8}$		
p_{4,δ_y}	$7.7893 \cdot 10^{-6}$		
p_{5,δ_y}	$-4.8379 \cdot 10^{-4}$		
p_{6,δ_y}	0.4750		
p_{7,δ_y}	0		
$\delta_{0,f}$	0.0757	deg	Measured on test bench
$\delta_{0,r}$	0.0846	deg	Measured on test bench
$\delta_{\varphi,f}(\varphi_{su,f})$	Polynomial	$deg(deg)$	Measured on test bench
$p_{1,\delta_{\varphi,f}}$	$5.5387 \cdot 10^{-5}$		
$p_{2,\delta_{\varphi,f}}$	$6.6425 \cdot 10^{-4}$		
$p_{3,\delta_{\varphi,f}}$	0.0010		
$p_{4,\delta_{\varphi,f}}$	0.0048		
$p_{5,\delta_{\varphi,f}}$	0		
$\delta_{\varphi,r}(\varphi_{su,r})$	Polynomial	$deg(deg)$	Measured on test bench
$p_{1,\delta_{\varphi,r}}$	$-2.9546 \cdot 10^{-5}$		
$p_{2,\delta_{\varphi,r}}$	$4.1039 \cdot 10^{-4}$		
$p_{3,\delta_{\varphi,r}}$	$8.2130 \cdot 10^{-4}$		
$p_{4,\delta_{\varphi,r}}$	0.0172		
$p_{5,\delta_{\varphi,r}}$	0		
$l_{\delta,f}$	0.087	m	Identified in Subsection 8.3.6
$l_{\delta,r}$	-0.170	m	Identified in Subsection 8.3.6
$C_{\delta,f}$	527	deg/Nm	Identified in Subsection 8.3.6
$C_{\delta,r}$	3370	deg/Nm	Identified in Subsection 8.3.6

Table 8.4: Parameters for the steer angle approach for *Vehicle A*, described in Section 2.5.

8.3.5 Parameters for the tire camber angle approach

Vehicle steering inputs also influence the tire camber angles and they are described in the suspension-tire model by a function depending on steering rack position. Figure 8.15 shows the tire camber angle as a function of rack input, $\gamma_{\delta,f}(y_r)$, resulting from the steering test bench maneuver described in Subsection 8.3.4. A linear approach is here applied to capture the camber angle change depending on steering rack position, $\gamma_{\delta,f}(y_r) = k_{\gamma,y_r} y_r$. This is sufficient since

the camber angle change is fairly linear within the range relevant for handling maneuvers on a flat road, see Figure 8.15(b), and since the lateral tire forces generated from tire camber angles are small in relation to the lateral forces due to side slip angle, α .

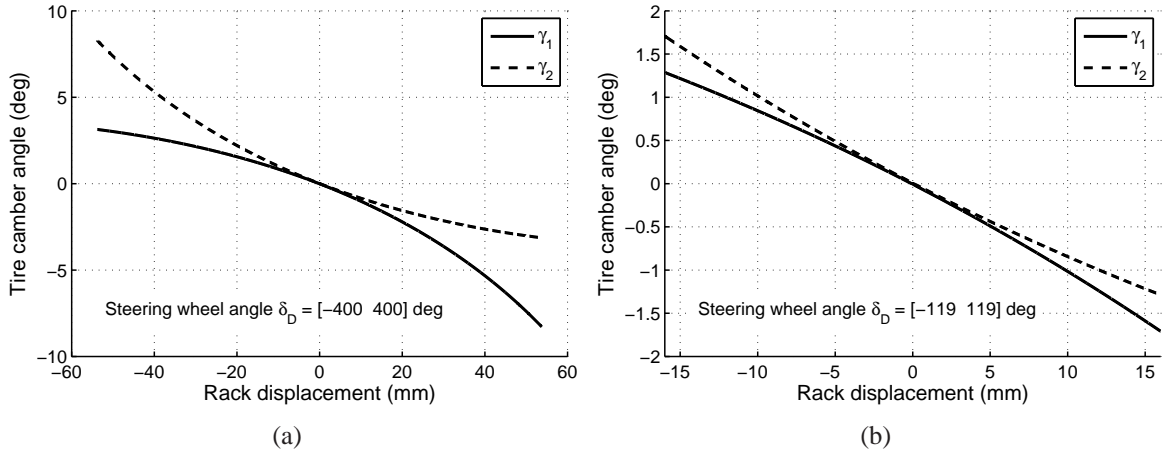


Figure 8.15: In (a) the tire camber angles at the front axle, γ_1 and γ_2 , in relation to the rack displacement y_r (reference vehicle A). (b) shows a zoom of (a) capturing rack displacements corresponding to steering wheel inputs reached during normal handling maneuvers, i.e. $\delta_D = [-120 \ 120]$.

Figure 8.16(a) and 8.17(a) show the suspension camber angle change due to suspension deflection for the front and rear axle. The static camber angles, $\epsilon_{0,j}$, are parameterized from the suspension camber angle at zero suspension deflection. With the same arguments as for the roll steer approach, the **AJR** maneuver is used when calculating the tire camber angle as a function of suspension roll angle, $\gamma_i(\phi_{su,j})$. For this calculation, the relation between vehicle roll angle, ϕ ; suspension camber angle, ϵ_i ; and tire camber angle γ_i , as illustrated in Figure 7.15 and defined in Equation (7.34) to (7.35), has been applied. Figure 8.16(b) and 8.17(b) show the resulting tire camber angle as a function of suspension roll angle, $\phi_{su,j}$.

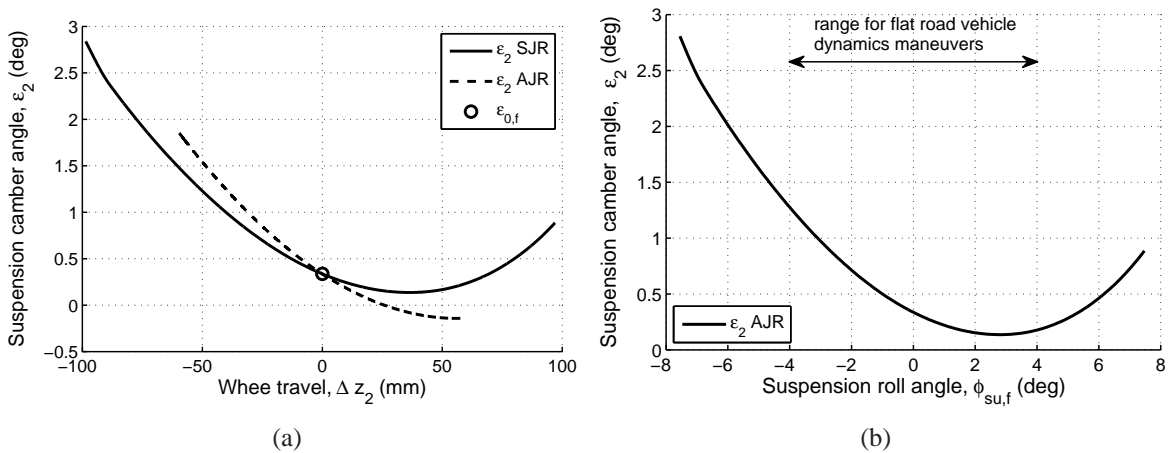


Figure 8.16: In (a) the front right suspension camber angle as a function of wheel travel, $\epsilon_2(\Delta z_2)$, during the maneuvers **SJR** and **AJR**. In (b) the resulting tire camber angle as a function of suspension roll angle, $\gamma_2(\phi_{su,f})$, derived from the **AJR** maneuver.

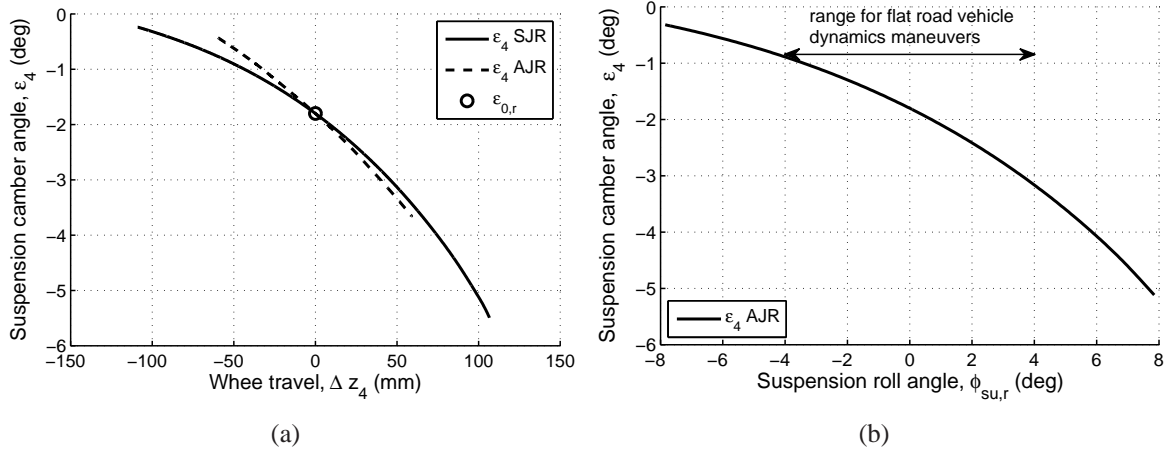


Figure 8.17: In (a) the rear right suspension camber angle as a function of wheel travel, $\varepsilon_4(\Delta z_4)$, during the maneuvers **SJR** and **AJR**. In (b) the resulting tire camber angle as a function of suspension roll angle, $\gamma_4(\phi_{su,r})$, derived from the **AJR** maneuver.

Parameter	Value	Unit	Source
$k_{\gamma,f}$	0.092	deg/mm	Measured on test bench
$\varepsilon_{0,f}$	0.34	deg	Measured on test bench
$\varepsilon_{0,r}$	-1.8	deg	Measured on test bench
$\gamma_{\delta,f}(y_r)$	Polynomial	deg(mm)	Measured on test bench
p_{1,γ_y}	$-4.8193 \cdot 10^{-6}$		
p_{2,γ_y}	$8.7092 \cdot 10^{-4}$		
p_{3,γ_y}	-0.0919		
p_{4,γ_y}	0		
$\varepsilon_{\phi,f}(\phi_{su,f})$	Polynomial	deg(deg)	Measured on test bench
$p_{1,\varepsilon_{\phi,f}}$	0.0246		
$p_{2,\varepsilon_{\phi,f}}$	-0.2178		
$p_{3,\varepsilon_{\phi,f}}$	0		
$\varepsilon_{\phi,r}(\phi_{su,r})$	Polynomial	deg(deg)	Measured on test bench
$p_{1,\varepsilon_{\phi,r}}$	-0.0116		
$p_{2,\varepsilon_{\phi,r}}$	-0.3458		
$p_{3,\varepsilon_{\phi,r}}$	0		

Table 8.5: Parameters for the tire camber angle approach for *Vehicle A*, described in Section 2.5.

8.3.6 Identification process

Tables 8.1 to 8.5 list 9 parameters difficult to measure; Δh , J_ψ , $J_{\phi,s}$, $h_{RC,f}$, $h_{RC,r}$, $l_{\delta,f}$, $l_{\delta,r}$, $C_{\delta,f}$ and $C_{\delta,r}$. These parameters, which here will be referred to as the **par**-vector, will be identified using an optimization tool with the objective of getting the extended 2-wheel model to simulate the same vehicle behavior as the reference simulations with the CASCaDE-DA model. Section 8.1 already described the driving maneuver used when generating the virtual measurements with the CASCaDE-DA model. Subsequently, the extended 2-wheel model will be simulated using (as model inputs) the same steering rack position, y_r , and longitudinal velocity, v_x , as measured in the virtual measurements with the CASCaDE-DA model. The objective in the optimization process is to minimize the function $G(\mathbf{par})$:

$$\min_{\mathbf{par}} G(\mathbf{par}) = \min_{\mathbf{par}} \begin{bmatrix} (a_{y,ref} - a_{y,mod})W_{ay} \\ (\dot{\psi}_{ref} - \dot{\psi}_{mod})W_{\dot{\psi}} \\ (\beta_{ref} - \beta_{mod})W_{\beta} \\ (\phi_{ref} - \phi_{mod})W_{\phi} \end{bmatrix} \quad (8.15)$$

where the index \square_{ref} refers to the reference model and the index \square_{mod} to the extended 2-wheel model. Hence, the difference in lateral acceleration, a_y ; yaw rate, $\dot{\psi}$; vehicle side slip angle, β ; and vehicle roll angle, ϕ , form the objective function for the optimization tool when finding the optimal **par**-vector. The resulting differences are furthermore weighted with the weighing factors W_{ay} , $W_{\dot{\psi}}$, W_{β} and W_{ϕ} , which have been chosen to normalize the different outputs with the respective maximum value from the virtual measurement. Hence, the weight factors are defined as:

$$W_{ay} = \max(|a_{y,ref}|) \quad (8.16)$$

$$W_{\dot{\psi}} = \max(|\dot{\psi}_{ref}|) \quad (8.17)$$

$$W_{\beta} = \max(|\beta_{ref}|) \quad (8.18)$$

$$W_{\phi} = \max(|\phi_{ref}|) \quad (8.19)$$

This is done since the different simulation outputs are of different magnitude and in this way, the difference of all objectives will be considered equally in the optimization process.

The optimization tool *lsqnonlin* from The MathWorks, Inc. has been used here, which makes use of Gauss-Newton and Levenberg-Marquardt methods for nonlinear least-squares optimization [33]. The use of such methods has already been discussed by Kobetz [20] and a detailed description of these methods is therefore left out here. The start values and the resulting end values are listed in Table 8.6.

Parameter	Start value	End value	Unit
Δh	0.5	0.54	<i>m</i>
J_Ψ	2500	2708	<i>kgm²</i>
$J_{\varphi,s}$	500	486	<i>kgm²</i>
$h_{RC,f}$	0.05	0.011	<i>m</i>
$h_{RC,r}$	0.05	0.075	<i>m</i>
$l_{\delta,f}$	0.1	0.087	<i>m</i>
$l_{\delta,r}$	-0.1	-0.143	<i>m</i>
$C_{\delta,f}$	1000	556	<i>Nm/deg</i>
$C_{\delta,r}$	1000	2528	<i>Nm/deg</i>

Table 8.6: Start and end values in the optimization process.

8.4 Resulting accuracy

The upper part of Figures 8.18 to 8.21 display the simulation outputs lateral acceleration a_y , yaw rate $\dot{\Psi}$, side slip angle β and vehicle roll angle φ , generated with the reference model CASCaDE-DA and the extended 2-wheel model after the identification process. The lower part of the figures furthermore show the corresponding difference between the reference model CASCaDE-DA and the extended 2-wheel model, displayed in percent of the maximum values $a_{y,max}$, $\dot{\Psi}_{max}$, β_{max} and φ_{max} respectively, see Table 8.7. This way of presenting the model accuracy has been chosen since the differences between the two models are too small to be recognized without presenting numerous figures zoomed in on different driving states. A more thorough examination of the differences between the extended 2-wheel model and the reference model CASCaDE-DA is provided in Chapter 9.

When observing the figures presenting the difference between the models, it is easy to see that the steady-state cornering behavior is captured very good and that the most errors occur in the transients. Especially the oscillating transients, i.e. during the steering angle sweep, is challenging for the extended 2-wheel model. Quite surprisingly, the extended 2-wheel model even captures the steady-state behavior at high lateral accelerations better than the oscillating transients at medium lateral accelerations. Only for the vehicle side slip angle the largest error occurs at the step steer input where the lateral acceleration reaches about 7 m/s^2 , but also here the error occurs during the transient part of the maneuver.

Table 8.7 presents the statistical difference between the outputs of the extended 2-wheel model and the reference model CASCaDE-DA. The root mean square error (RMS) is defined as (here exemplified for the lateral acceleration):

$$e_{RMS} = \sqrt{\frac{\sum_{i=1}^n (a_{y,ref,i} - a_{y,mod,i})^2}{n}} \quad (8.20)$$

where n is the total amount of samples i .

	Max value	Mean. diff. in % of max value	Max. diff. in % of max value	RMS differ- ence	Max. absolute difference
a_y	7.38 m/s^2	0.75 %	4.48 %	0.09 m/s^2	0.33 m/s^2
$\dot{\psi}$	28.87 deg/s	0.45 %	2.86 %	0.22 deg/s	0.81 deg/s
β	4.05 deg	0.64 %	4.53 %	0.04 deg	0.18 deg
φ	4.87 deg	0.56 %	3.32 %	0.04 deg	0.16 deg

Table 8.7: Root mean square (RMS) error and maximum error listed for the model outputs during the verification maneuver.

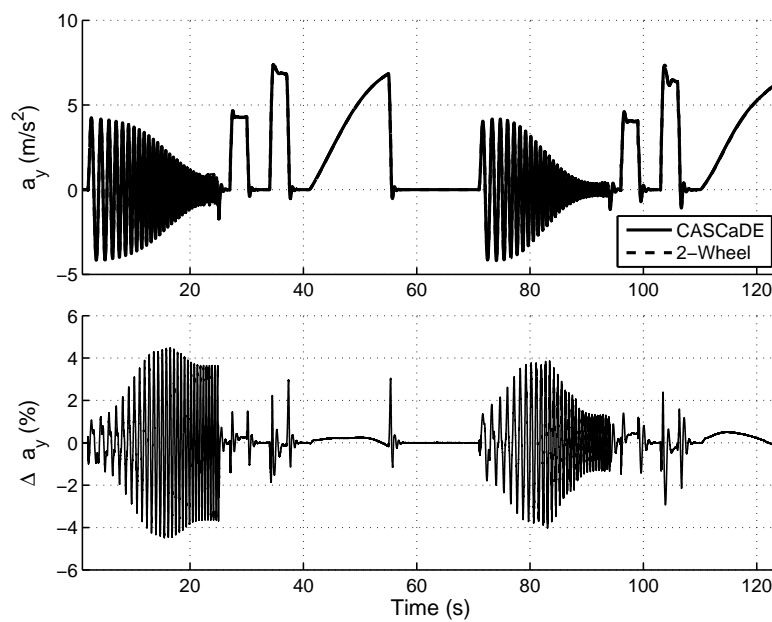


Figure 8.18: Lateral acceleration a_y in comparison between the CASCaDE model (solid line) and the extended 2-wheel model (dashed line) together with the corresponding proportional difference in relation to the maximum lateral acceleration, $a_{y,max}$.

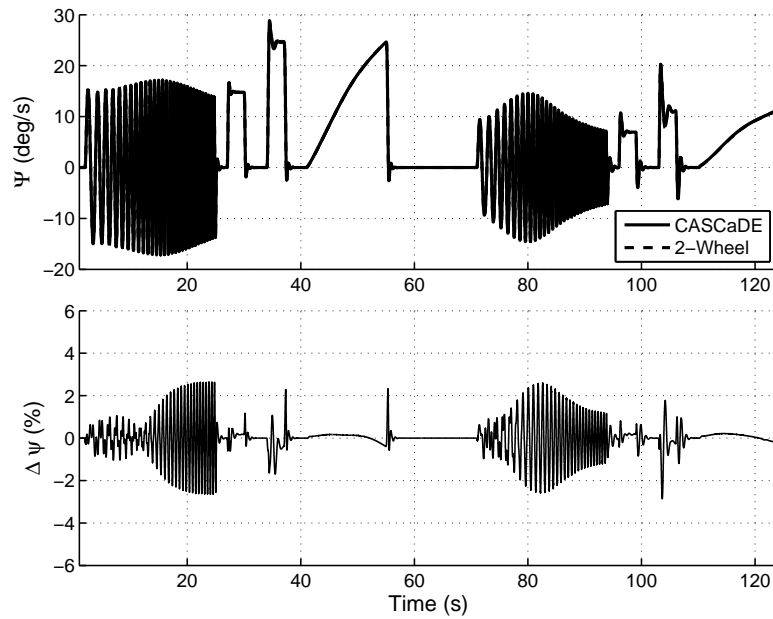


Figure 8.19: Yaw rate Ψ in comparison between the CASCaDE model (solid line) and the extended 2-wheel model (dashed line) together with the corresponding proportional difference in relation to the maximum yaw rate, Ψ_{max} .

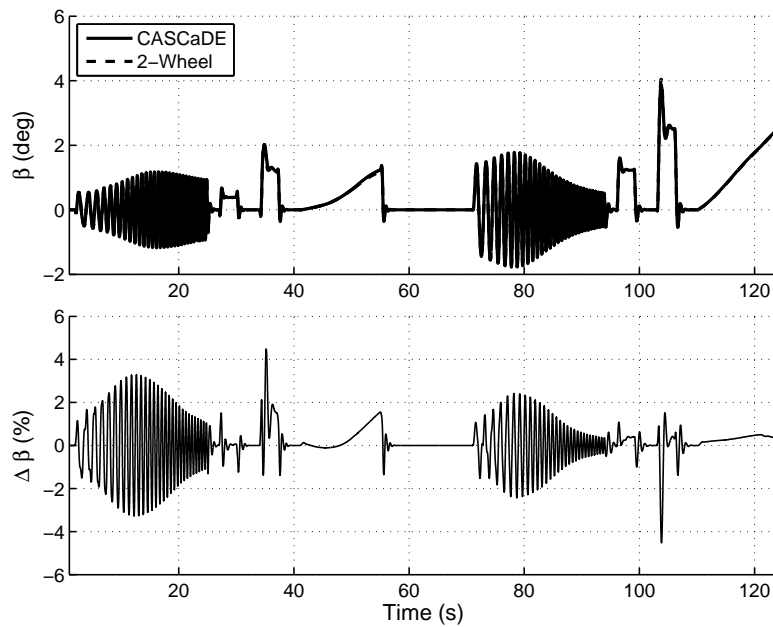


Figure 8.20: Vehicle side slip angle β in comparison between the CASCaDE model (solid line) and the extended 2-wheel model (dashed line) together with the corresponding proportional difference in relation to the maximum side slip angle β_{max} .

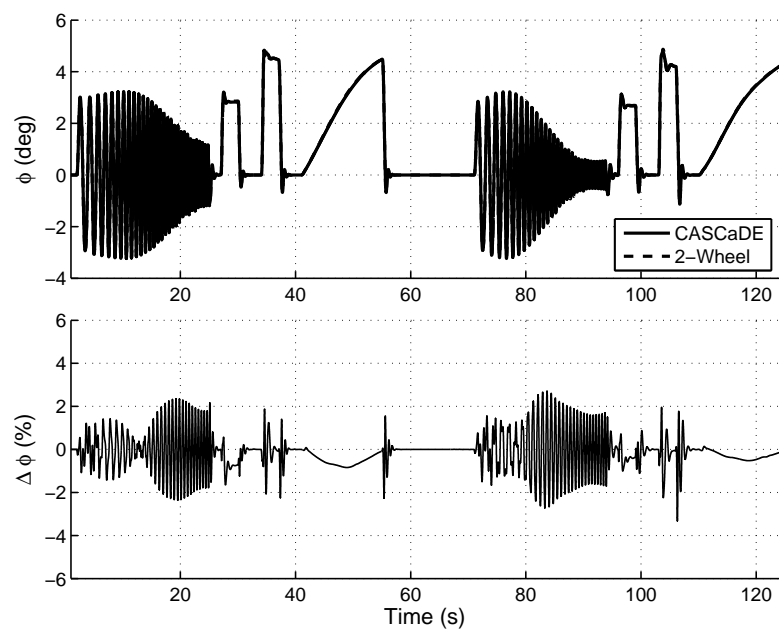


Figure 8.21: Roll angle ϕ in comparison between the CASCaDE model (solid line) and the extended 2-wheel model (dashed line) together with the corresponding proportional difference in relation to the maximum vehicle roll angle ϕ_{max} .

Chapter 9

The extended 2-wheel model – model verification

The performance of the extended 2-wheel model developed in Chapter 7 will be evaluated in this chapter using a verification maneuver. As in the identification process, the same tire parameters are used in both the extended 2-wheel model and the reference simulations with CASCaDE-DA. The tire model behavior has already been presented in Section 8.2. The model parameters for the extended 2-wheel model are the same as extracted in the identification process in Chapter 8.

9.1 The verification maneuver

As discussed in Chapter 8, the simulation model has to be able to simulate an accurate vehicle behavior in all possible lateral motion states and at different longitudinal velocities. However, showing simulation results for all these different driving states would be too much for this investigation and the step steer input maneuver has been chosen as the verification maneuver. This maneuver includes transient and steady-state steering inputs as well as a part where the oscillations are dying out inbetween. To cover the whole range of possible lateral accelerations, the step steer maneuver is driven with six different steering wheel amplitudes $\delta = 15, 30, 45, 60, 75$ and 90 degrees at a velocity of 80 km/h .

The inputs longitudinal velocity and rack displacement in the identification maneuver are exemplified in Figure 9.1. In this example, the maximum rack displacement corresponds to a 90 degree steering wheel input which is reached at a maximum steering wheel rate of 600 degrees per second. The longitudinal velocity in the reference simulations is kept constant as far as possible by controlling the throttle position with a PID-controller. Due to the additional resistance during cornering, the throttle position has to be adjusted during the maneuver. However, too much throttle position is also not good since the longitudinal tire forces effect the steering behavior of the vehicle and the investigations presented here foremost deal with the lateral dynamics. Hence, the tuning of the controller is a compromise between keeping a constant velocity and not introducing too much longitudinal dynamics.

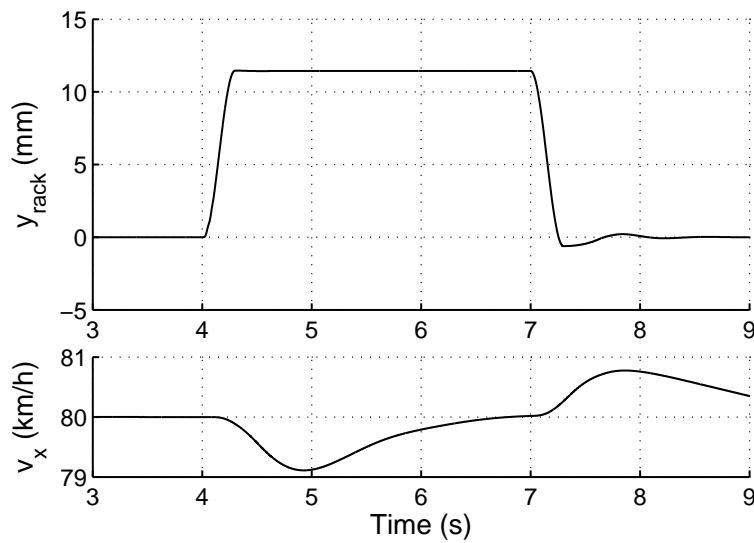


Figure 9.1: Rack displacement and longitudinal velocity during the verification maneuver. The maximum value of the rack displacement in this figure corresponds to a steering wheel amplitude of $\delta_H = 90$ degrees and the target longitudinal velocity is 80 km/h.

9.2 Simulation results

Figure 9.2 and 9.3 show comparisons of the vehicle motion states lateral acceleration, a_y ; yaw rate, $\dot{\psi}$; vehicle side slip angle, β ; and vehicle roll angle, ϕ ; calculated by the reference model and the extended 2-wheel model while simulating the verification maneuver with the steering wheel angle amplitudes $\delta = 15, 30, 45, 60, 75$ and 90 degrees at a constant velocity of 80 km/h.

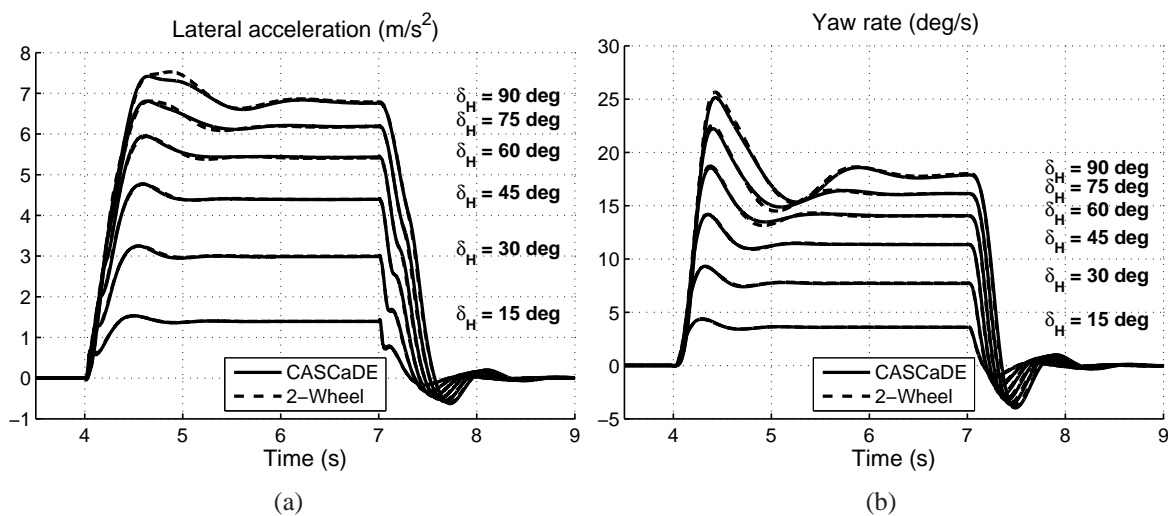


Figure 9.2: Comparison between the CASCaDE model (solid line) and the extended 2-wheel model (dashed line). In (a) lateral acceleration a_y and in (b) yaw rate $\dot{\psi}$.

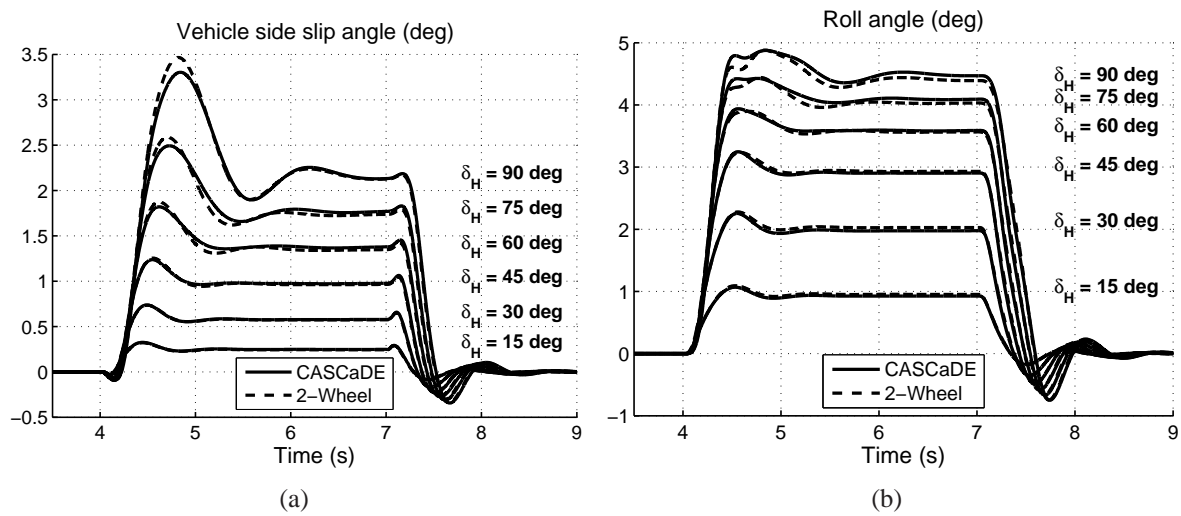


Figure 9.3: Comparison between the CASCaDE model (solid line) and the extended 2-wheel model (dashed line). In (a) vehicle side slip angle β and in (b) vehicle roll angle ϕ .

The results in Figure 9.2 and 9.3 will be further analyzed but for clarity, only the results for the steering wheel angle amplitudes $\delta = 45$ and 90 degrees will be observed. Figure 9.4(a) show the resulting lateral acceleration a_y followed by a zoomed in view in Figure 9.4(b). Figure 9.5 to 9.7 follow the same pattern with a zoomed view in (b) when analyzing the yaw rate ψ , the vehicle side slip angle β and the vehicle roll angle ϕ .

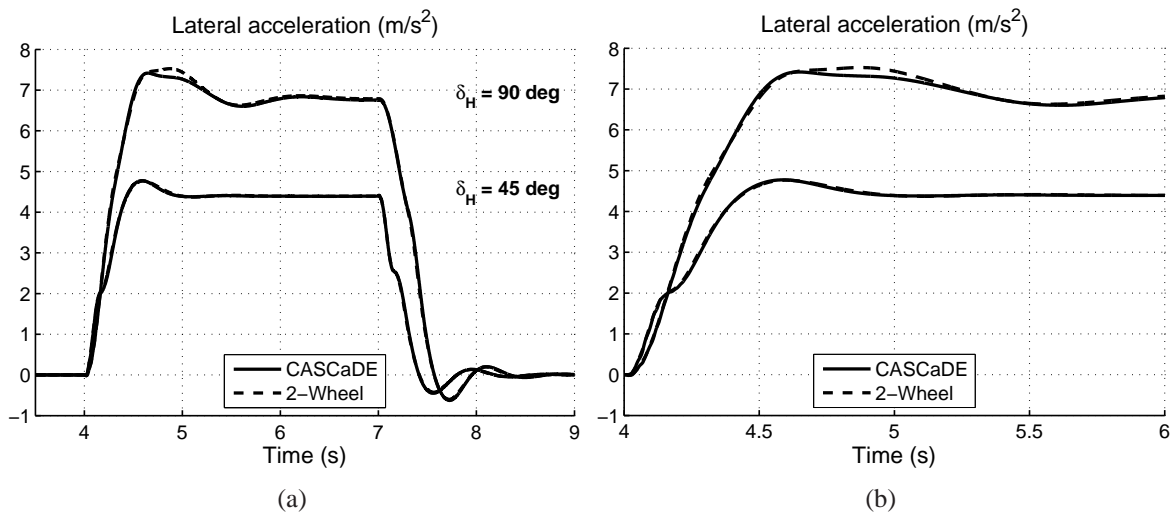


Figure 9.4: Comparison between the CASCaDE model (solid line) and the extended 2-wheel model (dashed line). In (a) lateral acceleration a_y and in (b) a zoomed view of the figure in (a).

The extended 2-wheel model captures the behavior of the reference vehicle except for a difference in the lateral acceleration for a short time period during the transient part in the maneuver driven with a steering wheel angle amplitude of 90 degrees. The occurring difference of approximately $0.2 m/s^2$ can be explained by the simplified vehicle roll model used in the extended 2-wheel model which amongst other simplifications neglects the body heave motion that occur

during severe lateral maneuvers. The difference in roll angle at the very same point in time supports this explanation, see Figure 9.7.

The vehicle side slip angle also shows a small difference during the same time period as the difference seen in the lateral acceleration, see Figure 9.6. This difference is a consequence of the error in lateral acceleration (the vehicle side slip angle is calculated from the vehicle lateral velocity which is a product of the lateral acceleration).

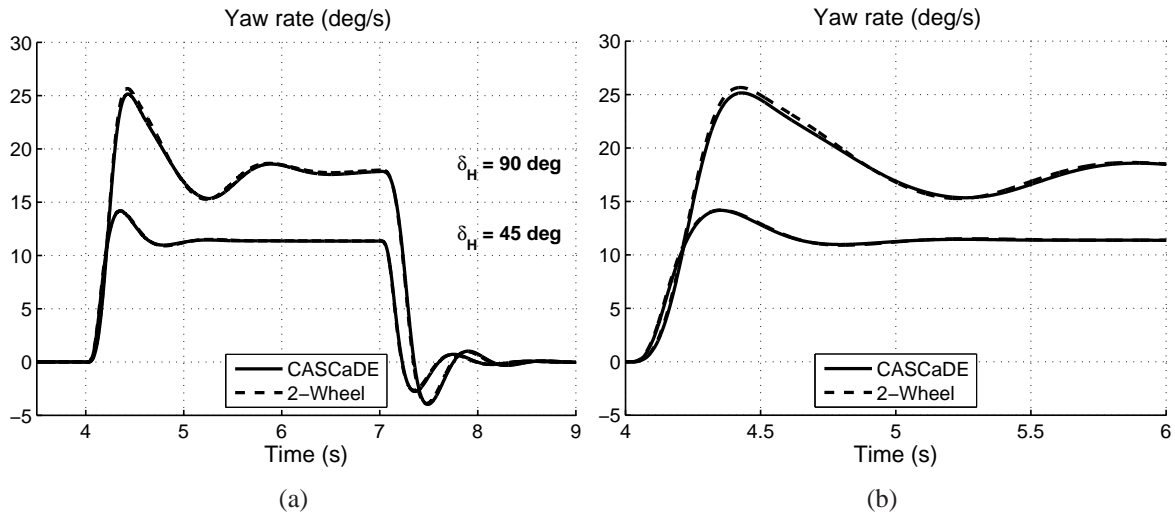


Figure 9.5: Comparison between the CASCaDE model (solid line) and the extended 2-wheel model (dashed line). In (a) yaw rate ψ and in (b) a zoomed view of the figure in (a).

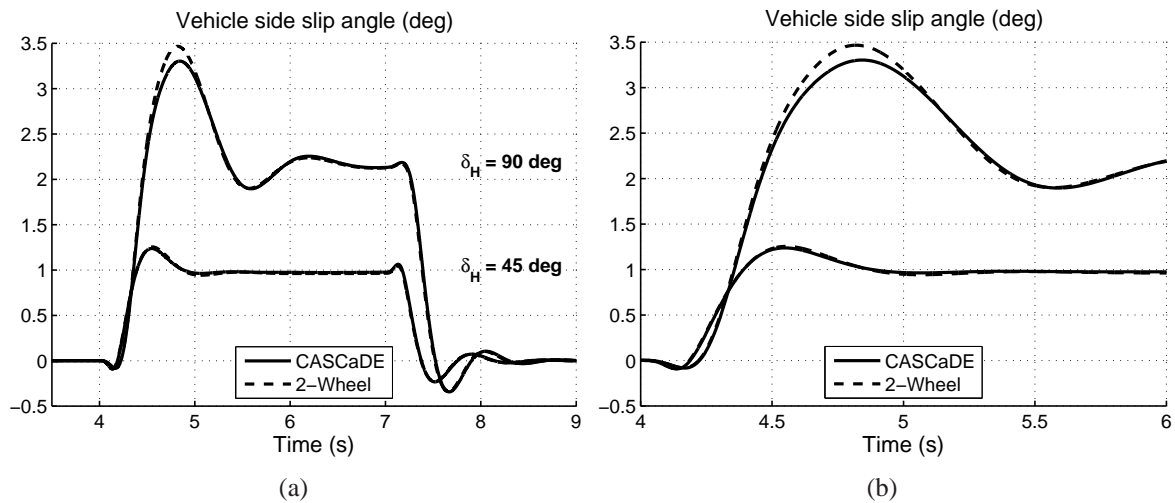


Figure 9.6: Comparison between the CASCaDE model (solid line) and the extended 2-wheel model (dashed line). In (a) vehicle side slip angle β and in (b) a zoomed view of the figure in (a).

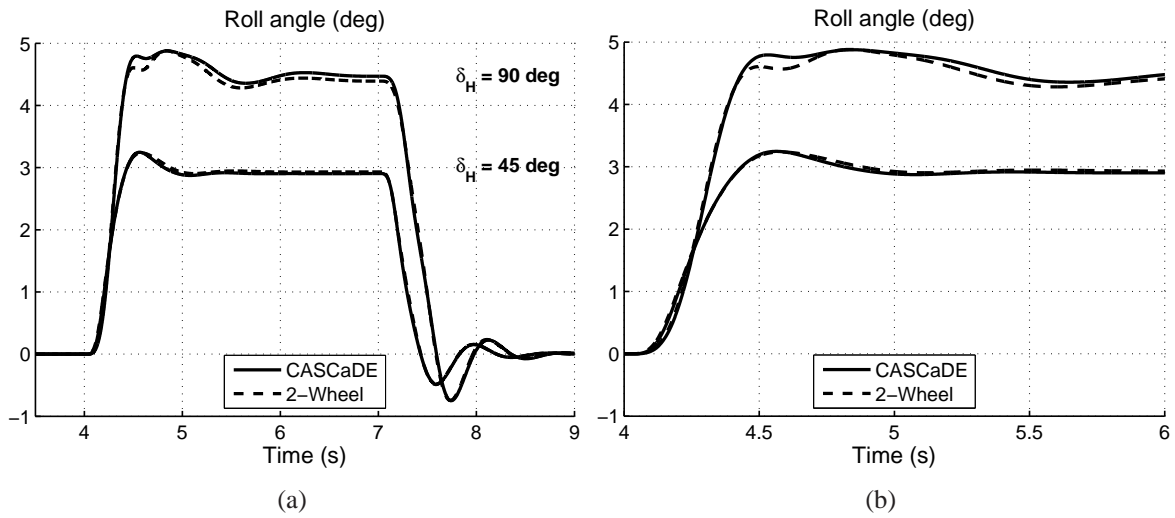


Figure 9.7: Comparison between the CASCaDE model (solid line) and the extended 2-wheel model (dashed line). In (a) vehicle roll angle ϕ and in (b) a zoomed view of the figure in (a).

A summary of the resulting model accuracy can be found in Table 9.1 where the root mean square (RMS) error (between 4 and 8.5 s) and the maximum error is listed for the lateral acceleration a_y , yaw rate $\dot{\psi}$, vehicle side slip angle β and vehicle roll angle ϕ during the verification maneuver. In this case, all steer angle amplitudes are represented.

$\hat{\delta}_H$ (deg)	a_y (m/s^2)		$\dot{\psi}$ (deg/s)		β (deg)		ϕ (deg)	
	RMS	max.	RMS	max.	RMS	max.	RMS	max.
90	0.058	0.18	0.179	0.56	0.034	0.11	0.036	0.13
75	0.041	0.16	0.127	0.45	0.029	0.10	0.027	0.10
60	0.035	0.13	0.077	0.37	0.019	0.05	0.025	0.09
45	0.031	0.11	0.064	0.29	0.011	0.04	0.025	0.07
30	0.027	0.10	0.058	0.22	0.007	0.03	0.018	0.04
15	0.019	0.14	0.041	0.14	0.004	0.02	0.008	0.02

Table 9.1: Root mean square (RMS) error and absolute value of the maximum error listed for the model outputs during the verification maneuver.

The model accuracy reached with the extended 2-wheel model can be considered very good. Although, state of the art measurement equipment would be accurate enough to measure the maximum differences occurring between these models, disturbance factors like for instance road roughness would (even on the best test track) cause larger oscillations in the motion outputs than the differences seen here. Figure 4.7 and 4.6 exemplifies this as well.

9.3 Test-to-test variation in real vehicle testing

In Section 9.2 the model accuracy was demonstrated using figures, RMS errors and maximum errors. To put the achieved model accuracy into perspective, this section examines measurements from vehicle dynamics tests. The vehicle measured here is not the same vehicle as being simulated in the previous section. However, the main purpose is to show the test-to-test variation in vehicle response in order to better grasp the meaning of the presented model accuracy.

In order to drive the vehicle the same way (as close as possible) in each test, the so called *controlled automated driving* was applied, where a path-controlled vehicle is driven along a specified path and is able to repeatedly perform the same step-steer maneuver at the same position. To realize this, actuators to control steering, brake and throttle have been installed in the test vehicle and an Inertial Measuring Unit (IMU) backed up by a Differential Global Position System (DGPS) make sure to drive the vehicle along a pre-defined path with an accuracy of ± 2 cm, [49]. Figure 9.8 shows the implementation of the driving robot in the test vehicle. This is one of the best technologies known today regarding precise driving with excellent repeatability and has been developed by Daimler AG in a cooperation project with Anthony Best Dynamics (ABD) and TU-Graz. More about this technology can be found in [16] and [49].

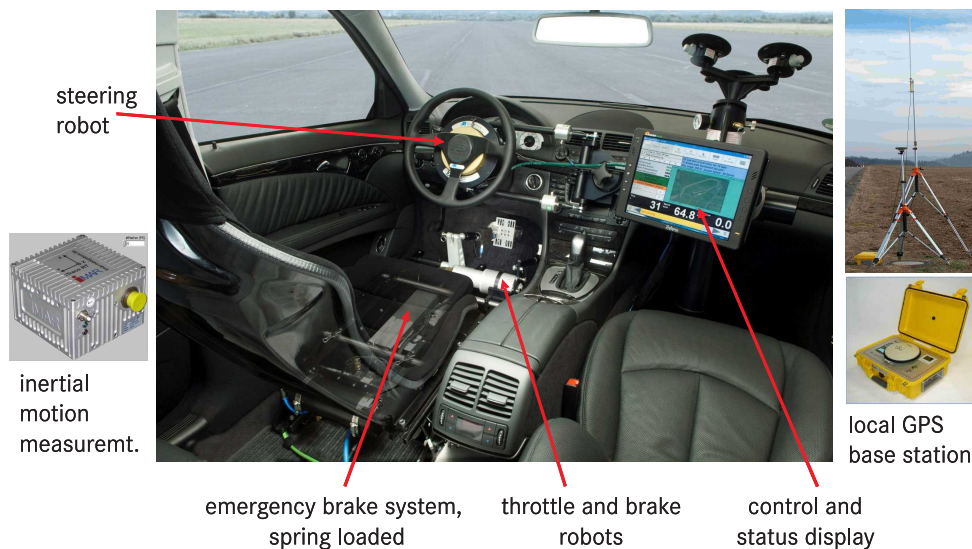


Figure 9.8: Driving robot implemented in test vehicle, from [49].

This technology enables the best possible repeatability regarding steering inputs, vehicle longitudinal velocity and road conditions (since the maneuver will be performed at the same location every time). However, test-to-test variation still exists due to a few factors: Tire wear and tire temperature change during testing causing a different vehicle response. This does not play a major role here since the step-steer maneuver is too short to cause significant tire wear or temperature increase. In addition to this, the test vehicle was driven on a warm-up round prior to the tests for the tires to reach operating temperature which minimizes the influence of tire temperature variations as much as possible. The weather conditions were also very good for vehicle testing, almost calm and 25 degrees Celcius. Despite that the robot vehicle is able to perform the step-steer maneuver at almost the exact same place every time, it is still an open-loop ma-

maneuver and the tires will not always drive over exactly the same road surface every time. Hence, the road surface irregularities will be slightly different and so will the dynamic vertical tire load variations. Finally, signal noise in the measurements and sensor inaccuracy also contribute to the observed test-to-test variations.

Figure 9.9(a) shows the lateral acceleration and Figure 9.9(b) the yaw rate for the 8 different tests. The black thin lines correspond to the different tests and the thick gray lines show the maximum and minimum envelopes. The IMU is located in the trunk, i.e. 0.7 m behind the rear axle, which explains the negative lateral acceleration in the beginning of the maneuver. All measurement data were filtered with a 15 Hz low-pass filter to eliminate signal noise.

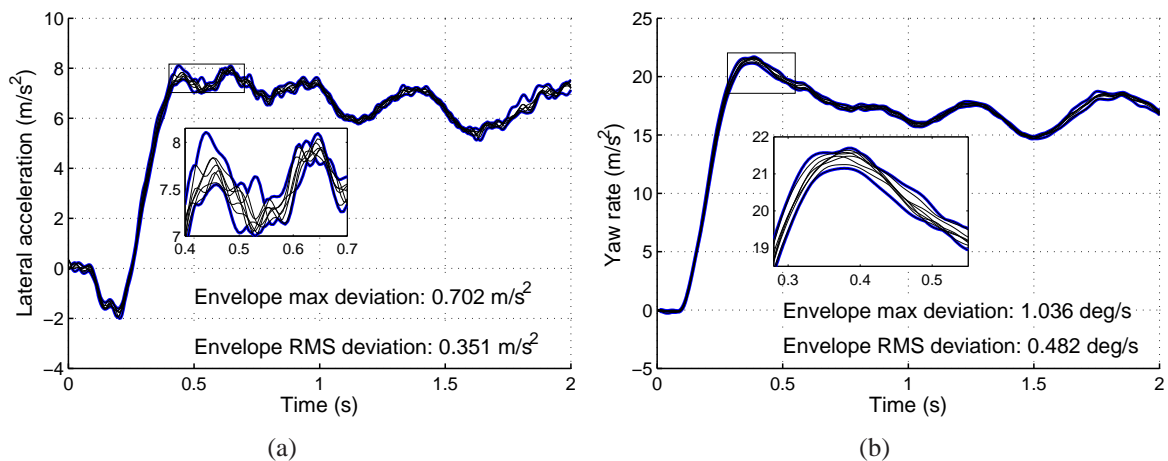


Figure 9.9: Resulting outputs during 8 step-steer maneuvers. In (a) lateral acceleration a_y and in (b) yaw rate $\dot{\psi}$. The thick gray lines represent the maximum and minimum envelopes.

The resulting vehicle side slip angles for the 8 tests are presented in Figure 9.10(a) and the vehicle roll angles are shown in Figure 9.10(b). Table 9.2 concludes the resulting envelope max deviation and RMS deviation for the 8 tests and when comparing this with the corresponding errors to demonstrate the model accuracy in Table 9.1, it is clear that the test-to-test variation spreads significantly more than the achieved model accuracy. This supports the statement that the model accuracy can be considered very good.

	Envelope max deviation	Envelope RMS deviation
a_y	0.702 m/s^2	0.351 m/s^2
$\dot{\psi}$	1.036 deg/s	0.482 deg/s
β	0.26 deg	0.185 deg
ϕ	0.343 deg	0.235 deg

Table 9.2: Resulting envelope maximum deviation and RMS deviation during 8 step-steer maneuvers.

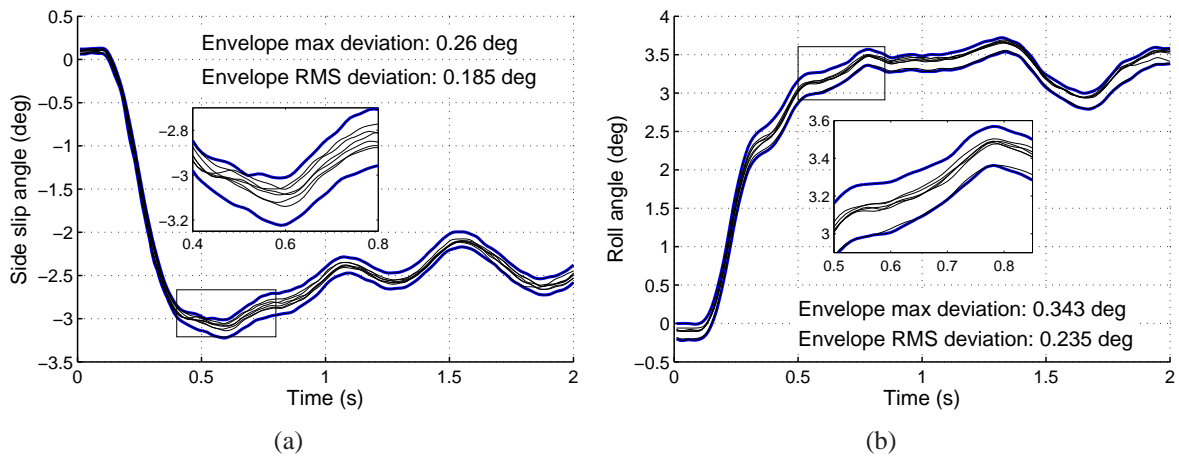


Figure 9.10: Resulting outputs during 8 step-steer maneuvers. In (a) vehicle side slip angle β and in (b) vehicle roll angle ϕ . The thick grey lines represent the maximum and minimum envelopes.

Since the driving robot has been programmed to not increase the throttle position too much as soon as the steering maneuver starts, the longitudinal velocity falls slightly over time due to the increased cornering resistance, see Figure 9.11. The test-to-test variation regarding longitudinal velocity is less than 0.6 km/h when comparing the 8 tests.

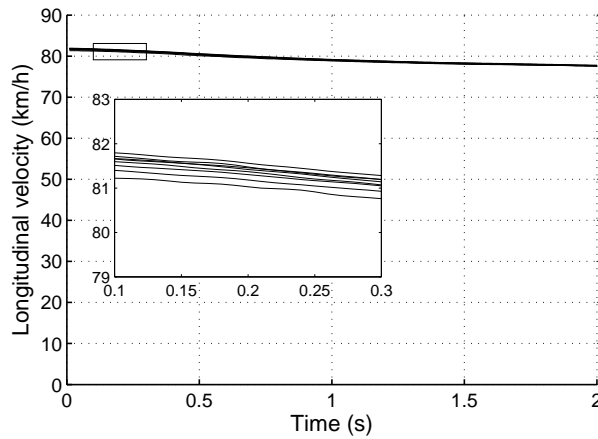


Figure 9.11: Vehicle longitudinal velocity v_x during the 8 step-steer maneuvers.

Chapter 10

Extrapolation using the extended 2-wheel model

The most significant disadvantage with the conventional 2-wheel model is its inability to predict the vehicle response after a change in vehicle set-up. For any change in the vehicle set-up, the conventional 2-wheel model requires the model parameters and lateral axle force characteristics to be identified again from driving measurements with the new vehicle set-up. Even different loading conditions require a repetition of the model parameter identification process. The lateral axle force characteristics for different loading conditions could, however, be approximated by a simplified approach as in [25] but this requires driving measurements to be performed at a few different loading conditions as well.

This chapter presents how the extended 2-wheel model can be used to predict the vehicle behavior with different anti-roll bar set-ups, tires and loading conditions. The only prerequisite is that the model parameters for the extended 2-wheel model have been identified once with known tire characteristics. All investigations presented in this chapter use the model parameters identified in Chapter 8. It is always assumed that the tire characteristics are known and for that reason, both the extended 2-wheel model and the reference model are simulated with the same tire model (MF 5.2) and tire parameters.

As in Chapter 9, the step steer maneuver is used when verifying the different extrapolation approaches.

10.1 Extrapolation to different anti-roll bar setups

10.1.1 Investigated anti-roll bar setups

The five different anti-roll bar configurations **ARB 1** to **ARB 5** are listed in Table 10.1 with the ARB stiffness factor describing how the stiffness of the anti roll bars are changed in relation to the base vehicle, e.g. an ARB stiffness factor of 1.5 on one of the axles denote a 50 % increase in anti roll bar stiffness on that axle. Equation (8.8) furthermore calculates the resulting total

roll stiffness, $C_{\varphi,j}$, of axle j . For this calculation, Equation (8.8) requires the tire roll stiffness, $C_{\varphi,ti,j}$ which is calculated using Equation (8.7) and the suspension roll stiffness, $C_{\varphi,su,j}$ which is received after linearizing the roll moment characteristics, $M_{\varphi,j}(\varphi_{su,j})$ (described in Equation (8.6)), around zero roll angle. The corresponding roll stiffness distribution ($C_{\varphi,f}/(C_{\varphi,f} + C_{\varphi,r})$) complete the information about the investigated anti-roll bar set-ups.

Nine possible configurations results from altering the ARB stiffness between 0, -50 and $+50$ % on the front and rear axle respectively. Only five of these configurations are shown here. The ARB configuration in **ARB 5** had to be adjusted to change with less then 50 % (ARB stiffness factor front 0.8 and rear 1.3) to keep the vehicle from skidding out at higher lateral accelerations.

Label	Description	ARB stiffness factor		Roll stiffness (Nm/deg)		Roll stiffness distribution
		Front	Rear	Front, $C_{\varphi,f}$	Rear, $C_{\varphi,r}$	
ARB 1	Base vehicle.	1.0	1.0	883.7	604.8	59.4 %
ARB 2	Roll stiff.	1.5	1.5	1094.8	714.4	60.5 %
ARB 3	Rear weak.	1.0	0.5	883.7	486.4	67.5 %
ARB 4	Front hard, rear weak.	1.5	0.5	1094.8	486.4	73.6 %
ARB 5	Front weak, rear hard.	0.8	1.3	788.9	671.4	55 %

Table 10.1: Investigated anti-roll bar set-ups for verifying the extrapolation approach.

The resulting vehicle response with the different anti-roll bar configurations can be seen in Figure 10.1 to 10.4 where simulation results from the reference vehicle CASCaDE-DA are compared. Only the step steer response for the steering wheel angle 90 degrees is shown here and the figure in (b) always shows a zoom of the figure in (a). The figures in this comparison show the spread between the different ARB configurations and serve as a reference when evaluating the accuracy of the extrapolation results. **ARB 4** show the most spread overall when comparing with the base configuration (**ARB 1**) and the simulation results for this configuration will therefore be studied in Subsection 10.1.3. The simulation results for the other configurations have been moved to Appendix B.1.

As expected, the resulting vehicle response with the **ARB 2** set-up is very similar to the **ARB 1** set-up except regarding the vehicle roll angle which is smaller. **ARB 2** is obviously stiffer but the roll stiffness distribution is more or less the same as in **ARB 1**, with a very similar under-steer behavior as a result.

The set-ups **ARB 3** and **ARB 4** are both more under steering in comparison to **ARB 1**, which can be seen in the decreased yaw rate and side slip angle. The roll behavior is however very different due to the stiffer set-up in **ARB 4**. The overall large difference between **ARB 1** and **ARB 4** makes these two set-ups especially adequate for evaluating the anti-roll bar extrapolation approach.

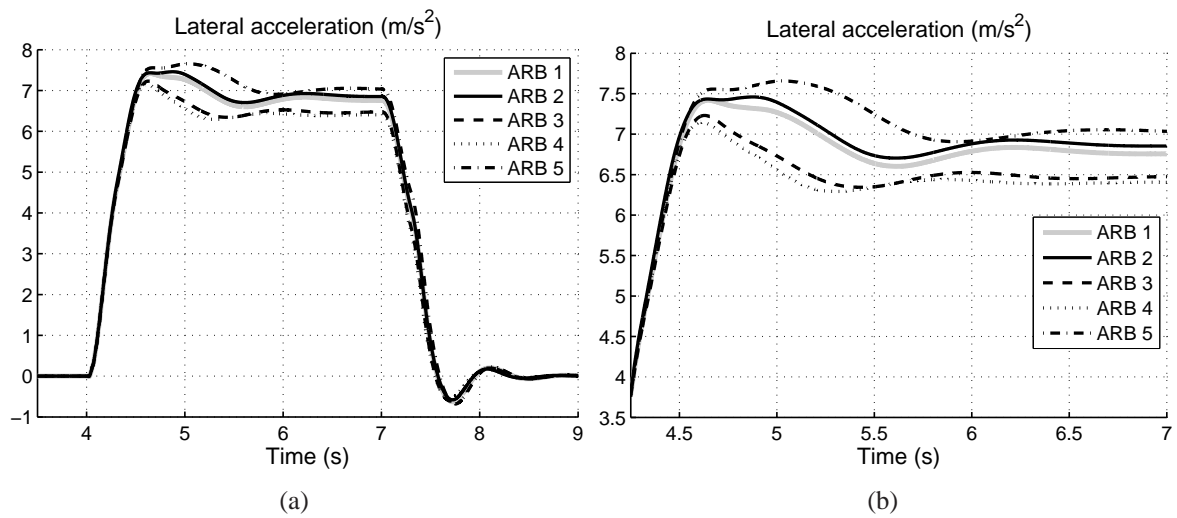


Figure 10.1: Comparison of the lateral acceleration achieved with the reference vehicle (CASCaDE-DA) for the different ARB configurations **ARB 1** to **ARB 5**. Step steer response with a 90 degree steering wheel amplitude. (b) shows a zoomed view of the figure in (a).

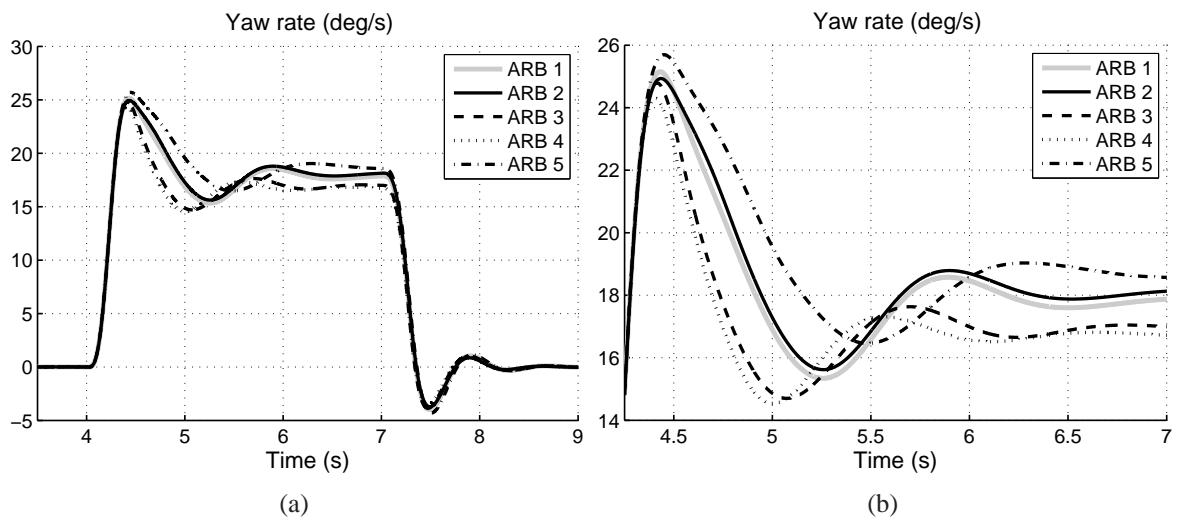


Figure 10.2: Comparison of the yaw rate achieved with the reference vehicle (CASCaDE-DA) and the different ARB configurations **ARB 1** to **ARB 5**. Step steer response with a 90 degree steering wheel amplitude. (b) shows a zoomed view of the figure in (a).

In **ARB 5** the roll stiffness distribution is very extreme in comparison to what is normal in a production vehicle. This results in vehicle with almost too little under steer which would make it very nervous to drive.

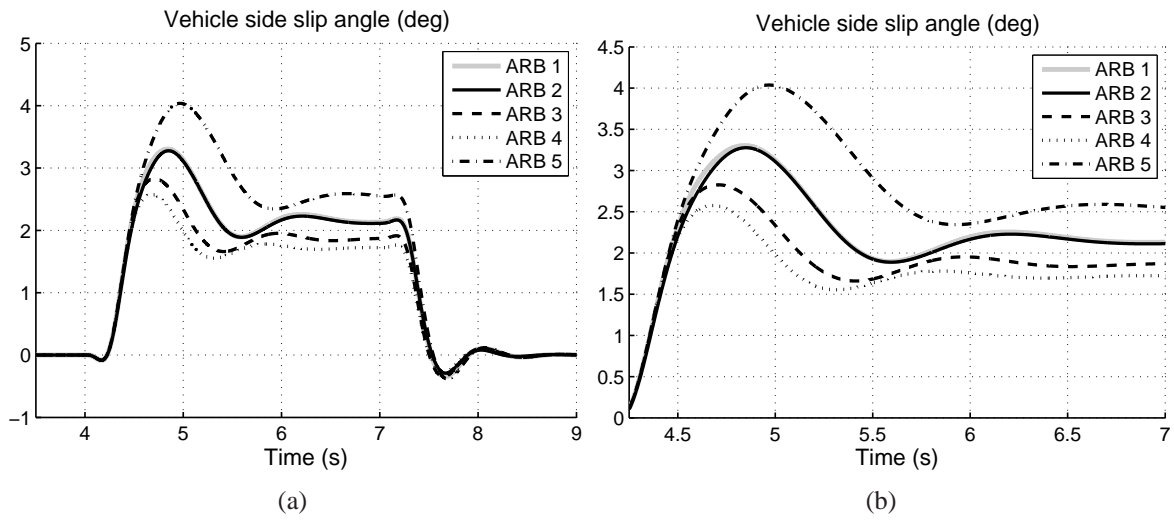


Figure 10.3: Comparison of the vehicle side slip angle achieved with the reference vehicle (CASCaDE-DA) and the different ARB configurations **ARB 1** to **ARB 5**. Step steer response with a 90 degree steering wheel amplitude. (b) shows a zoomed view of the figure in (a).

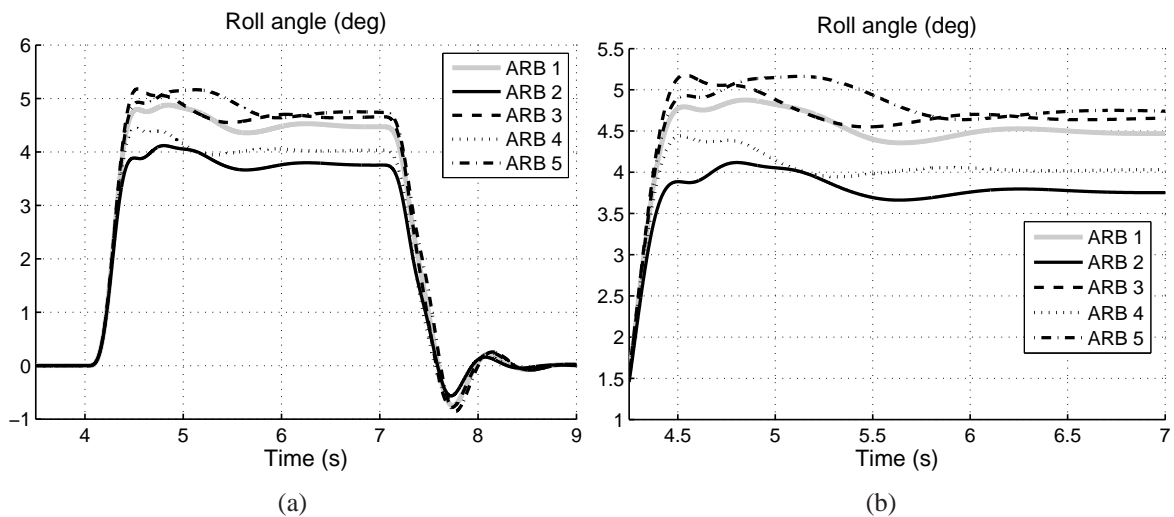


Figure 10.4: Comparison of the roll angle achieved with the reference vehicle (CASCaDE-DA) and the different ARB configurations **ARB 1** to **ARB 5**. Step steer response with a 90 degree steering wheel amplitude. (b) shows a zoomed view of the figure in (a).

10.1.2 Extrapolation approach for different anti-roll bar setups

The non-linearity in the roll moment characteristics presented in Section 8.3.2 is mainly caused by the non-linear jounce and rebound stops. A small contribution is also received from the suspension kinematics and non-linearities in rubber mounts. The anti-roll bar can be assumed to be a part with linear stiffness. However, the kinematics of the anti-roll bar, i.e. it's attachment points to the wheel carrier and how these move in jounce and rebound, as well as non-linear rubber mounts (if used) where the anti-roll bar is attached to the vehicle body can add a non-linear contribution to the overall roll stiffness related to the anti-roll bar. Nevertheless, the overall roll stiffness caused by the anti-roll bar, $C_{\phi,ARB}$, will be assumed to be a strictly linear parameter in this investigation.

Since the translation ratio between the vehicle roll angle and the torsion angle in the anti-roll bar $i_{\phi \rightarrow ARB}$, see Equation (8.9) and (8.10), is assumed to be constant, the overall ARB roll stiffness $C_{\phi,ARB}$ will increase with the same ratio as the torsional stiffness of the anti-roll bar. The ARB roll stiffness $C_{\phi,ARB}$ subsequently influences the total roll stiffness characteristics according to Equation (8.6).

10.1.3 Extrapolation results for anti-roll bar setup 4 – ARB 4

Figure 10.5 and 10.6 presents the resulting simulation outputs for the verification maneuver when the reference model CASCaDE-DA is simulated with the **ARB 4** setup and the 2-wheel model parameters are extrapolated to correspond to the **ARB 4** setup. Table 10.2 furthermore presents the corresponding root mean square (RMS) error and maximum error for the 2-wheel model in comparison to the reference model CASCaDE-DA. The accuracy of the extrapolated

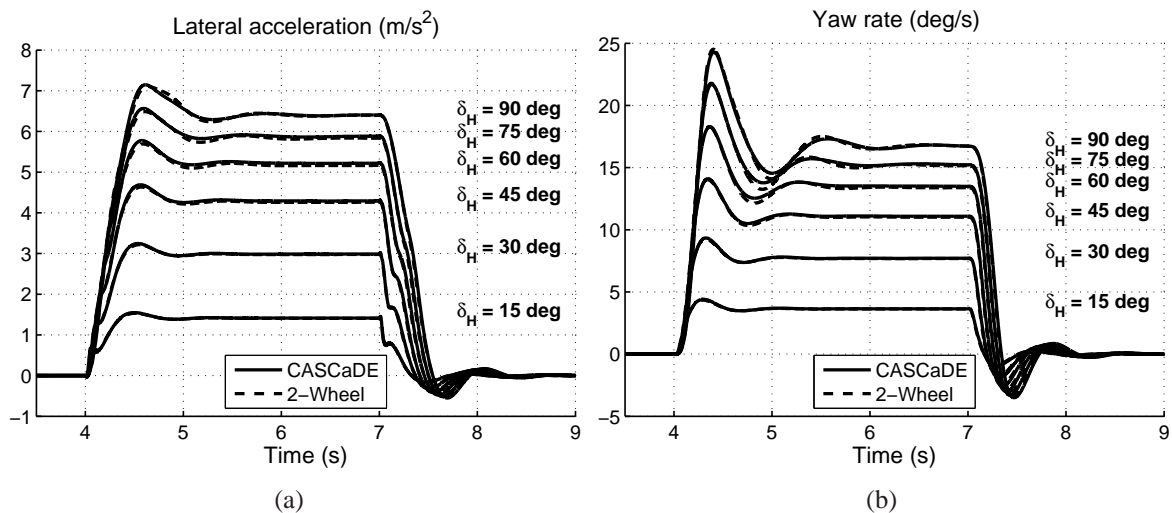


Figure 10.5: Extrapolation results for **ARB 4**. In (a) lateral acceleration and in (b) yaw rate.

2-wheel model is as good as the originally identified model without anti-roll bar modification. This is evident when comparing the results from the verification maneuver summarized in Table 9.1 with the extrapolation results in Table 10.2. As a matter of fact, the extrapolated results show

even less error for some of the results which can be seen as an indication that the difference seen is a matter of model complexity and not a matter of parameter tuning. Hence, in order to receive a better accuracy, the simulation model would have to be further developed.

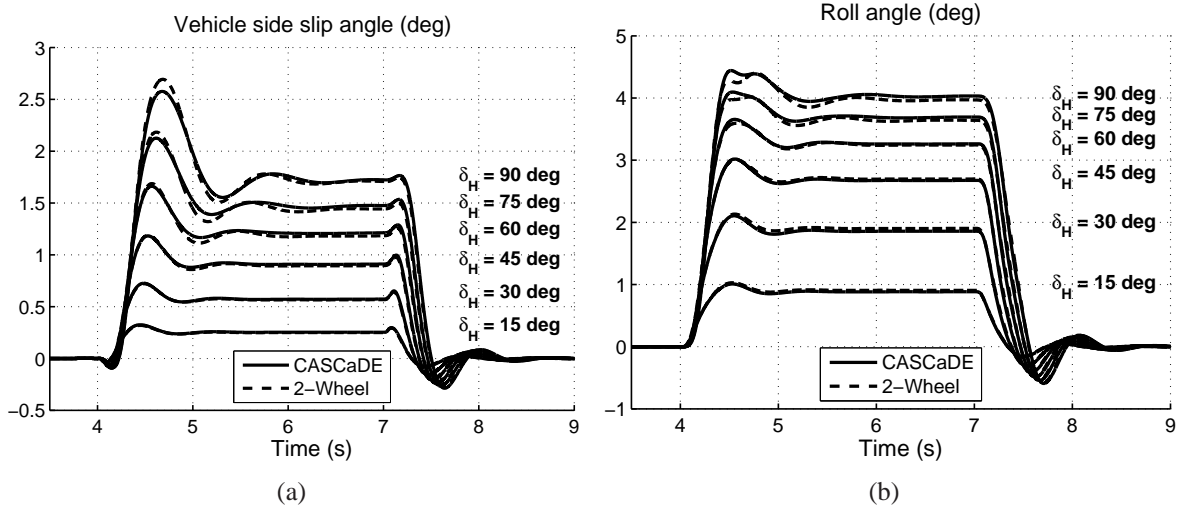


Figure 10.6: Extrapolation results for **ARB 4**. In (a) vehicle side slip angle and in (b) roll angle.

$\hat{\delta}_H$ (deg)	a_y (m/s^2)		$\dot{\psi}$ (deg/s)		β (deg)		φ (deg)	
	RMS	max.	RMS	max.	RMS	max.	RMS	max.
90	0.042	0.21	0.124	0.45	0.023	0.07	0.039	0.13
75	0.045	0.18	0.098	0.41	0.020	0.06	0.030	0.10
60	0.050	0.15	0.101	0.38	0.015	0.05	0.018	0.07
45	0.048	0.12	0.101	0.32	0.010	0.04	0.011	0.05
30	0.037	0.11	0.082	0.25	0.006	0.03	0.011	0.03
15	0.023	0.14	0.051	0.15	0.003	0.02	0.005	0.02

Table 10.2: Root mean square (RMS) error and maximum error when comparing the model outputs of the reference model CASCaDE-DA and the 2-wheel model with extrapolated model parameters to fit the **ARB 4** setup.

10.2 Extrapolation to different tire characteristics

The objective of this investigation is to extrapolate the vehicle behavior with different tires. In order to show this, the CASCaDE reference model is simulated with a number of different tire characteristics in a suggested verification maneuver. The same maneuver is simulated with the extended 2-wheel model from Chapter 7, with the model parameters identified in Chapter 8 using tire 1. It is always assumed that the tire characteristics are known and for that reason, both the extended 2-wheel model and the reference model are simulated with the same tire model (MF 5.2) and tire parameter sets.

10.2.1 Investigated tire characteristics

The tires have been selected to have a wide range of different properties, i.e. different sensitivity to vertical load and camber angle as well as different cornering stiffness and maximum force potential. At the same time, the tire diversity has been kept within the spread of real life tires. This has been accomplished by selecting tire parameter sets identified from measurements of tires designed for the specific reference vehicle.

As a quality assurance it is very important to study the tire behavior within the intended use case before performing any vehicle dynamics simulation. An assessment of the tire characteristics also serves as a tool when selecting the different tires used for this investigation. For this purpose, the so called *tire fingerprint*, presented in for instance [44], has been applied. In this fingerprint, the tire is evaluated at different load cases and the results are plotted in a set of standardized plots.

Tire 1 and 2 presented in this section both have the dimension 205/55 R16 but Tire 1 is mounted on a 6.5 inch wide rim and the rim for Tire 2 is 1 inch wider. Figure 10.7 and 10.8 present the parts of the fingerprint important in this investigation, comparing two tire parameter sets:

- Tire 1 (solid lines in Figure 10.7 and 10.8) was used when identifying the extended 2-wheel model, i.e. this tire was used in both the reference model and in the extended 2-wheel model when the vehicle and suspension parameters in the latter model were adjusted to fit the vehicle motion states of the simulated reference model.
- Tire 2 (dotted lines in Figure 10.7 and 10.8) is the extrapolation tire. Hence, this tire was used in simulations with both the reference model and the extended 2-wheel model in order to investigate how the latter model performed with a different set of tire parameters without changing any of the earlier identified vehicle and suspension parameters.

Figure 10.7(a) compares the lateral force characteristics at pure side slip conditions for tire 1 (solid lines) and tire 2 (dotted line). Tire 2 shows larger lateral forces than tire 1 as the vertical load increases. The aligning moment, however, is very similar when comparing tire 1 and 2 at smaller side slip angles, see Figure 10.7(b). At larger side slip angles, tire 2 shows slightly less aligning moment than tire 1.

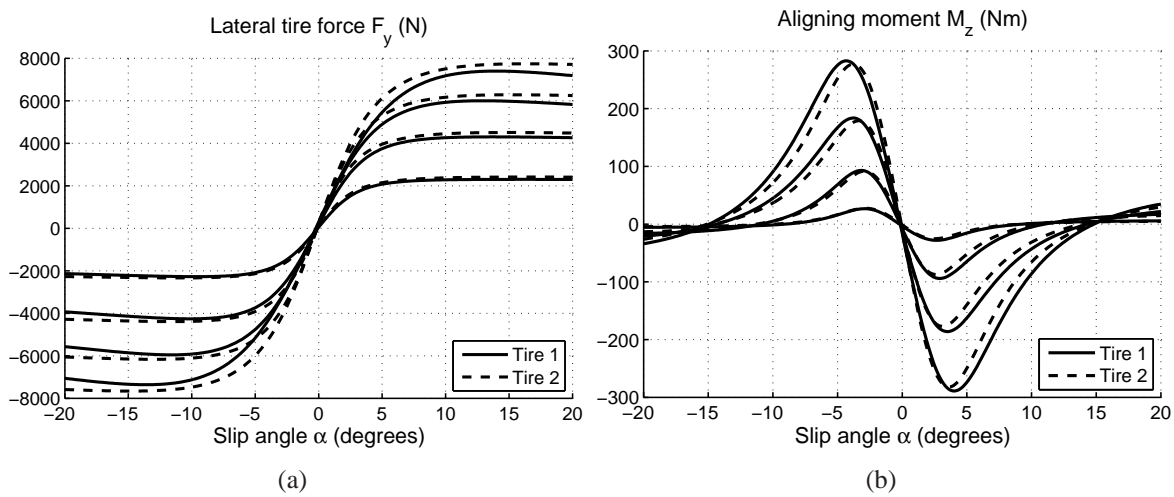


Figure 10.7: Lateral force and aligning moment characteristics of tire 1 and 2 at pure side slip condition. The characteristics are generated at the vertical tire loads $F_z = 2000, 4000, 6000$ and 8000 N

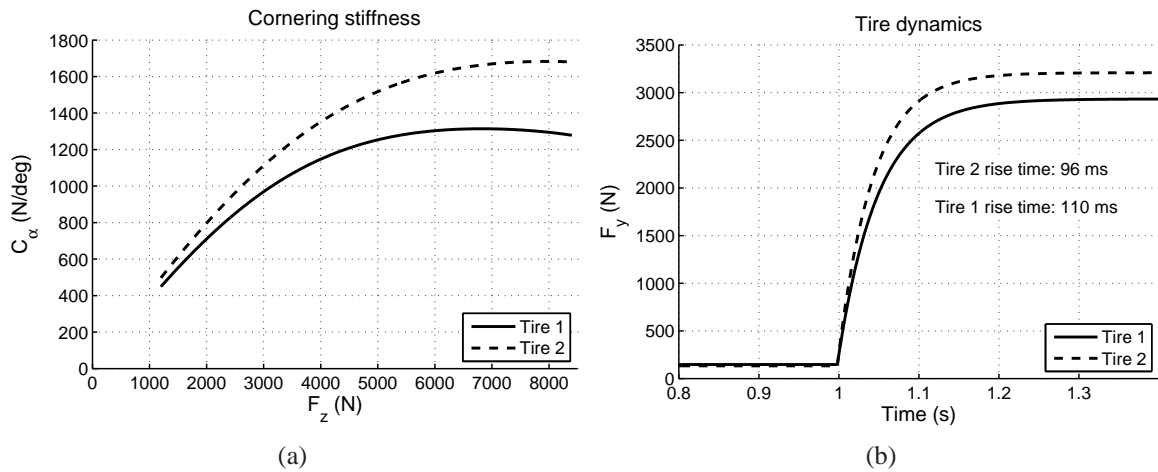


Figure 10.8: Comparison between tire 1 and 2. In (a) the tire cornering stiffness as a function of vertical tire load and in (b) a step response exemplifying the tire dynamics (tire vertical load 4000 N during a side slip angle step of 3 degrees and 40 km/h longitudinal velocity). 90% of the steady state lateral force is reached after 106 ms for tire 1 and after 96 ms for tire 2.

The most significant difference between tire 1 and 2 appears in the cornering stiffness $C_\alpha = \left. \frac{\partial F_y}{\partial \alpha} \right|_{\alpha=0}$, which for tire 2 is significantly larger than for tire 1, see Figure 10.8(a).

Also the transient behavior is very different between the two tires as Tire 2 responds almost 15% faster than tire 1, see Figure 10.8(b). The non zero lateral tire force prior to the step response despite zero side slip angle and zero tire camber angle, is caused by conicity and/or plysteer effects which are also captured by the tire model [51].

Figure 10.9 and 10.10 compare the vehicle response received when simulating the reference vehicle model CASCaDE-DA with tire 1 and tire 2. Especially the resulting vehicle side slip angle is influenced by the different tire characteristics but also the steady-state values for lateral acceleration and yaw rate are different. These differences in vehicle response depend mainly on

the difference in tire cornering stiffness.

The difference in dynamic response can also be seen in the faster build-up of lateral acceleration for tire 2, see Figure 10.9(a).

The roll angle steady-state values are very similar despite the higher lateral acceleration received with tire 2. This indicates that the overall roll stiffness has increased when changing the tires. This is also confirmed the radial tire stiffness which for tire 1 is 189 kN/m compared to 201 kN/m for tire 2.

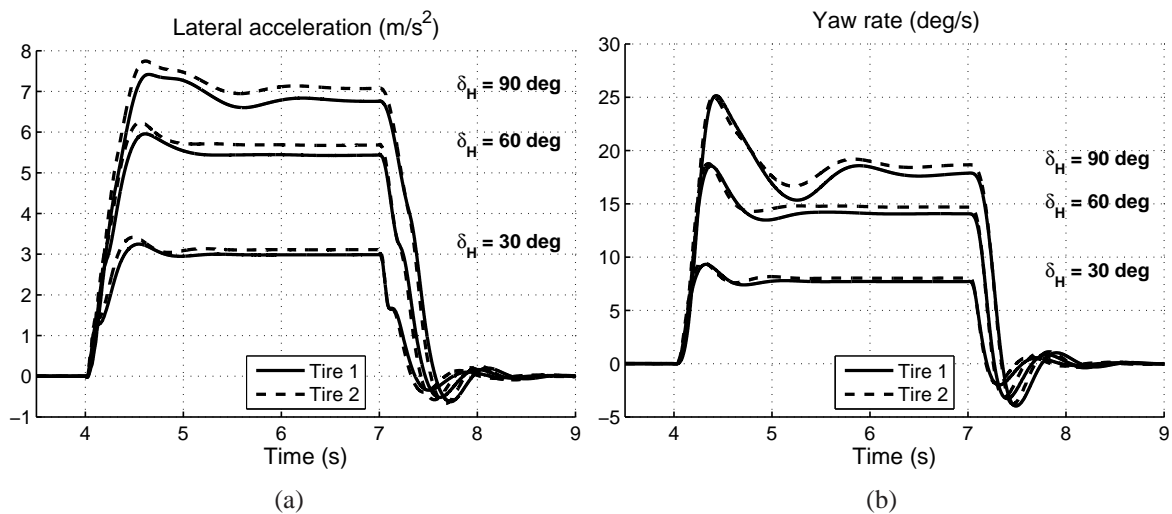


Figure 10.9: Comparison in vehicle response with tire 1 and tire 2. In (a) lateral acceleration and in (b) yaw rate.

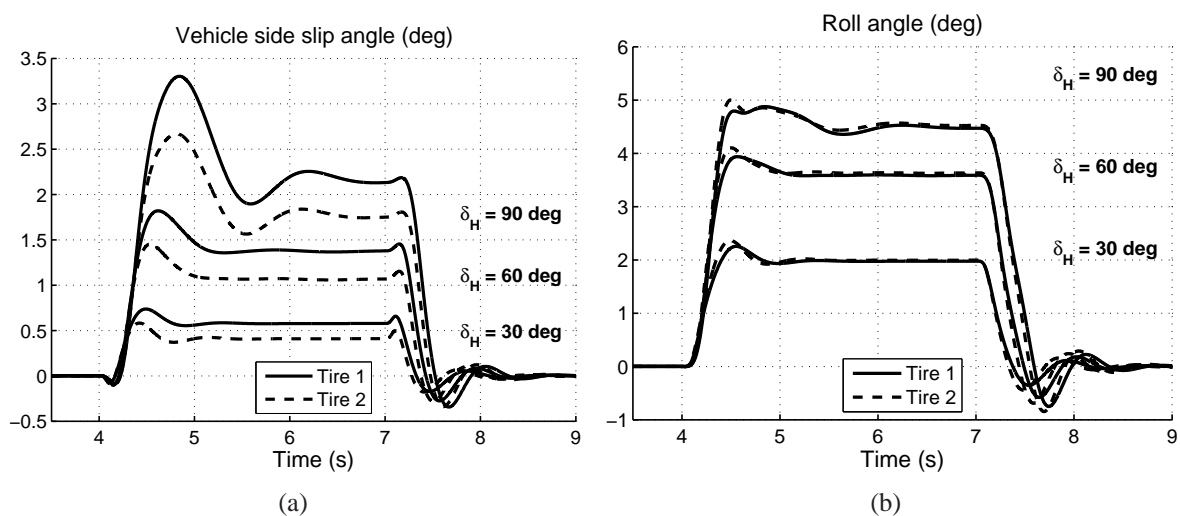


Figure 10.10: Comparison in vehicle response with tire 1 and tire 2. In (a) vehicle side slip angle and in (b) roll angle.

10.2.2 Extrapolation approach for different tire characteristics

The tire roll stiffness $C_{\phi,ti}$ is the only parameter in the suspension model influenced by a tire change, all other suspension parameters remain the same. As already defined in Section 8.3.2, the tire radial stiffness of the tires can be converted to a tire roll stiffness $C_{\phi,ti}$.

$$C_{\phi,ti} = \frac{C_{z,ti} \cdot b_j^2}{2} \quad (10.1)$$

If applying Equation (10.1) followed by Equation (8.8) using the radial tire stiffness 189 kN/m for tire 1 and 201 kN/m for tire 2 together with the vehicle parameters (track width and suspension roll stiffness) presented in Chapter 8, it can be shown that the total vehicle roll stiffness increases with approximately 1.28 % with tire 2 in comparison to tire 1 (whereas the radial tire stiffness of tire 2 is about 6.35 % stiffer than tire 1).

10.2.3 Extrapolation results for different tire characteristics

Figures 10.11 to 10.12 compare the resulting vehicle response for the extended 2-wheel model and the CASCaDE reference model when extrapolating the vehicle behavior with tire 2. The steady-state driving conditions are captured very good except for the roll angle where a small deviation can be seen. A small difference can also be detected for all outputs in the transient part when the steering wheel angle amplitude transcends 60 degrees.

Table 10.3 concludes the difference between the simulation outputs of the reference model CASCaDE-DA and the 2-wheel model, both using tire 2. A small degradation in model accuracy can be detected when comparing with the results from the verification simulations presented in Table 9.1. Only the roll angle keeps approximately the same accuracy as in the verification simulations but the other outputs, though small, are worse especially at the larger steering wheel angle inputs, i.e. at higher lateral accelerations.

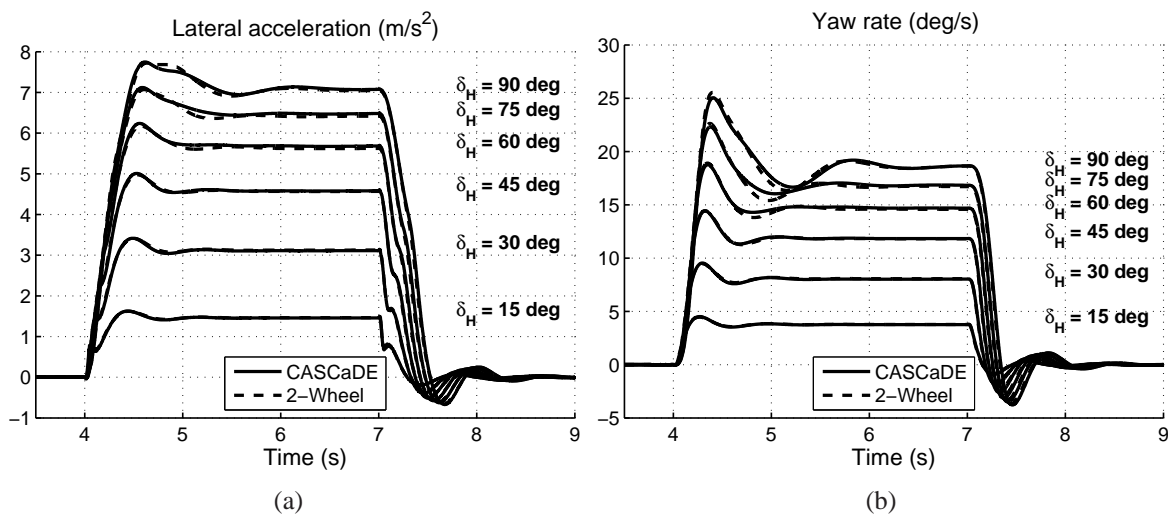


Figure 10.11: Extrapolation results for tire 2. In (a) lateral acceleration and in (b) yaw rate.

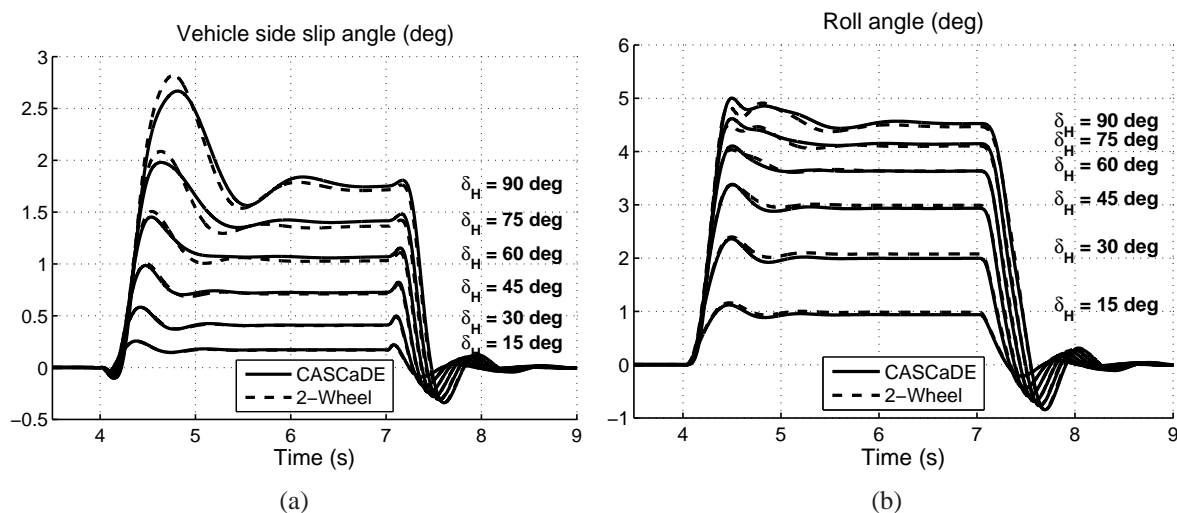


Figure 10.12: Extrapolation results for tire 2. In (a) vehicle side slip angle and in (b) roll angle.

$\hat{\delta}_H$ (deg)	a_y (m/s^2)		$\dot{\psi}$ (deg/s)		β (deg)		ϕ (deg)	
	RMS	max.	RMS	max.	RMS	max.	RMS	max.
90	0.067	0.28	0.188	0.74	0.050	0.17	0.039	0.14
75	0.069	0.24	0.166	0.66	0.039	0.14	0.035	0.14
60	0.064	0.19	0.136	0.48	0.024	0.07	0.038	0.13
45	0.052	0.15	0.112	0.37	0.013	0.05	0.040	0.11
30	0.039	0.13	0.084	0.26	0.007	0.04	0.031	0.06
15	0.023	0.17	0.050	0.17	0.003	0.02	0.016	0.03

Table 10.3: Root mean square (RMS) error and maximum error when comparing the model outputs of the reference model CASCaDE-DA and the 2-wheel model extrapolated with tire parameters from tire 2.

10.3 Extrapolation to different loading conditions

10.3.1 Investigated loading conditions

Table 10.4 shows the mass geometry and principal moments of inertia used for the different load variations investigated here. The location of the masses are provided in the design reference frame which is located in the middle of the front axle at wheel center height when the vehicle is standing on a flat surface in the design loading condition. The design reference frame is furthermore oriented in the same direction as the vehicle reference frame (positive x -direction is forward, y to the left and z upwards). The base vehicle is denoted **L1** and includes the vehicle with three passengers (driver with passengers front right and rear middle).

	Mass m , (kg)	Moment of Inertia $[J_{xx}, J_{yy}, J_{zz}]$, (kgm^2)	Location $[l_x, l_y, l_z]$, (m)	L1	L2	L3	L4	L5
Base Vehicle	1759.5	[542, 2411, 2777]	[-1.33, 0, 0.25]	X	X	X	X	X
Passenger RL	68	[1.3, 1.0, 0.6]	[-2.28, 0.38, 0.22]		X		X	
Passenger RR	68	[1.3, 1.0, 0.6]	[-2.28, -0.38, 0.22]		X		X	
Trunk load	100	[6.9, 2.5, 6.9]	[-3.37, 0, 0.38]		X		X	
Roof load	200	[12.6, 21.4, 31.4]	[-1.79, 0, 1.25]			X		X

Table 10.4: Mass geometry and principal moments of inertia of the loads used to create the load variations **L1** (base vehicle), **L2** and **L3**, see also Table 10.5.

In the loading condition denoted **L2**, two rear seat passengers and a 100 kg trunk load has been added to the base vehicle condition. This causes the center of gravity position to move significantly towards the rear. In the final load condition, **L3**, a 200 kg roof load is added to the base vehicle which increases the center of gravity height. Hence, the two load variations, **L2** and **L3**, represent two fairly extreme load conditions. Figure 10.13 shows the loads used in the investigated load variations.

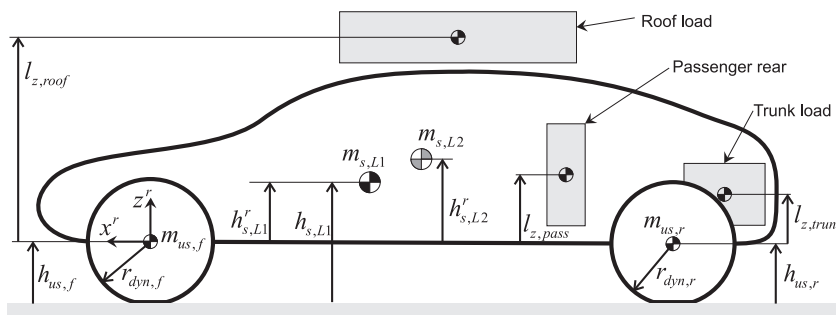


Figure 10.13: Loads for the mass variations.

For the load variations, **L2** and **L3**, the vehicle is equipped with an automatic ride height control system, i.e. the suspension deflection is zero at straight ahead driving independent of loading

condition ¹. The load variations **L4** and **L5** are loaded the same way as in **L2** and **L3** respectively, but the vehicle is on the other hand not equipped with an automatic ride height system. Consequently, the suspensions in the load variations **L4** and **L5** are deflected due to the additional load. The loading for the base vehicle **L1** corresponds to the design loading condition, i.e. the initial suspension deflection is per default zero in this vehicle.

The principal moments of inertia for the additional loads and passengers listed in Table 10.4 have been estimated from boxes with an even mass distribution. In some cases, the principal moment of inertia for the load, $J_{xx,i}$, could be neglected in comparison to the contribution from the point mass in the parallel axis theorem:

$$\Delta J_{xx} = J_{xx,i} + m_i (\Delta r_i)^2 \quad (10.2)$$

The point mass of the roof load, for instance, contributes to the total sprung mass roll inertia with about ten times more than the principal inertia of the load alone. Regarding the roof load's contribution to the yaw moment of inertia, the two elements in the equation above will contribute about equally but it is a small contribution in relation to the total yaw moment of inertia. In most cases when it comes to simulating vehicle handling for different load variations, it is sufficient to only consider the moment of inertia contribution from the point masses.

Table 10.5 in the next subsection show the resulting vehicle mass and mass distribution for the different load variations.

Figure 10.14 and 10.15 compare the vehicle motion states reached in all load variations for the virtual measurements, i.e. CASCaDE-DA simulations, when driven in the verification maneuver with a steering wheel angle amplitude of 90 deg. The motion outputs of the variants

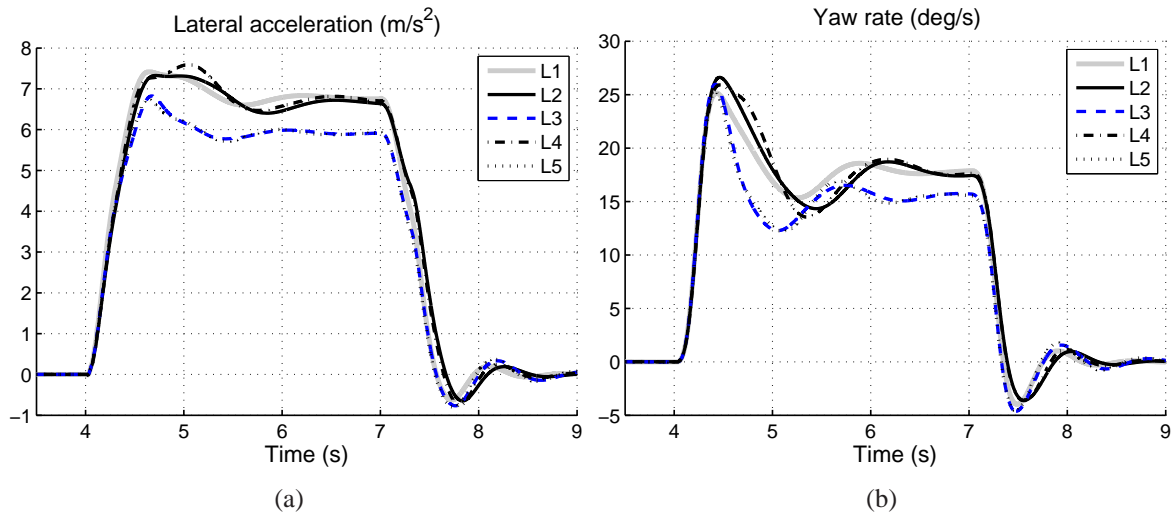


Figure 10.14: Comparison of simulation outputs for the different load variations **L1-L5**. In (a) lateral acceleration and in (b) yaw rate, reference simulations with CASCaDE-DA.

with the same additional loads (one with and one without an automatic ride height control system), e.g. **L3** and **L5**, show very similar results. The difference between these variants are

¹To ease the investigations, a virtual ride height system has been applied here by simply increasing the pre-load of the springs in the simulation model. If using an air spring to control the ride height, the increase in suspension spring stiffness with increased load would also have to be considered.

attributed to the changed initial suspension deflection. The difference in motion outputs between the load variants **L2** and **L4** (also with the same additional loads) are more significant than for **L3** and **L5**. This is attributed to the vertical axle load increase on the rear axle, which in **L2** (and **L4**) is about twice the increase in **L3** (and **L5**). Thus, the change in initial suspension deflection is more significant in load variant **L4** than in **L5**.

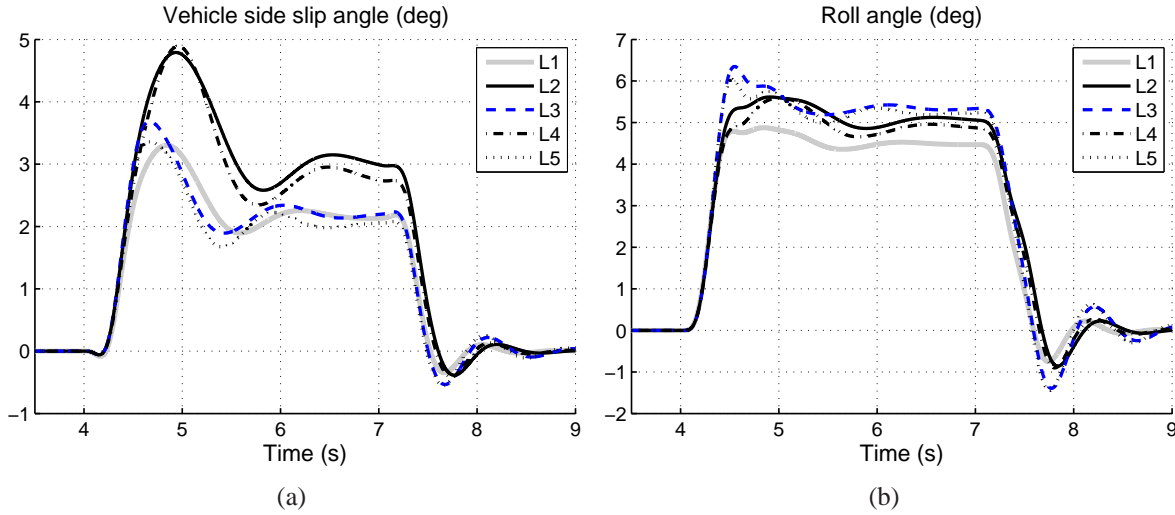


Figure 10.15: Comparison of simulation outputs for the different load variations **L1-L5**, reference simulations with CASCaDE-DA.. In (a) vehicle side slip angle and in (b) roll angle.

10.3.2 Extrapolation approach for different loading conditions

For the virtual measurements made with CASCaDE-DA, the loads listed in Table 10.4 are simply added to the vehicle parameter file and the vehicle model automatically calculates the new mass geometry and inertia properties of the vehicle body. In the extended 2-wheel model, however, approaches for changing these parameters are presented.

To start with, the mass geometry reference frame for the base vehicle, i.e. load variation **L1**, is determined, see Figure 10.13 and Table 10.4. The height of the sprung mass, h_s , has to be transformed to the vehicle reference frame, which for the base vehicle is located in the middle of the front axle at the same height as the center of the front wheels. The distance between wheel center and road is the same as the height of the unsprung mass, i.e. $h_{us,f} = r_{dyn,f} - \Delta z_{ti}(F_{z,i})$, see Figure 10.13. Consequently, the coordinates of the sprung mass given in the design reference frame is $h_s^r = h_s - h_{us,f}$ (this is an approximation since it in reality is a combination of the front and rear tire deflections).

With the mass geometry of the base vehicle as the starting point, simple relations can be used to calculate the new sprung mass, m_s , and its mass geometry, h_s^r , $l_{f,s}$ and $l_{r,s}$, when adding the different loads.

$$h_{s,L2}^r = \frac{m_{s,L1} h_{s,L1}^r + \sum m_i l_{z,i}^r}{m_{s,L2}} \quad (10.3)$$

The moments of of inertia for roll and yaw are calculated using the parallell axis theorem. For the roll moment of inertia, the sprung mass and the different additional loads are considered in the calculation.

$$J_{\varphi,L2} = J_{\varphi,L1} + m_{s,L1} (h_{s,L1}^r - h_{s,L2}^r)^2 + \sum \left(J_{xx,i} + m_i \left((l_{z,i}^r - h_{s,L2}^r)^2 + l_{y,i}^2 \right) \right) \quad (10.4)$$

$l_{y,i}$ and $l_{z,i}$ are the distances of the additional loads from the design reference frame, as presented in Table 10.4. For the yaw moment of inertia, the total vehicle mass (and geometry) is used in the parameter extrapolation:

$$J_{\psi,L2} = J_{\psi,L1} + m_{CG,L1} (l_{f,L1}^r - l_{f,L2}^r)^2 + \sum \left(J_{zz,i} + m_i \left((l_{z,i}^r - l_{f,L2}^r)^2 + l_{y,i}^2 \right) \right) \quad (10.5)$$

The final step in extrapolating the parameters for the load variations **L2** and **L3**, is to consider the new sprung mass height due to the additional tire deflection caused by the new tire loads, i.e. adjust $h_{us,j}$ and h_s with the additional tire deflection. This effect is, however, very small and could be neglected. Conclusively, the new h_{cg} can be calculated using Equation 7.6.

For the load variations **L4** and **L5**, the vehicle is equipped with coil springs and is lacking an automatic ride height control system. Thus, the spring deflections due to the additional vehicle loads have to be taken into consideration when extrapolating the parameters for the extended 2-wheel model. For this, the vertical load over suspension deflection from the **SJR** maneuver, $F_{z,SJR,f}(z_f)$, is used when estimating the new suspension deflection. Subsequently, the new suspension deflection is used to calculate the new sprung mass height, h_s , followed by the new center of gravity height, h_{cg} .

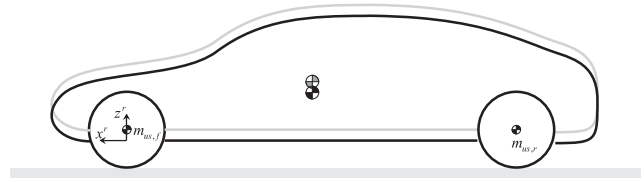


Figure 10.16: New sprung mass height due to suspension deflection.

Table 10.5 summarizes the most significant mass parameters changed in the extended 2-wheel model for the different load variations. Note how the center of gravity height is smaller for the load variations without the automatic ride height control system, i.e. **L4** and **L5** in comparison with **L2** and **L3**. This is not necessarily the case for real life vehicles since the algorithm of the ride height control system could be implemented to change the ride height at extreme loading conditions. In the virtual measurements for load variation **L2** and **L3**, the ride height is simply adjusted to be zero for all all load conditions.

As already mentioned in Subsection 8.3.2 and exemplified in Figure 8.6(b), the suspension deflection will also influence the front and rear elastic roll moment characteristics, $M_{\varphi,SJR,j}(\varphi_{su,j})$. Likewise, the static steer angles, $\delta_{0,j}$, and camber angles, $\epsilon_{0,j}$, as well as the roll characteristics, $\delta_{\varphi,j}(\varphi_{su,j})$ and $\epsilon_{\varphi,j}(\varphi_{su,j})$, for steer and camber angles are to be adjusted for the new initial condition regarding the suspension deflection.

	m (kg)	l_f (m)	l_r (m)	h_{CG} (m)	Δh (m)	J_ψ (kgm ²)	J_ϕ (kgm ²)
L1	1759.5	1.328	1.392	0.563	0.539	2708	486
L2	1995.5	1.495	1.225	0.567	0.542	3223	517
L3	1959.5	1.375	1.345	0.664	0.646	2763	657
L4	1995.5	1.495	1.225	0.541	0.514	3223	517
L5	1959.5	1.375	1.345	0.642	0.622	2763	657

Table 10.5: Most relevant extrapolated mass parameters in the extended 2-wheel model for the different load variations.

10.3.3 Extrapolation results for load variation L2 and L3

The results for the load variations are separated in two different subsections since **L2** and **L3** are simulated with an automatic ride height control system. Hence, the same load variations but without the automatic ride height control system will be investigated once again in Subsection 10.3.4.

Load condition L2:

Figure 10.17 shows a comparison of the resulting lateral acceleration and yaw rate from the virtual measurements with the CASCaDE-DA model and the extended 2-wheel model using the extrapolated parameters for the new load condition **L2**. The corresponding vehicle side slip angle and roll angle are furthermore compared in Figure 10.18. The model accuracy is in par with the other extrapolation results regarding extrapolating to other anti-roll bar and tire properties. The statistics of how accurate the extended 2-wheel model manages to copy the behavior of the virtual measurements are concluded in Table 10.6.

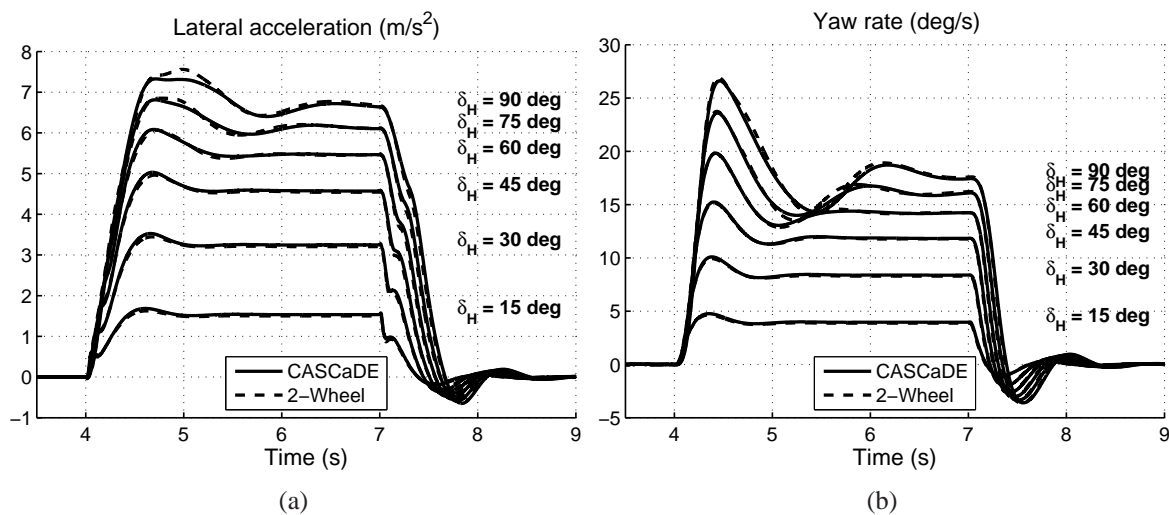


Figure 10.17: Extrapolation results for load variation **L2**. In (a) lateral acceleration and in (b) yaw rate.

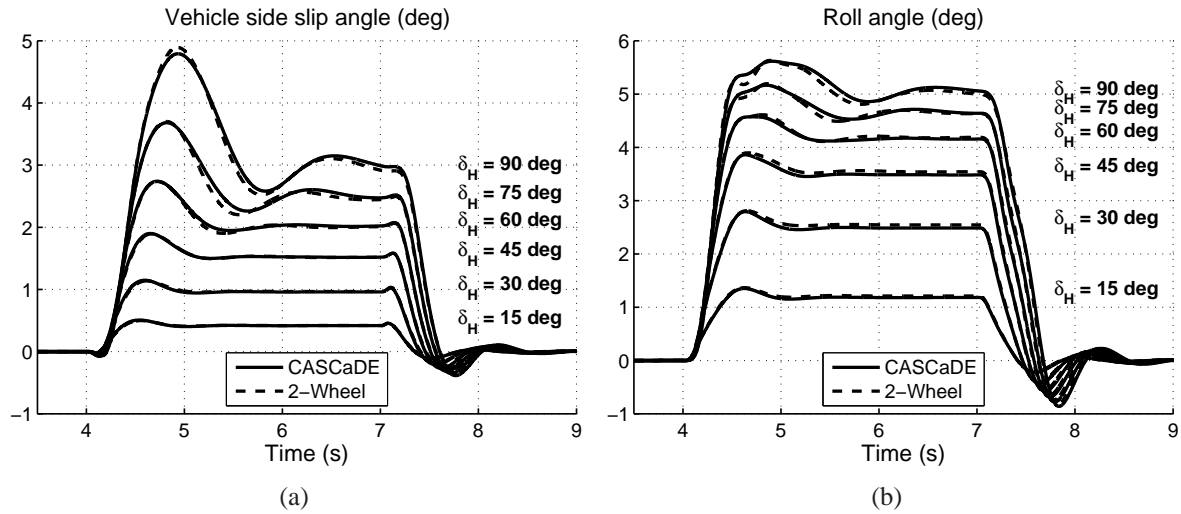


Figure 10.18: Extrapolation results for load variation **L2**. In (a) vehicle side slip angle and in (b) roll angle.

$\widehat{\delta}_H$ (deg)	a_y (m/s^2)		$\dot{\psi}$ (deg/s)		β (deg)		φ (deg)	
	RMS	max.	RMS	max.	RMS	max.	RMS	max.
90	0.080	0.25	0.239	0.78	0.045	0.14	0.060	0.18
75	0.056	0.20	0.190	0.64	0.039	0.17	0.041	0.11
60	0.041	0.17	0.097	0.52	0.020	0.07	0.032	0.09
45	0.041	0.13	0.074	0.43	0.009	0.03	0.047	0.09
30	0.040	0.12	0.083	0.32	0.011	0.03	0.040	0.08
15	0.030	0.13	0.069	0.19	0.004	0.01	0.021	0.04

Table 10.6: Root mean square (RMS) error and maximum error when comparing the model outputs of the reference model CASCaDE-DA and the 2-wheel model extrapolated with load variation **L2**.

Load condition L3:

Figure 10.19 compares the resulting lateral acceleration and yaw rate between the virtual measurements with the CASCaDE-DA model and the extended 2-wheel model with extrapolated parameters for the new load condition **L3**. The corresponding vehicle side slip angle and roll angle are furthermore compared in Figure 10.20. Also here the simulation outputs provided by the extended 2-wheel model can be considered to be sufficient results for such a significant change in loading condition. Only the transient part of the results provided in the maneuvers driven with steering wheel angle amplitudes of 75 deg and 90 deg could be criticized. Table 10.7 summarizes the statistics of the differences in motion outputs between the extended 2-wheel model and the virtual measurements.

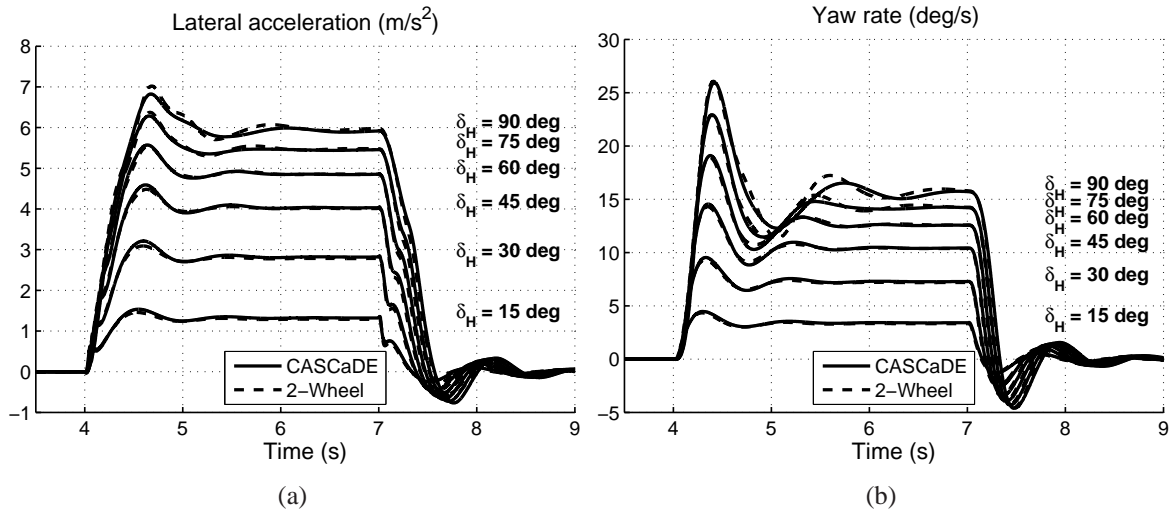


Figure 10.19: Extrapolation results for load variation **L3**. In (a) lateral acceleration and in (b) yaw rate.

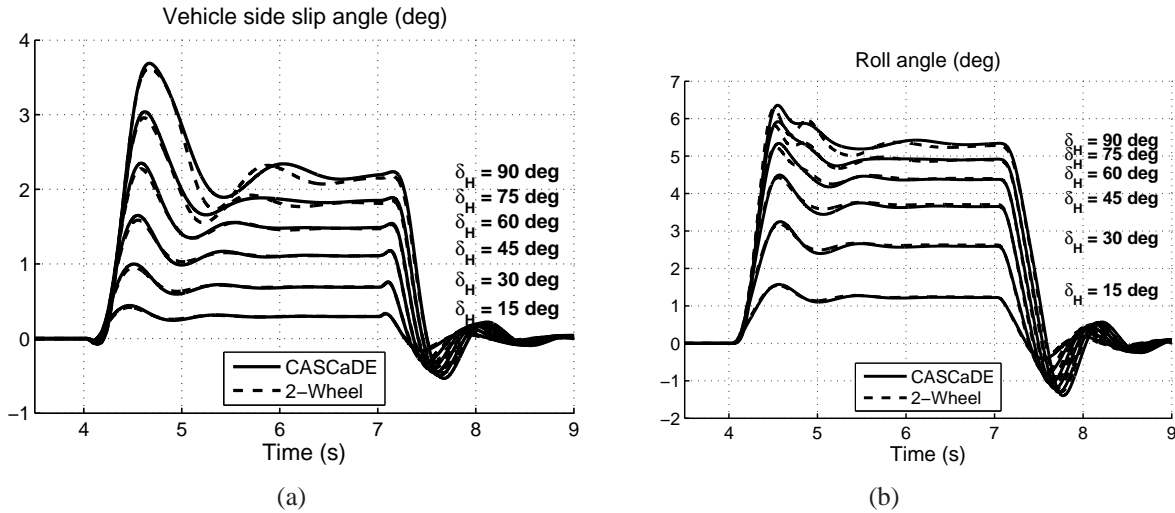


Figure 10.20: Extrapolation results for load variation **L3**. In (a) vehicle side slip angle and in (b) roll angle.

$\hat{\delta}_H$ (deg)	a_y (m/s ²)		$\dot{\psi}$ (deg/s)		β (deg)		φ (deg)	
	RMS	max.	RMS	max.	RMS	max.	RMS	max.
90	0.094	0.34	0.387	1.26	0.065	0.26	0.116	0.44
75	0.067	0.28	0.239	0.75	0.041	0.12	0.077	0.34
60	0.048	0.23	0.157	0.68	0.022	0.08	0.067	0.22
45	0.049	0.18	0.131	0.59	0.018	0.06	0.067	0.17
30	0.048	0.13	0.115	0.45	0.014	0.05	0.049	0.12
15	0.034	0.14	0.081	0.24	0.007	0.03	0.023	0.06

Table 10.7: Root mean square (RMS) error and maximum error when comparing the model outputs of the reference model CASCaDE-DA and the 2-wheel model extrapolated with load variation **L3**.

10.3.4 Extrapolation results for load variation L4 and L5

The same load variations as in Subsection 10.3.3 are investigated here as well but without the automatic ride height control system, i.e. the effects related to different initial suspension deflection as a result of other static axle loads are included in the load variations **L4** and **L5**.

Load condition L4:

Figure 10.21 presents the resulting lateral acceleration and yaw rate in a comparison between the virtual measurements with the CASCaDE-DA model and the extended 2-wheel model with extrapolated parameters for the new load condition **L4**. The corresponding vehicle side slip angle and roll angle are furthermore compared in Figure 10.22. In this case, the model accuracy for the maneuvers driven with steering wheel angle amplitudes larger than 60 deg can not be considered sufficient. The difference in motion outputs between the extended 2-wheel model and the virtual measurements are summarized in Table 10.8.

Several reasons can be listed regarding why the model is incapable of providing the correct simulation outputs when extrapolating the **L4** load case.

- The compliance approach used in the extended 2-wheel model only considers the lateral tire forces and aligning moments. Hence, the parameters in this approach have been tuned to be the best compromise for the driving states in which they were parameterized. In the load condition **L4**, the initial suspension deflection will be very different (especially at the rear axle) and therefore also the compliance response of the suspension at similar lateral tire forces and aligning moments.
- With the suspension springs being compressed much more due to the higher vertical loads (especially on the rear axle), the suspension springs are already in the progressive part of the force characteristics $F(\Delta z)$, causing a very non-linear response of the axle. This causes additional vertical force components in the suspension which excites a heave motion of the axle and consequently also different vertical tire forces. The only way to depict the same behavior would be to introduce heave in the roll model but this would also question the necessity of staying within the 2-wheel model concept – a model similar to the CASCaDE-Classic model (see Section 2.3) would then be more appropriate.
- The roll centers are assumed to be fixed in the extended 2-wheel model. This is a significant simplification, especially at different initial suspension deflections.

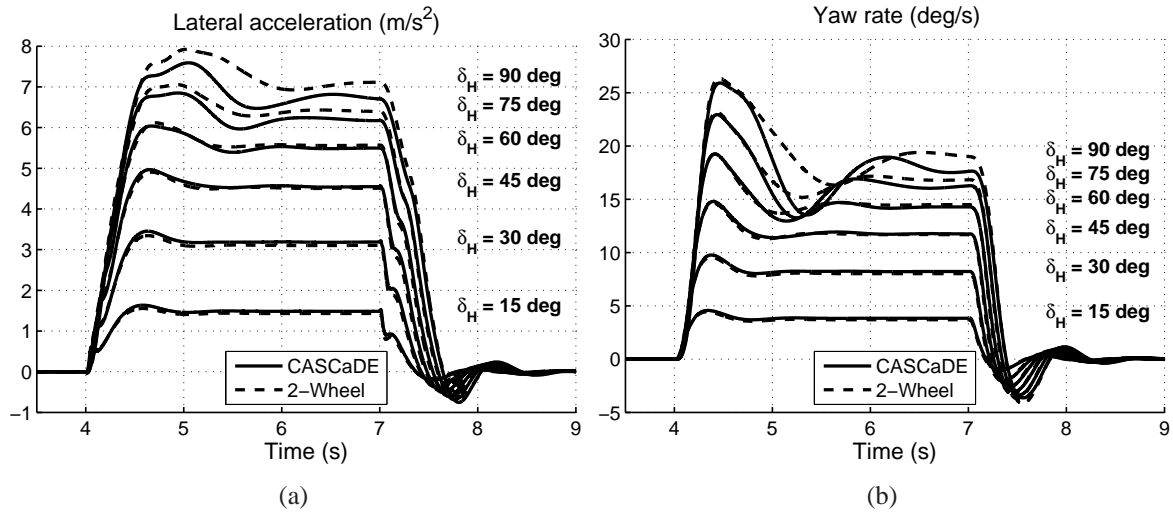


Figure 10.21: Extrapolation results for load variation **L4**. In (a) lateral acceleration and in (b) yaw rate.

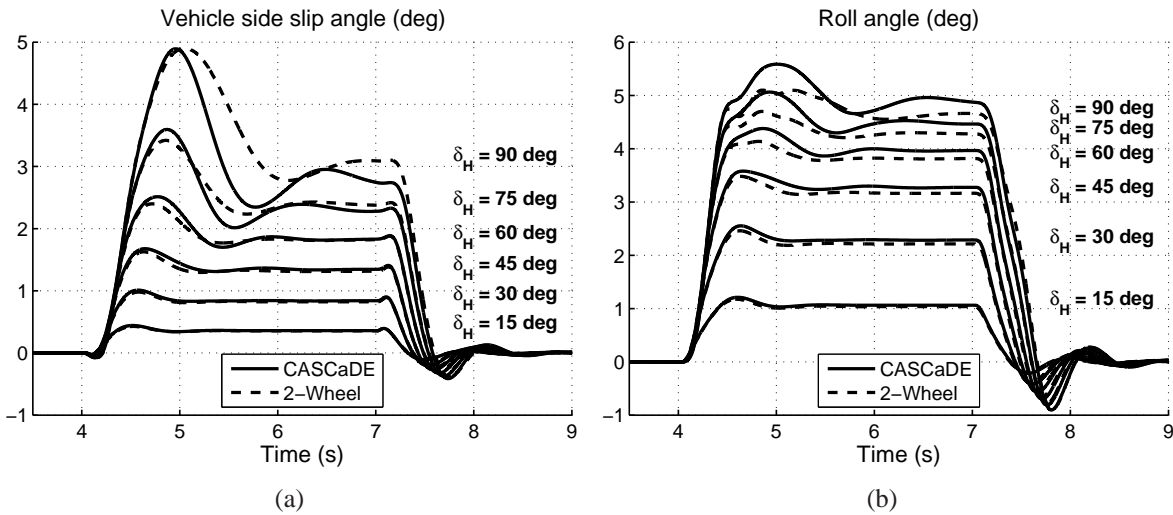


Figure 10.22: Extrapolation results for load variation **L4**. In (a) vehicle side slip angle and in (b) roll angle.

$\hat{\delta}_H$ (deg)	a_y (m/s ²)		ψ (deg/s)		β (deg)		φ (deg)	
	RMS	max.	RMS	max.	RMS	max.	RMS	max.
90	0.284	0.85	0.970	4.48	0.244	1.16	0.179	0.56
75	0.154	0.37	0.459	2.04	0.074	0.30	0.141	0.43
60	0.070	0.21	0.216	0.81	0.033	0.17	0.112	0.29
45	0.056	0.21	0.123	0.60	0.029	0.10	0.082	0.18
30	0.071	0.19	0.162	0.47	0.016	0.03	0.056	0.10
15	0.044	0.14	0.104	0.24	0.005	0.02	0.021	0.04

Table 10.8: Root mean square (RMS) error and maximum error when comparing the model outputs of the reference model CASCaDE-DA and the 2-wheel model extrapolated with load variation **L4**.

Load condition L5:

Figure 10.23 compare the resulting lateral acceleration and yaw rate between the virtual measurements with the CASCaDE-DA model and the extended 2-wheel model with extrapolated parameters for the new load condition **L5**. The corresponding vehicle side slip angle and roll angle are furthermore compared in Figure 10.24. The accuracy of the extended 2-wheel model is in this case not as questionable as for the **L4** but it is also not as good as in the rest of the extrapolation investigations. For the smaller discrepancies seen here, the same explanations regarding the model structure as given for the **L4** load condition can be applied here. The only difference in the **L5** load condition, is that the additional mass has been split up between the front and rear axle (in **L4** practically all additional mass was added to the rear axle) and, hence, the change in initial suspension deflection is not as significant here.

The statistics of how accurate the extended 2-wheel model manages to copy the behavior of the virtual measurements are concluded in Table 10.9.

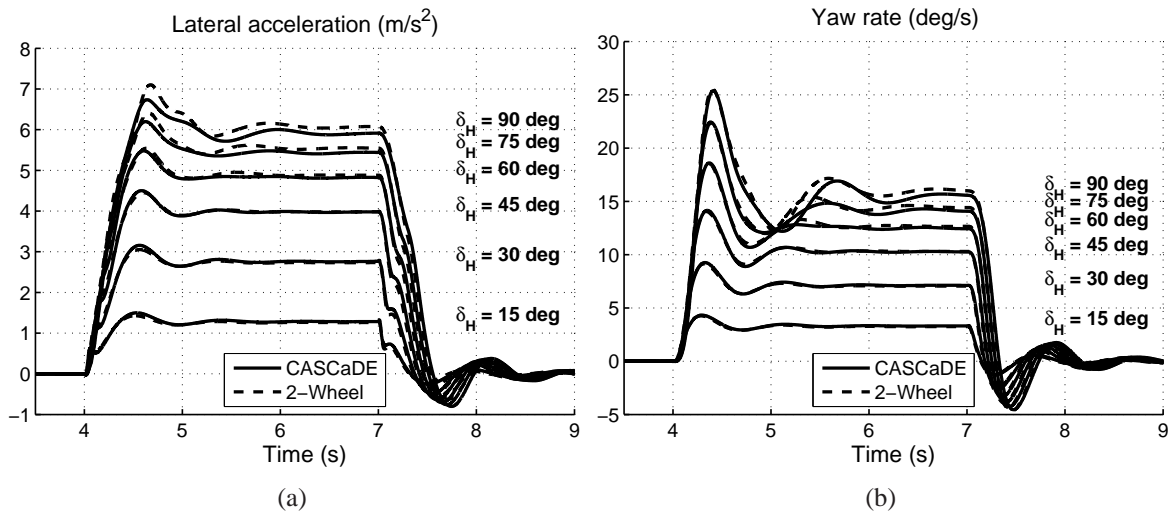


Figure 10.23: Extrapolation results for load variation **L5**. In (a) lateral acceleration and in (b) yaw rate.

$\hat{\delta}_H$ (deg)	a_y (m/s ²)		$\dot{\psi}$ (deg/s)		β (deg)		ϕ (deg)	
	RMS	max.	RMS	max.	RMS	max.	RMS	max.
90	0.158	0.43	0.420	1.52	0.067	0.26	0.204	0.44
75	0.119	0.32	0.317	1.09	0.056	0.18	0.169	0.32
60	0.082	0.28	0.216	0.72	0.038	0.08	0.133	0.24
45	0.049	0.23	0.117	0.62	0.024	0.08	0.101	0.21
30	0.049	0.16	0.097	0.46	0.014	0.06	0.072	0.16
15	0.032	0.14	0.066	0.24	0.008	0.03	0.038	0.09

Table 10.9: Root mean square (RMS) error and maximum error when comparing the model outputs of the reference model CASCaDE-DA and the 2-wheel model extrapolated with load variation **L5**.

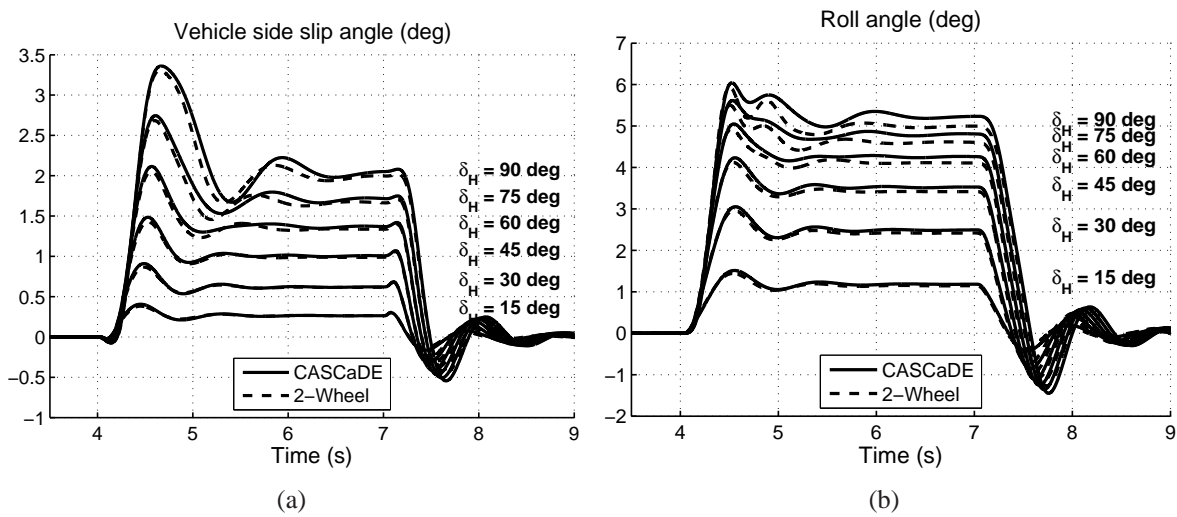


Figure 10.24: Extrapolation results for load variation L5. In (a) vehicle side slip angle and in (b) roll angle.

Chapter 11

Conclusions

This work focuses on the further development of the already existing non-linear 2-wheel model as described in Chapter 4 and also in Ammon [1], Kobetz [20] and Meljnikov [34], featuring a vehicle roll model and non-linear lateral axle force characteristics with a first order differential equation to capture the lateral force dynamics. The main objective of this work's further development is to overcome the model's drawbacks regarding extrapolation to different vehicle setups such as different tire properties, anti-roll bar stiffness and loading conditions (mass and mass geometry).

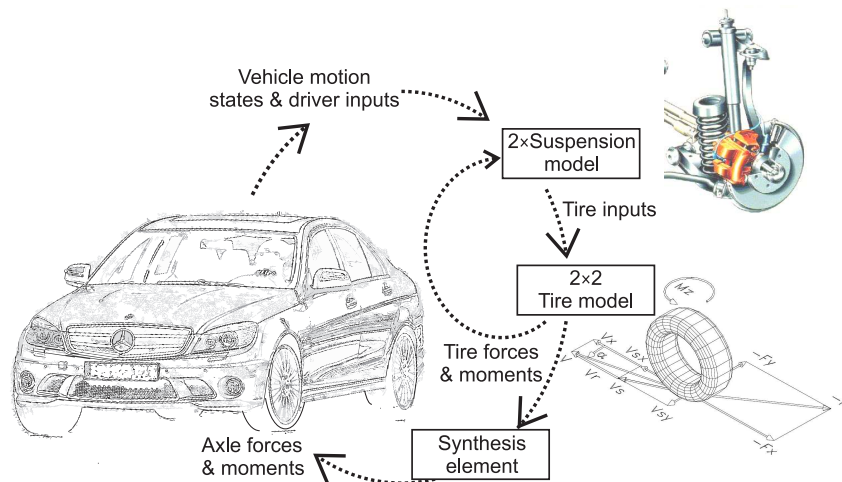


Figure 11.1: Outline of the tire suspension model.

In the proposed model, the lateral force characteristics front and rear (in the 2-wheel model) are replaced with a *suspension-tire-behavior model*, where the properties of the tires and the suspension have been separated into submodels, see Figure 11.1. Accordingly, vehicle motion states are used as inputs to the suspension submodels, which calculate the vertical tire loads, tire camber angles and lateral side slip angles. The outputs of the suspension submodels are furthermore used as inputs in the tire model, *Magic Formula MF-Tyre model version 5.2* [51]. In a final step, the lateral tire forces, $F_{y,i}$, and tire aligning moments, $M_{z,i}$, calculated by the tire model are concluded in a synthesis element to a front and rear axle lateral force, to be used in the 2-wheel model's equations of motion.

In order for the extended 2-wheel model to represent the correct vehicle behavior, the suspension subcomponents must reproduce the most important effects in the suspension. If, however, the subcomponents are too detailed, the model parameters will not be possible to identify through measurements. Hence, the model must follow the rule of thumb; *as detailed as necessary and as simple as possible*.

As an alternative to real driving measurements, virtual measurements created with the detailed MBS model CASCaDE-DA (see Section 2.2) were used in this work's investigations. The use of virtual measurements allow an expedient and thorough investigation of how different suspension setups influence the vehicle behavior, where in real driving tests would take more time. Moreover, unwanted influences from the environment as well as problems connected with measurement data may be avoided or, if wanted, they can be added synthetically. The results are also reproducible.

One of the main results in this work is the extended 2-wheel model including the *suspension-tire-behavior model* (presented in Chapter 7), accompanied by a description of how to identify its model parameters (Chapter 8). This is followed by a model validation to show the accuracy of the model (Chapter 9). Last but not least, the model's capabilities to be used in vehicle dynamics investigations is verified in a few investigations where model parameters are extrapolated (Chapter 10). First, it is shown that even very severe anti-roll bar setups can be extrapolated with the suggested model. In a second step, the extrapolation to different tire properties is carried out successfully. In a final step, extrapolation to different load variations has been tested. For vehicles equipped with an automatic ride height control system, the suggested approaches for extrapolation to different load conditions are as successful as for the previous extrapolation investigations. In case of vehicles without an automatic ride height control system, e.g. suspensions with normal coil springs and conventional dampers, the extreme load extrapolations are only successful to a steady-state lateral acceleration of approximately 5.5 m/s^2 . This model deficit can be explained by the change in initial suspension deflection due to the different loading condition, causing not only different roll center heights but also a change in the suspension compliance due to the different points of action for the forces acting in the suspension. The kinematic changes due to the different initial suspension deflection at different vehicle load conditions already have been taken into account by using the results from the kinematic test bench. However, the parameters regarding the suspension compliance (steer and camber angles) as well as the roll center heights would have to be adjusted for the different suspension deflections and this could not be included in these investigations and has therefore been left for future work.

It can therefore be concluded that the model can be used to extrapolate the vehicle behavior with different tires. This saves a significant amount of time in the development process where new vehicles have to be tested with all certified tires ¹. The model can also be used to predict how a suspension setup needs to be changed in order to reach a specific vehicle handling, e.g. how the anti-roll bar stiffness front and rear need to be changed to reach a certain under steer gradient and roll behavior. In addition, possible side effects due to a certain change in vehicle setup can also be detected in the simulations. Consequently, the prototype vehicles can be built more target oriented, saving both time and money. Also, the developed model can be used to

¹This does not replace vehicle dynamics testing but can speed up the process as critical driving states can be targeted in the testing justified by simulation studies.

predict the behavior of the vehicle at different loading conditions and, again, this can help speed up the testing process in the same way as described for the tire extrapolations.

Within this work, little effort has yet been spent on the longitudinal dynamics of the vehicle. To further benefit from the model presented here, it is recommended to continue the work by including also the longitudinal behavior in the model. Analogously to the vehicle roll model presented in this work, a pitch model could be included to capture the pitch dynamics of the vehicle. In addition to this, the present suspension compliance approach needs to be extended to also include the longitudinal forces. The drive train effects would also need to be investigated further, e.g. all-wheel drive, torque vectoring, etc. On the other hand, kinematic steer and camber angles due to pitch angle change are not expected to be significant. However, this also needs to be investigated further.

The model as it is today could already be used to simulate an active roll stabilization (ARS) system. This can be implemented by simply adding the active roll moments front and rear, $\Delta M_{ARS,j}$, to the total roll moment $M_{x,j}$ in Equation 7.3.

To further improve the model's useability, the possibility to simulate the vehicle driving over an uneven road could be implemented. For this, the uneven road can be described with for instance *OpenCRG* [40]. As the vehicle progresses over the surface, the left and right tire contact point can be used to calculate a road roll angle, $\phi_{road,j}$, at axle j , which are to be used as a further input to the vehicle roll model. With this model extension, the vehicle comfort behavior regarding roll dynamics can be evaluated and, if applicable, the benefit of an ARS system could be investigated.

Bibliography

- [1] D. Ammon. *Modellbildung und Systementwicklung in der Fahrzeugdynamik*. Teubner-Verlag, ISBN: 3-519-02378-4 Gb., 1997.
- [2] D. Ammon. Vehicle dynamics analysis tasks and related tyre simulation challenges. *Vehicle System Dynamics*, 43(Supplement 1):30–47, 2005.
- [3] D. Ammon, M. Gipser, J. Rauh, and J. Wimmer. High performance system dynamics simulation of the entire system tire-suspension-steering-vehicle. *Vehicle System Dynamics*, Vol. 27:435–455, 1997.
- [4] P. Bayle, J. F. Forissier, and S. Lafon. A new tyre model for vehicle dynamics simulations. *Automotive Technology International*, pages 193–198, 1993.
- [5] F. Böhm. *Zur Mechanik des Luftreifens*. Habilitationsschrift, Universität Stuttgart, 1966.
- [6] M. M. Chatillon, L. Jezequel, P. Coutant, and P. Baggio. Hierarchical optimisation of the design parameters of a vehicle suspension system. *Vehicle System Dynamics*, 44(11):817–839, November 2006.
- [7] C. Däsch. Lenkungsmodellierung für model- based- testing. Diplomarbeit, FHTE-Esslingen, 2004.
- [8] K. Desoyer and A. Slibar. Kraftschlußbeanspruchungen und Schräglauf der Räder eines Kraftfahrzeuges bei stationärer Kurvenfahrt. *Automobiltechnische Zeitschrift (ATZ)*, 72(6):206–212, 1970.
- [9] Deutsche Norm. *DIN 70000 Straßenfahrzeuge – Fahrzeugdynamik und Fahrverhalten – Begriffe*, 1994.
- [10] S. Frik. *Untersuchungen zur erforderlichen Modellkomplexität bei der Fahrdynamiksimulation*. Ph.d. thesis, Universität Duisburg, 1994. Mechanik und Mechatronik, Fortschritt-Berichte VDI Band 208.
- [11] M. Gipser. FTire, A New Fast Tire Model for Ride Comfort Simulations. International ADAMS User’s Conference Berlin 1999, available from <http://www.ftire.com>.
- [12] M. Gipser. Zur Modellierung des Reifens in CASCaDE. In *Dynamische Probleme*, pages 41–57, Hannover, Okt. 1990.

- [13] R. Gnadler. *Das Fahrverhalten von Kraftfahrzeugen bei instationärer Kurvenfahrt mit verschiedener Anordnung der Hauptträgheitsachsen und der Rollachse*. Ph.d. thesis, Universität Karlsruhe, 1971.
- [14] B. Heißling and M. Ersoy. *Fahrwerkhandbuch – Grundlagen, Fahrdynamik, Komponenten, Systeme, Mechatronik, Perspektiven*. Vieweg+Teubner Verlag, ISBN: 978-3-8348-0444-0, Wiesbaden, 2008.
- [15] W. Hirschberg, G. Rill, , and H. Weinfurter. User-appropriate tyre-modelling for vehicle dynamics in standard and limit situations. *Vehicle System Dynamics*, 38(3):103–125, 2002.
- [16] W. Hurich, J. Luther, and H.-P. Schöner. Koordiniertes Automatisiertes Fahren zum Entwickeln, Prüfen und Absichern von Assistenzsystemen. In *10. Braunschweiger Symposium AAET 2009, Automatisierungs-, Assistenzsysteme und eingebettete Systeme für Transportmittel*, Braunschweig, February 2009.
- [17] International Organization for Standardization. *ISO 8855 Road vehicles – Vehicle dynamics and road-holding ability – Vocabulary*, 1991.
- [18] S. Jansen, L. Verhoeff, and R. Cremers. MF-Swift simulation study using benchmark data. *Vehicle System Dynamics*, 43, Supplement:92–101, 2005.
- [19] B. Keßler. *Bewegungsgleichungen für Echtzeitanwendungen in der Fahrzeugdynamik*. Ph.d. thesis, Universität Stuttgart, Institut B für Mechanik, 1989.
- [20] C. Kobetz. *Modellbasierte Fahrdynamikanalyse durch ein an Fahrmanövern parameterisiertes querdynamisches Simulationsmodell*. Ph.d. thesis, Technischen Universität Wien, Institut für Mechanik, Abteilung für Angewandte Mechanik, Vienna, Austria, 2003.
- [21] C. Kobetz, P. Lugner, and R. Rutz. Modellbasierte Fahrdynamikanalyse. *Automobiltechnische Zeitschrift (ATZ)*, 106(11):1030–1037, 2004.
- [22] N. Kuralay. Einfluss von Fahrwerkselastizitäten und Reifenparametern auf das Fahrverhalten von PKW. *Automobil-Industrie 31, Heft 5*, pages 577–585, 1986.
- [23] M. Lahti. Modelling rubber bushings using non-linear elastic force, friction and fractional derivative. Master’s thesis, Royal Institute of Technology, Stockholm, Sweden, 2003.
- [24] M. Lahti, C. Daesch, W. Schindler, L. Diebold, and J. Haug. Einspurmodell für die Fahrdynamiksimulation und -analyse. *Automobiltechnische Zeitschrift (ATZ)*, 108(11):962–967, 2006.
- [25] V. Lima. Axle load influence in vehicle handling models. Master Thesis, FHTE-Esslingen, 2006.
- [26] LMS, Presents the simulation tool LMS Virtual.Lab Vehicle Motion from LMS. <http://www.lmsintl.com/simulation/vehicle-motion>, Read February, 2012.
- [27] P. Lugner. Untersuchungen über die stationäre Kurvenfahrt eines Kraftfahrzeugs auf überhöhter Fahrbahn. *Automobiltechnische Zeitschrift (ATZ)*, 75(8):286–289, 1973.

- [28] P. Lugner. The influence of the structure of automobile models and tire characteristics on the theoretical results of steady-state and transient vehicle performance. In *The dynamics of vehicles on roads and on Tracks*, pages 21–39, 1978. IUTAM Symposium, Vienna, Austria, 1977.
- [29] P. Lugner, K. Desoyer, and A. Novak. Abbremsung eines Kraftfahrzeuges in einer überhöhten Klotheide. *Automobil-Industrie Heft 1*, pages 19–26, 1977.
- [30] P. Lugner, R. Lorenz, and E. Schindler. The connexion of theoretical simulation and experiments in passenger car dynamics. *Vehicle System Dynamics*, Vol. 40:317–330, 1984.
- [31] P. Lugner, H. Pacejka, and M. Plöchl. Recent advances in tyre models and testing procedures. *Vehicle System Dynamics*, 43(6-7):413–436, June-July 2005.
- [32] P. Lugner and M. Plöchl. Modelling in vehicle dynamics of automobiles. *Zeitschrift für angewandte Mathematik und Mechanik* 84, pages 219–236, 2004. Institute of Mechanics, Vienna University of Technology, Austria.
- [33] The MathWorks, Inc. *Optimization Toolbox Users Guide*, September 2003, Version 2.
- [34] D. Meljnikov. *Entwicklung von Modellen zur Bewertung des Fahrverhaltens von Kraftfahrzeugen*. Ph.d. thesis, Universität Stuttgart, Institut A für Mechanik, 2003.
- [35] M. Minakawa and M. Higuchi. A theoretical study of vehicle roll behavior and its influence on transient handling. *11. Aachener Kolloquium Fahrzeug- und Motorentechnik*, pages 479–503, 2002.
- [36] M. Mitschke and H. Wallentowitz. *Dynamik der Kraftfahrzeuge*. Springer-Verlag, ISBN: 3-540-42011-8, Berlin Heidelberg New York, 4th edition edition, 2004.
- [37] MSC.Software Corporation. <http://www.mscsoftware.com/Products/CAE-Tools/Adams.aspx>, Read February, 2012.
- [38] T. Nakatsuka and K. Takanami. Cornering ability analysis based on vehicle dynamics system. *SAE Article 700368*, pages 210–225, 1970.
- [39] C. Oertel and A. Fandre. Das Reifenmodellsystem RMOD-K, ein Beitrag zum virtuellen Fahrzeug. *Automobiltechnische Zeitschrift (ATZ)*, 103(11):1074–1079, 2001.
- [40] OpenCRG, Presents OpenCRG which is a series of open file formats and open source tools for the detailed description, creation and evaluation of road surfaces. <http://www.opencrg.org/>, Read February, 2012.
- [41] H. Otto. *Lastwechselreaktion von PKW bei Kurvenfahrt*. Ph.d. thesis, Technische Universität Braunschweig, 1987.
- [42] H. Paknia. *Identifizierung von Reifenkennfeldern aus Fahrmessungen auf der Straße*. Ph.d. thesis, Institut für Kraftfahrwesen Aachen (ika) RWTH Aachen, 2001. Schriftenreihe Automobiltechnik.

- [43] J. Rauh. Virtual development of ride and handling characteristic for advanced passenger cars. *Vehicle System Dynamics*, Vol. 40:135–155, 2003.
- [44] J. Rauh and M. Mössner-Beigel. Tyre simulation challenges. *Vehicle System Dynamics*, 46(1):49–62, 2008.
- [45] A. Riedel. *Standard Tire Interface*. International Tire Working Group, June 1995, Release 1.2.
- [46] P. Riekert and T. Schunck. Zur Fahrmechanik des gummibereiften Kraftfahrzeugs. *Ingenieur-Archiv, Band 11*, pages 210–224, 1940.
- [47] G. Rill. *Simulation von Kraftfahrzeugen*. Verlag Vieweg, ISBN: 3-528-08931-8, Braunschweig/Wiesbaden, 1994.
- [48] M. Russo, R. Russo, and A. Volpe. Car parameters identification by handling manoeuvres. *Vehicle System Dynamics*, 34:423–436, 2000.
- [49] H.-P. Schöner, S. Neads, and N. Schretter. Testing and verification of active safety systems with coordinated automated driving. In *Technical Conference on the Enhanced Safety of Vehicles*, Stuttgart, June 2009.
- [50] U. Sorgatz. *Ein theoretisches Fahrzeugmodell zur Abbildung der Fahrdynamik bis in den Grenzbereich*. Ph.d. thesis, RWTH Aachen, Institut für Kraftfahrwesen, 1973.
- [51] TNO. *MF-Tyre 5.2 User Manual*, 2001.
- [52] H. Unrau and J. Zamow. *TYDEX-Format, Description and Reference Manual*. International Tire Working Group, July 1995, Release 1.1.
- [53] O. Winkelmann. Anforderungen an das Fahrverhalten von Kraftfahrzeugen. *Automobil-technische Zeitschrift (ATZ)*, 63(5):121–128, 1961.
- [54] A. Zomotor. *Fahrwerktechnik: Fahrverhalten*. Vogel Buchverlag, ISBN: 3-8023-0774-7, Würzburg, 2nd edition, 1991.
- [55] Z. Zomotor. *Online-Identifikation der Fahrdynamik zur Bewertung des Fahrverhaltens von Pkw*. Ph.d. thesis, Universität Stuttgart, Fakultät Verfahrenstechnik und Technische Kybernetik, 2002.

Appendix A

Nomenclature

The main part of all definitions in this thesis are primarily founded on the international standard ISO 8855 [17] and DIN 70000 [9]¹. However, since many symbols and corresponding indices have had to be added or changed, this section presents a list of the used axis systems, nomenclature and abbreviations.

A.1 Common definitions and terminology

- Matrices and vectors are denoted **bold**, e.g. the force $\mathbf{F} = (F_x, F_y, F_z)$.
- *Italics* are used when introducing new terms.
- Mathematic properties are written *slanted*.

A.2 Abbreviations

ABS	Antilock Braking System	DOF	Degrees Of Freedom
AJR	Alternating jounce and rebound	ESP	Elektronische Stabilitätsprogramm, in english Electronic Stability Control (ESC) ²
ARB	Anti-roll bar		
AWD	All Wheel Drive	max	Maximum
CASCaDE	Computer Aided Simulation of Car Driver and Environment	min	Minimum
		MBS	Multi Body System
CG	Center of Gravity	RAG	Roll Angle Gradient

¹DIN 70000 comprises an additional appendix with extra terms and definitions.

²ESC is a technology that improves the safety of a vehicle's stability by detecting and minimizing skids. When ESC detects loss of steering control, it automatically applies the individual brakes to help "steer" the vehicle where the driver intends to go.

RMS	Root mean square	SJR	Synchronized jounce and rebound
-----	------------------	-----	---------------------------------

A.3 Notation

F	Force [N]	γ	Tire camber angle ³ [rad]
M	Moment [Nm]	ε	vehicle camber angle ³ [rad]
h	Height [m]	β	Vehicle side slip angle ³ [rad]
Δh	Length of roll lever arm [m]	μ	tire-road adhesion coefficient [–]
C	Spring stiffness ³ [N/m] and [Nm/°]	i	Translation ratio [–], e.g. between wheel travel and spring deflection.
m	Mass [kg]	$\phi, \dot{\phi}, \ddot{\phi}$	Roll angle ³ , rate and acceleration [rad, rad/s, rad/s ²]
t	Time [s]	$\psi, \dot{\psi}, \ddot{\psi}$	Yaw angle ³ , rate and acceleration [rad, rad/s, rad/s ²]
Δt	Simulation time step [s]	J	Inertia [kgm ²]
v	Velocity [m/s or km/h]	$\Delta x, \Delta y, \Delta z$	Displacement in x, y and z direc- tion [m]
a	Acceleration [m/s ²]	C_α	Cornering stiffness ³ $\left. \frac{dF_y}{d\alpha} \right _{\alpha=0}$ [N/rad]
ω	Angular velocity ³ [rad/s]	B, C, D, E	Parameters in tire model MF 5.2
g	Gravitational acceleration [m/s ²]	n_P	Pneumatic trail [m]
l	Length [m] (wheel base when l without subscript)	ξ	Polynomial coefficients in the non- linear compliance approach for the CASCaDE-Classic model [–]
b	Track width [m]		
α	Tire side slip angle ³ [rad]		
s_x	Longitudinal tire slip [–]		
δ	Steer angle ³ [rad]		

A.4 Subscripts

i	Wheel i where $i = 1, 2, 3, 4$ equals front left, front right, rear left and rear right in the mentioned order	f	Front axle
		r	Rear axle
		j	Axle j , where $j = f, r$ equals front

³For better readability, all numbers in tables and figures are presented based on the unit degrees instead of radians, e.g. $N/^\circ$ instead of N/rad . However, in the presented equations the radian based values have to be used instead of degrees.

	and rear axle.	ψ	Vehicle yaw direction
x, y, z	Components of a vector pointing in longitudinal, lateral and vertical direction.	δ	Steering direction
		0	Static condition or parameter, e.g. δ_0 - static toe angle
su	Suspension		
ti	Tire	CG	Center of gravity, e.g. center of gravity height h_{CG}
D	Driver, e.g. δ_D is the steering wheel angle.	RC	Roll center
A	Ackerman steering angle δ_A	d	Damper
w	Wheel	k	Kinematics
r	Rack in a rack-and-pinion steering system	c	Compliance
ϕ	Vehicle roll direction	out, in	Outer and inner side

A.5 Superscripts

$dyn, stat$	Dynamic and steady-state	$2T$	Denote an equivalent axle force created by the sum of the axle's two tires, e.g. equivalent lateral axle force F_y^{2T} .
A	Axle, e.g. axle side slip angle α^A		

Appendix B

Additional extrapolation results

The following three pages show the figures of the simulation results left out in Section 10.1.

B.1 Anti-roll bar extrapolation results

B.1.1 Extrapolation results for ARB 2

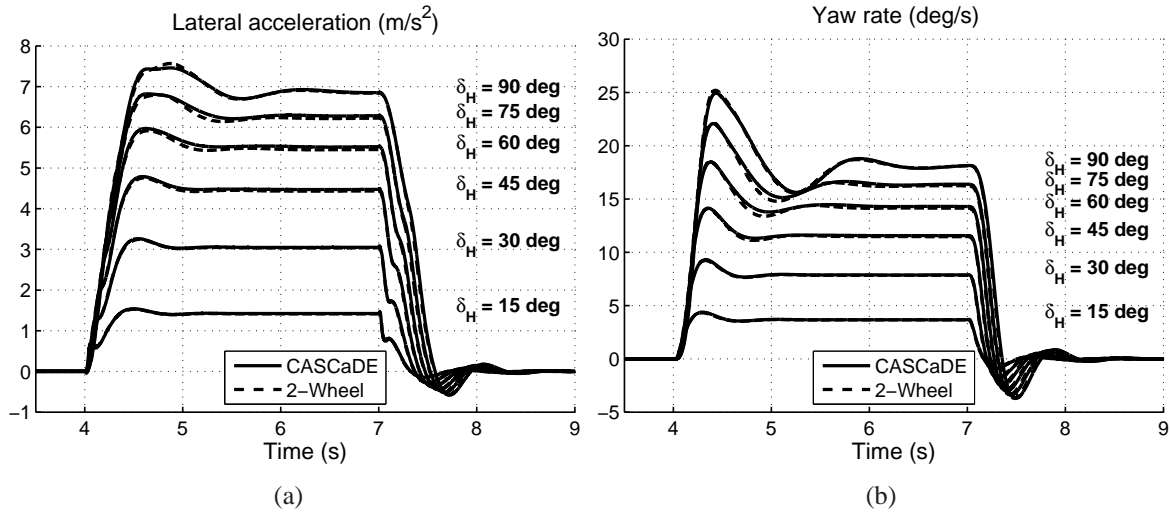


Figure B.1: Extrapolation results for **ARB 2**. In (a) lateral acceleration and in (b) yaw rate.

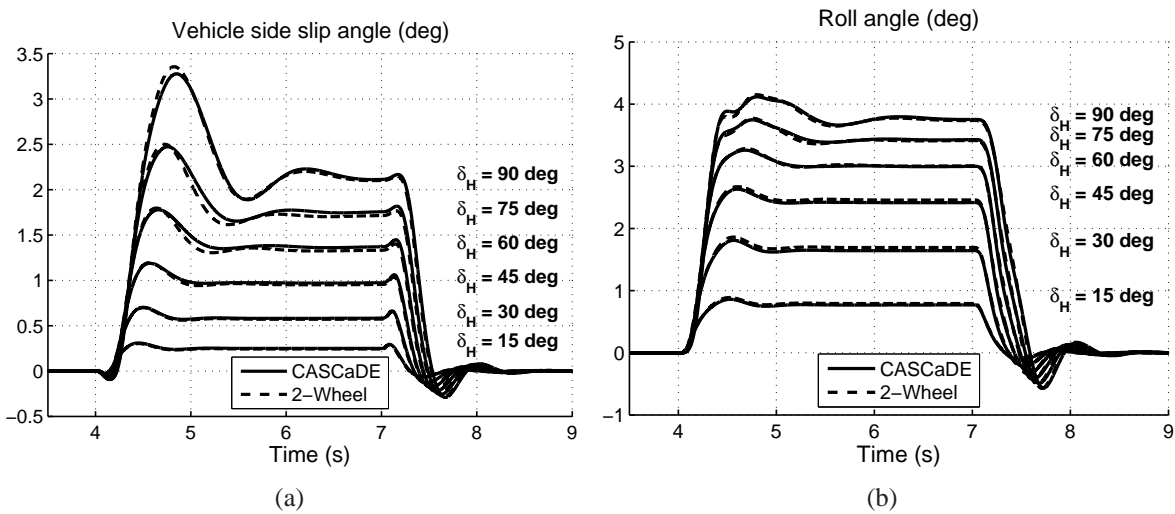


Figure B.2: Extrapolation results for **ARB 2**. In (a) vehicle side slip angle and in (b) roll angle.

B.1.2 Extrapolation results for ARB 3

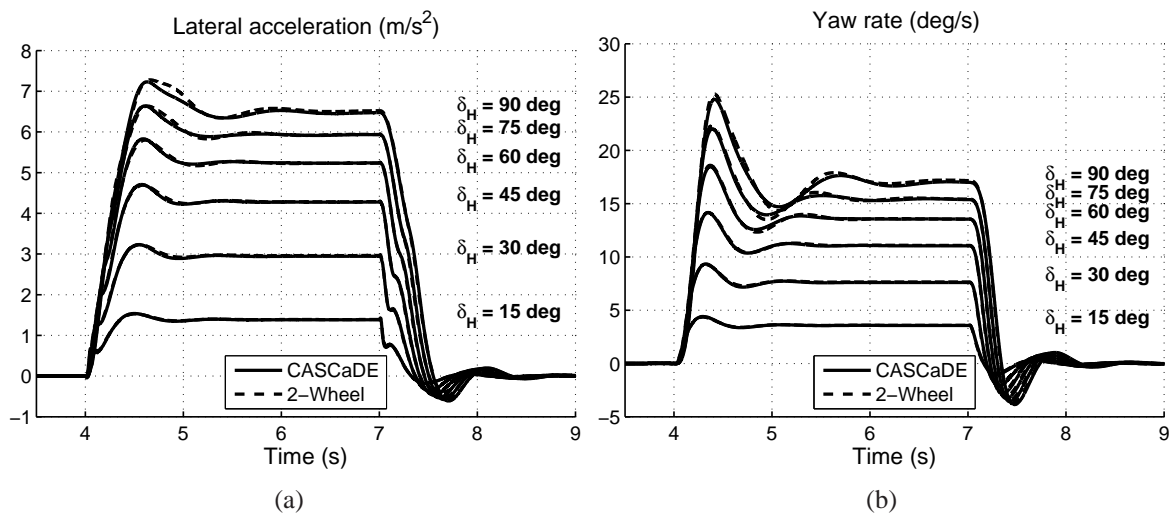


Figure B.3: Extrapolation results for ARB 3. In (a) lateral acceleration and in (b) yaw rate.

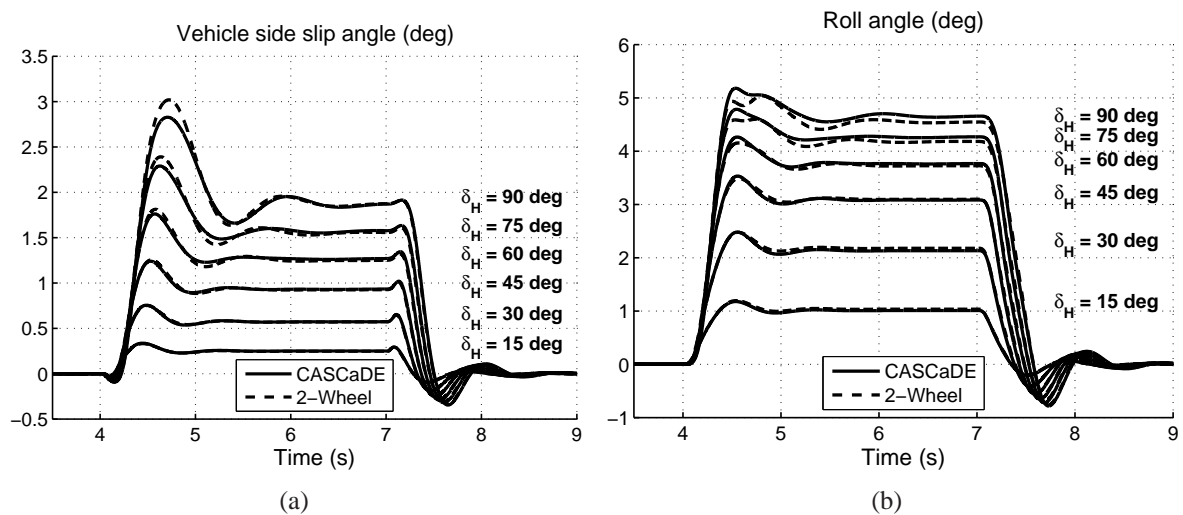


Figure B.4: Extrapolation results for ARB 3. In (a) vehicle side slip angle and in (b) roll angle.

B.1.3 Extrapolation results for ARB 5

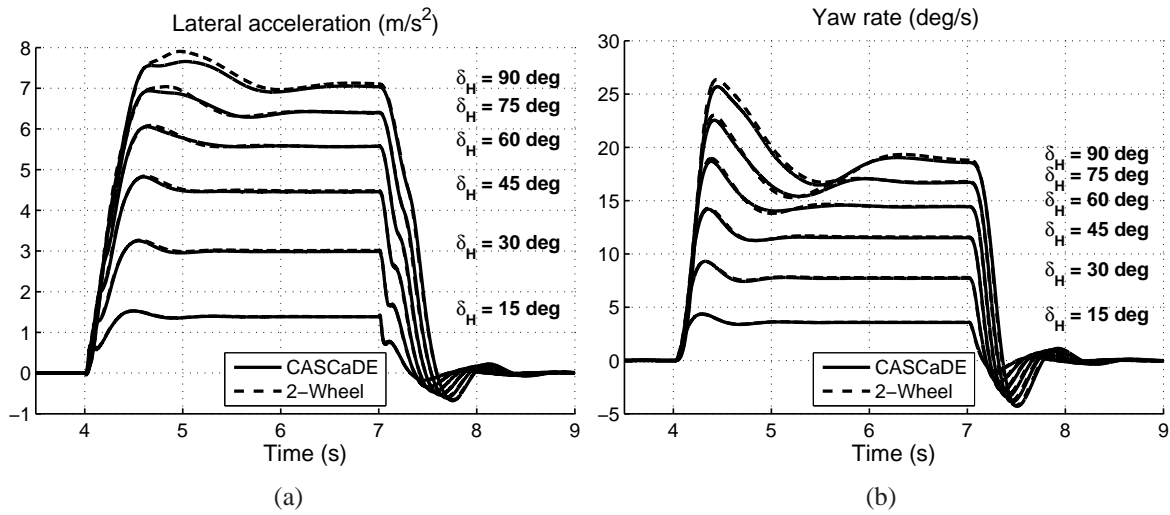


Figure B.5: Extrapolation results for ARB 5. In (a) lateral acceleration and in (b) yaw rate.

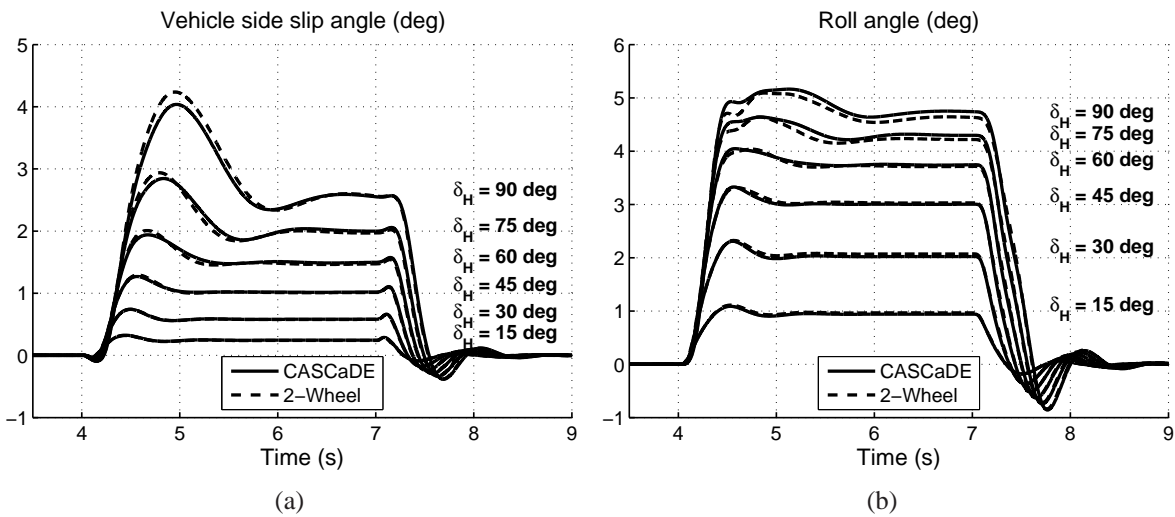


Figure B.6: Extrapolation results for ARB 5. In (a) vehicle side slip angle and in (b) roll angle.

LEBENS LAUF

- Name:** Magnus Lahti
- Geboren:** 13. Januar in Boden, Schweden
- Eltern:** Kapten Nils Erik Lahti
Karin Louise Lahti, geb. Fridlund
- Schulbildung:** 1994 – 1997 Abiturschule Björknässkolan in Boden, Schweden, Hauptfach Technik.
- Präsenzdienst:** 1997 – 1998 Wehrdienst als Gruppenleiter Spähtrupp bei MEKB 19 bei der Stadt Boden in Schweden.
- Studium:** 1998 – 2003 Master of Science, Automotive Engineering and Vehicle Dynamics bei der Königlichen Technischen Hochschule (KTH) in Stockholm, Schweden.
- 2003 Diplomarbeit bei der Daimler AG, mit dem Titel: Modeling Rubber Bushings using Non-linear Elastic Force, Friction and Fractional Derivatives.
- Beruf:** 2010 – derzeit, Entwicklungsingenieur Hard/Software im Team Funktionale Architektur für Fahrerassistenz- und Fahrwerksysteme.
- 2009 – 2010 Entwicklungsingenieur Hard/Software im Team Simulationstechnik.
- 2007 – 2008 Team Coordinator for Active and Chassis Systems bei MB RDNA (Mercedes-Benz Research and Development, North America) in Auburn Hills, Michigan.
- 2004 – 2007 Doktorand bei der Forschung und Vorentwicklungsabteilung GR/EAV, Daimler AG.
Promotionsthema: Fahrwerk-Reifen Wirkungsmodelle.
- 2002 Praktikum bei Scania in Södertälje, Schweden.
- 2000 – 2001 Mathematik- und Naturwissenschaftslehrer in der 7. bis 9. Klasse bei Källtorpsskolan in Järfälla, Schweden.